Hydrocarbon Adsorption Characteristics and Absolute Adsorption Estimation in Shale Nanoporous Media from Statistical Thermodynamics Approaches

by

Wanying Pang

A thesis submitted in partial fulfillment of the requirements for the degree of

Doctor of Philosophy

in

Petroleum Engineering

Department of Civil and Environmental Engineering

University of Alberta

ABSTRACT

Shale gas has become a very important unconventional energy resource and significantly increased the global energy supply. Due to the presence of large amount of specific surface area and nanopores in shale rock, the phenomenon of gas molecules accumulation on the solid surface is the so-called adsorption. The enhanced storage capacity of shale will control the production and provide additional gas during depletion. Therefore, understanding the sorption mechanism in shale nanoporous media and accurate characterization of methane absolute adsorption (m_{abs}) play an important role in the gas-in-place estimation and prediction of well productivity.

In the proposed dissertation, we first perform grand canonical Monte Carlo (GCMC) simulation to investigate the methane adsorption in organic mesopore at various pressures. Based on the density distributions, we characterize the transition zone between the first adsorption layer and free gas phase, then a modified Ono-Kondo (OK) lattice model with multilayer structure is proposed for accurately estimating m_{abs} converted from experimentally measured excess adsorption (m_{ex}) to better account for the effect of transition zone. In addition to methane which contributes shale gas compositions, propane is one of major heavier constituents in shale gases which can have multilayer adsorption behavior on the surface. Therefore, by studying the propane adsorption behavior from GCMC simulation, we propose a multi-layer OK model considering the correlation effect

arising from the strong adsorbate-adsorbate interactions beyond mean field theory (MFT) to regress m_{ex} and subsequently obtain the m_{abs}. However, shale has a widespread pore size distribution (PSD) and the adsorption behavior varies in micropores and mesopores. Based on the varying density profiles in different sized of nanopores obtained from GCMC, we propose the corresponding methane adsorption model in each nanopore. Combining the actual PSD and different adsorption behaviors in varying pores, by fitting m_{ex} in nanoporous media, OK lattice model can readily obtain m_{abs}. Large number of randomly generated PSDs are used to validate our model. Then, we assess various commonly used methods converting the m_{ex} to the m_{abs} systematically and comprehensively and give suggestions in experiment measurements. Furthermore, considering the continuous pore size distribution in shale, the OK model utilizing PSD lumping method has been proposed to account for the specific adsorption behavior in series of adsorption types over different range of nanopores. Lastly, since inorganic clay minerals are observed to also be responsible for gas adsorption, the methane adsorption capacity controlled by both complex confinement effect and heterogeneous rock type has been studies by molecular simulation. Then, we propose the OK-dual heterogeneity (OK-DH) model to consider the heterogeneity of shale rock arising from various rock type and pore sizes. The proposed model can account for different fluid-surface interactions between methane and substrates and thus provide accurate prediction of adsorption behavior in not only shale matrix but also in specific rock and pore sizes.

PREFACE

A version of Chapter 2 has been published as Pang, W., & Jin, Z. (2019). Revisiting methane absolute adsorption in organic nanopores from molecular simulation and Ono-Kondo lattice model. Fuel, 235, 339-349. Pang, W. is responsible for the theoretical development, performing molecular simulation and model construction, analysis, and manuscript composition. Jin Z. is the supervisory author and is involved in conceiving the problem, designing the project and manuscript composition.

A version of Chapter 3 has been published as Pang, W., & Jin, Z. (2019). Ono-Kondo lattice model for propane multilayer adsorption in organic nanopores in relation to shale gas. Fuel, 235, 158-166. Pang, W. is responsible for the theoretical development, performing molecular simulation and model construction, analysis, and manuscript composition. Jin Z. is the supervisory author and is involved in conceiving the problem, designing the project and manuscript composition.

A version of Chapter 4 has been published as Pang, W., He, Y., Yan, C., & Jin, Z. (2019). Tackling the challenges in the estimation of methane absolute adsorption in kerogen nanoporous media from molecular and analytical approaches. Fuel, 242, 687-698. Pang, W. is responsible for the theoretical development, performing molecular simulation and model construction, analysis, and manuscript composition. He, Y. is responsible for performing GCMC simulation and data analysis. Yan, C. is responsible for reviewing

manuscript. Jin Z. is the supervisory author and is involved in conceiving the problem, designing the project and manuscript composition.

A version of Chapter 5 has been published as Pang, W., Ye, Y., & Jin, Z. (2019). Assessment of various approaches in the prediction of methane absolute adsorption in kerogen nanoporous media. Energy & Fuels, 33(7), 6258-6263. Pang, W. is responsible for the theoretical development, performing molecular simulation and model construction, analysis, and manuscript composition. Ye, Y. is responsible for reviewing and polishing manuscript. Jin Z. is the supervisory author and is involved in conceiving the problem, designing the project and manuscript composition.

A version of Chapter 6 has been published as Pang, W., & Jin, Z. (2020). Methane Absolute Adsorption in Kerogen Nanoporous Media with Realistic Continuous Pore Size Distributions. Energy & Fuels, 34 (10), 12158-12172. Pang, W. is responsible for the theoretical development, performing molecular simulation and model construction, analysis, and manuscript composition. Jin Z. is the supervisory author and is involved in conceiving the problem, designing the project and manuscript composition.

A version of Chapter 7 will be submitted to Energy & Fuels for publication as Pang, W., & Jin, Z. (2020). Absolute Adsorption of Methane in Shale Nanoporous Media: Challenges Arising from Dual-Heterogeneity. Pang, W. is responsible for the theoretical development, performing molecular simulation and model construction, analysis, and manuscript

composition. Jin Z. is the supervisory author and is involved in conceiving the problem, designing the project and manuscript composition.

Chapter 1 outlines the research background, problem statement, research objectives, and structure of the thesis. Chapter 8 summarizes the conclusions reached in this thesis as well as the recommendations for future research. Chapters 1 section 1 has been partially published as Pang, W., Wang, Y., & Jin, Z. (2021). Comprehensive Review about Methane Adsorption in Shale Nanoporous Media. Energy & Fuels. Pang, W. is responsible for the theoretical development, literature review and manuscript composition. Wang, Y. is involved in data collection and manuscript composition. Jin Z. is the supervisory author and is involved in conceiving the problem, designing the project and manuscript composition. Chapter 7 is originally written by Pang W. and have never been published elsewhere.

DEDICATION

This dissertation is dedicated to my dearest parents: my mother Mrs. Fengyu Gao and my

father Mr. Xiangyang Pang.

ACKNOWLEDGMENTS

Table of Contents

List of Tables

List of Figures

gas zone are obtained by $\rho_{a1} = \int_A^B \rho(z)dz / z_{AB}$, $\rho_{a2} = \int_B^C \rho(z)dz / z_{BC}$,

$\rho_{a3} = \int_C^D \rho(z)dz / z_{CD}$, $\rho_{a4} = \int_D^E \rho(z)dz / z_{DE}$, $\rho_{a5} = \int_E^F \rho(z)dz / z_{EF}$, $\rho_{a6} = \int_F^G \rho(z)dz / z_{FG}$

CHAPTER 1 INTRODUCTION

1.1 Research Background

Different from the conventional reservoirs, the complex microscopic pore structures in shale formations leads to the unique characteristics of low porosity as well as permeability[1, 2], which ranges from nanodarcy (nD) to a few microdarcy (mD)[3]. The pores in shale have a broad range of size distributions from sub 1-nm to a few micrometers[4], while they are generally classified into micropores (pore size smaller than 2 nm), mesopores (pore size between 2 nm and 50 nm), and macropores (pore size larger than 50 nm)[5]. In addition, shale media consists of organic and inorganic matters[5, 6]. The inorganic matters include clay minerals, carbonates, and sandstones, etc., which are generally hydrophilic[5]. On the other hand, as the main constituent of organic matters, kerogen, which originates from sedimentary rocks by the decomposition of buried organic matters[7], is insoluble in polar organic solvents[7, 8]. Both organic and inorganic matters in shale can contain significant number of nano-scale pores, which greatly contribute to methane (the main constituent of natural gas) adsorption in shale. Gas sorption in shale media generally consists of free gas existing in mesopores, macropores and fractures; adsorbed gas which fills pore throats or adsorbed on the pore surface due to strong fluid-surface interaction; absorbed gas which is dissolved within kerogen matrix[9]. Among them, the adsorbed gas is estimated to account for 20%-85% of total shale gas-in-place

(GIP)[10]. Therefore, the accurate determination of shale gas adsorption is imperative to gas storage capacity estimation and well productivity[6].

The geophysical properties of shale rocks have been generally characterized by total organic carbon (TOC) analysis[11-13], rock eval pyrolysis[14-17] and X-ray diffraction (XRD) experiments[18-21] to determine the TOC content, thermal maturity, and chemical compositions. Generally, the adsorbed methane amount has a positive correlation with the TOC content in shale samples[5, 22, 23], while clay minerals can also significantly contribute to the shale gas adsorption[5]. On the other hand, the burial depth of shale reservoirs generally ranges from 800 m to 7000 m[24-29], leading to a temperature gradient from 20 K/km to 30 K/km[28, 30, 31], and a pressure gradient around 100-150 bar/km[25, 30, 32-34], resulting in typical shale reservoir temperature and pressure up to 450 K[28, 30, 35] and 700 bar[34, 36-38], respectively. As a result, a high-pressure and high-temperature gas adsorption measurement is necessary to mimic the *in-situ* pressure and describe the accurate adsorption behaviors[39, 40]. However, most shale gas adsorption measurements are limited to relatively moderate pressure conditions[35]. Moreover, the current gas adsorption measurements can obtain the excess adsorption from a ***macroscopic*** perspective, while the absolute adsorption amount which represents actual adsorption amount needs to be converted[41-43]. Generally, thermodynamic models such as Langmuir[30, 39, 44-48], supercritical Dubinin–Radushkevich (SDR)[35, 39, 49-51], BET or supercritical BET (SBET)[52-54], simplified local-density (SLD)[55-57] and Ono-

Kondo (OK) model[58-60] are applied for methane absolute adsorption conversion. All these models are built upon their own specific assumptions, which carry different degrees of limitations. In addition, the methane absorption in kerogen is reported to contribute up to 22% of total gas amount in shale[61, 62]. However, the effect of gas absorption has been rarely taken into account to convert the measured excess adsorption into the absolute adsorption due to the difficulties in distinguishing absorption and adsorption which occur simultaneously during gas adsorption measurements[63, 64].

While it is challenging for experiments to directly observe adsorption mechanism under nano-scale, statistical thermodynamic approaches such as Monte Carlo (MC) simulation, molecular dynamics (MD) simulation and density functional theory (DFT) enable researchers to take into account the characteristics of adsorbates as well as adsorbents and investigate gas adsorption mechanisms in shale from a ***microscopic*** perspective. The adsorption properties such as adsorption amount and density distributions have been studied by explicitly considering the effect of organic/inorganic matters[65, 66], pressure/temperature conditions[51], confinement[67, 68], pore structure[69, 70] and moisture content[71-74]. In addition, these statistical thermodynamic approaches have also been applied to study the conversion of excess adsorption into absolute adsorption[51, 52, 75]. Although these approaches provided important insights into the conversion of excess adsorption to absolute adsorption, daunting challenges still remain in current studies due to the complex shale media characteristics including rock heterogeneity and pore size

heterogeneity.

Generally, methane is considered as monolayer adsorption where the density in the adsorbed phase is higher than the bulk and that of free gas zone equals to the bulk. However, as revealed by simulation works, a transition zone where the density is still higher than the bulk can be found beyond the first adsorption layer, indicating the negative effect in m_{abs} estimation. As a result, a modified adsorption model which can capture multilayer adsorption is necessary. In addition, propane is one of the heavier hydrocarbons can exhibit a large quantity in shale reservoirs. The single-layered adsorption model is still applied, while heavier hydrocarbons can form multi-layered adsorption [76, 77]. Currently, there is no work on the characterization of hydrocarbon absolute adsorption considering the multi-layered adsorption structures which is crucial for propane m_{abs} estimation.

Moreover, in micropores (<2 nm), methane may have layering structures and there is no free gas zone. Due to different adsorption mechanisms in micropores and mesopores (>2 nm), it is necessary to consider the varying methane adsorption behavior in micropores and mesopores and the PSD effect to obtain the m_{abs}. There is no viable model to convert m_{ex} in nanoporous media to m_{abs} by considering the PSD effect. While commonly used methods have been extensively used to obtain m_{abs}, the assessments on these methods were conducted either in an indirect way, i.e. comparing the fitted adsorbed phase densities from experimental perspective[39, 47, 49], or in single pore size case from simulation

perspective[51]. To the best of our knowledge, no systematic and comprehensive assessment on various methods explicitly considering PSD in a direct way has been reported.

While previous works focus on either methane adsorption on single rock composition from simulation perspectives or purely applying adsorption models for experimentally measured data from shale samples without differentiating various rock compositions, it is difficult to account for the rock chemical heterogeneity couples with PSD effect in m_{abs} estimation for shale nanoporous media. The modification of currently applied OK model which assumes homogeneous surface for considering both pore size heterogeneity and rock type heterogeneity is needed to account for the actual energetically heterogeneous shale nanoporous media.

1.2 Problem Statement

While molecular simulation allows researchers to study the characteristic of adsorbate under atomic scale and provides an effective way to investigate the adsorption mechanism in shale. Problems still exists when developing effective adsorption models of hydrocarbon in shale nanoporous media, especially the conversion of absolute adsorption from experimentally measured excess adsorption. The main issues are addressed as follows.

- Considering the strong affinity of methane molecules on organic matters, how to explicitly account for the effect of transition zone in estimation of absolute adsorption in nanopores?

- The propane might exhibit multilayer adsorption structure in nanoporous media, how to take into account the multilayer adsorption behavior of propane adsorption in shale kerogen and develop the efficient adsorption model?

- Shale is characterized by multi-scale nanopores, how to consider the varying methane adsorption behavior in micropores and mesopores and the PSD effect to obtain the m_{abs} from the experimentally measured m_{ex}?

- How to systematically assess validity of commonly used adsorption models in the characterization of methane absolute adsorption in nanoporous materials such as kerogen and whether the experimental condition such as pressure can affect the accuracy for model application?

- The pore structure analysis investigated from experiments has shown that inorganic matter may contribute to micropores in some translational shale, while the methane adsorption plays an important role in clay-rich shales. In many works, the adsorption models have been modified in order to take into account the pore size effect or simply consider two heterogeneous sites with different adsorption

energy. Therefore, how to take into account both the rock type heterogeneity as well as pore size heterogeneity for calculation of adsorption capacity?

1.3 Objective

The objective of this research is to investigate hydrocarbon sorption characteristics and absolute adsorption estimation in shale nanoporous media from statistical thermodynamics approaches. To achieve this, the objectives are listed as follows.

- To investigate the methane adsorption in carbon nanopores at various pressures by molecular simulation and characterize methane excess and absolute adsorption capacity. Develop a modified OK model to accurately calculate m_{abs} with considering the effect of transition zone and multilayer adsorption model;

- To study the propane adsorption in shale nanopores over a wide range of pressures at temperature higher than the critical temperature. Propose a multi-layered adsorption model and use OK model with multi-layered structure to obtain the absolute adsorption in each layer based on excess adsorption data;

- To model methane adsorption in nanoporous media effectively by coupling GCMC simulations and PSD effect. Assess various commonly used methods converting the excess adsorption to the absolute adsorption systematically;

- To study the effect of rock type heterogeneity (organic and inorganic matters) on methane adsorption capacity in shale from GCMC simulation and develop modified Ono-Kondo dual-heterogeneity (OK-DH) model to characterize adsorption capacity by considering both PSD effect and various rock compositions.

1.4 Thesis Structure

There are eight chapters in this dissertation. Chapter 1 presents the research background, the problem statement, and the major research objectives. Chapter 2 develops OK multilayer methane adsorption model for mesopore on the basis of GCMC simulation. Chapter 3 presents propane adsorption in organic nanopore and the modification of fluid-fluid interaction considering correlation effect beyond mean field theory. Chapter 4 proposes the methane adsorption model in different nanopores which is applied in Ono-Kondo (OK) lattice model. Chapter 5 presents the systematic assessment on the validity of conversion methods based on some commonly used models such as Langmuir and SDR and calls for the accurate characterization of PSD in nanoporous materials to obtain their absolute adsorption capacity. Chapter 6 proposes OK model with PSD lumping to characterize CH_4 absolute adsorption in kerogen nanoporous media with pore sizes ranging from 0.7 to 50 nm. Chapter 7 develops the OK dual-heterogeneity (OK-DH) model to account for the shale gas adsorption heterogeneity arising from pore size effect and rock

type effect. In Chapter 8, we summarize the conclusions of the research and provides some

recommendations for future work.

CHAPTER 2 REVISITING METHANE ABSOLUTE ADSORPTION IN ORGANIC NANOPORES FROM MOLECULAR SIMULATION AND ONO-KONDO LATTICE MODEL

A version of this chapter has been published in *Fuel*.

Abstract

Accurate characterization of methane absolute adsorption in shale plays an important role in estimation of gas-in-place and prediction of well productivity. Previously, methane adsorption in shale nanopores was considered as a single-layer structure. However, it has been shown that due to strong fluid-surface interactions, methane can form transition zone between the first adsorption layer and free gas phase. Such transition zone can negatively affect the accuracy of the estimation of absolute adsorption from excess adsorption, which is the mostly measured adsorption property in experiments. In this work, we use grand canonical Monte Carlo (GCMC) simulations to characterize the transition zone and propose a modified adsorption model. Based on the modified adsorption model, which can explicitly take into account the effect of transition zone, we use the Ono-Kondo (OK) lattice model with multilayer structure to calculate the absolute adsorption in each layer and compare with GCMC simulations. The newly proposed OK model with multilayer structure only needs layer width as an input and calculate the density in each layer and subsequently the absolute adsorption by fitting the excess adsorption. While OK model can significantly reduce the calculation time, the discrepancy from GCMC simulation can be less than 6 %. Our work should provide important insights into the accurate characterization of the methane absolute adsorption from experimental measurement.

lattice model

2.1 Introduction

Shale gas has become a very important unconventional energy resource and significantly increased the global energy supply in the past decade [35, 38, 78, 79]. Unlike conventional reservoirs, where hydrocarbon fluids are stored in large pores in the range of micrometers and hundreds of nanometers [9], significant amount of pores in shale reservoirs may be in the range of a few nanometers [5, 80]. In small nanopores, hydrocarbon fluid properties are very different from bulk and surface adsorption plays an important role in the overall gas-in-place (GIP), which is one of the key parameters to assess shale gas capacity [81]. As a result, the adsorbed gas in shale reservoir which behaves differently from free gas, may contribute 20 %-85 % of total shale gas content [38, 78, 79, 81, 82]. Thus, the knowledge and understanding about adsorbed gas in shale plays a key role in the accurate estimation of GIP and the prediction of well productivity.

Shale is composed of two distinct matters: organic and inorganic [5]. The organic matter, which mainly consists of kerogen, is reported to have a dominant contribution to methane adsorption capacity in shale [5, 22, 71, 80, 83-87]. In addition, large amount of nano-sized pores are present in clay minerals which are important constituents of inorganic matters [5, 88], where gas adsorption can be significant [89]. While total organic carbon (TOC), maturity and kerogen type, specific surface area (SSA), moisture content, temperature and

surface functional groups are the controlling factors of the adsorption behavior in organic

matters [5, 90], in clay nanopores, SSA, moisture content and temperature are the dominant

factors [51, 89, 91, 92].

There have been a large number of experimental works to study gas adsorption behavior

in shale media [39, 47, 64, 93, 94]. Among them, gravimetric method and volumetric

method have been used to measure the Gibbs adsorption of various hydrocarbon species.

Gravimetric method, which uses magnetic suspension balance to obtain adsorption

isotherms [95], measures the excess adsorption capacity m_{ex} based on the difference

between gravity and buoyancy [96]. On the other hand, volumetric method measures total

gas uptake m_{tot} in porous media [97] and then, m_{ex} is obtained by subtracting the amount

of bulk free gas in all accessible pore volume V_p from m_{tot} [98, 99]. However, m_{ex} is

different from the absolute adsorption m_{abs}, which can describe the adsorbed gas capacity

in shale.

Methane adsorption in nanopores is generally considered as a single-layer adsorption

model [51, 100]. In large nanopores, methane density distributions in the middle of pores

are the same as bulk ρ_b [91], while in the vicinity of pore surfaces, they are very different

[51]. Based on the single-layer adsorption model, methane adsorption in nanopores can be

divided into adsorbed and free gas regions as shown in **Figure 2-1**. m_{abs} is defined as the

adsorbed amount in the adsorbed phase [101]. According to the adsorption model given in

Figure 2-1, m_{abs} can be converted from m_{ex} via the adsorbed phase density ρ_a [35,

102],

$$m_{abs} = \frac{m_{ex}}{1 - \rho_b / \rho_a} .\tag{2.1}$$

In previous works, ρ_a was assumed to be a constant as the liquid density of methane at normal boiling point [103-105]. Still assuming constant ρ_a, some empirical approaches such as Langmuir model [45], supercritical Dubinnin-Radushkevich model [47], and Ono-Kondo lattice model [81] have been used to characterize the absolute adsorption in shale by fitting experimentally measured m_{ex} using Eq. (2.1). However, it is well known that adsorbed phase density is dependent on pressure and temperature [91] and varying ρ_a at different pressures from grand canonical Monte Carlo (GCMC) simulations has been used to obtain m_{abs} [64].
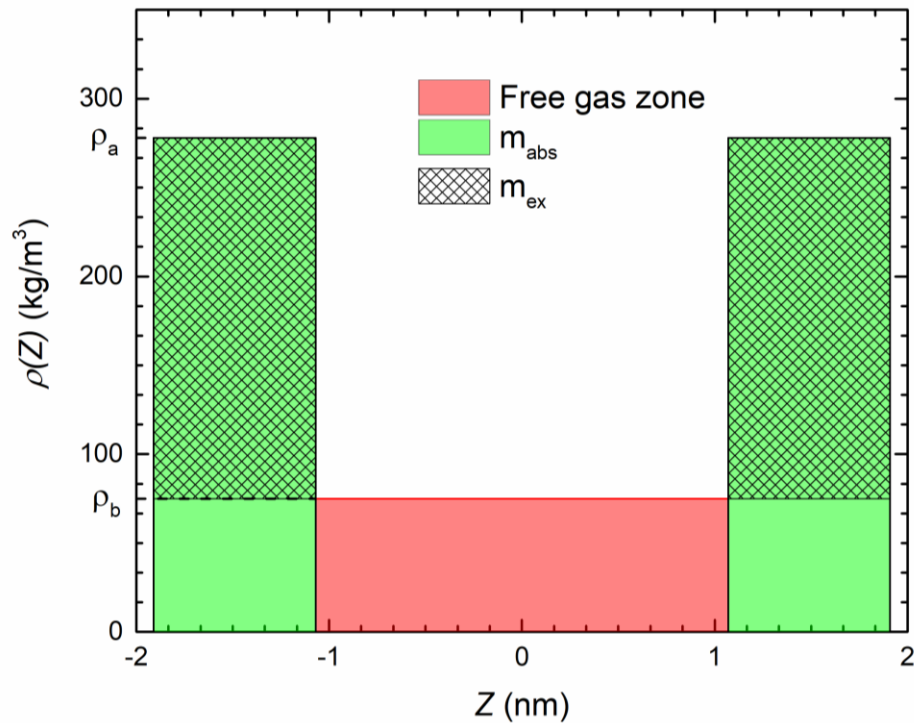
Figure 2-1 Schematic representation of methane adsorption model based on single-layer adsorption assumption.

Another approach is to use the adsorbed phase volume V_a to get m_{abs} from m_{ex},

$$m_{abs} = m_{ex} + V_a \rho_b \tag{2.2}$$

In our previous work [51], we used GCMC simulations to characterize the adsorbed phase from methane density distributions. The adsorbed phase was defined as the area between the boundary obtained from the effective pore volume and the local minima between the first and second adsorption layers at high pressures. We have shown that in micropores (less than 2 nm), methane density distribution is very different from bulk and total adsorption should be regarded as the absolute adsorption. For given adsorbed phase (given ρ_a and V_a), Eq. (2.2) provides better estimations of absolute adsorption than Eq. (2.1), but still showing noticeable over-estimation due to the presence of transition zone at intermediate pressure conditions [51, 106, 107]. While the transition zone is excluded from the adsorbed phase, it contributes to m_{ex}, and eventually m_{abs} as depicted in Eqs. (2.1) and (2.2) [51]. Although molecular simulation can be used to explicitly characterize the transition zone, it comes with expensive computational costs. Such computational burden associated with molecular simulations askes for more efficient and computationally less expensive approaches to accurately characterize the absolute adsorption, especially from experimental measurement.

Langmuir model [108] has been widely used to calculate the absolute adsorption of gas on

a solid surface [109]. It is based on a monolayer adsorption of gas molecules on an ideal planar surface, describing surface coverage [110]. Thus, Langmuir model cannot describe the effect of pore size distributions and confinement in shale. Dubinnin-Radushkevich (DR) model [111, 112] based on pore filling method, assuming a mean value for the force field for all adsorbate molecules in the pore [113], was used to study the gas adsorption up to the bulk saturation vapor pressure. Later, Sakurovs *et al*. [114] proposed supercritical DR (SDR) model by replacing vapor pressure by adsorbed phase density to study supercritical fluid adsorption in porous media. Although SDR has been widely used in the characterization of absolute adsorption in shale, the pore-filling model which does not differentiate the adsorbed and free gas phases is not in line with the adsorption model shown in Figure 1. Recently, Ono-Kondo (OK) model [115-119] based on lattice theory has been used to study the absolute adsorption in shale [81]. OK model assumes that gas molecules occupy the lattice sites in chemical equilibrium with bulk and can be used to study supercritical gas adsorption in nanopores. As we will show later, for a given layer width, it can readily calculate the excess adsorption without using Eqs. (2.1) and (2.2). In addition, because OK model can consider multilayer lattice structure [118], it can potentially characterize the transition zone. Previously, there have been some works using OK model with single-layer structure in nanopores [81, 120-122], neglecting the fluid-surface interactions and thus reducing to Langmuir model, which cannot take into account the transition zone.

Since slit-like pores widely exist in shale rocks [123, 124], in this work, we adopt the slit pore geometry as in our previous works [91, 125, 126] to perform GCMC simulations to investigate methane adsorption behavior in carbon nanopores under a wide range of pressures and compare with OK model with multilayer structure. Moreover, the slit pore geometry in GCMC simulation is in line with the cubic lattice structures assumed in OK model. We perform GCMC simulation to model methane adsorption in organic materials, which are mainly kerogen that have pores in nanometer range. There have been a number of works using full atomistic models to represent kerogen [127-129]. However, the rough surfaces used in these kerogen models may not represent a fair comparison between molecular simulation and OK model. In addition, the simplified carbon slit-pore model has shown excellent agreement with experiments on gas adsorption in shale [100]. Methane molecules are considered as single-site Lennard Jones (LJ) particles in our simulation. Excess adsorption is calculated based on the same approach as in the volumetric method, and the effective pore volume is obtained by helium adsorption. We also propose a modified adsorption model to take into account the transition zone. OK model with multilayer structure is used to fit the excess adsorption obtained from GCMC simulations to calculate the absolute adsorption in each layer. The number and width of layer in OK model are pre-determined based on the density distributions from GCMC simulation. In addition, we also compare the OK model with multilayer structure (OK-MU) with that with monolayer structure (OK-MO).

The remainder of this paper is organized as follows. In **section 2.2**, we describe the OK lattice model. In **section 2.3**, we introduce the molecular simulation methods and define the molecular models. In **section 2.4**, we will first study the methane excess adsorption and density distributions in carbon nanopores from GCMC simulations. Based on the characteristics of density distributions, we propose a modified adsorption model to study the effect of transition zone and absolute adsorption. Then, we will use OK-MU to compare with GCMC simulations on the absolute adsorption as well as OK-MO. In **section 2.5**, we summarize the key conclusions and discuss potential implications.

2.2 Ono-Kondo lattice model

In this work, following the work by Aranovich and Donohue [118], we consider lattice theory of three-dimensional cubic geometry for a single-component adsorbate, assuming the adsorbate is in contact with a planar surface at $i=0$. The details of Ono-Kondo lattice model can be found in **Appendix A**.

Assuming constant layer volume (width) V_a, the Gibbs (excess) adsorption amount can be given as,

$$m_{ex} = \rho_{am} V_a \sum_{i=1}^{n} (x_i - x_b).$$

(2.3)

where n is the number of layers and m_{ex} is the excess adsorption amount.

In some of previous works [81, 120-122], methane adsorption was only considered as

monolayer and methane-methane interaction is neglected, methane adsorption is only considered as monolayer and methane-methane interaction is neglected, reducing the adsorption behavior to Langmuir isotherm. In addition, the expression of excess adsorption in Bi *et al.*'s work [81] is mistaken as the absolute adsorption, leading to a significant error in the calculated adsorption capacity [130]. Benard *et al.* [131] used two-layer adsorption model to fit methane adsorption in activated carbon CNS-201 with temperature ranging from 243 to 333 K and pressure up to 16 MPa. They used a temperature-dependent variable to represent the maximum monolayer adsorption capacity and other fitting parameters are maximum monolayer adsorbed phase density, fluid-fluid interaction and fluid-surface interaction. Sudibandriyo *et al.* [58] and Merey *et al.* [132, 133] used Ono-Kondo model to fit methane adsorption isotherm with hexagonal lattice cell configuration and two-parameter OK model. In their so-called two-parameter OK model, the fluid-surface interaction is regressed for specific adsorption system, while the maximum monolayer adsorption capacity is fitted by each adsorption isotherm. The constant fluid-fluid interaction is obtained from the proportional relation to the well depth of the Lennard-Jones 12-6 potential and the constant maximum adsorbed phase density is estimated based on the saturated methane density under critical condition. In their regression, both of those two parameters are fixed. As a result, the adsorbed phase width is dependent on temperature and pressure. However, in previous molecular simulations [51], it has been shown that methane adsorption layer width is rather a constant close to the diameter of methane

molecule.

2.2.1 OK-MU

In our work, OK-MU considering interaction energy of both adsorbate-adsorbate and adsorbate-adsorbent are applied to characterize methane adsorption in nanopores. The width of adsorbed layer is fixed as the methane LJ diameter of 0.38 nm based on previous simulation works [51, 106]. In the case of 4 nm pore, as we will show later, beyond two noticeable adsorption layers, methane density distribution is close to the bulk. To ensure robust and reliable fittings to the excess adsorption and accurate prediction of the absolute adsorption in adsorption layers, we use three-layer structures in OK-MU, in which beyond the third layer the density is the same as bulk. In fact, as we will show later, the density of the third layer in OK-MU is close to the bulk density. Therefore, the OK-MU is given as,

$$
\begin{cases}
\ln\left(\dfrac{x_3\left(1-x_b\right)}{x_b\left(1-x_3\right)}\right) + \left(4x_3 + x_2 - 5x_b\right)\dfrac{\varepsilon}{k_B T} = 0 \\[2ex]
\ln\left(\dfrac{x_2\left(1-x_b\right)}{x_b\left(1-x_2\right)}\right) + \left(4x_2 + x_1 + x_3 - 6x_b\right)\dfrac{\varepsilon}{k_B T} = 0 \\[2ex]
\ln\left(\dfrac{x_1\left(1-x_b\right)}{x_b\left(1-x_1\right)}\right) + \left(4x_1 + x_2 - 6x_b\right)\dfrac{\varepsilon}{k_B T} + \dfrac{\varepsilon_s}{k_B T} = 0
\end{cases} \qquad . \qquad (2.4)
$$

Eq. (2.4) is a set of non-linear equations which can be solved iteratively.

2.2.2 OK-MO

For comparison, the OK-MO can be expressed as,

$$\ln\left(\frac{x_1(1-x_b)}{x_b(1-x_1)}\right) + (4x_1 - 5x_b)\frac{\varepsilon}{k_BT} + \frac{\varepsilon_s}{k_BT} = 0 \,. \qquad (2.5)$$

By combining Eqs. (2.3) and (2.4) for OK-MU and Eqs. (2.3) and (2.5) for OK-MO, we fit the excess adsorption from OK models to that from GCMC simulations with fitting parameters ρ_{am}, ε and ε_s. We use sequential quadratic programming (SQP) optimization method implemented in MATLAB to obtain those three parameters.

2.3 Molecular model and simulation

In this work, we carry out GCMC simulations to model methane adsorption behavior in carbon nanopores. The details of molecular model and simulation can be found in **Appendix B**.

The effective pore volume is necessary for the excess adsorption calculation in volumetric method. Helium adsorption is generally used to measure the effective pore volume assuming that helium fills the pore space instead of adsorbed on the surface [22, 89]. The details of calculation can be found in **Appendix C**.

In our work, the calculated effective pore width for 4 nm and 8 nm nanopores are 3.84 nm and 7.84 nm, respectively. The reduction of 0.16 nm is due to the finite size (excluded volume) effect of Helium molecules [134]. In GCMC simulation, the effective pore volume obtained by helium adsorption would affect the excess adsorption. At given pressure and temperature conditions, the excess adsorption is a linear function of the effective pore volume (width). We found that helium does show adsorption on the carbon surface as

21

shown in **Figure C-1**, which is different from our previous work for clay minerals [51]. Such helium adsorption on the surface can lead to an overestimation of the effective pore width.

2.4 Results and Discussion

In this section, we will first study the methane excess adsorption and density distributions in carbon nanopores from GCMC simulations. Based on the characteristics of density distributions, we propose a modified adsorption model to study the effect of transition zone and absolute adsorption. Then, we will use OK-MU to compare with GCMC simulations as well as OK-MO on the absolute adsorption.

2.4.1 Methane adsorption behavior from GCMC simulation

2.4.1.2 Excess adsorption and density profiles

In our GCMC simulation, excess adsorption is obtained based on the volumetric method shown in **Appendix B**.

Figure 2-2 shows the methane excess adsorption from GCMC simulation in nanopores of 4 nm and 8 nm at 333.15 K and pressures up to 50 MPa. The excess adsorption first increases to a maximum around 15 MPa, then decreases with pressure. When pressure is relatively low, methane molecules tend to adsorb on the surface and the bulk density is much lower than the adsorbed phase density. As pressure increases, the adsorbed phases

may have been readily filled, while methane molecules accumulate in the bulk phase. Thus, as pressure further increases, excess adsorption decreases. Additionally, despite some GCMC simulations stated that the excess adsorption decreases with increasing pore width even in mesopores [67, 135], we observe that the excess adsorption is independent to the pore width when $W \geq 4$ nm as reported by Chen *et al*. [136] and Tian *et al*. [51].
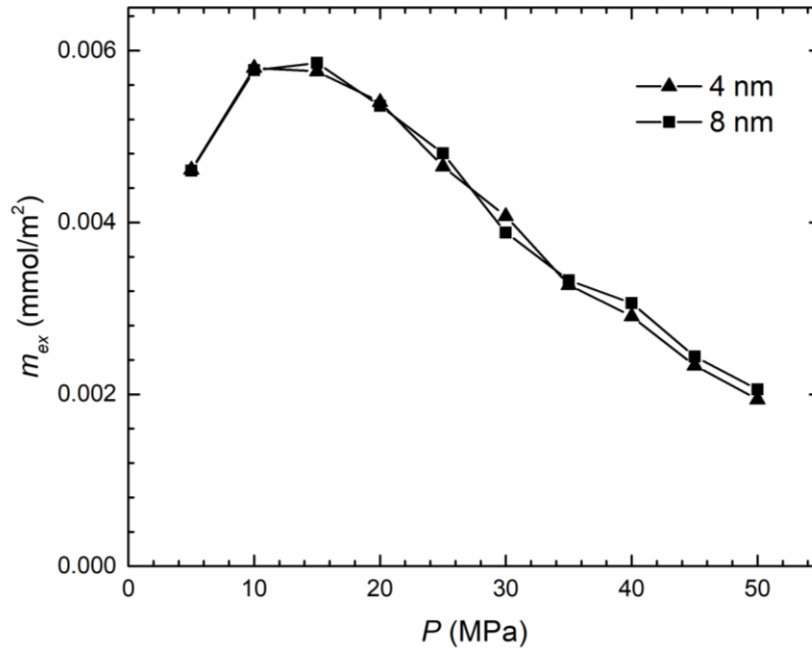
Figure 2-2 Excess adsorption amount per specific surface area from GCMC simulation in various sizes of carbon nanopores at 333.15 K.

To better understand adsorption behavior, we present the methane density distributions in carbon nanopores of $W = 4$ nm and $W = 8$ nm at various pressures and 333.15 K in **Figure 2-3**. Methane forms a strong surface adsorption and the density in the middle of the pores reaches bulk. Beyond the strong first adsorption layer, a second adsorption layer can be seen in line with other simulation works [51, 67, 107, 137]. The distance between the

peaks of first and second adsorption layers is close to the methane molecular size. Similar to our previous work [51], the positions of peak and local minima in density distributions at high pressures remain the same. Such second adsorption layer can be considered as transition zone. While transition zone is obvious at relatively low pressures (for example, 10 MPa), it becomes less significant at high pressures. The presence of transition zone contributes to the excess adsorption, and thus, negatively impacts the accuracy of absolute adsorption from Eq. (2.1). As a result, the consideration of the second adsorption layer is necessary for better estimation of the actual absolute adsorption. In our previous work [51], we also observed the second adsorption layer in methane adsorption in various clay nanopores, which can be "averaged out" in the free gas zone. However, due to the stronger fluid-surface interactions in carbon nanopores than that in clay nanopores, the second adsorption layer in this work is more significant. Therefore, we need to explicitly characterize the second adsorption layer in carbon nanopores. At high pressure conditions, beyond the second adsorption layer, a weak third adsorption layer can be observed. However, the average density deviation from bulk in the third adsorption layer is much smaller than that in the first and second adsorption layers.
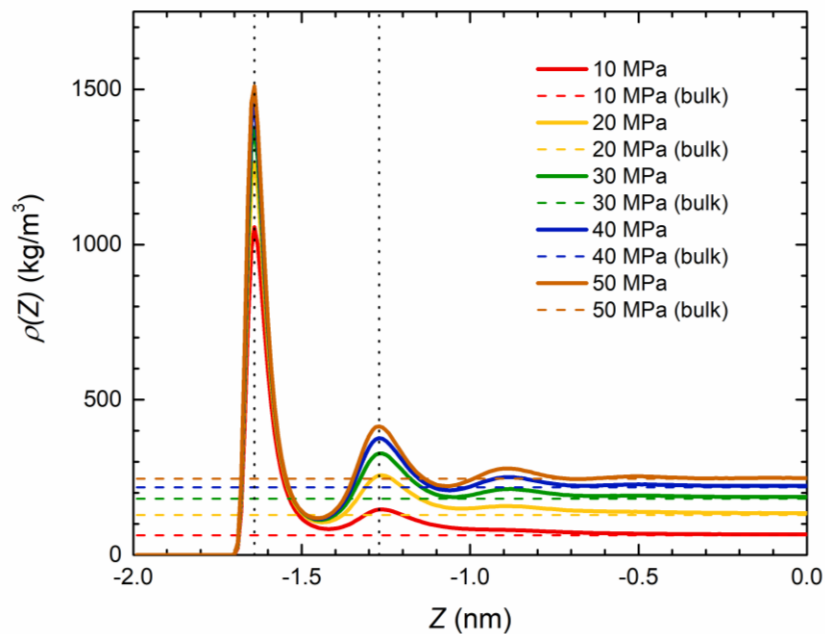
(a)
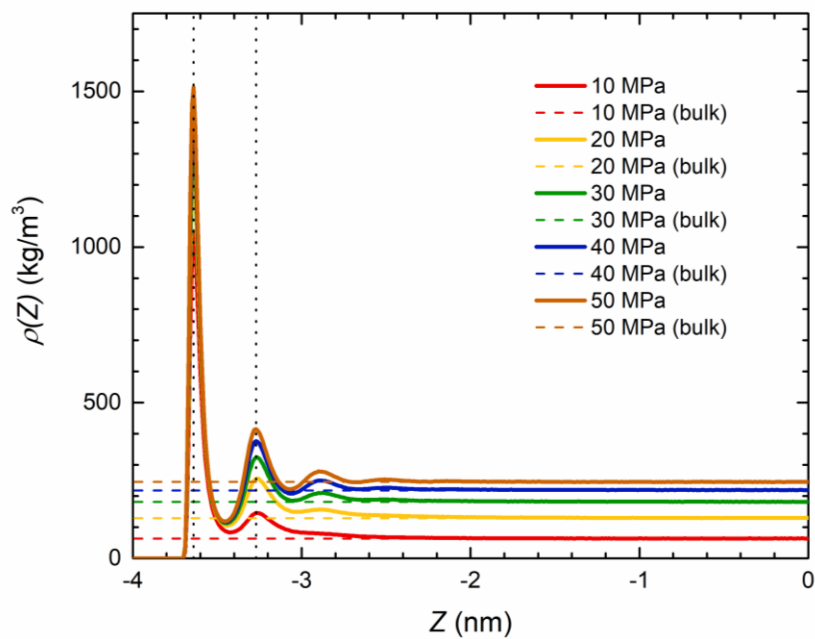
(b)

Figure 2-3 Methane density distributions from GCMC simulation at 333.15 K and various pressures in carbon nanopores of (a) $W = 4$ nm; (b) $W = 8$ nm. For comparison, the bulk

densities from NIST Chemistry Webbook are depicted as dashed lines. The dotted lines represent the peaks of the density profiles.

2.4.1.2 Characterization of methane adsorption model

Figure 2-4 exhibits the schematic representation of the first and second adsorbed layer in carbon nanopores based on GCMC simulation. The region $z_{AA'}$ defines the effective pore volume (width), which is obtained by $z_{AA'} = V_p / S_A$. The modified adsorption model can be separated into three distinct parts: the first adsorption layer, the second adsorption layer (transition zone) and free gas zone. The third adsorption layer is lumped into the free gas zone. The first adsorbed layer is defined as the zone between point A and point B, which is the local minima of the density profile between the first and second layer. The second adsorbed layer is defined as the region between point B and point C, which is the local minima of the density profile between the second layer and free gas zone. The point B and point C are defined from the density distributions at 50 MPa. A number of simulation works revealed that the width of adsorbed phase should equal to the diameter of LJ molecules [51, 67, 76, 106, 107]. In our work, we observe that the width of AB, $z_{AB} = 0.47$ nm is larger than the methane LJ diameter of 0.38 nm, because helium can form adsorption layer on carbon surfaces which in turn increases the effective pore volume. On the other hand, the width of BC is 0.38 nm. The region between C and C' is defined as the free gas zone. In **Figure 2-4**, the heights of the first adsorbed layer, second adsorbed layer and free gas zone are defined as $\rho_{a1} = \int_A^B \rho(z)\,dz\,/\,z_{AB}$, $\rho_{a2} = \int_B^C \rho(z)\,dz\,/\,z_{BC}$ and

26

$$\rho_f = \int_C^{C'} \rho(z)\, dz / z_{CC'},\ \text{respectively.}$$
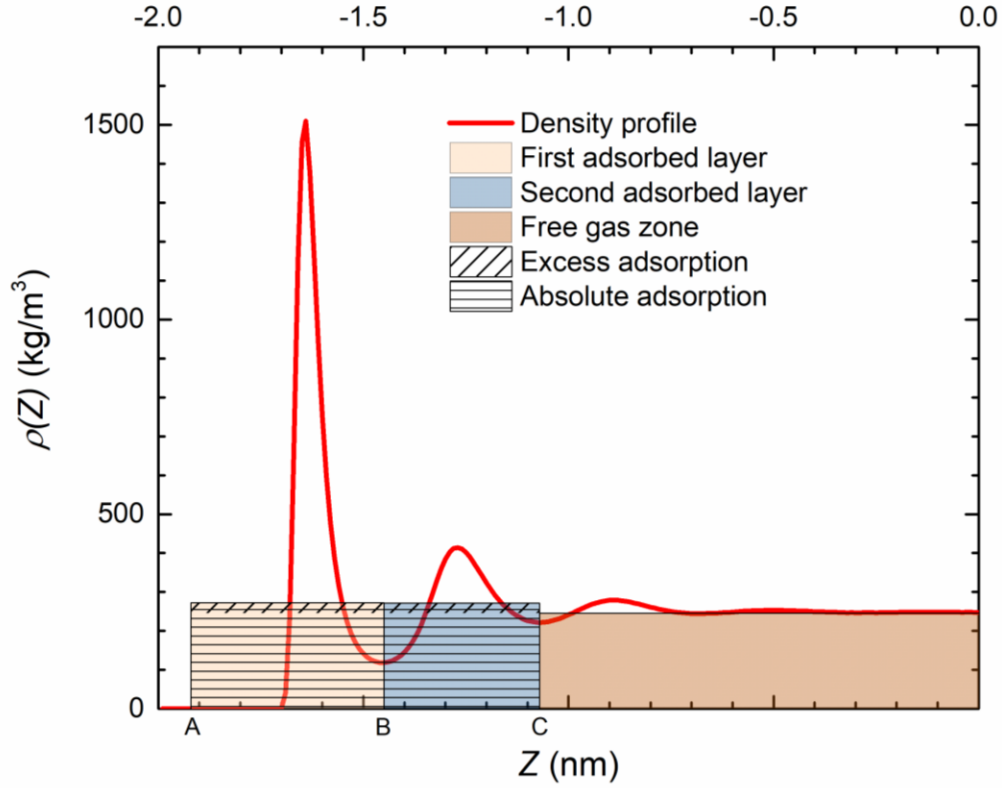
Figure 2-4 Schematic representation of the first and second adsorbed layer in carbon nanopore of $W = 4$ nm based on GCMC simulation at 333.15 K and 50 MPa. The heights of adsorbed phase density of the first adsorbed layer, second adsorbed layer and free gas zone are obtained by $\rho_{a1} = \int_A^B \rho(z)\, dz / z_{AB}$, $\rho_{a2} = \int_B^C \rho(z)\, dz / z_{BC}$, and

$$\rho_f = \int_C^{C'} \rho(z)\, dz / z_{CC'},\ \text{respectively.}$$

In order to calibrate our modified adsorption model, we depict the density of free gas zone from GCMC simulation comparing to the bulk density from NIST Chemistry Webbook in **Figure 2-5**. For clarity, we also present their relative errors $\delta_f = (\rho_f - \rho_b)/\rho_b$. At higher

pressures up to 50 MPa, the relative errors are less than 3 % for $W = 4$ nm and less than 1 % for $W = 8$ nm. At low pressures, the variation between ρ_f and ρ_b can be around 14 % at 10 MPa in 4 nm pores, due to strong fluid-surface interactions. Despite the relatively large difference between ρ_f and ρ_b at intermediate pressures, ρ_f approaches ρ_b as pressure increases.
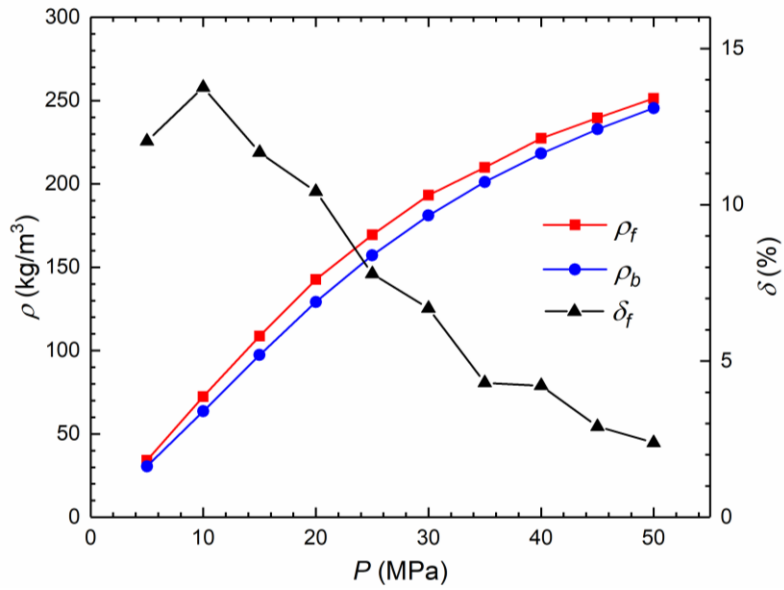
(a)
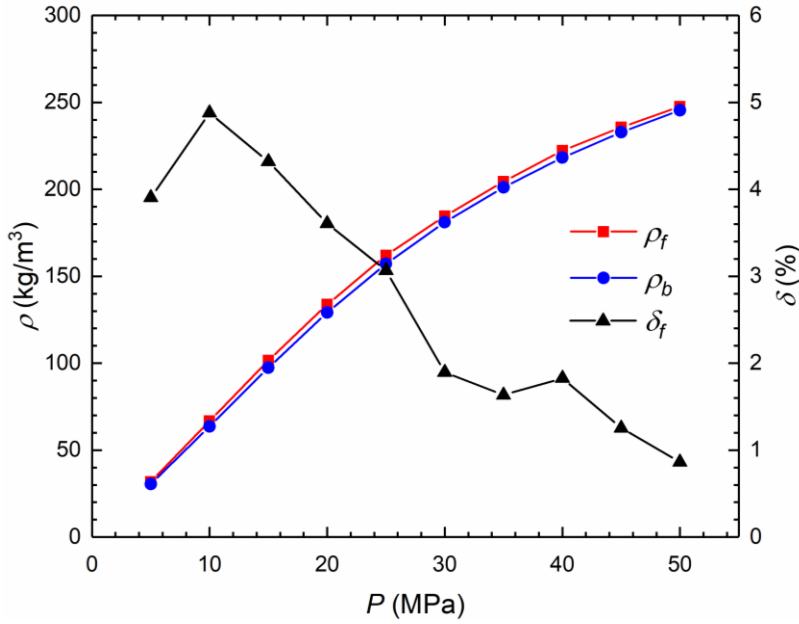
(b)

Figure 2-5 Comparison of free gas density from GCMC simulation and bulk density from NIST Chemistry Webbook and their relative error $\delta_f = (\rho_f - \rho_b)/\rho_b$ in carbon nanopores of (a) $W = 4$ nm; (b) $W = 8$ nm at 333.15 K.

In **Figure 2-6**, we present the adsorbed phase density in each adsorbed layer obtained by GCMC simulation and the relative difference $\delta_{a2} = (\rho_{a2} - \rho_b)/\rho_b$ in carbon nanopores of $W = 4$ nm and $W = 8$ nm at 333.15 K. Both ρ_{a1} and ρ_{a2} increase continuously with pressure. It is noted that ρ_{a2} is significantly higher than ρ_b. At high pressures (50 MPa), the discrepancy between ρ_{a2} and ρ_b is around 10 %; while, at low pressures, δ_{a2} can be as high as 95 %, indicating the strong effect of transition zone. It is necessary to explicitly consider the second adsorption layer, which is different from the free gas and contribute to the excess adsorption calculation. In our previous work [51], the methane

29

second adsorption layer in clay nanopores can be "averaged out" in the free gas zone. It is because fluid-surface interactions in clay nanopores are weaker than that in carbon nanopores.
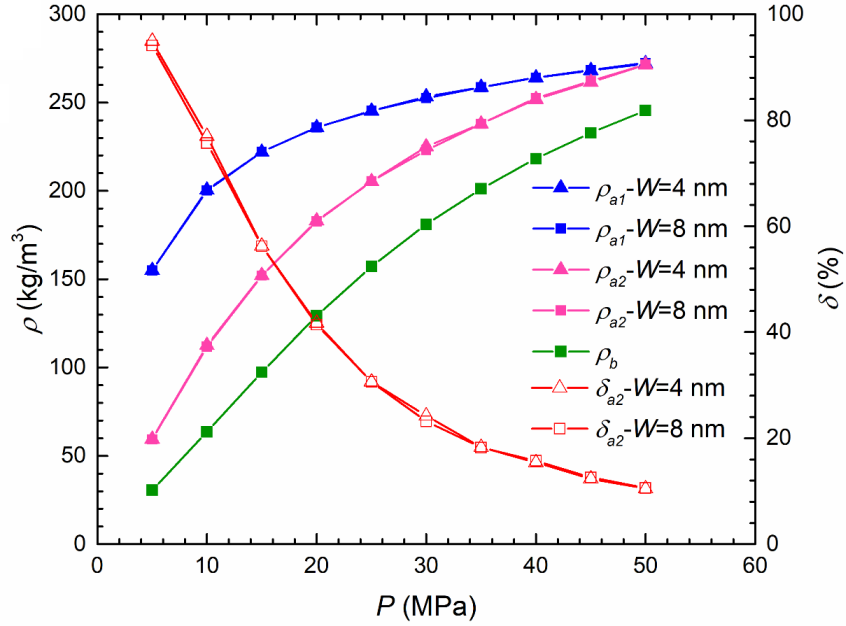
Figure 2-6 Adsorbed phase density in each adsorbed layer from GCMC simulation and bulk density from NIST Chemistry Webbook. We also present the relative difference $\delta_{a2} = (\rho_{a2} - \rho_b)/\rho_b$ in second layer in carbon nanopore of $W = 4$ nm and $W = 8$ nm at 333.15 K.

Based on the modified adsorption model as shown in **Figure 2-4**, the absolute adsorption can be divided by two parts:

$$m_{abs} = m_{abs}^{L1} + m_{abs}^{L2},\qquad(2.6)$$

where

$$\begin{cases} m_{abs}^{L1} = \rho_{a1}V_{a1} \\ m_{abs}^{L2} = \rho_{a2}V_{a2} \end{cases},\qquad(2.7)$$

$$\begin{cases} V_{a1} = 2S_A z_{AB} \\ V_{a2} = 2S_A z_{BC} \end{cases}, \tag{2.8}$$

in which, m_{abs} is the total adsorption amount in layer one and two, m_{abs}^{L1} and m_{abs}^{L2} represent the absolute adsorption amount in the first layer and second layer, respectively, V_{a1} and V_{a2} are the first and second adsorbed phase volume, respectively. In **Figure 2-7**, we present the calculated absolute adsorption amount per specific surface area of the first and second adsorbed layer in carbon nanopores of $W = 4$ nm and $W = 8$ nm at 333.15 K from GCMC simulation. The absolute adsorption amount increases continuously with pressure up to 50 MPa for both layers. As shown in **Figure 2-6**, because the density distributions near the surface are close when $W \geq 4$ nm, the absolute adsorption remains the same.
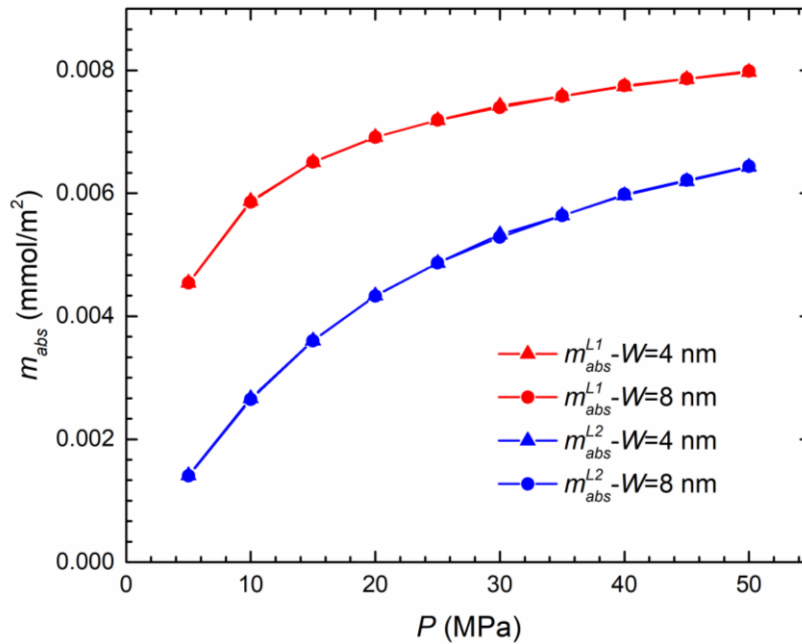
Figure 2-7 Absolute adsorption amount per specific surface area of the first and second adsorbed layer in carbon nanopores of $W=4$ nm and $W=8$ nm at 333.15 K from GCMC simulation.

2.4.2 Adsorption behavior from OK-MU

In this section, we assess the OK-MU by comparing to GCMC simulations and OK-MO. Since the methane density distribution in slit-pore is symmetric and excess adsorption amount is expressed as per specific surface area, we only simulate methane adsorption on one carbon surface assuming three-layer structures. We fit the excess adsorption with constant layer width of $z_{OK}=0.38$ nm for methane adsorption isotherm in carbon nanopore of $W=4$ nm at 333.15 K as shown in **Figure 2-8**. The three fitting parameters have fitting ranges as: $0<\rho_{am}<700$ kg/m³, $-1<\varepsilon/k_BT<0$ and $-10<\varepsilon_s/k_BT<0$ [116-119]. The calculated fitting parameters are $\rho_{am}=335.32$ kg/m³, $\varepsilon/k_BT=-0.49$ and $\varepsilon_s/k_BT=-1.82$ with R-square of $R^2=0.9976$ for OK-MU; $\rho_{am}=390.82$ kg/m³, $\varepsilon/k_BT=-0.83$ and $\varepsilon_s/k_BT=-1.19$ with R-square of $R^2=0.9663$ for OK-MO. To be noted that in actual experimental measurements, these fitting parameters may vary from different experimental conditions and samples.
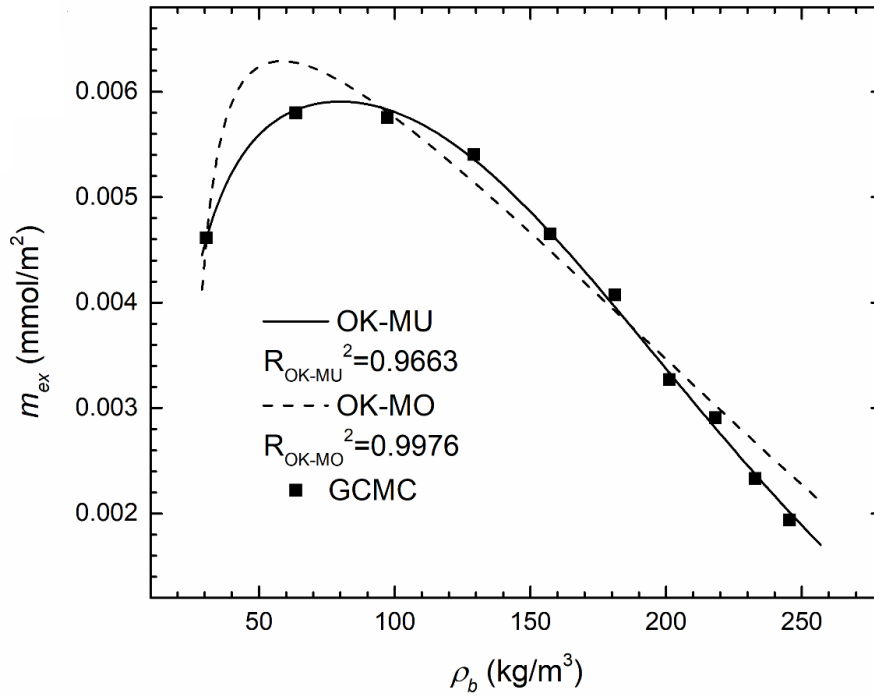
Figure 2-8 OK-MU and OK-MO with constant adsorbed phase width of 0.38 nm for fitting methane excess adsorption from GCMC simulation in carbon nanopore of $W = 4$ nm at 333.15 K.

Overall, while OK-MU shows an excellent agreement with GCMC simulation, OK-MO shows some discrepancies. There have been a number of works using a constant adsorbed phase density as 424 kg (the liquid methane density at its boiling point of 112 K and 0.1 MPa) or 373 kg/m^3 (the saturated methane density at critical point, 190.56 K and 4.58 MPa) [50, 81, 138]. In addition, assuming a constant adsorbed phase density which is independent of pressure, it can also be obtained by fitting the measured excess adsorption with models such as Langmuir, SDR and OK [39, 45, 47, 81, 120]. Do *et al.* [139] claimed that the adsorbed phase density could be very close to the liquid methane density at high pressure, but would not be equal or higher than that. Tian *et al.* [47] used both Langmuir

and SDR models to fit experimental excess adsorption data. They found that the adsorbed phase density fitted by Langmuir model would exceed liquid methane density, while that from SDR model is generally smaller than 424 kg/m^3, ranging from 297 kg/m^3 to 415 kg/m^3. Bi *et al.* [81] found that by using OK model regression, the free fitting result of maximum adsorbed phase density is unreasonable (higher than 424 kg/m^3). Thus, they fixed the adsorbed phase density as a constant value of 373 kg/m^3. In the work by Sudibandriyo *et al.* [58], the regressed methane adsorbed phase density on dry activated carbons from OK model is 345 kg/m^3. In our work, the maximum adsorbed phase density from OK-MU is lower than liquid methane density.

Figure 2-9 (a) presents the corresponding densities of each layer from OK-MU at various pressures. The densities of the first and second layer are significantly higher than ρ_b, while the density of the third layer is close to ρ_b. We also plot the calculated densities in OK-MO for comparison in **Figure 2-9 (b)**. The adsorption layer densities are much higher than bulk densities and become readily saturated as pressure increases. In **Figure 2-10**, we present the absolute adsorption amount per specific surface area in the first and second layer from OK-MU and GCMC as well as the first layer from OK-MO, and their relative differences $\delta = \left(m_{abs-GCMC} - m_{abs-OK} \right) / m_{abs-GCMC}$. For OK-MU, the calculated absolute adsorption of the first and second layers are expressed as $m_{abs,OK}^{L1} = \rho_{a1,OK} z_{OK}$ and $m_{abs,OK}^{L2} = \rho_{a2,OK} z_{OK}$, respectively. Overall, the agreement between OK-MU and GCMC simulation is very good. It can be seen from **Figure 2-10 (a)** that when only monolayer is

considered in OK model, the calculated absolute adsorption amount is always overestimated comparing to GCMC simulation and maximum δ is around -33%. As shown in **Figure 2-10 (b)**, the absolute adsorption obtained by OK-MU is firstly higher than that obtained by GCMC simulation and then underestimates the absolute adsorption from 30 MPa, while maximum δ is around -13 %. As shown in **Figure 2-10 (c)**, the second layer absolute adsorption from OK-MU is underestimated over given pressure range and δ decreases with pressure and is around 5 % at pressure up to 50 MPa.

(a)
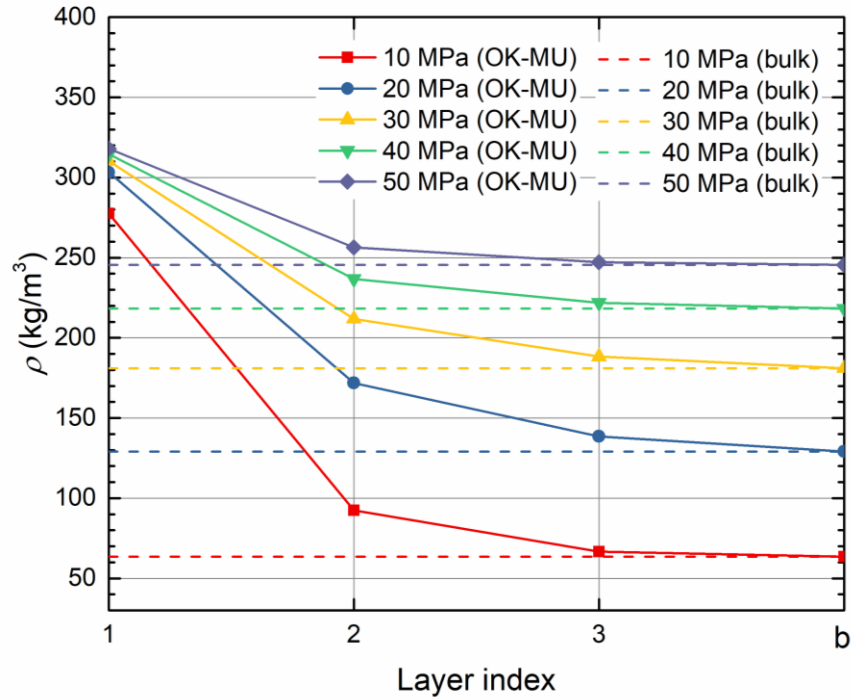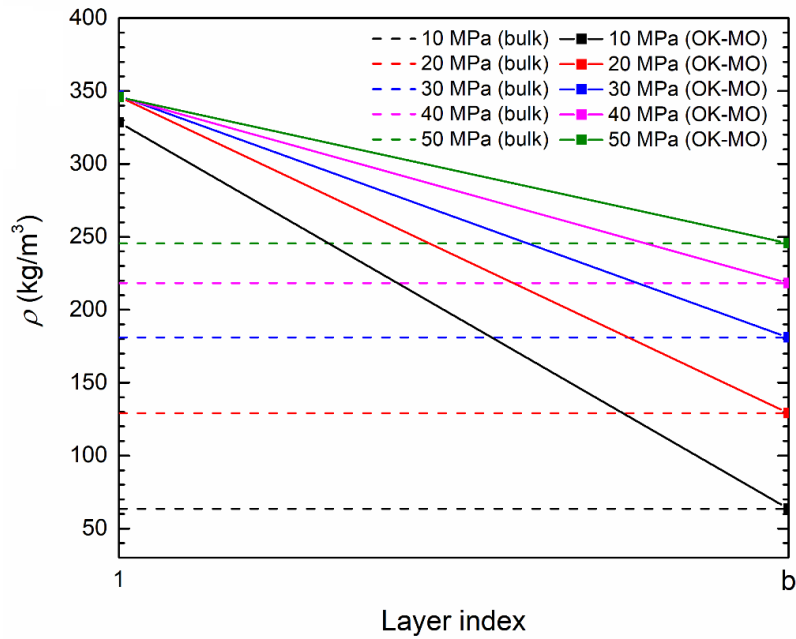
Figure 2-9 Densities of each layer from (a) OK-MU; (b) OK-MO in carbon nanopores of $W = 4$ nm at 333.15 K.
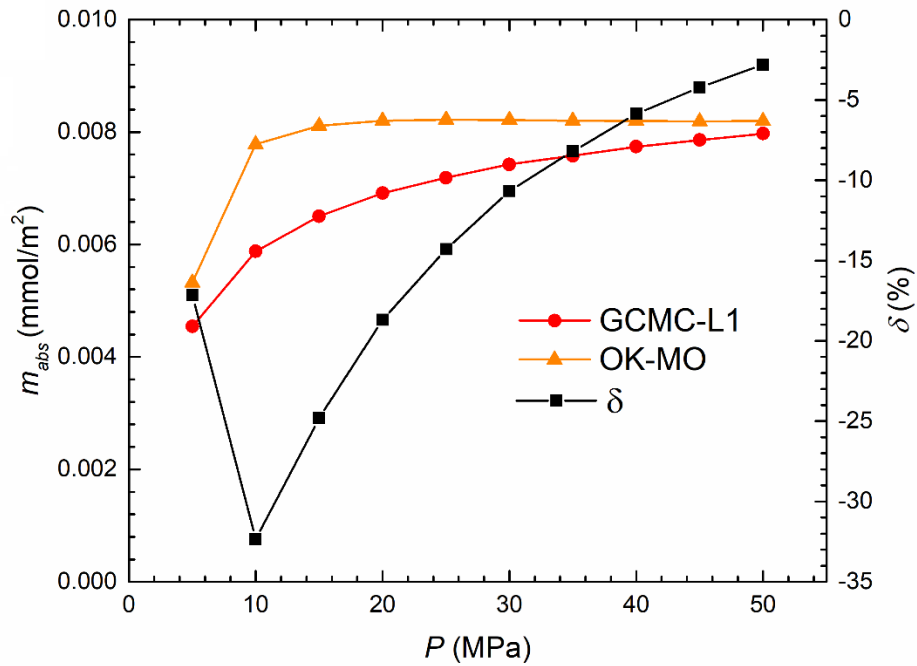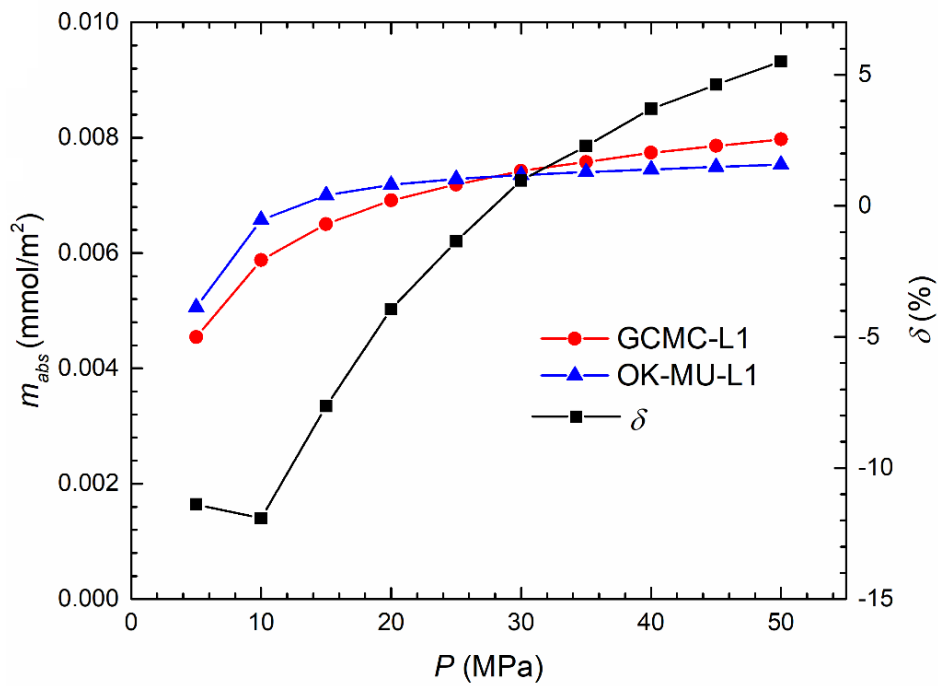
(b)
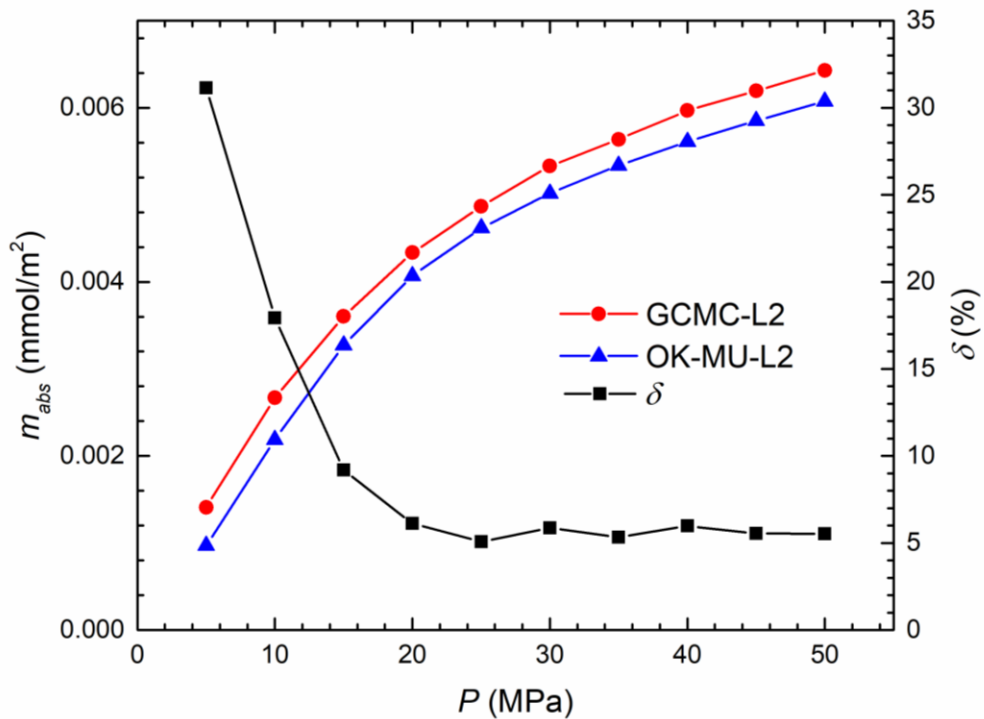
(c)

Figure 2-10 Absolute adsorption amount per specific surface area from GCMC simulation, OK-MU, OK-MO and relative differences $\delta = \left(m_{abs-GCMC} - m_{abs-OK} \right) / m_{abs-GCMC}$ of $W = 4$ nm at 333.15 K. (a) The first layer from OK-MO; (b) The first layer from OK-MU; (c) The second layer from OK-MU.

We present the combined methane absolute adsorption amount in the first and second layers from OK-MU and GCMC simulation in **Figure 2-11**. The maximum relative deviation $\delta = \left(m_{abs-GCMC} - m_{abs-OK} \right) / m_{abs-GCMC}$ is less than 6 %, indicating an excellent agreement between OK model and GCMC simulation.
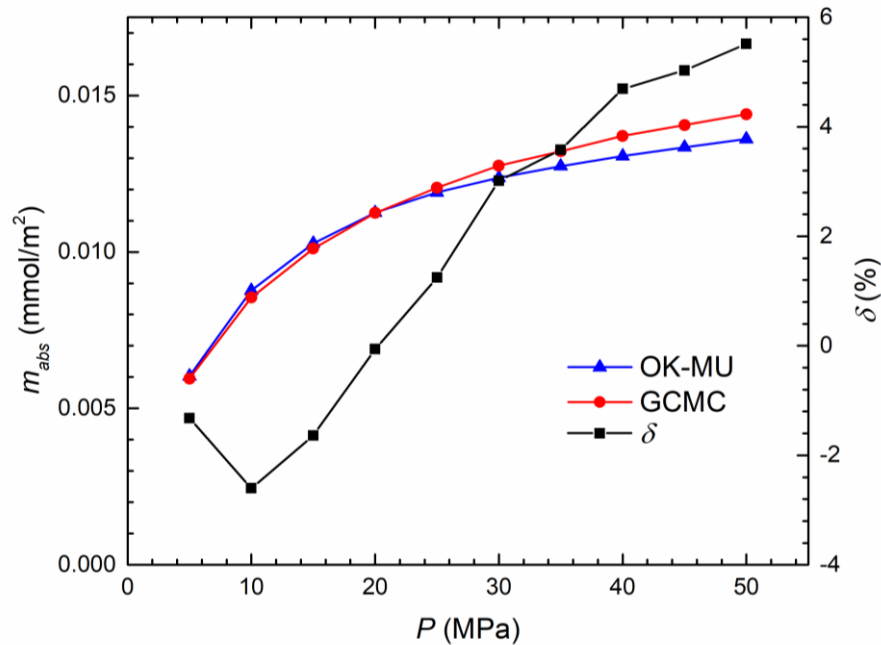
Figure 2-11 Comparison of combined absolute adsorption amount per specific surface area obtained by OK-MU and GCMC simulation and their relative error $\delta = \left(m_{abs-GCMC} - m_{abs-OK} \right) / m_{abs-GCMC}$ in carbon nanopore of $W = 4$ nm at 333.15 K.

In addition, the excess adsorption is sensitive to the effective pore volume [134]. Do and his coworkers mentioned that the effective pore volume would significantly affect the

excess adsorption [140]. Moreover, the effective pore volume of the sample cannot be directly measured in the gravimetric method. Thus, in this work, we arbitrarily change the effective pore volume to test the performance of OK-MU. We plot the excess adsorption assuming effective pore width of 4 nm for $W = 4$ nm pores and that with actual effective pore width of 3.84 nm in **Figure 2-12**. Even for arbitrarily chosen pore volume, OK model shows a good agreement with GCMC simulation for combined absolute adsorption as shown in **Figure 2-13**. It is shown that the maximum relative error is still less than 9 %.
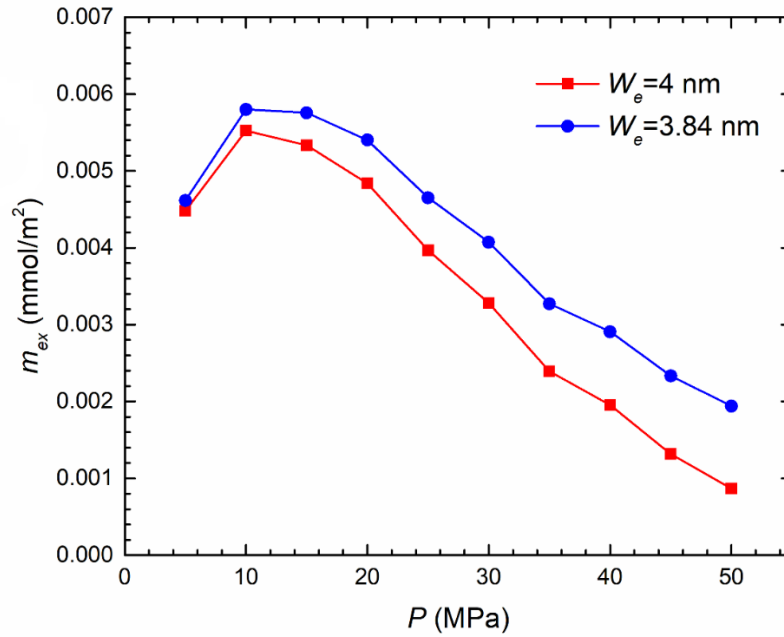
Figure 2-12 Comparison of excess adsorption amount per specific surface area with different effective pore widths W_e in carbon nanopores at 333.15 K.
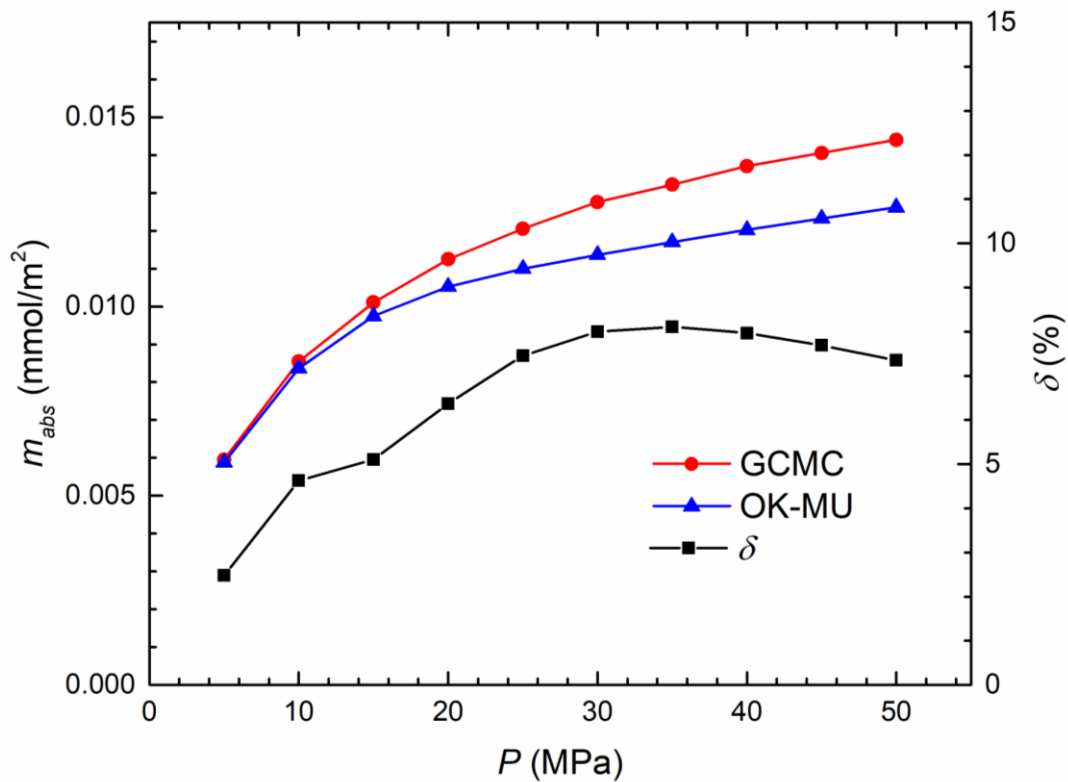
Figure 2-13 Comparison of combined absolute adsorption amount per specific surface area and their relative error $\delta = \left(m_{abs-GCMC} - m_{abs-OK} \right) / m_{abs-GCMC}$ from GCMC simulation and OK-MU in carbon nanopore of $W_e = 4$ nm at 333.15 K.

2.5 Conclusions

In this work, we performed GCMC simulation to investigate the methane adsorption in carbon nanopores at various pressures. We used the volumetric method to calculate the excess adsorption, using helium adsorption to determine the effective pore volume. Based on the density distributions, we proposed a modified adsorption model for methane to better take into account the effect of transition zone.

Our simulation results showed that the excess adsorption per specific surface area is insensitive to the pore size, when $W \geq 4$ nm. The second adsorption layer is observed and the density can be very different from the bulk, indicating the transition zone. Such transition zone can negatively affect the accuracy of the absolute adsorption calculation based on the monolayer adsorption model as shown in **Figure 2-1**. By using a modified adsorption model, the transition zone can be readily taken into account. OK-MU have shown excellent agreement with GCMC simulations on the excess adsorption and accurately characterize the transition zone. We found that the absolute adsorption calculated by OK-MU yields a good agreement with GCMC simulation, and the maximum relative error between these two methods is less than 6 %. In addition, we used the arbitrary effective pore width to test OK-MU. Even though a significant change in excess adsorption occurs, the OK-MU can still predict the methane absolute adsorption with an excellent agreement with GCMC simulations. In contrast to OK-MU, the prediction from OK-MO shows noticeable discrepancies from GCMC simulations. By using the modified adsorption model and OK-MU, the methane adsorption behavior in carbon nanopores can be readily characterized. Our work should provide important insights into the accurate estimation of methane absolute adsorption, especially in experimental applications.

Although a good agreement of methane adsorption can be found between OK-MU and GCMC simulation, the limitations of our work still exist. Our newly proposed adsorption model is only applicable when $W \geq 4$ nm. However, it is well known that shale has

extensive amount of micropores ($W \leq 2$ nm). Jin [84] reported that the adsorption behavior in micropores can be different from the adsorption model shown in **Figure 2-4**. We have been conducting a separate work to take into account the effect of pore size distribution (PSD) in OK-MU to accurately and efficiently characterize the methane adsorption behavior in shale porous media.

Acknowledgements

CHAPTER 3 ONO-KONDO LATTICE MODEL FOR PROPANE MULTILAYER ADSORPTION IN ORGANIC NANOPORES IN RELATION TO SHALE GAS

A version of this chapter has been published in *Fuel*.

Abstract

Accurate characterization of shale gas adsorption capacity is of great importance to the gas-in-place estimation and prediction of well productivity. Propane is one of major constituents in shale gases which can have multilayer adsorption behavior on the surface. While experiments can measure excess adsorption, the absolute adsorption, which describes the adsorbed gas capacity, has to be converted from the excess adsorption. In previous works, absolute adsorption is usually calculated from excess adsorption with adsorbed phase volume or density based on the single-layer adsorption model. However, for heavier alkanes, such as ethane and propane, which can have multilayered adsorption behavior, single-layer adsorption model becomes invalid. While molecular simulation can characterize the multi-layered adsorption behavior, it comes with expensive computational cost. Currently, there is no viable model to characterize the absolute adsorption of hydrocarbons which can have multi-layered adsorption behavior. In this work, we conduct grand canonical Monte Carlo (GCMC) simulation to study propane adsorption in shale nanopores over a wide range of pressures at temperature higher than the critical temperature. We find that propane can form multiple adsorption layers, thus, using single-layer adsorption model to obtain the absolute adsorption becomes unjustifiable. Based on the propane density distribution characteristics, we propose a multi-layered adsorption model and use Ono-Kondo (OK) lattice model with multi-layered structure to regress propane excess adsorption and subsequently obtain the absolute adsorption in each layer.

For propane, we take into account the correlation effect arising from the strong adsorbate-adsorbate interactions beyond mean field theory (MFT) and the only predetermined parameters are number of layers and adsorption layer width. The proposed OK model shows an excellent agreement with GCMC simulations on the excess adsorption and absolute adsorption in each layer, with discrepancies less than 6 % above 50 bar. The proposed OK model can readily take into account the propane multi-layered adsorption behavior, while significantly reduce the calculation time. Our method presents a reliable and highly-efficient approach for accurate characterization of adsorption of hydrocarbons with multi-layered structures and provide important insights into the gas-in-place estimation in shale.

Keywords: Excess adsorption; Absolute adsorption; Propane; Multilayer adsorption; Organic nanopores; Molecular simulations

3.1 Introduction

Shale gas has become a very important unconventional fossil fuel thanks to the advancement of fracturing technologies and greatly increased global energy supply [35, 38, 78, 79]. Unlike the conventional reservoir, where hydrocarbons are stored in porous media with pore sizes in the range of hundreds of nanometers or a few micrometers, there are extensive amount of nanosized pores as small as a few nanometers in shale [5, 9, 80, 82, 94]. In nanopores, where the pore size is comparable to the hydrocarbon molecular size,

the fluid distribution is inhomogeneous and surface adsorption becomes significant [100]. The adsorbed gas behaves differently from free gas and may contribute 20%-85% of the total gas content [141]. Therefore, the characterization of adsorbed gas in shale is key to the accurate estimation of gas-in-place and prediction of well productivity.

There have been a large number of experimental measurement on the methane excess adsorption in shale, based on both gravimetric and volumetric methods. Gasparik *et al.* [46] measured high-pressure methane excess adsorption isotherm in shale and found that excess adsorption has a maximum within the pressure range of 0-25 MPa at 65 °C and the shape of excess adsorption is mainly controlled by thermal maturity and clay mineralogy. Rexer *et al.* [35] measured maximum methane excess adsorption uptake within the temperature range of 300-473 K and found that it decreases with increasing pressure at high pressures. Zhou *et al.* [39] found that methane excess adsorption firstly reaches maximum and then decreases with increasing pressures. Although these experimental works provided important understanding about the methane adsorption behavior, the mainly reported values are excess adsorption and the absolute adsorption, which represents the actual gas adsorption capacity, still needs to be converted from the excess adsorption.

While methane is the major constituent of shale gas, the heavier hydrocarbon such as ethane, propane and butane still can exhibit a large quantity in shale reservoirs [142]. However, there has been only limited number of experimental works for heavier hydrocarbon adsorption in shale. Zhao *et al.* [64, 94] studied the adsorption behavior of

methane, ethane, propane, n-butane and iso-butane in isolated kerogen. They found that ethane, propane, n-butane and iso-butane present a significant hysteresis in adsorption/desorption isotherms in entire pressure range [94]. Gasparik *et al.* [143] measured ethane excess adsorption and found that excess adsorption amount firstly increases with pressure and then decreases. Liu *et al.* [142] measured excess adsorption/desorption isotherms of methane and n-butane on shale and reported higher adsorption capacity of n-butane than methane.

The excess adsorption amount measured in those works adopt gravimetric method, which uses the high-resolution balance to directly measure the adsorption isotherms. In order to convert excess adsorption m_{ex} to absolute adsorption m_{abs}, the adsorbed phase density ρ_a is generally used as [64],

$$m_{abs} = \frac{m_{ex}}{1 - \dfrac{\rho_b}{\rho_a}}. \tag{3.1}$$

Since it is well known that the adsorbed phase density depends on pressure and temperature conditions [91], Liu *et al.* [142] and Zhao *et al.* [64] calculated absolute adsorption by applying varying adsorbed phase density from GCMC simulation. In Liu *et al.*'s work [142], the adsorption layer is defined by the effective pore width and the saddle point from GCMC density distribution, and adsorbed phase density of n-butane is the average density within such layer. They found that the adsorbed phase density obtained from GCMC can be higher than n-butane liquid density (502 kg/m^3). On the other hand, Zhao *et al.* [64]

47

calculated the adsorbed phase density as the average density within the region between the first and second peak in the density distributions from GCMC simulation. These conversions are conducted based on the single-layered adsorption model, which has been widely used for methane adsorption. However, unlike methane, heavier hydrocarbons can form multi-layered adsorption [76, 77]. As a result, simply using single adsorbed phase density to convert the excess adsorption to absolute adsorption as depicted in Eq. (3.1) becomes invalid for heavier hydrocarbons. Currently, there is no work on the characterization of hydrocarbon absolute adsorption considering the multi-layered adsorption structures.

While molecular simulation can characterize the multi-layered adsorption behavior, it comes with expensive computational cost. Ono-Kondo lattice model [115-119] based on lattice theory has been used to study methane absolute adsorption in shale [81]. This model assumes that the adsorbate molecules can occupy the lattice space in pores and readily calculate the excess and absolute adsorption. Very recently, we applied OK lattice model with multi-layered structures to take into account the transition zone in methane adsorption and greatly improved the accuracy of absolute adsorption calculation [144]. It only requires pre-determined adsorption layer width to fit with experimentally or computationally obtained excess adsorption. Because OK lattice model can explicitly consider multi-layered structures, it can potentially characterize adsorption behavior with multi-layered adsorption structures and absolute adsorption in each layer.

In this work, we conduct grand canonical Monte Carlo (GCMC) simulation to study propane adsorption in shale nanopores over a wide range of pressures at temperature higher than the critical temperature. Carbon materials have been used to study hydrocarbon adsorption in organic matter, which is a main constituent of shale [100]. We use united atom model to simulate propane molecules. Propane excess adsorption is obtained following the same approach as in volumetric method, in which helium adsorption is used to calculate the effective pore volume. Based on the propane density distributions, we propose a modified OK model considering correlation effect due to strong adsorbate-adsorbate interactions beyond mean field theory (MFT) to regress excess adsorption. The number and width of adsorption layer can be determined by density distributions from GCMC simulation. Based on multilayer structure, OK model can calculate the absolute adsorption in each layer.

The remainder of this work is organized as follows. In **section 3.2**, we introduce the proposed OK model. In **section 3.3**, we describe the molecular simulation methods and models used in this work. In **section 3.4**, we will study the propane adsorption behavior in carbon nanopores, including the density distributions and excess adsorption. We then characterize propane adsorption model based on GCMC results and then use the proposed OK model to regress propane excess adsorption. Afterwards, we will compare the absolute adsorption in each layer between OK model and GCMC simulation. In **section 3.5**, we present the key conclusions.

3.2 Ono-Kondo lattice model

Basic equations of Ono-Kondo model can be found in **Appendix A**. For propane, due to strong adsorbate-adsorbate interactions, adsorbate-adsorbate interactions based on MFT may not describe adsorption behavior accurately [145]. To take into account such correlation effect, in this work, we expand the adsorbate-adsorbate interactions in the power of density, where the first term in the expansion can be regressed to the original MFT [146]. Based on the work by Aranovich and Donohue [146], the expansion of the interaction energy between molecules at layer $i+1$, $i-1$ and i can be given as,

$$
\begin{cases}
\varepsilon z_1 x_{i+1} + \alpha_p x_{i+1}^2 + \beta_p x_{i+1}^3 + \dots \\
\varepsilon z_1 x_{i-1} + \alpha_p x_{i-1}^2 + \beta_p x_{i-1}^3 + \dots, \\
\varepsilon z_2 x_i + \alpha_m x_i^2 + \beta_m x_i^3 + \dots
\end{cases}
\tag{3.1}
$$

where α_p and β_p represent the interaction coefficients of neighboring molecules in the same layer, α_p and β_p represent the interaction coefficients of neighboring molecules in adjacent layers. By taking the first and second order terms of interaction energy only, the modified enthalpy change can be given as:

$$
\begin{cases}
\Delta H_i = -\varepsilon \left(z_1 x_{i+1} + z_2 x_i + z_1 x_{i-1} - z_0 x_b \right) - \alpha_p \left(x_{i+1}^2 + x_{i-1}^2 - 2x_b^2 \right) - \alpha_m \left(x_i^2 - x_b^2 \right), \quad i \geq 2 \\
\Delta H_i = -\varepsilon \left(z_1 x_{i+1} + z_2 x_i - z_0 x_b \right) - \alpha_p \left(x_{i+1}^2 - 2x_b^2 \right) - \alpha_m \left(x_i^2 - x_b^2 \right) - \varepsilon_s, \quad i = 1
\end{cases}
$$

$$
\tag{3.2}
$$

As a result, the general form of OK model at equilibrium can be given as,

$$\begin{cases} \ln\left[\dfrac{x_i\left(1-x_b\right)}{x_b\left(1-x_i\right)}\right] + \left(z_1 x_{i+1} + z_2 x_i + z_1 x_{i-1} - z_0 x_b\right)\dfrac{\varepsilon}{k_B T} + \left(x_{i+1}^2 + x_{i-1}^2 - 2x_b^2\right)\dfrac{\alpha_p}{k_B T} + \left(x_i^2 - x_b^2\right)\dfrac{\alpha_m}{k_B T} = 0, \quad i \geq 2 \\ \ln\left[\dfrac{x_1\left(1-x_b\right)}{x_b\left(1-x_1\right)}\right] + \left(z_1 x_2 + z_2 x_1 - z_0 x_b\right)\dfrac{\varepsilon}{k_B T} + \left(x_{i+1}^2 - 2x_b^2\right)\dfrac{\alpha_p}{k_B T} + \left(x_i^2 - x_b^2\right)\dfrac{\alpha_m}{k_B T} + \dfrac{\varepsilon_s}{k_B T} = 0, \quad i = 1 \end{cases}$$

$$(3.3)$$

The excess adsorption amount can be expressed in terms of maximum monolayer adsorption capacity, adsorbed phase density and bulk density,

$$m_{ex} = m_{abs,m} \sum_{i=1}^{n}\left(x_i - x_b\right),$$

$$(3.4)$$

where n is the number of adsorbed lattice layers, and $m_{abs,m}$ is the maximum monolayer absolute adsorption amount in each layer. Considering constant layer volume (width) V_a, the excess adsorption of OK model can be obtained [144],

$$m_{ex} = \rho_{am} V_a \sum_{i=1}^{n}\left(x_i - x_b\right).$$

$$(3.5)$$

We apply the OK model considering multilayer adsorption and correlation effect to characterize propane adsorption in carbon nanopores. Unlike methane adsorbed phase width given as the LJ parameter of 0.38 nm [51, 106], the fixed propane adsorbed layer width used in OK model is 0.47 nm, obtained from propane density distributions by GCMC simulation as we will show later. In addition, when pressure is above 100 bar, the propane density distribution tends to have three noticeable peaks, indicating a three-layered

adsorption; when pressure is lower than 100 bar, only beyond the distance of six layers, the propane density is close to the bulk. Therefore, we consider 6 adsorption layers on each surface for all pressure conditions in OK model to account for the excess adsorption. Such assumption only applies to large nanopores and when the pore size is small, propane densities in the middle of the pores do not regress to bulk. In that case, the OK model should be reconstructed.

The OK model used in this work is given as,

$$
\begin{cases}
\ln\left(\dfrac{x_6(1-x_b)}{x_b(1-x_6)}\right) + (4x_6 + x_5 - 5x_b)\dfrac{\varepsilon}{k_BT} + (x_5^2 - x_b^2)\dfrac{\alpha_p}{k_BT} + (x_6^2 - x_b^2)\dfrac{\alpha_m}{k_BT} = 0 \\[2mm]
\ln\left(\dfrac{x_5(1-x_b)}{x_b(1-x_5)}\right) + (4x_5 + x_4 + x_6 - 6x_b)\dfrac{\varepsilon}{k_BT} + (x_4^2 + x_6^2 - 2x_b^2)\dfrac{\alpha_p}{k_BT} + (x_5^2 - x_b^2)\dfrac{\alpha_m}{k_BT} = 0 \\[2mm]
\ln\left(\dfrac{x_4(1-x_b)}{x_b(1-x_4)}\right) + (4x_4 + x_3 + x_5 - 6x_b)\dfrac{\varepsilon}{k_BT} + (x_3^2 + x_5^2 - 2x_b^2)\dfrac{\alpha_p}{k_BT} + (x_4^2 - x_b^2)\dfrac{\alpha_m}{k_BT} = 0 \\[2mm]
\ln\left(\dfrac{x_3(1-x_b)}{x_b(1-x_3)}\right) + (4x_3 + x_2 + x_4 - 6x_b)\dfrac{\varepsilon}{k_BT} + (x_2^2 + x_4^2 - 2x_b^2)\dfrac{\alpha_p}{k_BT} + (x_3^2 - x_b^2)\dfrac{\alpha_m}{k_BT} = 0 \\[2mm]
\ln\left(\dfrac{x_2(1-x_b)}{x_b(1-x_2)}\right) + (4x_2 + x_1 + x_3 - 6x_b)\dfrac{\varepsilon}{k_BT} + (x_1^2 + x_3^2 - 2x_b^2)\dfrac{\alpha_p}{k_BT} + (x_2^2 - x_b^2)\dfrac{\alpha_m}{k_BT} = 0 \\[2mm]
\ln\left(\dfrac{x_1(1-x_b)}{x_b(1-x_1)}\right) + (4x_1 + x_3 - 6x_b)\dfrac{\varepsilon}{k_BT} + (x_2^2 - 2x_b^2)\dfrac{\alpha_p}{k_BT} + (x_1^2 - x_b^2)\dfrac{\alpha_m}{k_BT} + \dfrac{\varepsilon_s}{k_BT} = 0
\end{cases}
$$

(3.6)

The proposed OK model is applied to regress excess adsorption from GCMC simulation by combing Eqs. (3.5) and (3.6). The fitting parameters are ρ_{am}, ε, ε_s, α_m and α_p. Eq. (3.6) is a set of nonlinear equations that can be solved iteratively. In this work, we use

simulated annealing (SA) optimization method implemented in MATLAB to solve those

five parameters.

3.3 Results and Discussion

The details of molecular simulation and model can be found in **Appendix B**. **Appendix C**

show the details of calculating effective pore volume using helium molecules.

3.4 Results and Discussions

In this section, the propane excess adsorption and density profiles in carbon nanopores

obtained from GCMC simulation are firstly studied. We then propose a multi-layered

adsorption model for propane adsorption based on density distributions. Afterwards, we

use the modified OK model with multilayered structures to calculate the absolute

adsorption and compare with GCMC simulation.

3.4.1 Propane adsorption behavior from GCMC simulation

Based on volumetric method, excess adsorption in our GCMC simulation can be calculated

as,

$$m_{ex} = \frac{\left\langle N_{C_3} \right\rangle / N_A - V_p \rho_{C_3,b}^m}{2S_A},$$

(3.7)

where $\left\langle N_{C_3} \right\rangle$ is the ensemble averaged number of propane molecules at given temperature

and pressure in the nanopores, $\rho_{C_3,b}^m$ is the propane molar density in the bulk at given

conditions and S_A is the specific surface area of the pore. The unit mmol/m^2 is used in this work to describe excess adsorption amount.

In **Figure 3-1**, we present the propane excess adsorption in carbon nanopore of 8 nm at isothermal condition of 393.15 K and pressures from 10 bar to 300 bar. The excess adsorption firstly increases to a maximum at around 50 bar and then decreases with pressure, which is similar to methane excess adsorption behavior [144]. This is because at lower pressure conditions, propane molecules are strongly attracted to the surface, so that the adsorbed phase density is much higher than the bulk density. Then, the adsorbed phase tends to be saturated by propane molecules and the difference in the adsorbed phase density and bulk density becomes smaller as pressure increases. Similar to methane adsorption, propane excess adsorption in carbon nanopores becomes independent on pore size when $W \geq 8$ nm (not shown here).
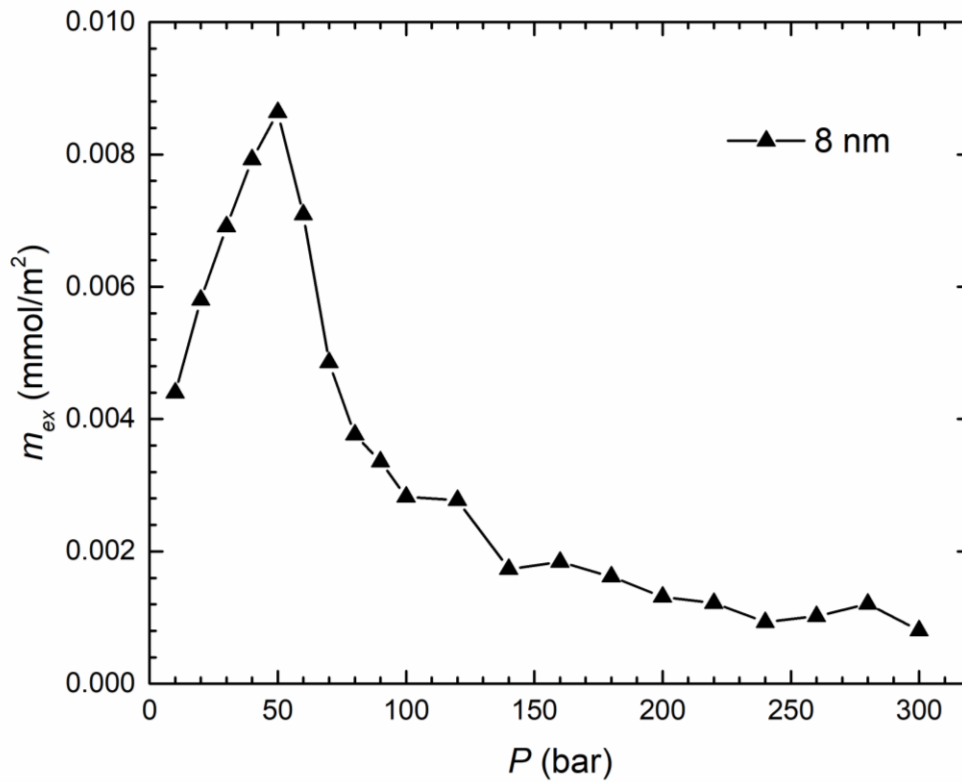
Figure 3-1 Excess adsorption amount per specific surface area from GCMC simulation in carbon nanopore of $W=8$ nm at 393.15 K.

In order to study propane multilayer adsorption behavior, we present the propane density profiles in carbon nanopore of $W=8$ nm at 393.15 K and various pressures in **Figure 3-2**. It shows that propane forms two strong adsorption layers and the density in the middle of the pore approaches to bulk density. Moreover, an obvious third peak can be observed from density distributions at pressures above 100 bar, indicating a third adsorption layer. However, even though the third peak is less significant at pressures lower than 100 bar, the propane density in the region far away from the pore surfaces is higher than the bulk density, indicating large transition zone [144]. Such transition zone contributes to the excess adsorption. As a result, if we only consider three adsorption layers without taking

into account the transition zone, the accuracy of absolute adsorption in each layer obtained

from excess adsorption will be negatively affected. Similar to our previous work [51], the

locations of the peaks and saddle points in propane density profiles remain the same as

pressure increases. Due to the multilayered adsorption behavior of propane, the commonly

used approaches to convert excess adsorption to absolute adsorption by Eqs. (3.1) becomes

unjustifiable. Thus, an adsorption model which can consider the multi-layered adsorption

structure is necessary for the accurate characterization of propane adsorption behavior and

absolute adsorption.
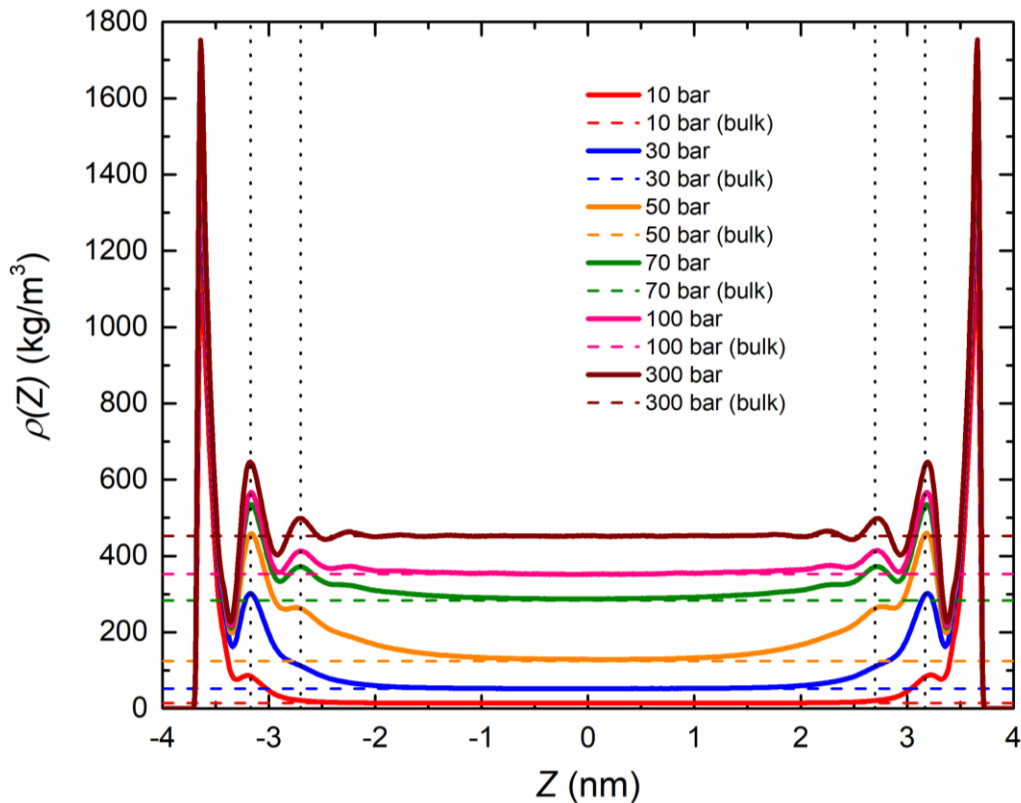
Figure 3-2 Propane density distributions from GCMC simulation at 393.15 K and various pressures in carbon nanopores of $W = 8$ nm. For comparison, the bulk densities from

NIST Chemistry Webbook are depicted as dashed lines. For clarity, we also use dotted lines to depict the locations of peaks of each adsorption layer.

3.4.1.1 Characterization of propane adsorption model

Figure 3-3 depicts the schematic representation of the first, second and third adsorbed layer in activated carbon nanopore of $W = 8$ nm based on GCMC simulation at 393.15 K and various pressures. We consider two different adsorption models: pressure above 100 bar as shown in **Figure 3-3 (a)** and below 100 bar in **Figure 3-3 (b)**. In both models, the region $z_{AA'}$ defines the effective pore volume (width), which is given as $z_{AA'} = V_p / S_A$. In **Figure 3-3 (a)**, the adsorption model contains four different parts: first, second, the third adsorption layers and free gas zone. The first adsorption layer is defined as the phase between point A and point B, which is the saddle point of the density profile between the first and second layers. The second adsorption layer is defined as the zone between point B and point C, which is the saddle point of the density profile between the second and third adsorption layers. The third adsorption layer is defined as the region between point C and point D, which is the saddle point of the density profile between the third adsorption layer and free gas zone. Therefore, the free gas zone is characterized between point D and D'. It is noted that the point B, C and D are from density profiles at 300 bar. In this work, we find that the widths of those points are $z_{AB} = 0.53$ nm, $z_{BC} = 0.44$ nm and $z_{CD} = 0.47$ nm, respectively. The heights of the first, second, third and free gas zone are given as

$$\rho_{a1} = \int_A^B \rho(z)\,dz / z_{AB} \quad , \qquad \rho_{a2} = \int_B^C \rho(z)\,dz / z_{BC} \quad , \qquad \rho_{a3} = \int_C^D \rho(z)\,dz / z_{CD} \qquad \text{and}$$

57

$$\rho_f = \int_D^{D'} \rho(z)\,dz\,/\,z_{DD'}\,,$$ respectively. When pressure is lower than 100 bar, due to large

transition zone, more adsorption layers should be considered as depicted in **Figure 3-3 (b)**.

The characterization of the first three adsorption layers remains the same as **Figure 3 (a)**.

We find that the distance between three peaks in density distributions at high pressures is

around 0.47 nm, which can be used as adsorption layer width at lower pressure. As a result,

we define the widths of the fourth, fifth and sixth adsorption layer as $z_{DE} = 0.47$ nm,

$z_{EF} = 0.47$ nm and $z_{FG} = 0.47$ nm and the free gas region is characterized between point

G and G'. The heights of the fourth, fifth, sixth and free gas zone are defined as

$$\rho_{a4} = \int_D^E \rho(z)\,dz\,/\,z_{DE}\quad,\qquad \rho_{a5} = \int_E^F \rho(z)\,dz\,/\,z_{EF}\quad,\qquad \rho_{a6} = \int_F^G \rho(z)\,dz\,/\,z_{FG}\qquad \text{and}$$

$$\rho_f = \int_G^{G'} \rho(z)\,dz\,/\,z_{GG'}\,,$$ respectively.
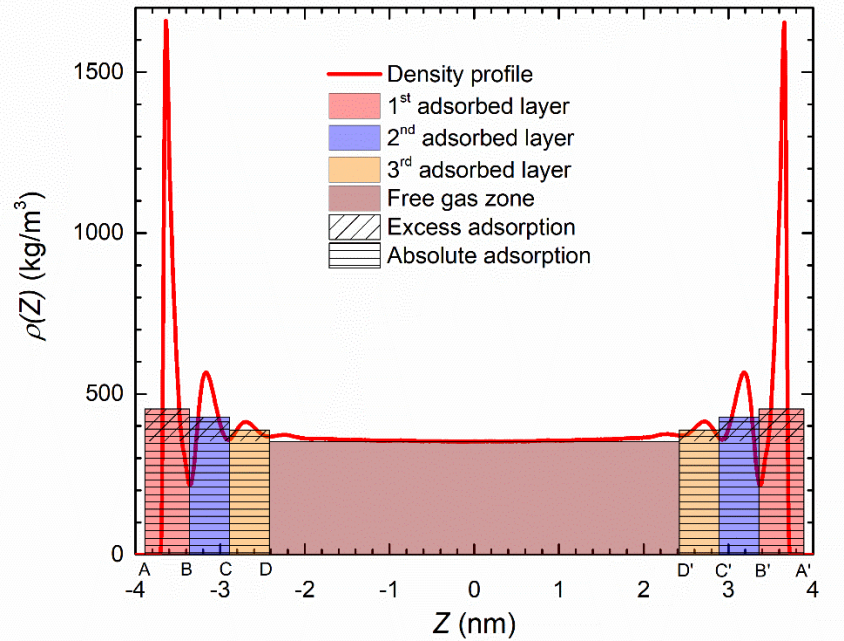
(a)
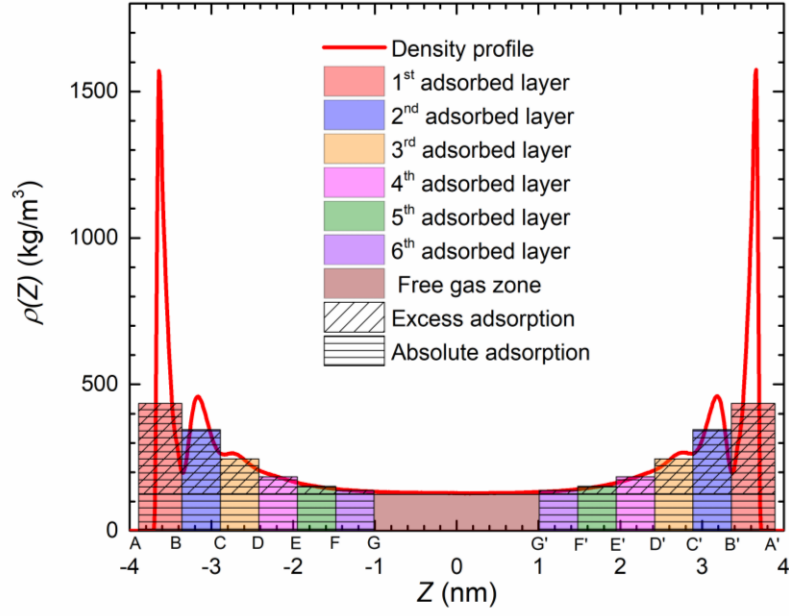
(b)

Figure 3-3 Schematic representation of the first, second and third adsorbed layer in carbon nanopore of $W = 8$ nm based on GCMC simulation at 393.15 K and (a) 100 bar; (b) 50 bar. In Figure 3-3 (a), the heights of adsorbed phase density of the first, second, third layers and free gas zone are obtained by $\rho_{a1} = \int_{A}^{B} \rho(z) dz / z_{AB}$, $\rho_{a2} = \int_{B}^{C} \rho(z) dz / z_{BC}$,

$\rho_{a3} = \int_{C}^{D} \rho(z) dz / z_{CD}$ and $\rho_{f} = \int_{D}^{D'} \rho(z) dz / z_{DD'}$, respectively. In Figure 3-3 (b), the heights of adsorbed phase density of the first, second, third, fourth, fifth and sixth layers and free gas zone are obtained by $\rho_{a1} = \int_{A}^{B} \rho(z) dz / z_{AB}$, $\rho_{a2} = \int_{B}^{C} \rho(z) dz / z_{BC}$,

$$\rho_{a3} = \int_{C}^{D} \rho(z)\,dz\,/\,z_{CD}, \quad \rho_{a4} = \int_{D}^{E} \rho(z)\,dz\,/\,z_{DE}, \quad \rho_{a5} = \int_{E}^{F} \rho(z)\,dz\,/\,z_{EF}, \quad \rho_{a6} = \int_{F}^{G} \rho(z)\,dz\,/\,z_{FG}$$

and $\rho_f = \int_{G}^{G'} \rho(z)\,dz\,/\,z_{GG'}$, respectively.

To validate our proposed propane adsorption model, we compare the free gas density from GCMC simulation and the bulk density obtained from NIST Chemistry Webbook as depicted in **Figure 3-4**. In **Figure 3-4 (a)**, we depict the free gas density that is calculated based on three adsorption layers for all pressure conditions and the relative errors between free gas density and bulk density as $\delta_f = (\rho_f - \rho_b)\,/\,\rho_b$. δ_f is less than 2 % at high pressures, while it is larger than 10 % at low pressure conditions and reaches a maximum of around 18 % at 50 bar. Considering six adsorption layers for all pressure conditions, the calculated free gas density and relative errors of GCMC results and bulk density are shown in **Figure 3-4 (b)**. It is noted that by using 6-layer adsorption model, the discrepancy between ρ_f and ρ_b is less than 5 % for all pressure conditions; while at high pressures, the relative error is around only 1 %. Thus, we use 6-layer adsorption model to characterize propane adsorption behavior.
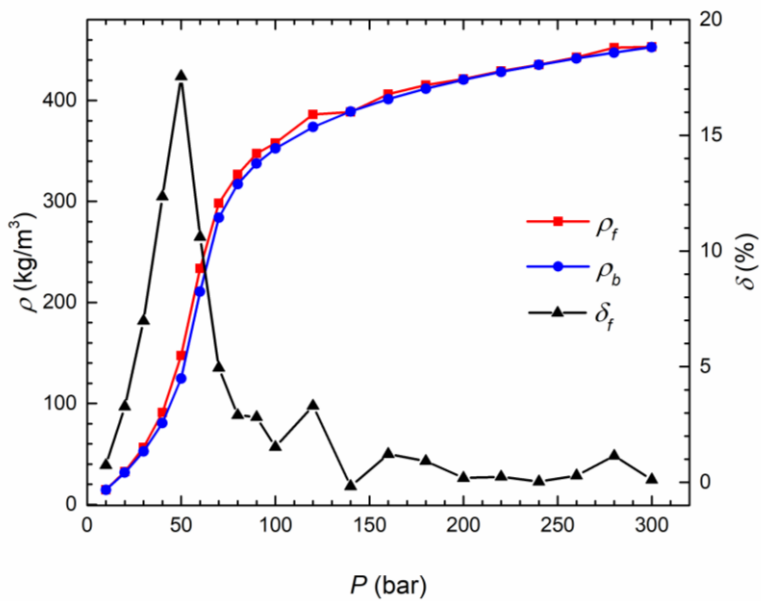
(a)
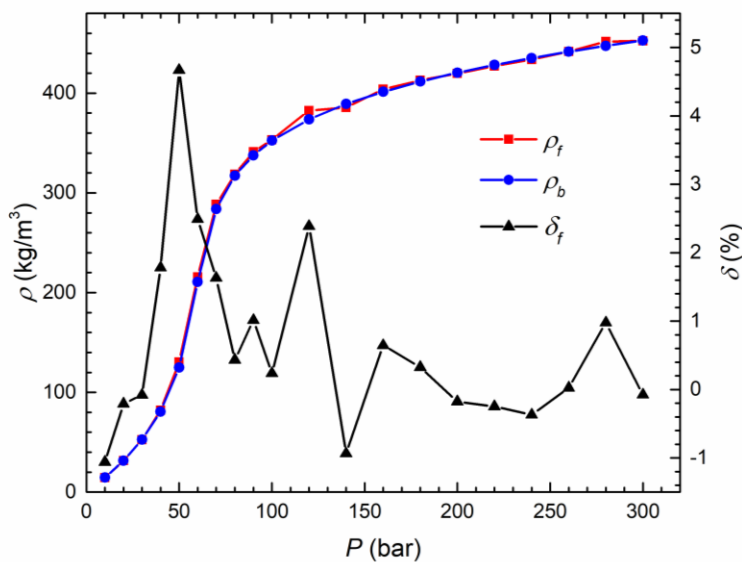
(b)

Figure 3-4 Comparison of free gas density from GCMC simulation and bulk density from NIST Chemistry Webbook and their relative error $\delta_f = \left(\rho_f - \rho_b \right) / \rho_b$ in carbon nanopores of considering (a) three adsorbed layers; (b) six adsorbed layers at 393.15 K.

In **Figure 3-5 (a)**, we present the adsorbed phase density in each layer from GCMC

simulation in carbon nanopore of $W = 8$ nm at 393.15 K. Obviously the densities of the first, second, and third adsorption layers are much higher than the bulk. The density of each layer increases with pressure while the density of the first layer readily approaches a plateau around 100 bar, indicating that the first layer is saturated. The density of the second layer increases rapidly at low pressures and then tends to be comparable to the density of the first layer at high pressures. The second layer density becomes higher than the first layer when pressure is higher than 200 bar, which is possibly due to difference in the adsorption layer widths. The density of the third adsorption layer is still higher than bulk density, while the densities of the fourth, fifth and sixth layer are slightly higher than bulk at low pressures and then become similar as pressure increases. Such trend can be also found in **Figure 3-5 (b)**, which presents the enhancement of each adsorbed phase density with respect to the bulk density.
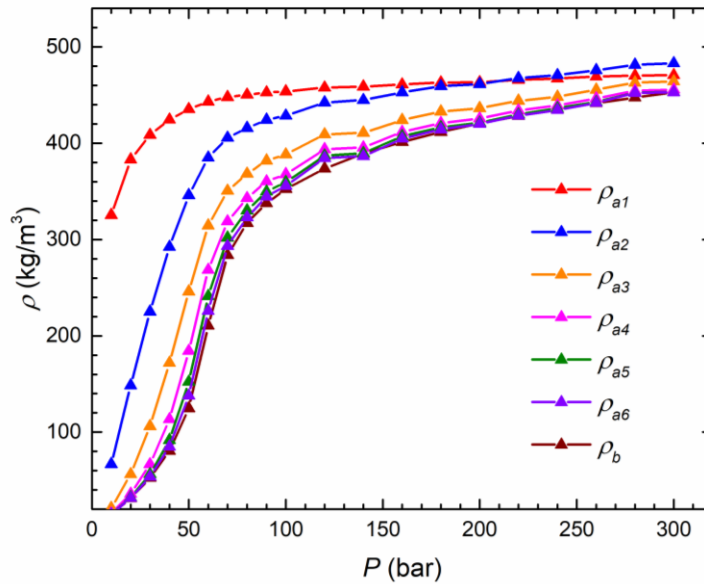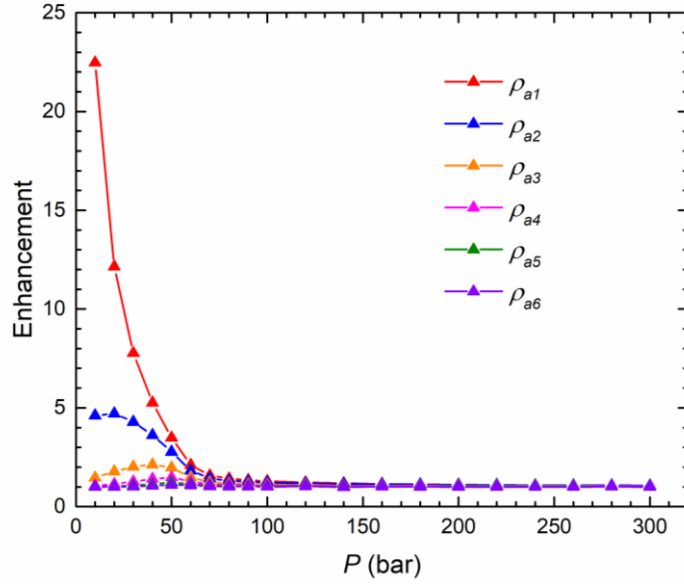
Figure 3-5 Adsorbed phase density in each adsorbed layer of $W = 8$ nm from GCMC simulation and bulk density from NIST Chemistry Webbook at 393.15 K. (a) adsorbed phase density; (b) enhancement of adsorbed phase density with respect to bulk density.

As a result, the absolute adsorption of each layer can be obtained by the adsorbed phase width and density,

$$m_{abs}^{Li} = \rho_{ai} V_{ai} , \qquad (3.8)$$

$$V_{ai} = 2 S_A z_i , \qquad (3.9)$$

where m_{abs}^{Li}, ρ_{ai}, V_{ai} and z_i are the absolute adsorption, adsorbed phase density, adsorbed phase volume and adsorbed phase width of layer i, respectively.

3.4.2 Adsorption behavior from Ono-Kondo lattice model

Based on the propane adsorption model we proposed in the last section, we use our modified OK model with multilayer structure to fit with GCMC simulation on the excess adsorption. We assume six adsorption layers on each pore surface that contributes to excess and absolute adsorption in a symmetric pore space and the density beyond the six layers reaches bulk. The width of each layer used in OK model is defined as the width between peaks of $z_{OK} = 0.47$ nm in density distributions from GCMC simulation. The regression of excess adsorption obtained from GCMC simulation using OK model is presented in Figure 6. The five fitting parameters with different ranges are given as follows: $0 < \rho_{am} < 700$ kg/m³, $-1 < \varepsilon / k_B T < 0$, $-10 < \varepsilon_s / k_B T < 0$, $-3 < \alpha_m < 3$ and $-3 < \alpha_p < 3$. The calculated fitting parameters are $\rho_{am} = 516.3236$ kg/m³, $\varepsilon / k_B T = -0.7917$, $\varepsilon_s / k_B T = -3.9509$, $\alpha_m / k_B T = 2.6970$ and $\alpha_p / k_B T = -0.7732$ with the root mean square deviation of $R^2 = 0.9927$. The OK model shows an excellent agreement with GCMC simulation.
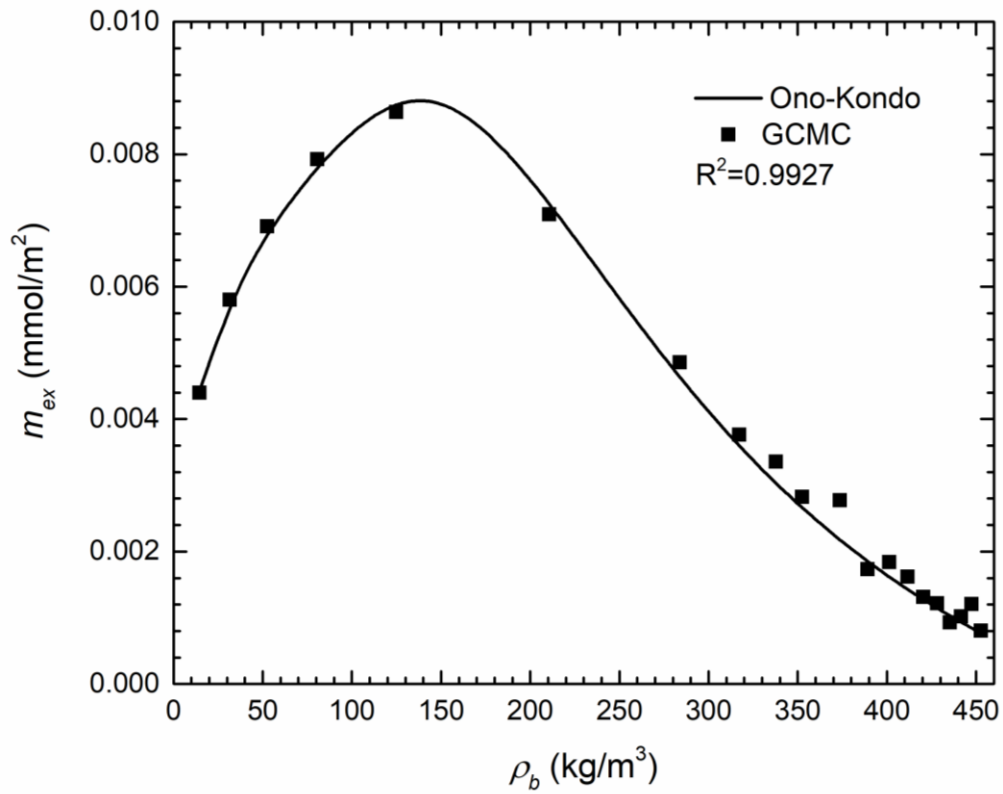
Figure 3-6 Ono-Kondo model with 6-layer structure and constant adsorbed phase width of 0.47 nm for fitting propane excess adsorption from GCMC simulation in carbon nanopore of $W = 8$ nm at 393.15 K.
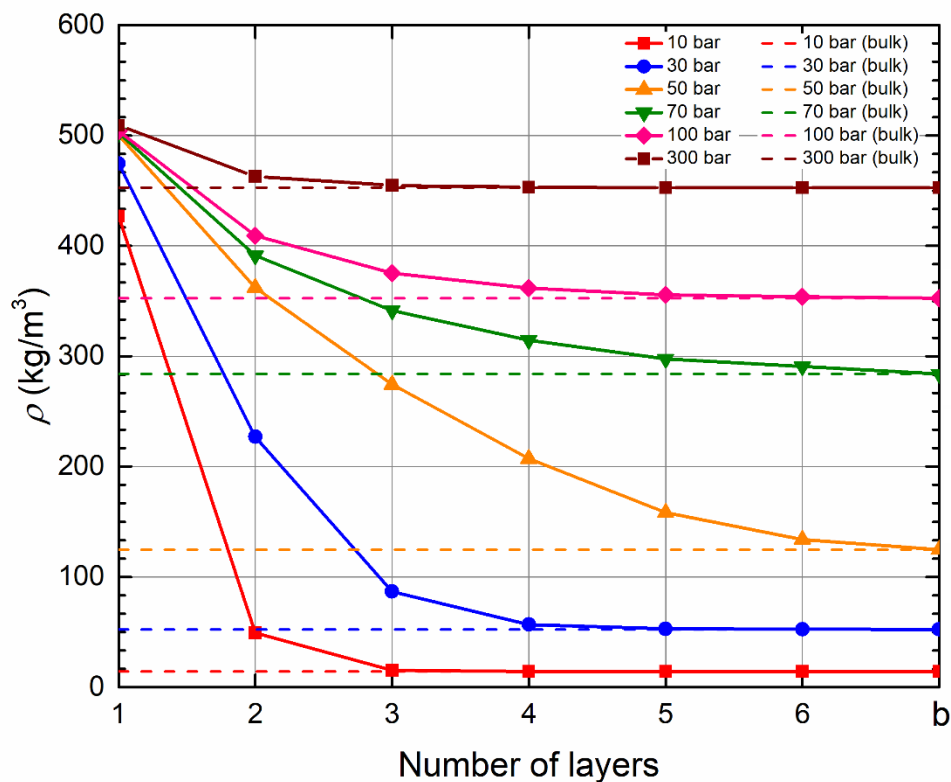
Figure 3-7 Densities of each layer from OK lattice model in carbon nanopores of $W = 8$ nm at 393.15 K. The seventh layer represents the bulk phase.

In **Figure 3-7**, we plot each layer densities obtained from OK model at different pressures. For all pressure conditions, the densities of the first and second layer are higher than the bulk. At 10 bar, the densities from the third to sixth adsorption layer are close to the bulk; as pressure increases to 100 bar, the length of transition zone first increases then decreases. As pressure further increases and then the densities of third to sixth layers become close to bulk. Such behavior is in line with that observed from GCMC simulation.

In **Figure 3-8**, we present the absolute adsorption amount per specific area calculated by GCMC and OK model. The absolute adsorption of OK model is calculated by adsorbed

phase density and width:

$$m_{abs,OK}^{Li} = \rho_{ai,OK} V_{ai,OK},\qquad(3.10)$$

$$V_{ai,OK} = 2S_A z_{i,OK},\qquad(3.11)$$

where m_{abs}^{Li}, ρ_{ai}, V_{ai} and z_i are the absolute adsorption, adsorbed phase density, adsorbed phase volume and adsorbed phase width of layer i in OK model, respectively. Overall, OK lattice model shows an excellent agreement with GCMC simulation. The absolute adsorption of the first layer calculated by OK model is firstly overestimated and then becomes less than GCMC simulation from 60 bar, while that of the second and third layer have a good agreement with GCMC simulation at lower pressure conditions and then become underestimated from 60 bar. It can be seen from **Figure 3-8 (b)** that the absolute adsorption of the fourth, fifth and sixth layer calculated by OK model agrees well with GCMC simulation.
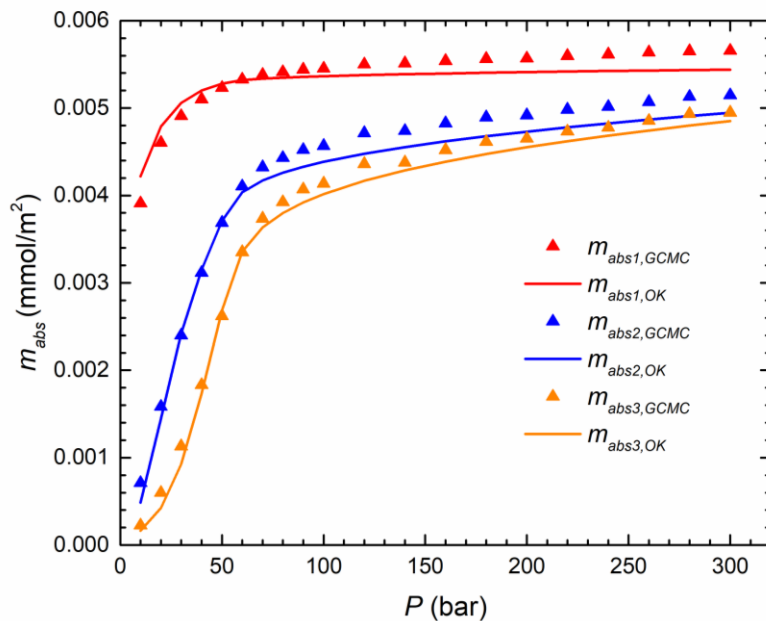
(a)
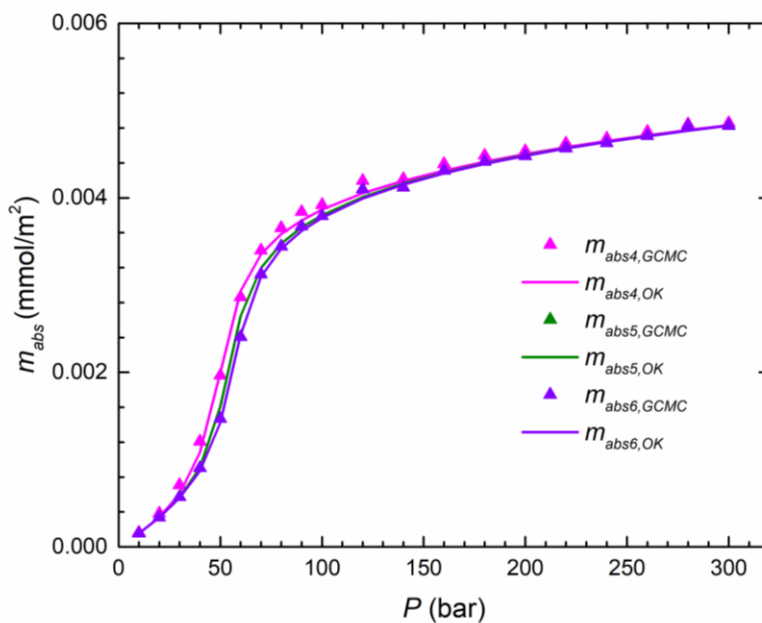
(b)

Figure 3-8 Absolute adsorption amount per specific surface area from GCMC simulation and OK model of $W = 8$ nm at 393.15 K. (a) The first, second and third adsorbed layers; (b) The fourth, fifth and sixth layers.
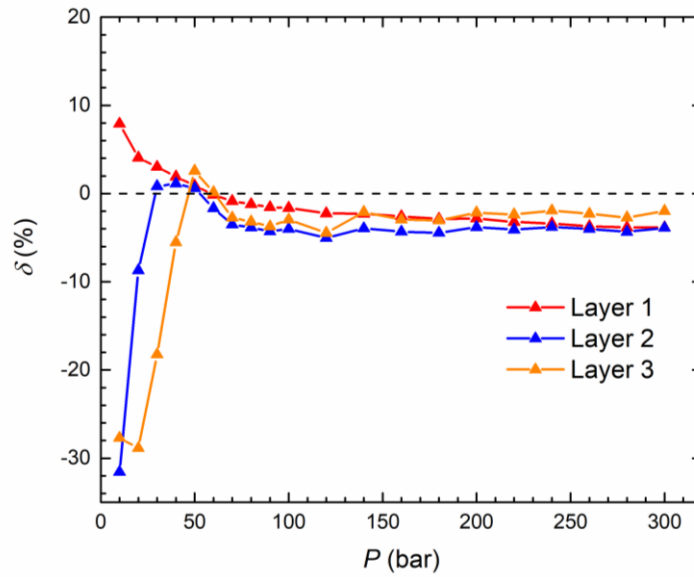
(a)
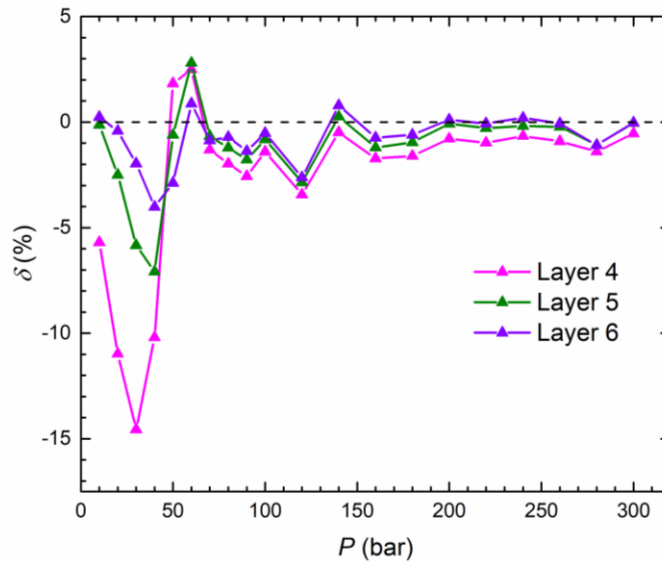
(b)

Figure 3-9 Relative differences $\delta = \left(m_{abs-GCMC} - m_{abs-OK}\right)/m_{abs-GCMC}$ of absolute adsorption amount per specific surface area from GCMC simulation and OK model of $W = 8$ nm at 393.15 K. (a) The first, second and third adsorbed layers; (b) The fourth, fifth and sixth layers.

We present the relative differences $\delta = \left(m_{abs-GCMC} - m_{abs-OK}\right)/m_{abs-GCMC}$ of absolute

adsorption amount per specific surface area from GCMC simulation and OK model in

Figure 3-9. The maximum relative error of each layer appears at low pressure conditions; the maximum overall relative error is around -32% for the second layer at 10 bar. When pressure is above 50 bar, the relative errors of absolute adsorption in first three layers become constantly within 6%, while the maximum relative error for the last three layers is around 4%.

3.5 Conclusions

In this work, we conduct GCMC simulation to investigate propane adsorption in carbon nanopores at various pressures at 393.15 K. The volumetric method is used to obtain excess adsorption from GCMC simulation. We use helium adsorption to obtain effective pore volume. We observe that propane forms multilayer adsorption structures. Based on propane density distributions, we use 6-layer structure to characterize the propane adsorption for all pressure conditions. As a result, simply applying Eq. (3.1), which is based on the monolayer adsorption model, may become inapplicable for propane absolute adsorption estimation.

Our simulation shows that for pressure above 100 bar, three adsorption layers can be found clearly from density distributions. When pressure is lower than 100 bar, the effect of the fourth, fifth and sixth layer is non-negligible. Then, we apply OK model with multilayered structure with predetermined number and width of adsorbed phase from GCMC results to

regress the excess adsorption. Moreover, the correlation effect arising from the strong adsorbate-adsorbate interactions beyond MFT are taken into account in our modified OK model.

Our newly proposed OK model shows excellent agreement with GCMC simulation on excess adsorption. We find that the calculated absolute adsorption for each layer yields good agreement with GCMC simulations, with maximum relative error less than 6 % above 50 bar. Our work should provide important insights into the accurate characterization of heavier hydrocarbon multilayer adsorption behavior and the estimation of absolute adsorption in shale, especially in experimental applications.

Acknowledgments

CHAPTER 4 TACKLING THE CHALLENGES IN THE ESTIMATION OF METHANE ABSOLUTE ADSORPTION IN KEROGEN NANOPOROUS MEDIA FROM MOLECULAR AND ANALYTICAL APPROACHES

A version of this chapter has been published in *Fuel*.

Abstract

Accurate characterization of methane absolute adsorption in shale nanoporous media is of great importance to the gas-in-place (GIP) estimation and well productivity. Because experimental measurement can only provide the excess adsorption, the absolute adsorption is generally converted from the excess adsorption based on the single-layer adsorption model. However, it is well known that shale has a widespread pore size distribution (PSD), ranging from sub 2-nm to hundreds of nanometers. In micropores (<2 nm), methane may have layering structures, which deviates from the commonly used adsorption model. Thus, it is necessary to take into account the varying methane adsorption behavior in micropores and mesopores and consider the PSD effect to obtain the absolute adsorption from the experimentally measured excess adsorption. In this work, we propose a number of artificially generated PSDs and study methane adsorption in each nanopore by using grand canonical Monte Carlo (GCMC) simulations. By coupling GCMC simulations and varying PSDs, we effectively model methane adsorption in nanoporous media. Based on the varying density profiles in different nanopores obtained from GCMC, we propose the corresponding methane adsorption model in each nanopore. Combining the actual PSD and different adsorption behaviors in varying pores, by fitting the excess adsorption in nanoporous media, OK lattice model can readily obtain the absolute adsorption. In order to validate our model, 1000 sets of randomly generated PSDs are used. We find that our proposed OK model has an excellent agreement with GCMC simulation, while the

commonly used method to convert the excess adsorption to the absolute adsorption without considering the PSD shows noticeable deviations. Moreover, the optimized constant adsorbed phase densities are very different from the commonly used values as 424 kg/m^3 and 373 kg/m^3. Our work proposes a simple, efficient and accurate empirical model to calculate the absolute adsorption in nanoporous media. This work should provide important insights into accurate characterization methane absolute adsorption and the gas-in-place estimation in shale.

Keywords: Methane absolute adsorption; Excess adsorption; GCMC simulation; Ono-Kondo lattice model; Shale nanoporous media

4.1 Introduction

Thanks to the advancement of hydraulic and horizontal fracturing technologies, shale gas has become an important natural gas resource which can greatly enhance the global energy supply [147]. Unlike conventional reservoirs, where pores are large in the range of hundreds of nanometers or a few micrometers, shale has extensive amount of nanoscale pores, ranging from sub-2 nm to hundreds of nanometers [123]. In small nanopores, fluid distributions are inhomogeneous and surface adsorption is significant [5, 80, 82, 148]. As a result, adsorbed gas can consist up to 85% of the total gas content in shale [38, 141, 149]. The properties of adsorbed gas are greatly different from free gas and cannot be described by the conventional equation of state modeling. Thus, the characterization of adsorbed gas

in shale plays a critical role in the accurate estimation of gas-in-place (GIP) and well productivity [148, 150].

There have been a number of experimental measurements to characterize gas adsorption in shale [39, 47, 93, 94], mainly using gravimetric and volumetric methods. Unfortunately, both approaches can only measure the excess adsorption m_{ex}, while the absolute adsorption m_{abs} which dictates the adsorbed gas amount needs to be converted from m_{ex}. Assuming single-layered adsorption model in various shale nanopores as shown in **Figure 4-1(a)**, m_{abs} can be converted from m_{ex} based on the adsorbed phase density ρ_a [35, 102],

$$m_{abs} = \frac{m_{ex}}{1 - \rho_b / \rho_a},$$ (4.1)

where ρ_b is the free gas density. In a large number of previous works, ρ_a is assumed to be a constant as the liquid methane density at the normal boiling point (424 kg/m^3) or the methane Van der Waals density (373 kg/m^3) [151-153]. Assuming that m_{abs} can be modeled by Langmuir [44, 46, 47] and supercritical Dubinin-Radushkevich (SDR) [50, 51] methods, the constant ρ_a can be obtained by fitting experimentally measured m_{ex} based on Eq. (4.1). On the other hand, Gensterblum *et al.* [154] and Clarkson and Haghshenas [155] demonstrated that the constant ρ_a can be obtained from the linear intercept of m_{ex} versus ρ_b. However, molecular simulations revealed that ρ_a is dependent on the pressure

and temperature, and thus, cannot be considered as constant [64]. In addition, the presence

of transition zone [51, 106, 107] which is beyond the first adsorption layer can negatively

affect the accuracy of Eq. (4.1), when converting m_{ex} to obtain m_{abs}. As shown in **Figure 4-1 (b)**, since the density of transition zone is higher than that of free gas, it contributes to

m_{ex}, while Eq. (4.1) cannot take into account such effect. Recently, we explicitly

characterized the transition zone by using a modified multilayer adsorption model (as

shown in **Figure 4-1 (b)**) coupled with the Ono-Kondo (OK) lattice theory and accurately

obtained the methane absolute adsorption in kerogen mesopores [156]. While these works

have greatly advanced the understanding about the methane absolute adsorption in shale

nanopores, they did not consider the varying methane adsorption behavior in different sized

nanopores. For example, in micropores (<2 nm), depending on the pore size, methane may

exhibit layering structures and there is no free gas zone [67, 157, 158], which is very

different from the single-layer adsorption model as depicted in **Figure 4-1 (a)**. Therefore,

one cannot simply use Eq. (4.1) to convert m_{ex} in nanoporous media to obtain m_{abs}. Due

to different adsorption mechanisms in micropores and mesopores (>2 nm), it is necessary

to explicitly consider the effect of pore size distribution (PSD) on the conversion of m_{ex}

to m_{abs}. While molecular simulations can characterize the varying adsorption behaviors in

different sized nanopores, they often come with expensive computational cost. To the best

of our knowledge, there is no viable model to convert m_{ex} in nanoporous media to m_{abs}

by considering the PSD effect.

Comparing to molecular simulations, OK lattice model can significantly reduce calculation time, while it can potentially characterize the varying adsorption behavior and methane layering structures in micropores [118, 156]. In this work, we propose a number of artificially generated PSDs and study methane adsorption in each nanopore by using grand canonical Monte Carlo (GCMC) simulations. By coupling GCMC simulations and varying PSDs, we effectively model methane adsorption in nanoporous media. Molecular simulation allows researchers to study the characteristic of adsorbate under atomic scale and provides an effective way to investigate the adsorption mechanism in shale. However, the realistic behavior of gas adsorption in reservoir is much more complex due to various shale rock compositions [5], pore structures [45], organic-matter type and thermal maturity [22, 46], which remain as challenging problems and limitations for performing molecular simulation. Shale is composed of organic and inorganic matter. There are some recent simulation works (both GCMC and molecular dynamics) focusing on the gas adsorption and diffusion in clay minerals such as illite, kaolinite and montmorillonite, and adsorption capacity with controlling factors including temperatures, pressures, pore size and water content is investigated [45, 51, 65, 91, 159-161]. Tian *et al.* [51] used GCMC to observe methane adsorption in clay minerals, found the specific surface area (SSA) plays a dominant role in adsorption capacity and excess adsorption amount per SSA is similar in different clay minerals at given condition. Xiong *et al.* [65] concluded from GCMC simulation that the methane adsorption capacity showing organic pore> clay mineral pore>

quartz pore, and two typical oxygen containing groups (-COOH and -OH) are used to model different maturity level in organic pore. As for adsorption in kerogen which is the main constituent of the organic matters in shale [5], some researchers adopted full atomistic model to construct the pore wall [127-129]. However, it is reported that no effective way to represent the realistic kerogen molecular structure [162] because of its complex structure and composition [7]. For simplicity, we use the carbon slit-nanopores to simulate kerogen, which may relate to kerogen with higher carbon content. In addition, the simplified slit-like pore structure adopted in molecular simulation has the same geometry as in OK lattice model. Methane molecules are treated as single site Lennard-Jones (LJ) particles in our simulation. Excess adsorption can be obtained following the experimental volumetric method [89], while the effective pore volume is obtained by helium adsorption. Based on the varying density profiles in different nanopores obtained from GCMC, we propose the corresponding methane adsorption model in each nanopore. Combining the actual PSD and different adsorption behaviors in varying pores, by fitting m_{ex} in nanoporous media, OK lattice model can readily obtain m_{abs}. In order to validate our model, 1000 sets of randomly generated PSDs are used. We find that our proposed OK model has an excellent agreement with GCMC simulation, while using commonly applied constant ρ_a as 424 kg/m^3 or 373 kg/m^3 in Eq. (4.1) shows noticeable deviations. In addition, the optimized constant ρ_a by fitting m_{ex} and m_{abs} from GCMC as shown in Eq. (4.1) is very different from these two widely used parameters and dependent on temperature. Our work should provide important

insights into the conversion of m_{ex} in nanoporous media to m_{abs} and the accurate estimation of GIP in shale.

The remainder of this paper is organized as follows. In **section 4.2**, we explain the nanoporous media model. In **section 4.3**, we describe the molecular model and simulation. In **section 4.4**, we describe the proposed OK models in varying nanopores. In **section 4.5**, we firstly study the excess adsorption in different sized nanopores and characterize the adsorption models based on density distributions. Then, OK model is used to regress the excess adsorptions in 1000 different nanoporous media of varying PSDs and compare the absolute adsorption with GCMC simulations. In **section 4.6**, we summarize the key findings and conclusions.

4.2 Nanoporous Media Model

Due to the widespread pore size distribution in shale, the different methane adsorption behaviors in micro- and meso-pores should be taken into account explicitly. By using molecular dynamics (MD) simulations, Jin [158] observed varying methane density profiles in nanopores from 0.7 to 5 nm. Mosher *et al.* [67] carried out GCMC simulation to study methane adsorption in different sized nanopores from 0.4 nm to 9 nm. They found that in micropores, the proximity of pore walls leads to the strong overlap of adsorbate-adsorbent interactions, which greatly affects the adsorption behavior as shown in **Figure 4-2**, based on our GCMC simulations. For example, in 1-nm nanopores, methane forms a

two-layered structure with one strong adsorption layer on each surface; in 1.5-nm nanopores, methane forms a three-layered structure with a relatively weaker layer in the middle of the pore; in 2-nm nanopores, such layer in the middle of the pore is splitted into two weak adsorption layers forming on each side of the pore. When pore size is larger than 2 nm, methane density in the middle of the pore is the same as free gas. In our previous works [51, 156], we found that m_{ex} per specific surface area (SSA) is independent of pore size W, when $W \geq 4$ nm in line with Chen *et al.* [136]. However, the second adsorption layer (i.e. transition zone) should be explicitly considered in $W \geq 4$ nm carbon nanopores [156]. According to the varying methane density distributions in different micropores, we divide the pores in shale into four distinct parts in our nanoporous media model, i.e. $W = 1$ nm, 1.5 nm, 2 nm, and ≥ 4 nm. While shale contains pores up to hundreds of nanometers [123], since m_{ex} per SSA is independent of W when $W \geq 4$ nm, we consider pore size up to 10 nm to represent the mesopores and macropores. Overall, seven different sizes of nanopores are considered as $W = 1$ nm, 1.5 nm, 2 nm, 4 nm, 6 nm, 8 nm and 10 nm. The validity of OK model coupling with PSD is tested by using 1000 randomly generated PSDs as depicted in **Figure 4-3**.
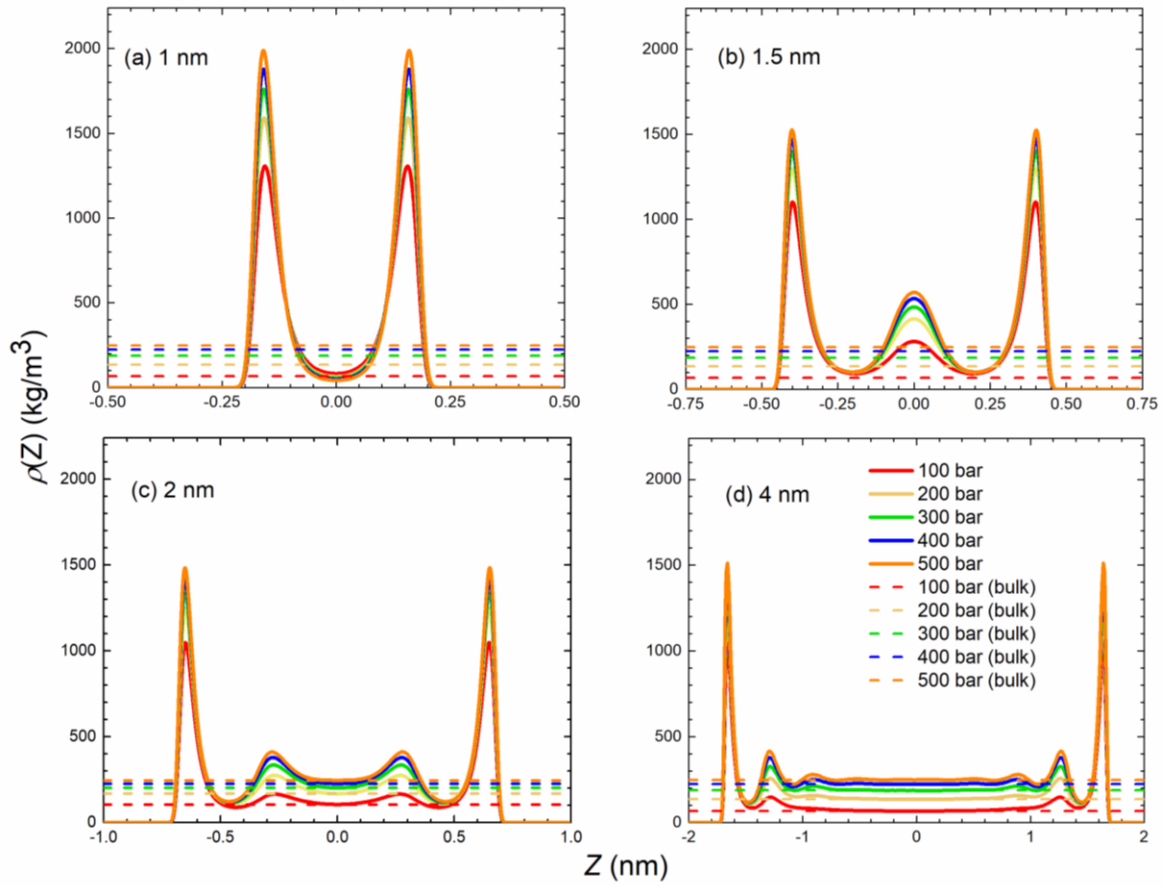
Figure 4-2 Methane density distribution from GCMC simulation at 333.15 K and various pressures in carbon nanopores of (a) $W = 1$ nm; (b) $W = 1.5$ nm; (c) $W = 2$ nm; (d)

$W = 4$ nm. For comparison, the bulk densities from NIST Chemistry Webbook are depicted as dashed lines.
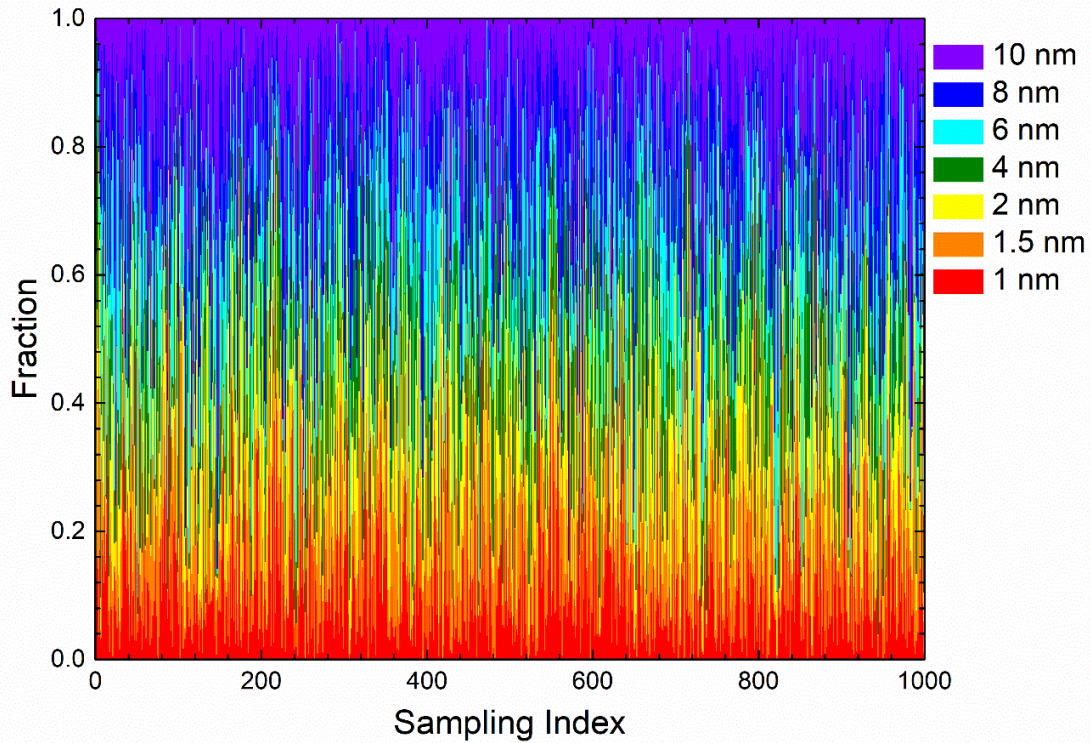
Figure 4-3 Pore size distribution of 1000 randomly generated samples.

4.3 Molecular model and simulation

The molecular simulation model and helium detected effective pore volume are shown in **Appendix B** and **C**, respectively. The total excess adsorption in nanoporous media $m_{ex,T}^{MC}$ is given as,

$$m_{ex,T}^{MC} = \sum_k^p PSD_k m_{ex,k}^{MC} ,$$

(4.2)

where p is the number of types of pore in porous media and PSD_k is the pore size distribution of specific pore k.

82

4.4 Ono-Kondo lattice model

The detailed derivation of OK model is listed in **Appendix A**.

Based on our previous work [156], the excess adsorption in a given nanopore k per SSA can be described as,

$$m_{ex,k}^{OK} = \rho_{am} W_a \sum_{i=1}^{n_k} (x_i - x_b),$$ (4.3)

where n_k is the number of layers in nanopore k, $m_{ex,k}^{OK}$ is the excess adsorption in nanopore k, and W_a is the layer width fixed as 0.38 nm, which is the methane LJ diameter based on previous simulation works [51, 106, 156]. As in our recent study on methane adsorption in specific nanopores of $W \geq 4$ nm [156], ρ_{am}, ε and ε_s are three unknown parameters and obtained by fitting the excess adsorption from GCMC simulations. Subsequently, the actual adsorbed phase densities in each layer are obtained.

Therefore, the total excess adsorption at given temperature and pressure from OK model considering PSD effect is described as,

$$m_{ex,T}^{OK} = \sum_{k}^{p} PSD_k \left[\rho_{am} W_a \sum_{i=1}^{n_k} (x_{ki} - x_b) \right],$$ (4.4)

where $m_{ex,T}^{OK}$ and x_{ki} are total excess adsorption in nanoporous media from OK model and the adsorbed phase fraction of the ith layer in nanopore k, respectively.

In this work, we consider four distinct lattice types based on the different adsorption

behavior in micropores and mesopores from GCMC density distributions as we show in the Section 4.4. The governing equations of each type are different, but use the same parameters (ρ_{am}, ε and ε_s).

4.4.1 OK-micropore model ($W \leq 2$ nm)

Based on the adsorption mechanism in micropores as shown in **Figure 4-2**, we divide OK lattice model in micropores into three different types:

Type I ($W = 1$ nm)**:** As shown in **Figure 4-2 (a)**, methane forms only one strong adsorption layer on each pore surface, while these two layers are adjacent to each other. The OK model used in this type is given as,

$$\ln\left(\frac{x_1(1-x_b)}{x_b(1-x_1)}\right) + (5x_1 - 6x_b)\frac{\varepsilon}{k_BT} + \frac{\varepsilon_s}{k_BT} = 0$$

$$(4.5)$$

Due to the symmetry in slit-shaped pores, we only present the 1$^{\text{st}}$-layer equation which represents the strong surface adsorption layer.

Type II ($W = 1.5$ nm)**:** As shown in **Figure 4-2 (b)**, methane forms a three-layered structure with a relatively weaker layer in the middle of the pore. The equilibrium equations are given as,

$$\begin{cases} \ln\left(\frac{x_2(1-x_b)}{x_b(1-x_2)}\right) + (4x_2 + 2x_1 - 6x_b)\frac{\varepsilon}{k_BT} = 0 \\ \ln\left(\frac{x_1(1-x_b)}{x_b(1-x_1)}\right) + (4x_1 + x_2 - 6x_b)\frac{\varepsilon}{k_BT} + \frac{\varepsilon_s}{k_BT} = 0 \end{cases}$$

$$(4.6)$$

As in Type I, we present the 1st- and 2nd-layer equations due to symmetry.

Type III ($W = 2$ nm): As shown in **Figure 4-2 (c)**, adsorption layer in the middle of the pore is splitted into two weak adsorption layers forming on each side of the pores. However, the pore size is not large enough to ensure the free gas region in the middle of the pore. Therefore, for Type III, it has a four-layer structure in nanopores and the OK equations are expressed as (due to symmetry, only 1st- and 2nd-layer equations are presented),

$$
\begin{cases}
\ln\left(\dfrac{x_2(1-x_b)}{x_b(1-x_2)}\right) + (5x_2 + x_1 - 6x_b)\dfrac{\varepsilon}{k_BT} = 0 \\[3mm]
\ln\left(\dfrac{x_1(1-x_b)}{x_b(1-x_1)}\right) + (4x_1 + x_2 - 6x_b)\dfrac{\varepsilon}{k_BT} + \dfrac{\varepsilon_s}{k_BT} = 0
\end{cases}
. \tag{4.7}
$$

4.4.2 OK-mesopore model ($W > 2$ nm)

Type IV: When pore size is larger than 2 nm, as shown in **Figure 4-2 (d)**, methane forms a strong first adsorption layer and a weaker second adsorption layer (transition zone) on each surface. The density in the middle of the pore reduces to bulk density. As in our previous work [156], three-layer OK structure on each surface is used in Type IV and the density beyond the third layer is the same as the bulk. In fact, while the first and second layers can represent the strong adsorption layer on the surface and the transition zone, respectively, the third layer density is very close to the bulk [156]. The OK equations for Type IV are given as,

$$
\begin{cases}
\ln\left(\dfrac{x_3\left(1-x_b\right)}{x_b\left(1-x_3\right)}\right)+\left(4x_3+x_2-5x_b\right)\dfrac{\varepsilon}{k_BT}=0 \\[3mm]
\ln\dfrac{x_2\left(1-x_b\right)}{x_b\left(1-x_2\right)}+\left(4x_2+x_1+x_3-6x_b\right)\dfrac{\varepsilon}{k_BT}=0 \\[3mm]
\ln\left(\dfrac{x_1\left(1-x_b\right)}{x_b\left(1-x_1\right)}\right)+\left(4x_1+x_2-6x_b\right)\dfrac{\varepsilon}{k_BT}+\dfrac{\varepsilon_s}{k_BT}=0
\end{cases}
$$

$$. \tag{4.8}$$

Eqs. (4.13)- (4.16) are sets of non-linear equations that can be solved iteratively. Overall, by combing the Eqs. (4.13)- (4.16) with PSD, the total excess adsorption in nanoporous media by three-parameter OK model $m_{ex,T}^{OK}$ as described in Eq. (4.12) is fitted with $m_{ex,T}^{MC}$ from GCMC simulations to obtain ρ_{am}, ε and ε_s, and subsequently m_{abs} in each pore and nanoporous media.

4.5 Results and discussion

In this section, firstly we study methane excess adsorption in different sized nanopores at a wide range of pressures from GCMC simulations. Based on the density distributions, we propose adsorption models in nanopores with different sizes to obtain the total absolute adsorption coupling with PSD. Then, we assess the applicability of the OK model by comparing to GCMC simulations.

4.5.1 Methane adsorption from GCMC simulation

4.5.1.1 Excess adsorption

$m_{ex,k}^{MC}$ in GCMC simulation is calculated by Eq. (4.5) following the volumetric method.

Figure 4-4 shows $m_{ex,k}^{MC}$ in nanopores of 1 nm, 1.5 nm, 2 nm, 4 nm, 6 nm, 8 nm and 10 nm at 333.15 K and pressures up to 50 MPa. $m_{ex,k}^{MC}$ in different nanopores generally shows the following trend: it first increases with pressure and then decreases [54], except that for $W = 1$ nm. At relatively low pressures, methane molecules tend to adsorb on the surface rather than accumulate in the bulk phase. When pressure increases to a certain value, $m_{ex,k}^{MC}$ reaches maximum and adsorbed phase is readily filled with methane. As pressure increases continuously, the accumulation of molecules in the bulk leads to the decrease in $m_{ex,k}^{MC}$. The decreasing trend in 1 nm pore is probably due to the strong surface interactions, resulting in the adsorption layer saturated even at low pressures. The pressures corresponding to the maximum $m_{ex,k}^{MC}$ per SSA are around 5 MPa, 10 MPa and 15 MPa of $W = 1$ nm, $W = 1.5$ nm and $W \geq 2$ nm, respectively, and increase with pore size as reported by Tan and Gubbins [163] and Liu *et al*. [164]. These corresponding pressures from experimental findings are generally between 10 and 23 MPa [35, 86, 165]. Our findings indicate that $m_{ex,k}^{MC}$ per SSA increases with pore size from $W = 1$ nm to $W = 4$ nm, and becomes independent of pore size when $W \geq 4$ nm in line with the previous studies [51, 136, 156, 164].
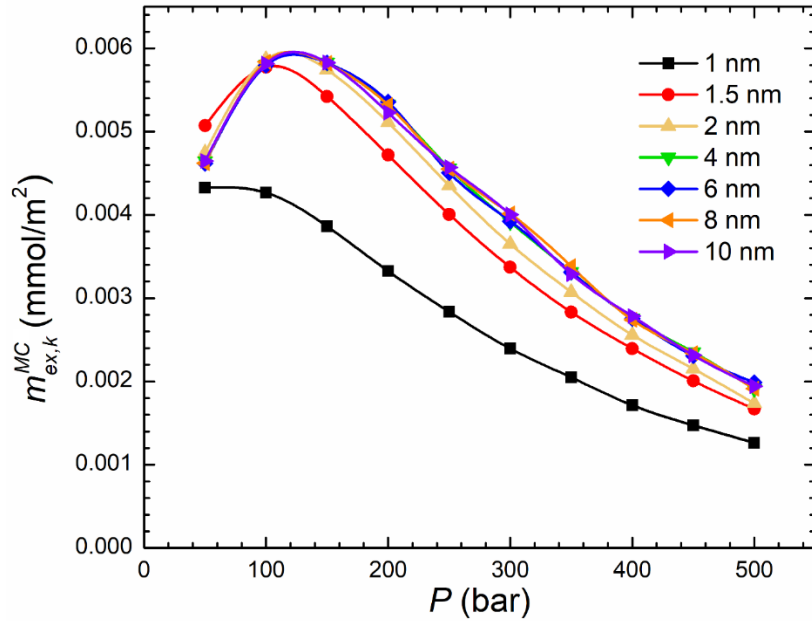
Figure 4-4 $m_{ex,k}^{MC}$ per SSA from GCMC simulations in various nanopores at 333.15 K.

4.5.1.2 Characterization of methane adsorption model in nanoporous media

The methane density distributions in various nanopores from GCMC simulations are presented in **Figure 4-2**. Methane shows varying adsorption behaviors in micropores and mesopores as observed in previous works [67, 158]. Based on the density profiles from GCMC simulations, we characterize our adsorption models in different sized nanopores as shown in **Figure 4-5**. The length of $z_{AA'}$ corresponds to the effective pore width defined as $z_{AA'} = V_p / S_A$. The proposed model in **Figure 4-5 (a)** shows the methane adsorption in 1-nm pore and the point B (B') is set at the middle of the pore. In 1.5-nm pores, as shown in **Figure 4-5 (b)**, methane forms a three-layer structure in nanopore. The first adsorption layer is defined as the region between the point A and point B, which is the local minima

between first and second layer in the density profile. The point B' is symmetric with point B, and the zone between B and B' comprises the second layer. When $W = 2$ nm as depicted in **Figure 4-5 (c)**, point C (C') is the middle of the pore and two adsorption layers exist on each side of the surface, while the second layer density is higher than ρ_b. As for the adsorption model for $W \geq 4$ nm shown in **Figure 4-5 (d)**, the point B is defined the same as that in **Figure 4-5 (c)**, while point C is the local minima between the second adsorption layer and the free gas region at high pressures [156]. To be noted that the locations of Point A, B, and C are the same for $W = 6$, 8, and 10 nm as $W = 4$ nm. The widths of adsorption layers in different sizes of nanopores are listed in **Table 4-1**. It is reported that for methane, the adsorption layer width is equal to the LJ diameter (0.38 nm) [106]. We find that the widths of the first layers in all model types and second layers in micropores are larger than that value. This discrepancy might be due to two reasons: First, the helium surface adsorption may overestimate the effective pore volume [156]; second, the pore space is limited when W is relatively small, leading to the overlap of the second layer in micropores. In **Figure 4-5**, the heights of each layer represent the corresponding densities, which can be expressed as $\rho_{a1} = \int_A^B \rho(z) dz / z_{AB}$, $\rho_{a2} = \int_B^C \rho(z) dz / z_{BC}$ and

$\rho_f = \int_C^{C'} \rho(z) dz / z_{CC'}$, respectively.
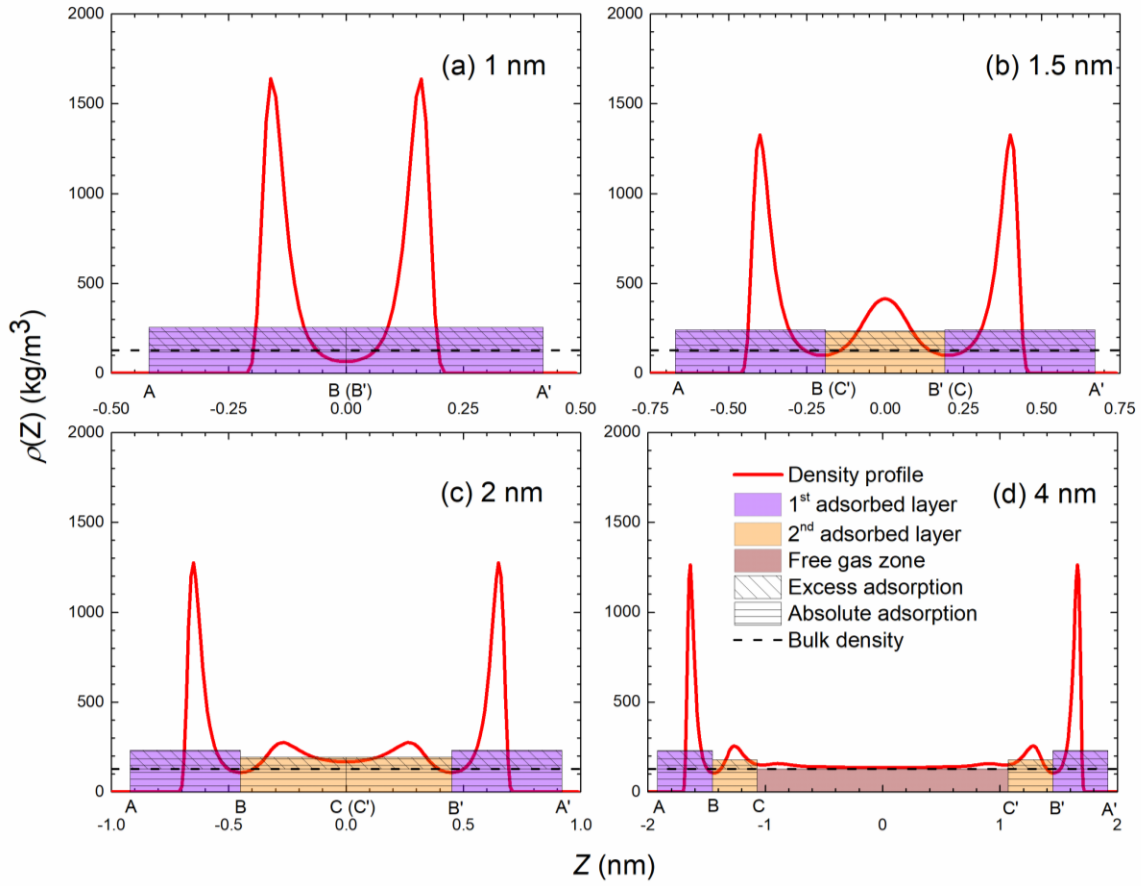
Figure 4-5 Schematic representation of the adsorption models in nanopores of (a) $W = 1$ nm; (b) $W = 1.5$ nm; (c) $W = 2$ nm; (d) $W = 4$ nm. The heights of adsorbed phase density of the first adsorbed layer, second adsorbed layer and free gas zone are obtained by

$$\rho_{a1} = \int_A^B \rho(z) dz / z_{AB}, \quad \rho_{a2} = \int_B^C \rho(z) dz / z_{BC}, \text{ and } \rho_f = \int_C^{C'} \rho(z) dz / z_{GG'}, \text{ respectively.}$$

Table 4-1 Width of adsorption layer in different sizes of nanopores in GCMC simulation

W (nm)	Effective pore width (nm)	First layer width (nm)	Second layer width (nm)
1	0.84	0.42	
1.5	1.34	0.48	0.38
2	1.84	0.47	0.45
≥ 4	3.84	0.47	0.38

In **Figure 4-6**, we compare the densities of second layers in $W = 1.5$ nm, $W = 2$ nm and $W \geq 4$ nm from GCMC simulations with bulk densities from NIST at 333.15 K. We find that the second layer density continuously increases with pressure and is significantly higher than that of bulk, especially in small nanopores. While in Tian *et al.* [51], the effect of second adsorption layer in clay nanopores can be "averaged out" at higher pressures in mesopores, it is necessary to consider the second adsorption layer which behaves differently from the free gas region in both micropores and mesopores.
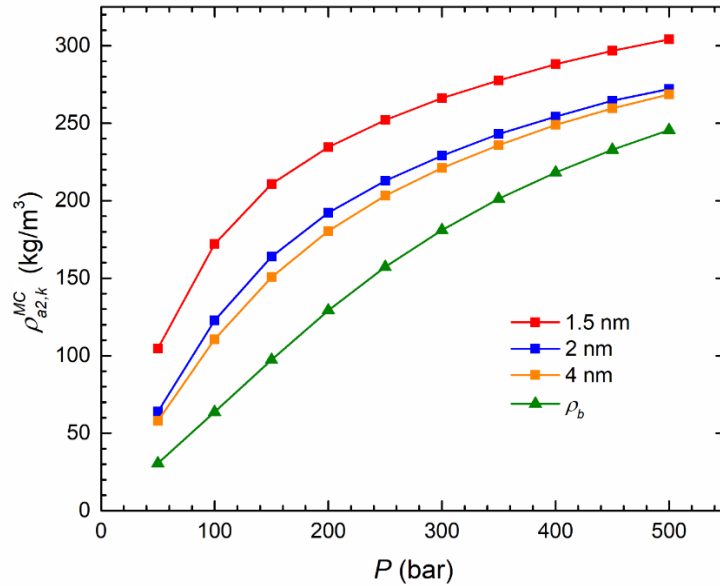
Figure 4-6 Average densities of the second layers in nanopores from GCMC simulation and bulk density from NIST Chemistry Webbook at 333.15 K and various pressures.

Based on the proposed adsorption model shown in **Figure 4-5**, m_{abs} in each layer from GCMC simulation can be calculated on the basis of the adsorbed phase density and width,

$$\begin{cases} m_{abs,k}^{L1,MC} = \rho_{a1,k}^{MC} V_{a1,k}^{MC} \\ m_{abs,k}^{L2,MC} = \rho_{a2,k}^{MC} V_{a2,k}^{MC} \end{cases}, \tag{4.9}$$

where $m_{abs,k}^{L1,MC}$ and $m_{abs,k}^{L2,MC}$ represent the absolute adsorption in the first and second layer of nanopore k, respectively; $\rho_{a1,k}^{MC}$ and $\rho_{a2,k}^{MC}$ represent the averaged density of the first and second layer of nanopore k, respectively; $V_{a1,k}^{MC}$ represents the volume of the first layer of nanopore k given as,

$$V_{a1,k}^{MC} = 2S_a z_{AB,k}.\qquad(4.10)$$

On the other hand, $V_{a2,k}^{MC}$ represents the volume of the second layer of nanopore k: for $W = 1.5$ nm given as,

$$V_{a2,k}^{MC} = S_a z_{BC,k},\qquad(4.11)$$

and for $W = 2$ nm and $W \geq 4$ nm given as,

$$V_{a2,k}^{MC} = 2S_a z_{BC,k}.\qquad(4.12)$$

The total absolute adsorption in the first and second layers in nanoporous media $m_{abs,T}^{L1,MC}$ and $m_{abs,T}^{L2,MC}$, respectively, are given as,

$$\begin{cases} m_{abs,T}^{L1,MC} = \sum_{k}^{p} PSD_k m_{abs,k}^{L1,MC} \\ m_{abs,T}^{L2,MC} = \sum_{k}^{p} PSD_k m_{abs,k}^{L2,MC} \end{cases}.\qquad(4.13)$$

Thus, the total absolute adsorption in nanoporous media $m_{abs,T}^{MC}$ is given as

$$m_{abs,T}^{MC} = m_{abs,T}^{L1,MC} + m_{abs,T}^{L2,MC} .$$
(4.14)

4.5.2 Methane adsorption behavior from OK model

We fit the total excess adsorption obtained from GCMC simulation by using OK model. $W = 1$ nm, $W = 1.5$ nm, $W = 2$ nm and $W \geq 4$ nm correspond to OK adsorption model of Type I, II, III and IV, respectively, with constant layer width as 0.38 nm. Three regression parameters have the constraints as: $0 < \rho_{am} < 700$ kg/m³, $-1 < \varepsilon / k_B T < 0$ and $-10 < \varepsilon_s / k_B T < 0$ [116-119, 156]. With 1000 different PSD samples, we obtain 1000 sets of regression parameters. **Figure 4-7** shows the comparison between $m_{ex,T}^{MC}$ from GCMC simulations and $m_{ex,T}^{OK}$ from OK model. It should be noted that there are 10 pressure points for each PSD sample, and thus the comparison is for 10,000 data points. It shows that the R^2 can be as high as 0.9992 for 333.15 K, indicating the excellent agreement between OK model and GCMC simulation.
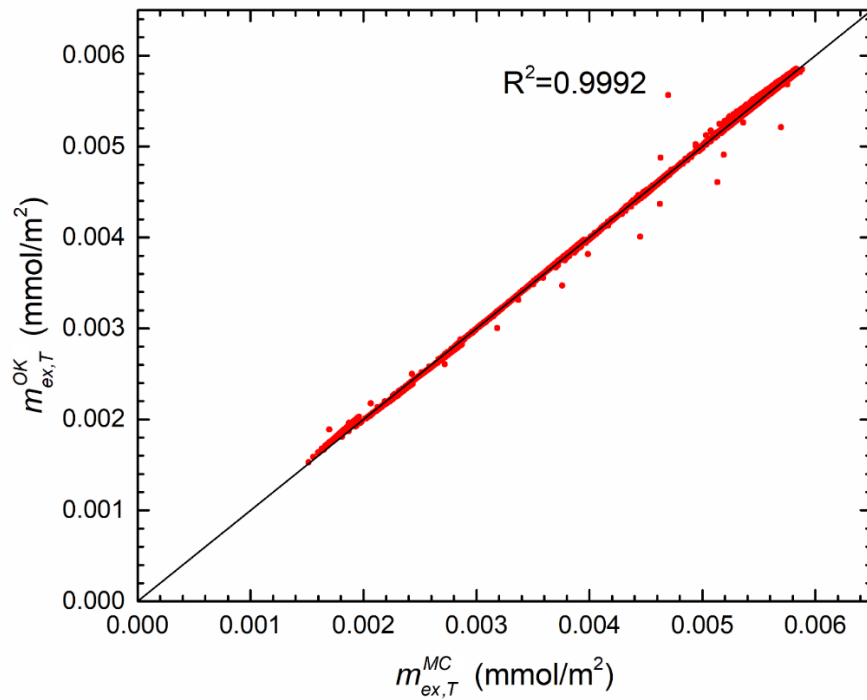
Figure 4-7 Comparison between $m_{ex,T}^{MC}$ from GCMC simulation and $m_{ex,T}^{OK}$ from OK model with 1000 PSD samples at 333.15 K.

Figure 4-8 presents $m_{ex,k}^{MC}$ and $m_{ex,k}^{OK}$ in various nanopores at 333.15 K. It is noted that

OK model results are based on the average of 1000 PSD samples. For clarity, the error bars

in OK model are presented. Overall, OK model shows a good agreement with GCMC

simulations in $W = 1.5$ nm, $W = 2$ nm and $W \geq 4$ nm, while showing a noticeable

deviation in $W = 1$ nm. It is probably due to the mismatch in the adsorption layer width

between GCMC and OK model as we discuss later.
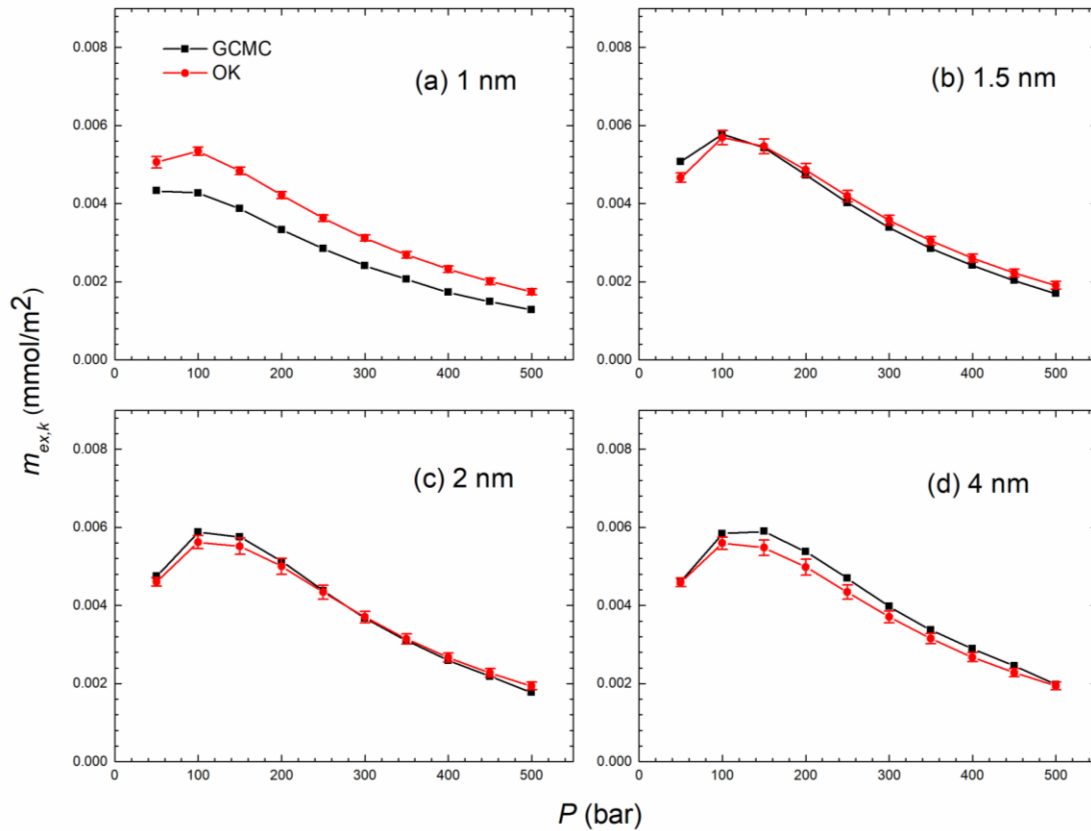
Figure 4-8 Excess adsorption in nanopores of (a) $W = 1$ nm; (b) $W = 1.5$ nm; (c) $W = 2$ nm; (d) $W = 4$ nm from GCMC and OK model at 333.15 K. OK model results are based on the average of 1000 PSD samples. For clarity, the error bars in OK model are presented.

Similar to GCMC simulations, m_{abs} in the first layer of given nanopore k from OK

model is,

$$m_{abs,k}^{L1,OK} = 2x_{1,k}\rho_{am}S_aW_a, \tag{4.15}$$

where $m_{abs,k}^{L1,OK}$ represents the absolute adsorption in the first layer of nanopore k. For Type II, m_{abs} in the second layer $m_{abs,k}^{L2,OK}$ is given as,

$$m_{abs,k}^{L2,OK} = x_{2,k}\rho_{am}S_aW_a, \tag{4.16}$$

and for Type III and IV,

$$m_{abs,k}^{L2,OK} = 2x_{2,k}\rho_{am}S_aW_a. \tag{4.17}$$

The total absolute adsorption in the first and second layers in nanoporous media $m_{abs,T}^{L1,OK}$ and $m_{abs,T}^{L2,OK}$, respectively, are given as,

$$\begin{cases} m_{abs,T}^{L1,OK} = \sum_{k}^{p} PSD_k m_{abs,k}^{L1,OK} \\ m_{abs,T}^{L2,OK} = \sum_{k}^{p} PSD_k m_{abs,k}^{L2,OK} \end{cases}. \tag{4.18}$$

Thus, the total absolute adsorption in nanoporous media $m_{abs,T}^{OK}$ is given as

$$m_{abs,T}^{OK} = m_{abs,T}^{L1,OK} + m_{abs,T}^{L2,OK}. \tag{4.19}$$

We present the calculated $m_{abs,k}^{L1,MC}$ and $m_{abs,k}^{L1,OK}$ in various nanopores at 333.15 K in

Figure 4-9. It is noted that $m_{abs,k}^{L1,OK}$ is the average of 1000 PSD samples. For comparison, we also present the absolute adsorption based on the single-layer adsorption model (as depicted in **Figure 4-1 (a)**) with commonly used constant adsorbed phase density as 424 kg/m³ and 373 kg/m³, while using $m_{ex,k}^{MC}$ in Eq. (4.1). GCMC simulations show that $m_{abs,k}^{L1,MC}$ increases with pressures in all kinds of nanopores, even at high pressures, in line with our previous works [51, 156]. Overall, OK model shows a very good regression performance comparing to GCMC simulations in almost all types of nanopores. For 1-nm pore, OK model shows a slight overestimation at relatively low pressures, while it becomes close to GCMC simulation at higher pressures. Since excess adsorption can be expressed as the absolute adsorption subtracted by the free gas amount in the adsorption layer, the smaller layer width in OK model would lead to a higher excess adsorption amount as depicted in **Figure 4-8 (a)**. Moreover, the absolute adsorption obtained from the commonly used constant adsorbed phase density have the same trend as excess adsorption, i.e. it first increases with pressure and then decreases, showing a significant deviation from GCMC simulations. Unlike excess adsorption, absolute adsorption describes the amount of molecules in certain layers, which should not decrease with pressure. Our findings clearly indicate that neither 424 kg/m³ nor 373 kg/m³ could provide a reliable conversion from m_{ex} to m_{abs}.
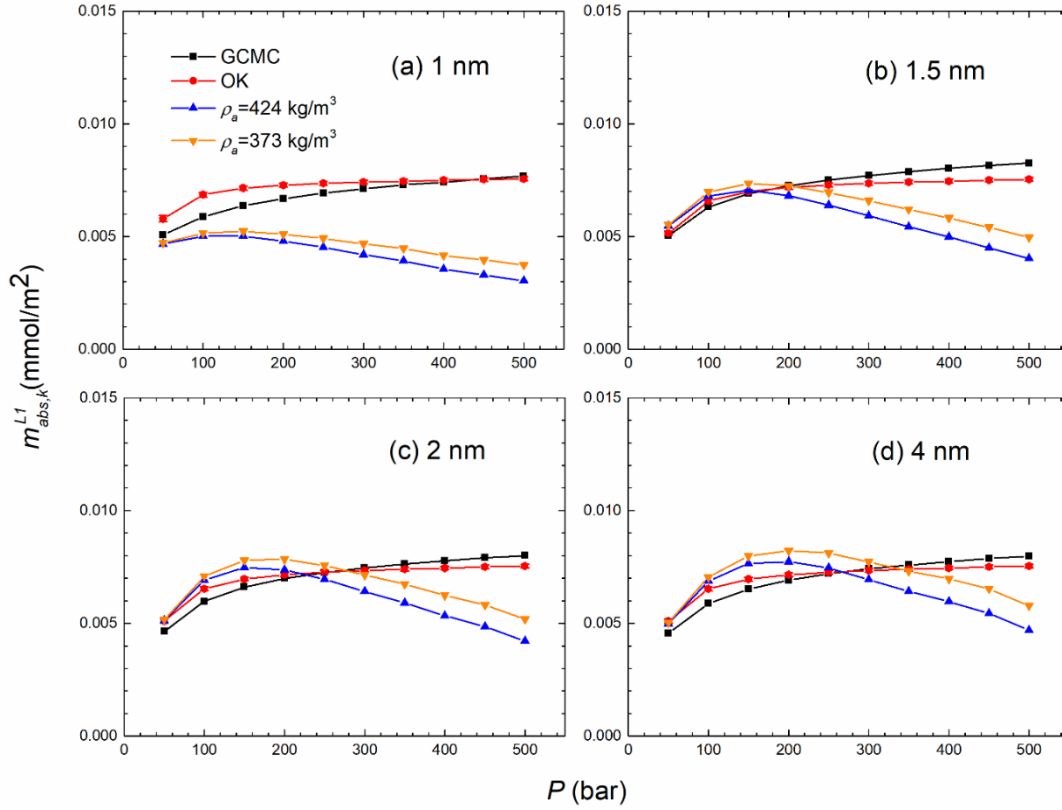
Figure 4-9 Comparison of absolute adsorption in the first layer calculated by GCMC and OK model at 333.15 K and in nanopores of (a) $W = 1$ nm; (b) $W = 1.5$ nm; (c) $W = 2$ nm; (d) $W = 4$ nm. $m_{abs,k}^{L1,OK}$ is based on the average of 1000 PSD samples. For comparison, we also present the absolute adsorption based on the constant adsorbed phase density of $\rho_a = 424$ kg/m^3 (liquid methane density at boiling point) and $\rho_a = 373$ kg/m^3 (methane Van der Waals density).

Figure 4-10 presents $m_{abs,k}^{L2,MC}$ and $m_{abs,k}^{L2,OK}$ at 333.15 K. It shows that $m_{abs,k}^{L2,OK}$ is always lower than $m_{abs,k}^{L2,MC}$ as in our previous work [156]. In **Figure 4-10 (d)**, We also present the relative error δ between $m_{abs,k}^{L2,MC}$ and $m_{abs,k}^{L2,OK}$, which is defined as

$$\delta = \left(m_{abs,k}^{L2,MC} - m_{abs,k}^{L2,OK} \right) / m_{abs,k}^{L2,MC} . \tag{4.20}$$

It shows that δ decreases with pressure and reach a plateau at high pressures, which are

more relevant to shale gas reservoir conditions. The deviations between OK model and GCMC simulations in mesopores are around 7% at high pressures, while in 2-nm pore the relative error can reach 21%. According to **Figs. 4-7** and **4-9**, the excess adsorption $m_{ex,k}$ and the absolute adoption of the first layer $m_{abs,k}^{L1}$ calculated by OK model and GCMC are very close. Since the second layer can be described as $m_{abs,k}^{L2} = m_{ex,k} - m_{abs,k}^{L1} + \rho_b V_a$, the smaller V_a in OK model results in the underestimation of $m_{abs,k}^{L2}$.
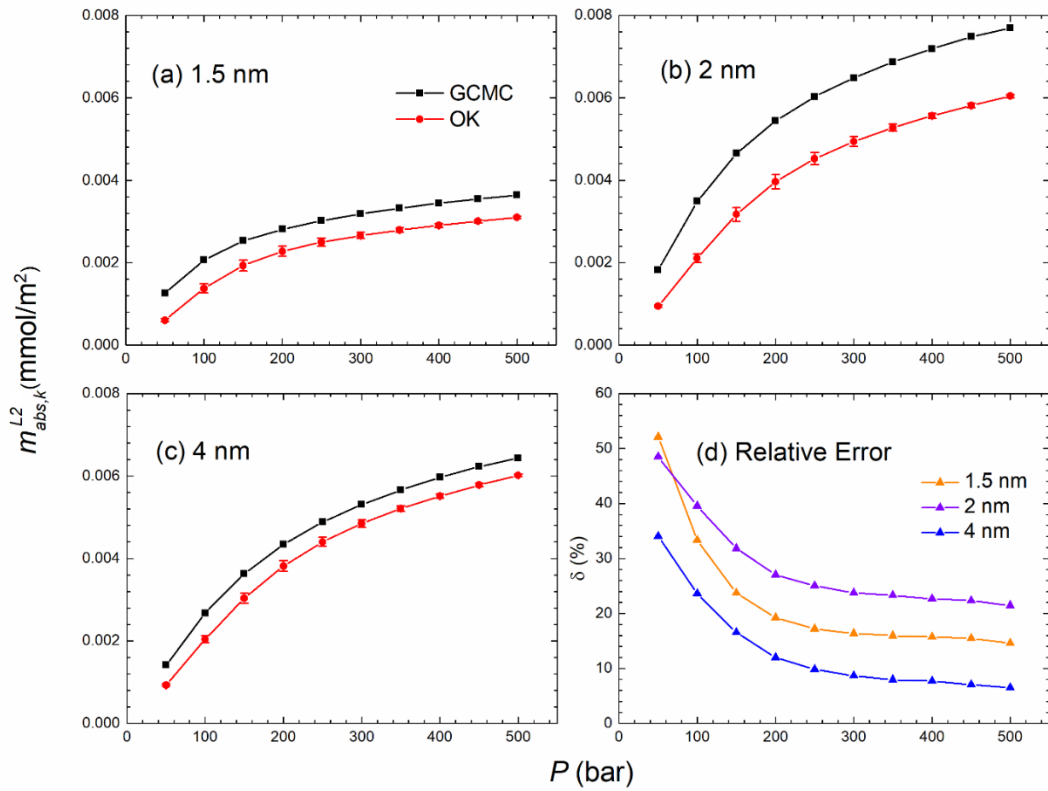
Figure 4-10 Comparison of absolute adsorption in the first adsorption layer calculated by GCMC and OK model at 333.15 K and in nanopores of (a) $W = 1.5$ nm; (b) $W = 2$ nm; (c) $W = 4$ nm. (d) The relative error δ.

In order to validate the proposed OK model, we compare $m_{abs,T}^{L1,OK}$ and $m_{abs,T}^{L1,MC}$ as depicted in **Figure 4-11**. For comparison, we also present the total absolute adsorption based on the

single-layer adsorption model with constant adsorbed phase density as 424 kg/m^3 and 373 kg/m^3, while using $m_{ex,T}^{MC}$ in Eq. (4.1). The root-mean square deviation (RMSD) is defined as

$$RMSD = \sqrt{\frac{1}{q}\sum_{i=1}^{q}\left(\left(m_{abs,tested}^{L1}\right)^2 - \left(m_{abs,GCMC}^{L1}\right)^2\right)}. \qquad (4.21)$$

where q is the total number of samples. It shows that OK model performs the best regression results among those three methods with $RMSD = 0.0004$ mmol/m^2, while the RMSDs of the conversion using 424 kg/m^3 and 373 kg/m^3 are 0.0018 mmol/m^2 and 0.0013 mmol/m^2, respectively, indicating significant deviations. Although Eq. (4.1) is not in line with methane adsorption behavior in various nanopores, it still provides a simple conversion method and can be applied in experiments and actual fields. The optimized adsorbed phase density based on Eq. (4.1) using $m_{ex,T}^{MC}$ and $m_{abs,T}^{L1,MC}$ is 330.5 kg/m^3 with the $RMSD = 0.0009$ mmol/m^2 at 333.15 K, indicating a better performance in absolute adsorption calculation than those of using 424 kg/m^3 and 373 kg/m^3. Gasparik *et al.* [46] applied Langmuir model to fit methane adsorption on black shale at 333 K and pressures up to 250 bar. The regressed adsorbed densities in their study ranges from 295-323 kg/m^3. The Ono-Kondo fitted adsorbed phase density of methane adsorption on dry activated carbon at 318 K is 345 kg/m^3 by Sudibandriyo *et al.* [58]. Our previous work have shown the methane adsorbed phase density in mesopores regressed by OK multilayer adsorption

model is 335.32 kg/m^3 [156]. In **Figure 4-12**, we compare $m_{abs,T}^{L2,OK}$ and $m_{abs,T}^{L2,MC}$ at 333.15

K. The *RMSD* equals to 0.0009 mmol/m^2 and $R^2 = 0.8544$, showing a good agreement

with GCMC simulations. In **Figure 4-13**, we also present $m_{abs,T}^{OK}$ and $m_{abs,T}^{MC}$ at 333.15 K.

The *RMSD* equals to 0.0007 mmol/m^2 and $R^2 = 0.9157$. The deviations shown in **Figs.**

4-12 and **4-13** are mainly due to the mismatch in the second layer width between GCMC

and OK model.
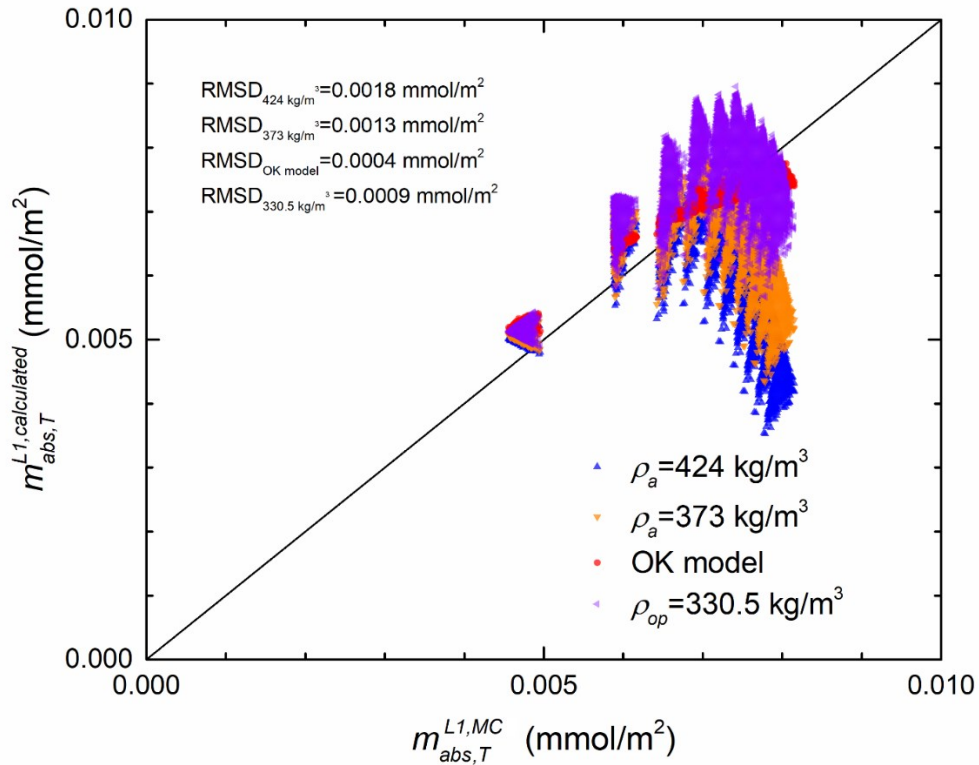
Figure 4-11 Comparison of absolute adsorption of the first adsorption layer in total pore space calculated by GCMC, OK model with 1000 sampling of PSD, constant adsorbed phase density of $\rho_a = 424$ kg/m^3 (liquid methane density at boiling point) and $\rho_a = 373$ kg/m^3 (methane Van der Waals density) at 333.15 K.
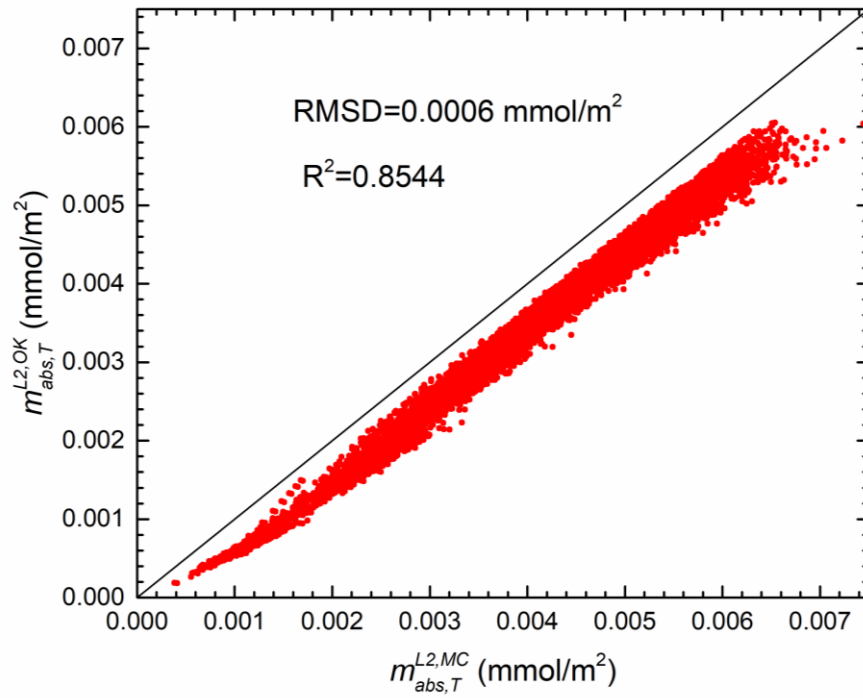
Figure 4-12 Comparison between absolute adsorption of the second adsorption layer in total pore space calculated by GCMC and OK model with 1000 sampling of PSD at 333.15 K.
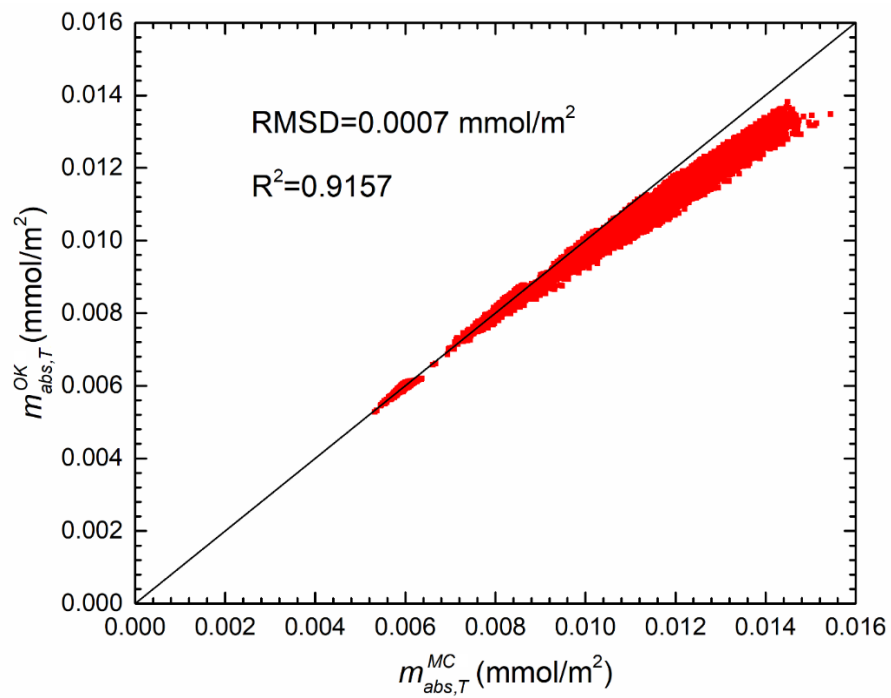
Figure 4-13 Comparison between combined absolute adsorption in total pore space calculated by GCMC and OK model with 1000 sampling of PSD at 333.15 K.

4.6 Conclusion

In this work, we used GCMC simulation to investigate methane adsorption in nanoporous media at a wide range of pressures and 333.15 K. The volumetric method is applied to calculate excess adsorption, while using helium adsorption to obtain the effective pore volume in each nanopore. We studied the excess adsorption in different sized nanopores and characterized the adsorption model in porous media based on the density profile obtained from GCMC simulation. By coupling GCMC simulations and varying PSDs, we effectively modeled methane adsorption in nanoporous media.

Our results showed that m_{ex} per SSA increases with pore size when $W < 4$ nm and becomes insensitive to the pore size when $W \geq 4$ nm. Methane shows varying adsorption behavior in micropores and mesopores. Therefore, it is necessary to consider the effect of PSD in the conversion of m_{ex} to obtain m_{abs}. Although molecular simulations can characterize the varying adsorption behavior in different nanopores, they come with an expensive computational cost. Thus, we used Ono-Kondo model to simulate the methane adsorption in nanopores considering PSD effect. Based on the different density distributions in various nanopores, we classify four distinct adsorption models: $W = 1$ nm, $W = 1.5$ nm, $W = 2$ nm and $W \geq 4$ nm. Coupling the PSD, we only need three parameters in OK model to fit the excess adsorption from GCMC simulations to obtain the

absolute adsorption.

Our proposed OK model presents an excellent agreement with GCMC simulations in the absolute adsorption in the first layer, while commonly used constant adsorbed phase densities as $\rho_a = 424$ kg/m^3 and $\rho_a = 373$ kg/m^3 based on single-layer adsorption model show noticeable deviations. Moreover, the optimized adsorbed phase density is quite different from these two values.

Collectively, we propose to use actual PSD obtained from experimental measurements coupled with varying methane adsorption behaviors in micropores and mesopores based on OK lattice model to efficiently predict the absolute adsorption in shale nanoporous media. It also emphasizes the importance of reliable PSD in GIP estimation and the widely used single-layer adsorption model may bring large deviations. Our work should provide important insights into the accurate estimation of absolute adsorption in shale nanoporous media based on the excess adsorption, especially in experimental studies.

CHAPTER 5 ASSESSMENT OF VARIOUS APPROACHES IN THE PREDICTION OF METHANE ABSOLUTE ADSORPTION IN KEROGEN NANOPOROUS MEDIA

A version of this chapter has been published in *Energy & Fuels*.

Abstract

It is crucial to accurately characterize methane absolute adsorption in kerogen nanoporous media for gas-in-place evaluation and well productivity prediction. Assuming that methane forms a single-layer adsorption in kerogen nanopores, a large number of approaches have been reported to convert the experimentally measured excess adsorption to the absolute adsorption. Recently, we have shown that methane adsorption behavior depends on pore size and may be very different from the single-layer adsorption model, such as the Langmuir model. Thus, it is necessary to explicitly consider the pore size distribution (PSD). While these conversion methods have been extensively used, their validity in the characterization of methane absolute adsorption in nanoporous materials, such as kerogen, has not been systematically assessed. As in our previous work, we used model kerogen with varying PSDs and grand canonical Monte Carlo (GCMC) simulations to model methane adsorption up to 500 bar to assess various commonly used methods converting the excess adsorption to the absolute adsorption. We find that the predetermined density methods using 373 or 424 kg/m^3 may show unphysical phenomena and Langmuir as well as SDR models can largely overestimate the absolute adsorption. On the other hand, the Ono-Kondo (OK) lattice model with PSD can accurately characterize the absolute adsorption in nanoporous media. Interestingly, Langmuir and SDR models coupled with PSD can provide comparable predictions to OK with PSD. In addition, we also suggest to use the high-pressure excess adsorption data (up to 500 bar), instead of commonly used

low-pressure excess adsorption measurements (up to 150 bar). Our work also calls for the accurate characterization of PSD in nanoporous materials to obtain their absolute adsorption capacity.

Keywords: Hydrocarbons; Porosity; Adsorption; Layers; Shale

5.1 Introduction

Shale gas, which is one of unconventional natural gas resources, has greatly enhanced global energy supply in the past decade[129]. Unlike conventional reservoirs, where gas is mainly stored as free gas, adsorbed gas in shale may take up to 85% of total gas content[38, 141, 166], as a result of the presence of abundant nanoscale pores. In such small nanopores, surface adsorption plays an important role and gas molecule distribution is inhomogeneous[80, 82, 148], which cannot be predicted by the conventional equation of state modeling. Thus, accurate characterization of the adsorbed gas in shale is critical for assessing gas-in-place (GIP) as well as well productivity[35, 48, 167].

While experimental measurements can obtain the excess adsorption m_{ex}, absolute adsorption m_{abs}, which describes the adsorbed gas amount, needs to be converted from m_{ex} [39]. Assuming that methane forms a single-layer adsorption in shale nanopores, there have been a large number of methods reported for such conversion, including the constant adsorbed phase density ρ_a as 373 or 424 kg/m^3 [63, 64, 142], ρ_a from grand canonical Monte Carlo (GCMC) simulation[51, 63, 64, 142], the slope method[39, 45, 154, 168],

various adsorption models, such as Langmuir[22, 30, 39, 44-49] and supercritical Dubinin-Radushkevich (SDR)[35, 39, 49-51], and adsorbed phase volume V_a as well as bulk density ρ_b [35, 139]. It is known that the adsorbed phase density depends on temperature and pressure rather than a constant[64]. Do and Do[139] argued that the adsorbed phase density of gas at high pressures can be close to but never equal to or beyond its liquid density. However, by applying the monolayer Langmuir model and the adsorption-potential-based SDR model, it is observed that the fitted adsorbed phase density may exceed the liquid methane density at the boiling point (424 kg/m^3)[48, 167, 169]. In addition, as reported by Li *et al.*[170], although the fitted ρ_a from the Langmuir model is generally larger than that from SDR model, the fitted maximum adsorption amount is consistent. The fitted adsorbed phase densities from Langmuir and SDR show a noticeable deviation at a relatively low pressure range (less than 150 bar)[47], but such difference becomes negligible at a high pressure range (up to 350 bar)[170]. In our recent works[51, 156], we reported that the presence of a transition zone can negatively affect m_{abs} calculations, indicating that the single-layer adsorption model becomes inapplicable. In addition, we illustrated the importance of considering pore size distribution (PSD) in the accurate estimation of m_{abs} from measured m_{ex} [75]. We proposed to use the Ono-Kondo (OK) lattice model[117] with multilayer adsorption coupled with PSD to obtain m_{abs} in kerogen nanoporous media[75]. While all of above-mentioned methods[22, 30, 35, 39, 44-51, 63, 64, 75, 139, 142, 154, 156, 167-169] have been extensively used to convert m_{ex} to

obtain m_{abs} in shale (kerogen) nanoporous media, the assessments on these methods were conducted in either an indirect way, i.e., comparing the fitted adsorbed phase densities from an experimental perspective[39, 47, 49], or a single pore size case from a simulation perspective[45, 51]. To the best of our knowledge, no systematic and comprehensive assessment on various commonly used methods explicitly considering PSD in a direct way has been reported. In addition, most of the experimental measurements[63, 64, 120, 171, 172] on the methane excess adsorption were conducted in a relatively low-pressure range (up to 150 bar), while the actual shale gas reservoir pressure can be up to 500 bar[173, 174]. Zhou *et al.*[39] reported that the low-pressure fitting may bring underestimation in absolute adsorption calculation. Therefore, it is also necessary to assess the performance of the absolute adsorption calculation based on low-pressure excess adsorption data.

In this paper, we assess various methods using model kerogen nanoporous media which is the main constituent of shale, as in our previous work[75]. We use 1000 sets of randomly generated PSDs to ensure that each sample has a distinct specific surface area (SSA) and pore volume (PV). Combining the PSDs and varying adsorption models in different pores, we assess the performance of m_{abs} calculation using predetermined adsorbed densities (373 kg/m^3, 424 kg/m^3 and GCMC density), constant adsorbed phase volume, and various adsorption models (Langmuir, SDR and OK), by comparing to GCMC simulations. We also assess the performance of m_{abs} calculations with low-pressure excess adsorption data. Our work provides important insights into the accurate estimation of absolute adsorption

and GIP in shales.

5.2 Methodology

5.2.1 Molecular Simulation and Porous Media Model

The detailed simulation descriptions can be found in **Appendix B**. As in our previous work[75], the characterization of methane adsorption can be divided into four parts according to pore size W_p: W_p =1, 1.5, 2, and $\geq$ 4 nm. On the basis of the effective pore volume V_p by helium adsorption, m_{ex} for specific pore k ($m_{ex,k}^{MC}$) can be obtained according to Eq. (4.5) of the **Chapter 4**. Subsequently, coupling with PSDs, the total excess adsorption in kerogen nanoporous media $m_{ex,T}^{MC}$ is,

$$m_{ex,T}^{MC} = \sum_{k}^{p} m_{ex,k}^{MC} PSD_k \tag{5.1}$$

The absolute adsorption amount in the first layer of specific pore k, $m_{abs,k}^{L1,MC}$, can be obtained from GCMC of the **Chapter 4**. It should be noted that, although GCMC can identify the adsorption in any layer, we focus on the first adsorption layer, because most models assessed in this work are based on the single-layer adsorption assumption. The total absolute adsorption in the first layer $m_{abs,T}^{L1,MC}$ is given as,

$$m_{abs,T}^{L1,MC} = \sum_{k}^{p} m_{abs,k}^{L1,MC} PSD_k \ . \tag{5.2}$$

5.2.2 Predetermined Density Method

In this method, the absolute adsorption using the predetermined density method ($m_{abs,T}^{pre}$) is directly calculated from $m_{ex,T}^{MC}$,

$$m_{abs,T}^{pre} = m_{ex,T}^{MC} / \left(1 - \rho_b / \rho_{a,pre}\right), \tag{5.3}$$

where ρ_b is methane bulk density obtained from National Institute of Standards and Technology (NIST) Chemistry Webbook and $\rho_{a,pre}$ is the predetermined adsorbed phase density. Three types of $\rho_{a,pre}$ have been assessed: 424 kg/m³ (liquid methane density at its boiling point), 373 kg/m³ (methane van der Waals density), respectively and the adsorbed phase density from GCMC density profile of a 4 nm pore as in the studies of Wu *et al.* [63] and Liu *et al.* [142], which is a function of pressure.

5.2.3 Langmuir, SDR and OK Models

Measured m_{ex} values are usually fitted by m_{abs} based on Langmuir (LA) or SDR and ρ_a [39] as,

$$m_{ex,T}^{LA} = m_{L,LA} P \left(1 - \rho_b / \rho_{a,LA}\right) / \left(P_L + P\right), \tag{5.4}$$

$$m_{ex,T}^{SDR} = m_{L,SDR} \left\{ -D \left[\ln\left(\rho_{a,SDR} / \rho_b\right)\right]^2 \right\} \left(1 - \rho_b / \rho_{a,SDR}\right), \tag{5.5}$$

where $m_{ex,T}^{LA}$ and $m_{ex,T}^{SDR}$ represent excess adsorptions from LA and SDR, respectively; $m_{L,LA}$ and $m_{L,SDR}$ are maximum adsorption capacities in LA and SDR, respectively; $\rho_{a,LA}$ and $\rho_{a,SDR}$ represent the maximum adsorbed phase densities from LA and SDR, respectively;

P_L is the equilibrium pressure in LA; D is the interaction constant in SDR. Then, $m_{abs,T}^{LA}$ and $m_{abs,T}^{SDR}$ are given as,

$$m_{abs,T}^{LA} = m_{L,LA}P/(P_L+P),\qquad(5.6)$$

$$m_{abs,T}^{SDR} = m_{L,SDR}\left\{-D\left[\ln\left(\rho_{a,SDR}/\rho_b\right)\right]^2\right\}.\qquad(5.7)$$

In addition, two extended LA and SDR models are proposed by describing maximum adsorption capacity with ρ_a and fixed methane adsorption layer width as $W_a = 0.38$ nm[51, 75, 156, 175] coupled with PSDs. Therefore, the LA-0.38 and SDR-0.38 models are expressed as:

$$m_{ex,T}^{LA-0.38} = P\rho_{a,LA-0.38}W_a\left(\sum_{k}^{p}PSD_k\right)\left(1-\rho_b/\rho_{a,LA-0.38}\right)/(P_L+P),\qquad(5.8)$$

$$m_{ex,T}^{SDR-0.38} = \rho_{a,SDR-0.38}W_a\left(\sum_{k}^{p}PSD_k\right)\left\{-D\left[\ln\left(\rho_{a,SDR-0.38}/\rho_b\right)\right]^2\right\}\left(1-\rho_b/\rho_{a,SDR-0.38}\right).\qquad(5.9)$$

Thus, $m_{abs,T}^{LA-0.38}$ and $m_{abs,T}^{SDR-0.38}$ are described as,

$$m_{abs,T}^{LA-0.38} = P\rho_{a,LA-0.38}W_a\left(\sum_{k}^{p}PSD_k\right)/(P_L+P),\qquad(5.10)$$

$$m_{abs,T}^{SDR-0.38} = \rho_{a,SDR-0.38}W_a\left(\sum_{k}^{p}PSD_k\right)\left\{-D\left[\ln\left(\rho_{a,SDR-0.38}/\rho_b\right)\right]^2\right\}.\qquad(5.11)$$

Within the framework of OK with PSD (OK-PSD) [75], the total excess adsorption amount and total absolute adsorption amount in the first layer can be given as,

$$m_{ex,T}^{OK-PSD} = \sum_{k}^{p}PSD_k\left[\rho_{am}W_a\sum_{i=1}^{n_k}\left(x_{ki}-x_b\right)\right],\qquad(5.12)$$

$$m_{abs,T}^{L1,OK-PSD} = \sum_{k}^{p} PSD_k \rho_{am} W_a x_{k1}.$$ (5.13)

in which ρ_{am} is the maximum adsorbate density in each layer, x_{ki} represents the fraction of absorbed phase molecules that occupies the layer i of specific pore k, and x_b is the fraction of molecules in the bulk phase. The fitting parameters in OK model are ρ_{am}, ε and ε_s, in which ε and ε_s are adsorbate-adsorbate and adsorbate-adsorbent interaction energies, respectively. More details about OK-PSD can be found in Ref. [75].

5.2.4 Constant adsorbed phase volume

The m_{abs} value based on the constant adsorbed phase volume $V_{a-0.38}$ using $W_a = 0.38$ nm and PSD is given as,

$$m_{abs,T}^{CVA} = m_{ex,T}^{MC} + \sum_{k}^{p} \rho_b PSD_k W_a.$$ (5.14)

5.3 Results and Discussion

5.3.1 High-Pressure Fitting

In **Figure 5-1(a)**, we present the fitting between the total excess adsorption from GCMC simulation and five different models. While LA, SDR and OK-PSD yield excellent agreement with excess adsorption from model nanoporous media with R^2 up to 0.99, both LA-0.38 and SDR-0.38 show noticeable deviations. The total absolute adsorption in the first adsorption layer obtained by those methods and GCMC simulation are depicted in

114

Figure 5-2. The predetermined density approaches show larger deviations compared to LA, SDR and OK-PSD models. In addition, the predetermined density approaches using 373 or 424 kg/m³ as well as the constant V_a method predict that $m_{abs,T}$ firstly increases with pressure and then decreases. It is because the excess adsorption first increases and then decreases as pressure increases. In addition, the adsorbed phase density from GCMC simulations is generally much lower than 373 or 424 kg/m³[64, 156]. Although $m_{abs,T}^{pre}$ increases with pressure using GCMC density, it significantly deviates from $m_{abs,T}^{L1,MC}$. Such discrepancy is probably due to the negligence of the transition zone in mesopores and the mismatches between adsorption behaviors in micropores and the single-layer adsorption model. We observe that the LA-0.38 and SDR-0.38 present smaller root-mean-square deviation (RMSD) of calculated absolute adsorption amount between tested samples by different models and GCMC results (see Eq. (A5.25) in **section A6.2** of the **Appendix**) than LA and SDR, which largely overestimate $m_{abs,T}$, especially at high-pressure conditions. LA is based on the assumption of ideal gas adsorption on an ideal flat homogeneous surface [108] and SDR is based on the pore filling mechanism which cannot differentiate adsorbed gas and free gas [176]. Therefore, both models are considered as empirical models, and the overestimated absolute adsorption values are subject to fitting equations and parameters used. Although we illustrated the presence of a transition zone in mesopores and varying adsorption behaviors in micropores in our previous works[75, 156], methane adsorption in nanoporous media is mainly dominated by the first adsorption

layer, different from heavier hydrocarbons that may display multilayer adsorption behavior[148]. In other words, methane adsorption in nanoporous media is mainly determined by surface area[89]. Coupling with surface area, LA-0.38 and SDR-0.38 are in excellent agreement with GCMC simulations, because the equations and parameters used can provide reasonable fittings to the first adsorption layer in various pores. However, they cannot provide information about the second adsorption layer, which is available in the OK-PSD model[75]. On the other hand, the OK model can consider the layered structures and varying adsorption behaviors in different pores. As a result, OK-PSD shows the smallest *RMSD*, indicating the best performance.
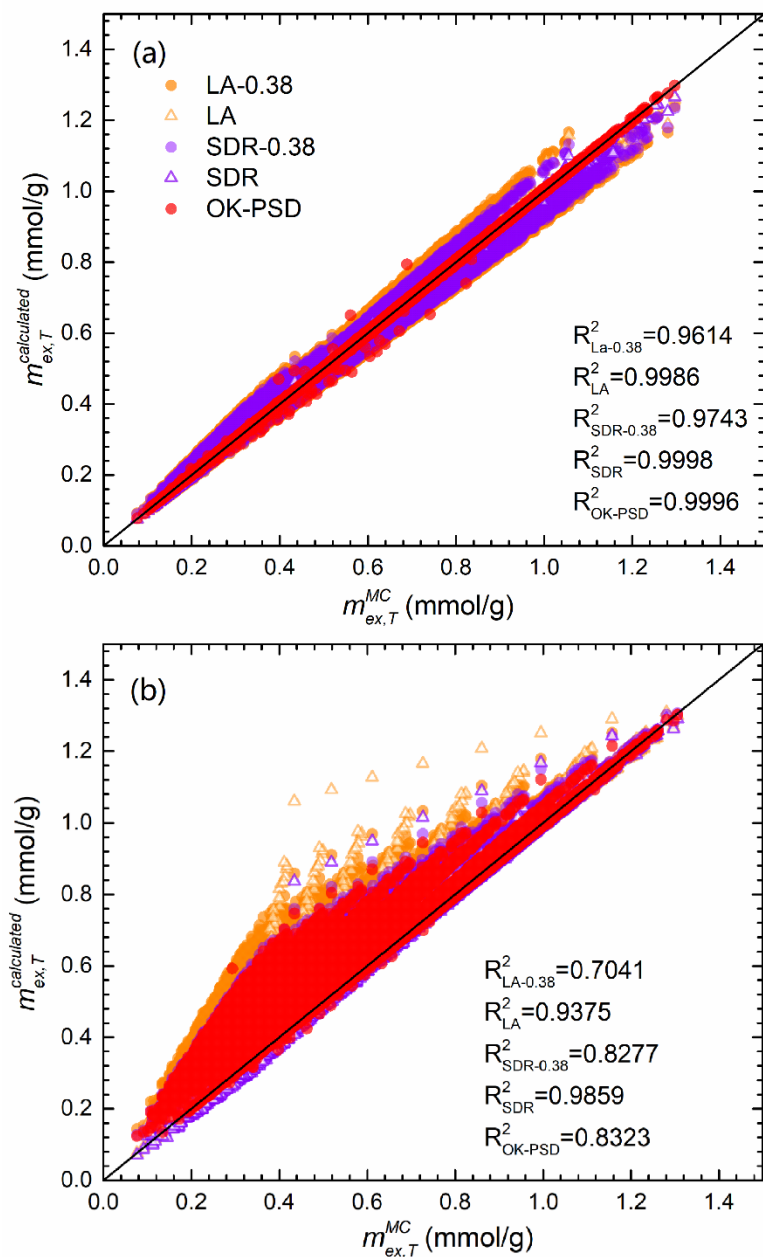
Figure 5-1 Comparison between $m_{ex,T}^{MC}$ from GCMC simulation and $m_{ex,T}^{calculated}$ from various methods with 1000 PSDs at 333.15 K using (a) high-pressure and (b) low-pressure fittings, respectively. LA and LA-0.38 represent the Langmuir model and modified Langmuir model with fixed adsorption layer width of W=0.38 nm, respectively. SDR and SDR-0.38 represent the SDR model and modified SDR model with fixed adsorption layer

width of $W=0.38$ nm, respectively. OK-PSD is the OK model associated with the PSD effect proposed in our work. Details can be found in **section 5.2.3**.
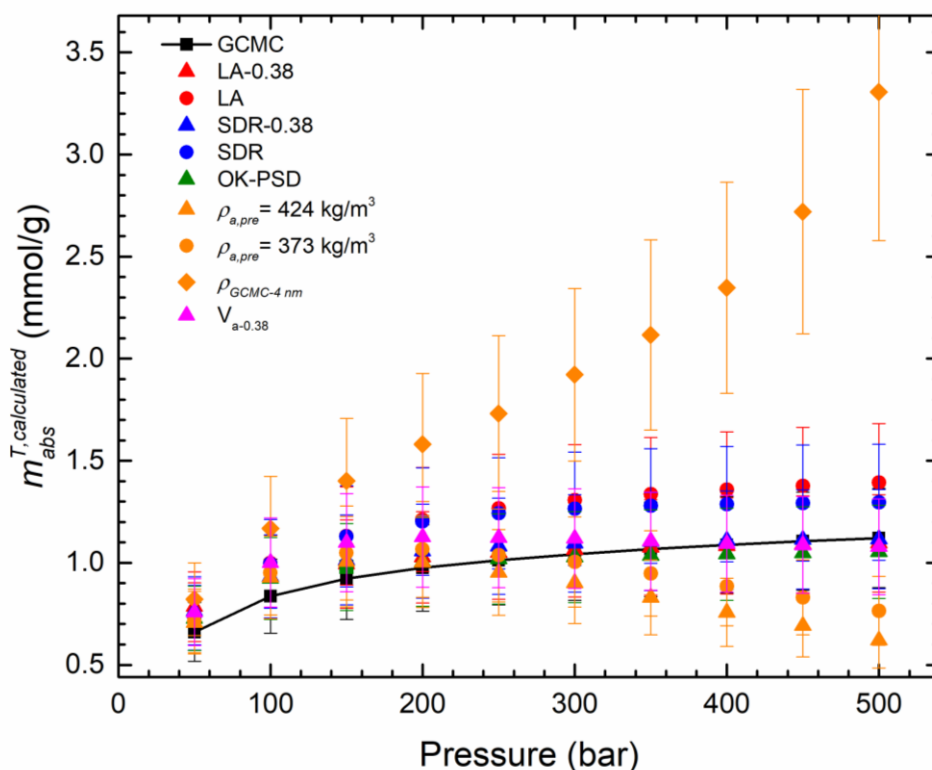
Figure 5-2 $m_{abs,T}^{L1,MC}$ and $m_{abs,T}$ at 333.15 K from various methods. The symbols represent

the averaged results of 1000 samples, and error bars depict the range of results. $\rho_{a,pre}$

represents the predetermined adsorbed phase density method, which directly converts m_{ex}

to m_{abs} using fixed density (424 kg/m³ or 373 kg/m³) (see **section 5.2.2**). $\rho_{GCMC-4nm}$ refers

to the adsorbed phase density from GCMC density profile of a 4 nm pore (see **section**

5.2.2). $V_{a-0.38}$ is the constant adsorbed phase volume method using $W_a = 0.38$ nm (see

section 5.2.4).

5.3.2 Low-Pressure Fitting

A number of experimental measurements have been conducted with pressures only up to

150 bar[63, 64, 120, 171, 172], which is much lower than the *in situ* reservoir pressure. In this subsection, we assess the performance of various methods when only the low-pressure excess adsorption results are available. We present the fitting between the total excess adsorption from GCMC simulation and five different models as shown in **Figure 5-1(b)**, using the excess adsorption between 25 bar and 150 bar, while higher pressure results are based on the extrapolation. Non-negligible deviations may occur at high pressures as shown in **Figure 5-A2(b)** of the **Appendix**, while all adsorption models regress well with GCMC simulation under a low-pressure range. Both LA and SDR show better fitting results compared to LA-0.38 and SDR-0.38. The excess adsorption predicted by the SDR model shows better agreement with GCMC simulations than that by Langmuir model, while OK-PSD exhibits similar results as SDR-0.38.

We present the $m_{abs,T}$ from various methods based on high-pressure and low-pressure fittings in panels a-c of **Figure 5-3**. We observe that all methods overestimate $m_{abs,T}$ based on low-pressure fitting, compared to $m_{abs,T}^{L1,MC}$. While low-pressure fitting causes the increases in $m_{abs,T}$ from OK-PSD, LA-0.38, and SDR-0.38, the opposite is true for LA and SDR. As a result, while the performances of OK-PSD, LA-0.38, and SDR-0.38 become better, as shown in **Figure 5-3 (d)**. It is because LA and SDR overestimate $m_{abs,T}$. The *RMSD* of OK-PSD with high-pressure fitting is the smallest, while LA-0.38 has the smallest *RMSD* among low-pressure fitting. Zhou *et al.* [39] compared absolute adsorption from SDR with high-pressure fitting to that from LA with low-pressure fitting. They found

that low-pressure fitting may lead to smaller $m_{abs,T}$. However, both LA and SDR with high-pressure and low-pressure fittings overestimate $m_{abs,T}$. Collectively, it is suggested to perform high-pressure adsorption experiments, which lays the foundation for more reliable absolute adsorption prediction than the low-pressure measurements.
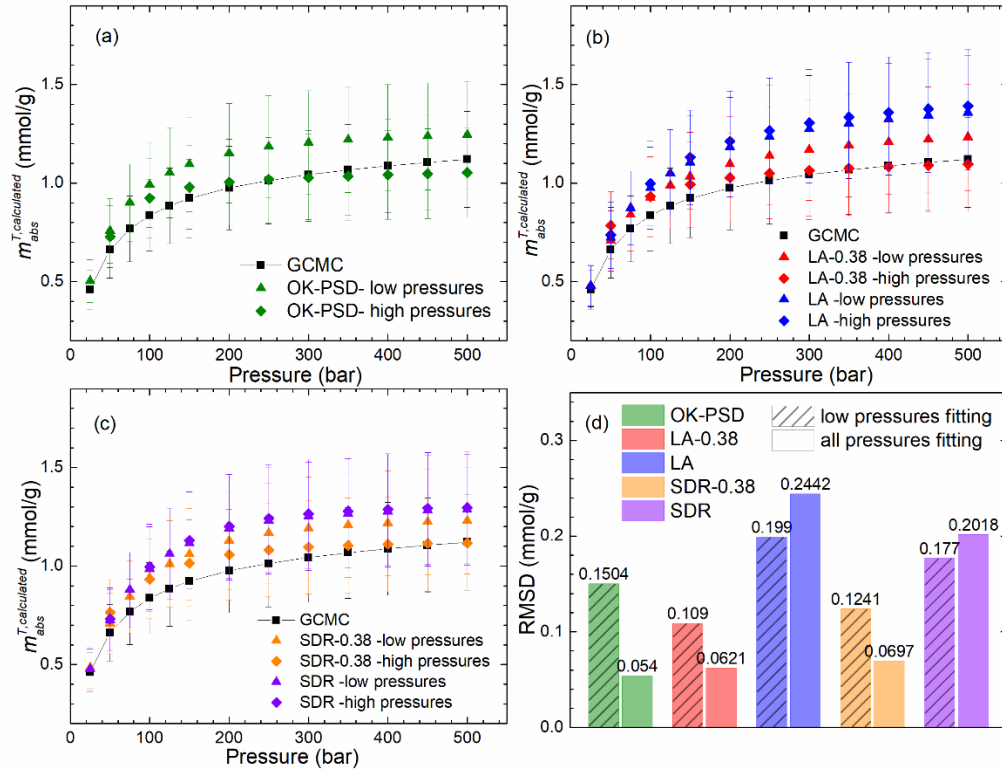
Figure 5-3 $m_{abs,T}^{L1,MC}$ and $m_{abs,T}$ from (a) OK-PSD; (b) LA and LA-0.38, and (c) SDR and SDR-0.38 based on high- and low-pressure fittings 333.15 K. (d) *RMSD* from low-pressure and high-pressure fittings.

5.4 Conclusion

In this work, we used model kerogen nanoporous media and GCMC simulations to assess the performance of various methods to obtain m_{abs}, including predetermined adsorbed

phase density method (373 kg/m^3, 424 kg/m^3 and that from GCMC density), the constant adsorbed phase volume method, and various adsorption models, including Langmuir, SDR and OK models. We found that OK-PSD shows the best agreement with GCMC results, while the predetermined density methods using 373 or 424 kg/m^3 may show unphysical phenomena. The popular LA and SDR can largely overestimate the total absolute adsorption, while LA-0.38 and SDR-0.38 show much better performances and can be comparable to OK-PSD. We also suggest to use the high-pressure excess adsorption data, instead of commonly used low-pressure excess adsorption measurements.

Collectively, we suggest to couple the adsorption models (such as OK, LA, and SDR) with PSDs (or SSA) to reliably predict the absolute adsorption in nanoporous media. It also asks for the urgent need of accurate PSD characterizations. While LA-0.38 and SDR-0.38 also show excellent agreement with GCMC simulations in model nanoporous media, OK-PSD can also provide information about the second adsorption layers and transition zones in various pores[75]. In addition, in this work, we did not consider the effect of various rock compositions[5], while methane adsorption in some inorganic matters may be non-negligible[89]. In our future works, we would study the effect of various rock compositions and PSD on the accurate characterization of methane absolute adsorption in shale nanoporous media and provide important insights into GIP estimation.

5.5 Acknowledgement

CHAPTER 6 METHANE ABSOLUTE ADSORPTION IN KEROGEN NANOPOROUS MEDIA WITH REALISTIC CONTINEOUS PORE SIZE DISTRIBUTIONS

A version of this chapter has been published in *Energy & Fuels*.

Abstract

Accurate estimation of CH_4 absolute adsorption amount is essential for shale gas-in-place (GIP) evaluation as well as well productivity. Recent studies have shown that pore size distribution (PSD) plays an important role in the determination of the absolute adsorption. However, previous studies only contain some discretized pore sizes, while a continuous PSD has not been fully taken into account. In this work, CH_4 adsorption behaviors in various nanopores are firstly investigated via the grand canonical Monte Carlo (GCMC) simulations. The CH_4 adsorption in nanopores is divided into six distinct adsorption types based on density distributions. Then, the Ono-Kondo (OK) model with PSD lumping is used to characterize CH_4 absolute adsorption in kerogen nanoporous media with pore size ranging from 0.7 nm to 50 nm. The validity of our proposed OK model with PSD lumping is tested by 5 cases with varying micropore volume proportions from 5% to 35%, with each case containing 250 sets of randomly generated PSD samples. We find that by fitting the excess adsorption isotherm, the OK model with PSD lumping has an excellent agreement in terms of the absolute adsorption amounts with those obtained from the GCMC simulation, while deviations increase as micropore volume proportion increases. Overall, the OK model with PSD lumping outperforms the popular single-layered Langmuir and SDR models as well as multilayer models such as supercritical BET (SBET) and single-parameter OK model without PSD considerations for absolute adsorption predictions in kerogen nanoporous media with a continuous PSD.

6.1 Introduction

Shale gas has become one of the most important unconventional energy resources to meet the ever-growing global energy demand[177]. Comparing to the conventional reservoirs where pores are large in the range of hundreds of nanometers or a few micrometers, shale contains an extensive amount of nanoscale pores, ranging from sub-1 nm to hundreds of nanometers[123]. In small nanopores, fluid distributions are heterogeneous due to strong fluid-wall interaction and surface adsorption is significant[5, 148, 178]. As a result, the adsorbed gas can consist up to 85% of the total gas content in shale[141]. Therefore, the accurate characterization of adsorbed gas amount is imperative to determine gas-in-place (GIP) and well productivity, which are crucial to assess the economic viability of shale reservoirs[179].

Shale rocks consist of organic and inorganic matters. As shown in previous works, the strong correlation between CH_4 adsorption uptake and total organic carbon (TOC) indicates that CH_4 adsorption capacity is highly related to TOC[65, 164, 165, 180]. There have been a number of experimental measurements on CH_4 excess adsorption (m_{ex}) in isolated kerogens, using either gravimetric or volumetric method[63, 93, 94, 180], while the absolute adsorption m_{abs} which represents the total adsorbed gas amount needs to be converted from m_{ex} [156]. Although m_{ex} and m_{abs} are nearly identical at low

pressures[35, 63, 181], their difference becomes pronounced at high pressures, which are relevant to shale exploitation condition[30].

Assuming a single-layer adsorption, two common methods are often adopted for conversion: using a constant adsorbed phase density ρ_a [39, 182, 183]; semi-empirical models[46, 51, 89, 184, 185] such as the supercritical Dubinin-Radushkevich (SDR) model[184, 185] and the Langmuir model[165, 186, 187] to regress the experimentally measured m_{ex}. However, a number of molecular simulation works[70, 150] have shown that ρ_a is dependent on pressure, temperature, and pore size. They also showed that CH$_4$ adsorption behavior is drastically different in micropores and mesopores[67, 75, 158]. For example, while in micropores (≤ 2 nm), CH$_4$ can have a layering structure without free gas zone[67, 164], in mesopores (≥ 2 nm), the presence of transition zone beyond the first adsorption layer[51, 137, 156, 188] can negatively affect m_{abs} calculation. Thus, it is essential to explicitly take into account the pore size distribution (PSD) in shale and the corresponding adsorption behaviors.

While molecular simulations have greatly advanced the understanding about adsorption characteristics, their expensive computational cost calls for relatively-simple yet highly-efficient adsorption models to describe CH$_4$ adsorption in shale nanoporous media. A few works developed adsorption models considering different adsorption behaviors depending on pore size. Ottiger *et al.*[189, 190] applied the Ono-Kondo (OK) model considering a dual-micropore system (1.2 nm and 1.6 nm) to represent micropores and one large pore (20

nm) to represent meso- and macro-pores in a dry coal. Mohammad *et al.*[191] used the simplified local-density (SLD) model to describe pure gas adsorption in coal. The SLD model considers fluid-wall interaction coupled with an equation of state to account for adsorbate chemical potentials. However, the slit length of coal nanopores is used as one of regression parameters and their model characterizes an apparent pore size, while neglecting PSD. Liu *et al.*[179] applied a two-parameter SLD model to describe CH_4 excess adsorption in shale. In their work, the dominant pore width is determined by the peak value in PSD. While the above-mentioned works utilize a single pore size, Li *et al.*[30] proposed a Langmuir model associated with adsorption energy distribution (AED) as a function of PSD to account for CH_4 adsorption in Longmaxi shale samples. AED is calculated by using the Steele 10-4 potential[192] for each specific pore, while the adsorbed phase is regarded as liquid with a constant density coupled with a thermal expansion effect over all studied pore size ranges. Our recent works[40, 75] applied the OK model associated with varying adsorption models in different pores and PSD to reliably predict m_{abs} in kerogen nanoporous media. Four adsorption types are included in the OK model based on the typical CH_4 density distributions in micropores and mesopores from the grand canonical Monte Carlo (GCMC) simulation. However, the considered nanoporous media consists of only seven discretized pores, while a realistic kerogen PSD covers a continuous range of pore sizes. Therefore, a general adsorption model which can account for varying adsorption characteristics in a continuous PSD is urgently needed.

In this work, we propose 1250 randomly generated kerogen PSDs covering a continuous pore sizes ranging from 0.7 nm to 50 nm. Since shale gas mainly consists of dry gas in which CH_4 can account up to 95 mol%[193, 194], we study pure CH_4 adsorption in kerogen nanoporous media by using GCMC simulations. While some experiments found that inorganic matters significantly contribute to the specific surface area (SSA) and specific pore volume (SPV) in over-mature translational shales[88], it is revealed that in organic-rich marine shales[195], CH_4 adsorption in kerogen plays a dominant role in total GIP. The PSD generation in each kerogen sample assumes an equivalent total SPV, while five different cases with varying proportions of micropore volume are used to test the validity of our model. Carbon slit-nanopores are used to represent kerogen for simplicity in GCMC simulations. The use of slit-like carbon pore structure, instead of a more complex and physically realistic kerogen model, is not only beneficial for computational efficiency, but also provides the same geometry as in the OK model. m_{ex} from molecular simulations follows the definition of the volumetric method and helium adsorption is used to obtain the effective pore volume (void volume). According to the GCMC simulations, we characterize six adsorption types in terms of pore sizes. The pores within a specific pore size range are lumped into the corresponding adsorption type in the OK model to account for different adsorption behaviors in micropores and mesopores. By coupling PSD and adsorption types, the OK model with PSD lumping (OK-PSD-L) can regress m_{ex} in kerogen nanoporous media excellently with GCMC simulations and provide an accurate

prediction of m_{abs}, while outperforming Langmuir and SDR models which are two commonly used models to obtain m_{abs} from experimentally measured m_{ex}. In addition to the widely used monolayer adsorption model, our OK-PSD-L model shows a better agreement with GCMC simulations comparing to the supercritical Brunauer-Emmett-Teller (SBET) model[54] and OK-single parameter model[59] which take into account the multilayer adsorption. Our work should provide important insights into CH4 adsorption in kerogen nanoporous media as well as the conversion of m_{ex} to m_{abs} for accurate estimations of GIP in shale.

6.2 Methodology

6.2.1 Molecular model and simulation

GCMC simulation is used to characterize CH4 adsorption in various carbon nanopores. We use graphite slabs to represent pore surfaces with the dimensions in the *x*-direction as $L_x = 6$ cm and in the *y*-direction as $L_y = 6$ nm in the $x - y$ plane with a two-dimensional periodic boundary condition. The separation distance between two rigid planar structureless carbon surfaces in the *z*-direction is defined as pore size W_i of pore i ranging from micropores to mesopores (spanning 0.7, 0.8, 0.9, 1.0, 1.1, 1.2, 1.3, 1.4, 1.5, 1.6, 1.7, 1.8, 1.9, 2.0, 2.1, 2.2, 2.3, 2.4, 2.5, 3.0, 4.0, 6.0, 8.0 and 10.0 nm). We will show later that the adsorption behavior in large nanopores is insensitive to W_i in terms of m_{ex} and m_{abs} per surface area (SA) of pore i, which is given as $2S_a$ with $S_a = L_x \times L_y$.

TraPPE model[196] is used to represent CH$_4$ molecules and 10-4-3 Steele potential[48] is used to describe the fluid-wall interaction in carbon slit pores (details can be found in **Appendix B**). The calculations of effective pore volume in the volumetric method can be found in **Appendix C**.

Then, the excess adsorption $m_{ex,i}^{MC}$ per SA in a given pore i is given as,

$$m_{ex,i}^{MC} = \frac{\left\langle N_{C_1,i} \right\rangle / N_A - \rho_{C_1,b}^m V_{p,i}}{2 S_a},$$ (6.1)

where $\left\langle N_{C_1,i} \right\rangle$ is the ensemble averaged number of CH$_4$ molecules in pore i, N_A is the Avogadro constant and $\rho_{C_1,b}^m$ is the CH$_4$ bulk molar density. In this work, mmol/m^2 is used as the unit for the adsorption amount per SA in pore i, while mmol/g is adopted to describe the adsorption amount by coupling PSD as in experimental measurements, which we will discuss later.

6.2.2 Characterization of CH$_4$ adsorption behaviors and types from GCMC simulation

In this section, we first investigate CH$_4$ adsorption behaviors via density distributions from the GCMC simulations, and m_{ex} per SA is investigated in terms of W_i. Then, based on characterization of adsorption behaviors from density profiles, different adsorption types are defined and m_{abs} in each adsorption layer in various nanopores over a wide range of pressures are obtained.

6.2.2.1 Description of CH4 adsorption behaviors from GCMC simulation

CH4 density distributions in several nanopores at various pressures and 333.15 K from the GCMC simulations are shown in **Figure E3**. For $W_i = 0.7$ nm, there is only one significant peak due to the strong overlap of fluid-wall interactions. The available pore space can only accommodate one CH4 adsorption layer with a high packing fraction, and the density distributions are nearly identical from 100 to 500 bar. As W_i increases, the available pore space increases to accommodate more CH4 adsorption layers, leading to varying adsorption behaviors. We found that density profiles behave differently in 1 nm, 1.5 nm, 2 nm and 4 nm pores in our previous work[75], in which the nanoporous media model reflects four adsorption behaviors: in 1 nm pores, it forms a two-layered structure with one strong adsorption layer on each pore surface; in 1.5 nm pores, there is a weaker adsorption layer in the middle of the pores to form a three-layered structure; in 2 nm pores, due to the increase of pore space, it can accommodate four CH4 adsorption layers with one strong adsorption layer and one weaker adsorption layer on each pore surface, and the densities of both adsorption layers are higher than ρ_b; in 4 nm pores, there is a free gas zone where the density is the same as the bulk fluid beyond the second adsorption layer. In addition, we find that the region between two weak adsorption layers in small mesopores (e.g. 2.1-2.4 nm) has a higher density than the bulk. The relative difference can be up to 50 % in 2.1 nm pores at 150 bar, for instance. The density in the middle of the pores contributes to m_{ex}, which would negatively affect m_{abs} calculation, if treated as a free gas

zone. As a result, this pore size range can be characterized as the transition pores from micropore-to-mesopore. When $W_i > 2.5$ nm, a free gas zone exists in the middle of the pores. As observed in **Figure E3 (d)**, when $W_i \geq 3$ nm, the peak value and width of each adsorption layer in the vicinity of the pore surface and the density of free gas phase are identical for varying pore sizes. Similar findings regarding adsorption behavior evolution in terms of pore sizes have been discussed in previous works[65, 67, 164, 197].

m_{ex} per SA for various nanopores at 333.15 K and pressures up to 500 bar is shown in **Figure E4 (a)**. When $W_i \geq 1.1$ nm, m_{ex} per SA firstly increases with pressure and then decreases, in line with the previous findings[134, 150, 198]. The increase in m_{ex} per SA with pressure is because the accumulation of CH_4 molecules mainly occurs near the pore surface at a relatively low pressure, while the density in the middle of the pores is negligible. However, as pressure further increases, the increment in ρ_b is larger than that in the adsorbed phase, so that m_{ex} per SA declines with pressure. It is noted that m_{ex} per SA of $W_i = 0.8$ nm at 500 bar is very close to zero, indicating that ρ_b approaches the adsorbed phase density. At certain pressures, m_{ex} per SA reaches maximum with the corresponding pressure ranging between 50 and 150 bar and increases with W_i, in line with the previous findings[164]. When $0.7 \, \text{nm} \leq W_i \leq 1.1 \, \text{nm}$, m_{ex} per SA keeps declining with pressure. It is because due to the strong overlap of fluid-wall interactions, the adsorbed phase is nearly saturated at a relatively low pressure. Moreover, we compare m_{ex} per SA from our work with previous experimental measurements in shale/kerogen in **Figure E4**

(b). The unit in experimental results is adopted as adsorption amount per SA, which is converted based on adsorption amount per unit mass of adsorbent and the Brunauer-Emmett-Teller (BET) SSA obtained from N_2 adsorption at 77 K. Overall, the results from our simulations are in semi-quantitative agreement with the previous experimental works[30, 39, 48, 65, 199]. The discrepancies might be attributed to the continuous PSDs in shale/kerogen samples, while only specific pore results from the GCMC simulations are presented. In addition, the purity, PSD and SSA measurements from experiments may also have a non-negligible influence[65, 200].

On the other hand, a non-monotonic behavior of m_{ex} per SA in terms of W_i at 300 bar and 333.15 K is observed, as shown in **Figure E5 (a)**. The dependence of m_{ex} per SA on W_i can be expressed as five stages, which can be explained by CH4 LJ diameter ($\sigma_f = 0.373$ nm) and CH4 configurations in small nanopores[67, 164]. In the first stage ($0.7 \text{ nm} \leq W_i \leq 0.9 \text{ nm}$), the pore space can hold only one CH4 layer. The decrease in m_{ex} per SA with W_i is because the loading (number) of CH4 molecules does not increase, while $V_{p,i}$ increases with W_i. When $1 \text{ nm} \leq W_i \leq 1.2 \text{ nm}$, the pore space can accommodate two adsorption layers with one on each pore wall, and m_{ex} per SA increases with W_i. The pore can accommodate three layers when $1.2 \text{ nm} \leq W_i \leq 1.4 \text{ nm}$, while m_{ex} per SA slightly decreases with W_i. The fourth stage ($1.5 \text{ nm} \leq W_i \leq 2.5 \text{ nm}$) represents a monotonic increase of m_{ex} per SA with W_i, while in the fifth stage ($W_i > 2.5$ nm) m_{ex} per SA is independent of W_i.

6.2.2.2 Characterization of adsorption types from GCMC simulation

Based on the varying CH_4 density distributions in various nanopores, we characterize our adsorption models into six distinct types as depicted in **Figure 6-1**, following the characterizations as in our previous works[51, 75, 156]. The corresponding W_i ranges for each adsorption type are classified as: **Type I**: 0.7-0.9 nm; **Type II**: 0.9-1.2 nm; **Type III**: 1.2-1.6 nm; **Type IV**: 1.6-2 nm; **Type V**: 2-2.5 nm; **Type VI**: ≥2.5 nm. The effective pore width $W_{p,i}$ obtained from helium adsorption (details provided in **Appendix** section **A1.2**) determines the pore space CH_4 molecules could occupy. Different adsorption layers are dictated by the local minima in density profiles at high pressures (500 bar) as in our previous works[75].

Therefore, m_{abs} per SA can be obtained based on the adsorbed phase density and volume in each pore and the expressions in various adsorption type are given as:

$$
\begin{cases}
\text{Type I:} & \begin{cases} m_{abs1,i}^{MC} = 0.5\rho_{a1,i}^{MC}W_{a1,i}^{MC} = 0.5\rho_{a1,i}^{MC}z_{AB,i} \\ m_{abs2,i}^{MC} = 0 \end{cases} \\[2em]
\text{Type II:} & \begin{cases} m_{abs1,i}^{MC} = \rho_{a1,i}^{MC}W_{a1,i}^{MC} = \rho_{a1,i}^{MC}z_{AB,i} \\ m_{abs2,i}^{MC} = 0 \end{cases} \\[2em]
\text{Type III:} & \begin{cases} m_{abs1,i}^{MC} = \rho_{a1,i}^{MC}W_{a1,i}^{MC} = \rho_{a1,i}^{MC}z_{AB,i} \\ m_{abs2,i}^{MC} = 0.5\rho_{a2,i}^{MC}W_{a2,i}^{MC} = 0.5\rho_{a2,i}^{MC}z_{BC,i} \end{cases} \\[2em]
\text{Type IV:} & \begin{cases} m_{abs1,i}^{MC} = \rho_{a1,i}^{MC}W_{a1,i}^{MC} = \rho_{a1,i}^{MC}z_{AB,i} \\ m_{abs2,i}^{MC} = \rho_{a2,i}^{MC}W_{a2,i}^{MC} = \rho_{a2,i}^{MC}z_{BC,i} \end{cases} \\[2em]
\text{Type V:} & \begin{cases} m_{abs1,i}^{MC} = \rho_{a1,i}^{MC}W_{a1,i}^{MC} = \rho_{a1,i}^{MC}z_{AB,i} \\ m_{abs2,i}^{MC} = \rho_{a2,i}^{MC}W_{a2,i}^{MC} + 0.5\rho_{a3,i}^{MC}W_{a3,i}^{MC} = \rho_{a2,i}^{MC}z_{BC,i} + 0.5\rho_{a3,i}^{MC}z_{CC',i} \end{cases} \\[2em]
\text{Type VI:} & \begin{cases} m_{abs1,i}^{MC} = \rho_{a1,i}^{MC}W_{a1,i}^{MC} = \rho_{a1,i}^{MC}z_{AB,i} \\ m_{abs2,i}^{MC} = \rho_{a2,i}^{MC}W_{a2,i}^{MC} = \rho_{a2,i}^{MC}z_{BC,i} \end{cases} \\[2em]
m_{abs,i}^{MC} = m_{abs1,i}^{MC} + m_{abs2,i}^{MC}
\end{cases}
\tag{6.2}
$$

where $m_{abs1,i}^{MC}$, $m_{abs2,i}^{MC}$ and $m_{abs,i}^{MC}$ depict m_{abs} per SA in the strong first adsorption layer, weak adsorption layers (2nd and 3rd) and combined layers of pore i, respectively; $\rho_{a1,i}^{MC}$, $\rho_{a2,i}^{MC}$, and $\rho_{a3,i}^{MC}$ represent the averaged densities of 1st, 2nd, and 3rd layer of pore i, respectively, which can be obtained by averaging the density profiles over specific adsorption layer width (details are shown in **Appendix E**) as in our previous works[51, 75]; $W_{a1,i}^{MC}$, $W_{a2,i}^{MC}$ and $W_{a3,i}^{MC}$ represent the widths of 1st, 2nd, and 3rd layer of pore i, respectively.

We plot m_{abs} per SA for the 1st layer ($m_{abs1,i}^{MC}$), 2nd layer ($m_{abs2,i}^{MC}$) and the combined layers ($m_{abs,i}^{MC}$) of various nanopores in **Figure E4 (c)**. It shows that m_{abs1} per SA almost

monotonically increases with pressure and the slope becomes smaller at higher pressures, while those in the pores of $W_i = 0.7$ nm and 0.8 nm saturate at low pressures. As W_i increases to around 1.3 nm, the adsorption layer beyond the 1st layer takes place, and the increase in the adsorption layer thickness leads to the increase in m_{abs} per SA in the combined layers. In order to verify the representativeness of simulating mesopores up to 10 nm only, we present the m_{abs} per SA in the 1st and the weak adsorption layers, and densities in each adsorption layers as well as in free gas zone (defined as the space between two transition layers in mesopores[51, 156]) in **Figure E5**. It shows that when $W_i \geq 6$ nm, $m_{abs1,i}^{MC}$ per SA, $m_{abs2,i}^{MC}$ per SA, $\rho_{a1,i}^{MC}$, and $\rho_{a2,i}^{MC}$ become independent of W_i, while $\rho_{f,i}^{MC}$ can regress to ρ_b. Therefore, one can use the GCMC simulations for mesopores up to 10 nm to represent larger mesopores. Therefore, while **Type VI** actually covers W_i larger than 2.5 nm, the adsorption behaviors in pores of $W_i > 10$ nm can be approximated by those in $W_i = 10$ nm.

The excess and absolute adsorption in kerogen nanoporous media in terms of adsorption type j and total amount are given as,

$$
\begin{cases}
m_{ex,j}^{MC} = \displaystyle\sum_{i \in Type\ j} \frac{2V_{s,i}}{W_i} m_{ex,i}^{MC} \\
m_{ex,T}^{MC} = \displaystyle\sum_{j=1}^{6} m_{ex,j}^{MC}
\end{cases}
, \qquad (6.3)
$$

$$
\begin{cases}
m_{abs1,j}^{MC} = \sum_{i \in Type\ j} \dfrac{2V_{s,i}}{W_i} m_{abs1,i}^{MC}; \ m_{abs1,T}^{MC} = \sum_{j=1}^{6} m_{abs1,j}^{MC} \\[3mm]
m_{abs2,j}^{MC} = \sum_{i \in Type\ j} \dfrac{2V_{s,i}}{W_i} m_{abs2,i}^{MC}; \ m_{abs2,T}^{MC} = \sum_{j=1}^{6} m_{abs2,j}^{MC} \\[3mm]
m_{abs,j}^{MC} = m_{abs1,j}^{MC} + m_{abs2,j}^{MC}; \ m_{abs,T}^{MC} = m_{abs1,T}^{MC} + m_{abs2,T}^{MC}
\end{cases}
\tag{6.4}
$$

where $V_{s,i}$ is the incremental pore volume of pore i based on PSD in the unit of cm^3/g; $m_{ex,j}^{MC}$ is the excess adsorption in adsorption type j in the unit of mmol/g; $m_{ex,T}^{MC}$ is the total excess adsorption in nanoporous media in the unit of mmol/g; $m_{abs1,j}^{MC}$ and $m_{abs2,j}^{MC}$ represent the 1st layer and beyond the 1st layer (weak adsorption layers) absolute adsorption amount in adsorption type j in the unit of mmol/g, respectively; $m_{abs1,T}^{MC}$ and $m_{abs2,T}^{MC}$ represent the 1st layer and beyond the 1st layer (weak adsorption layers) absolute adsorption amount in the unit of mmol/g, respectively; $m_{abs,j}^{MC}$ is the total absolute adsorption amount in adsorption type j; $m_{abs,T}^{MC}$ is the total absolute adsorption amount. It should be noted that in **Type III, IV** and **VI**, $m_{abs2,i}^{MC}$ and $m_{abs2,T}^{MC}$ correspond to absolute adsorption amount only in the 2nd layer, while in **Type V**, $m_{abs2,i}^{MC}$ and $m_{abs2,T}^{MC}$ include the contribution of adsorption amount in both 2nd and 3rd adsorption layers.

6.2.3 OK model in nanoporous media with pore size lumping

Similar to our previous work[156], we adopt a three-dimensional OK model with a simple cubic geometry and mean-field approximation. The detailed derivations of OK model and governing equations for each adsorption layer in different adsorption types are given in

Appendix A.

Based on the characterization shown in **Figure 6-1**, the OK models are divided into six types. In contrast to the GCMC simulations, a constant adsorption layer width $W_a = 0.38$ nm is applied in the OK model[40]. From **Type I** to **Type V** in the OK model, the density in each layer is higher than ρ_b, while in **Type VI**, the density in the 3$^{\text{rd}}$ layer in mesopore is very close to ρ_b and the region beyond the 3$^{\text{rd}}$ layer is regarded as free gas. It should be noted that the occupation in each layer k in different adsorption type can be different, which is given as $x_{k,j} = \rho_{a,k,j} / \rho_{am}$, where j is the specific adsorption type.
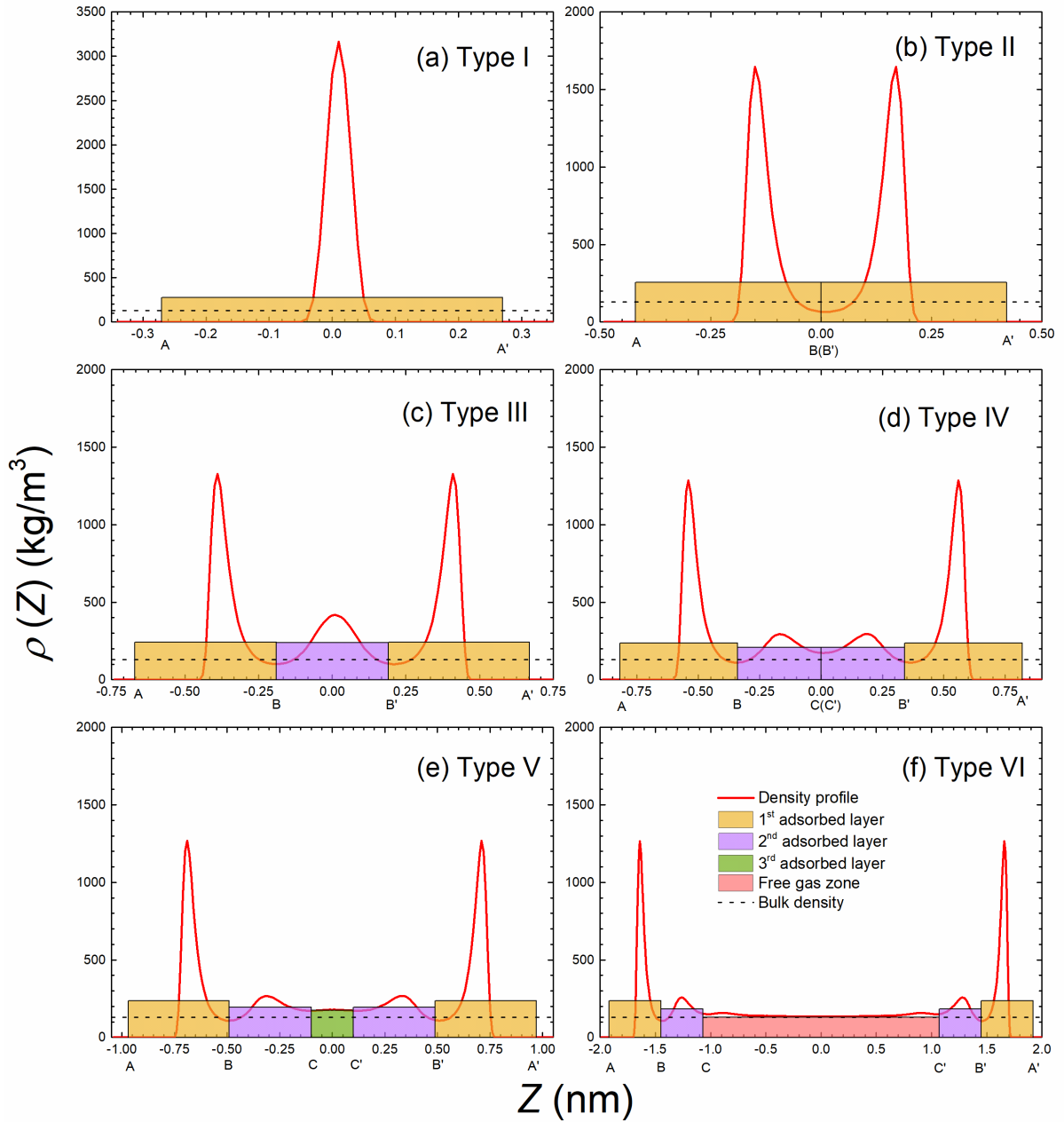
Figure 6-1 Schematic representations of various adsorption models. The density profiles obtained from GCMC simulation are at 333.15 K and 200 bar for W_i of (a) 0.7 nm; (b) 1 nm; (c) 1.5 nm; (d) 1.8 nm; (e) 2.1 nm; (f) 4 nm.

Therefore, the excess adsorption per SA in Type j is given as,

$$m_{ex,j}^{OK-PSD-L} = \rho_{am}^{OK-PSD-L} W_a \sum_{k=1}^{n_j} \left(x_{k,j} - x_b \right), \qquad (6.5)$$

where n_j and $m_{ex,j}^{OK-PSD-L}$ are the number of layers and excess adsorption per SA in adsorption type j, respectively; $\rho_{am}^{OK-PSD-L}$ is the maximum adsorbed density in each layer. While in the GCMC simulations, explicit characterization of adsorption behavior in each pore is available, in the OK-PSD-L model, the pore size range in the same adsorption type is lumped. Therefore, m_{ex} in kerogen nanoporous media obtained from the OK-PSD-L model is given as,

$$m_{ex,T}^{OK-PSD-L} = \sum_{j=1}^{6} \sum_{i \in Type\ j} \frac{2V_{s,i}}{W_i} \left[\rho_{am}^{OK-PSD-L} W_a \sum_{k=1}^{n_j} \left(x_{k,j} - x_b \right) \right], \qquad (6.6)$$

in which $\displaystyle\sum_{i \in Type\ j} \frac{2V_{s,i}}{W_i}$ represents the summation of incremental pore volume divided by W_i of pore i which belong to Type j with PSD lumping, m²/g. The proposed OK-PSD-L model in Eq. (6.6) is applied to regress $m_{ex,T}^{MC}$ given in Eq. (6.3). The constraints for fitting parameters follow our previous works and other modelling works[201-203] as:

$0 < \rho_{am}^{OK-PSD} < 700$ kg/m³, $-1 < \varepsilon / k_B T < 0$ and $-10 < \varepsilon_s / k_B T < 0$. m_{abs} per SA of Type j obatined from the OK model are given as,

$$
\begin{cases}
m_{abs1,j}^{OK-PSD-L} = \begin{cases} 0.5\rho_{a1,j}^{OK-PSD-L}W_a & (j=\text{Type I}) \\ \rho_{a1,j}^{OK-PSD-L}W_a & (j \neq \text{Type I}) \end{cases} \\
m_{abs2,j}^{OK-PSD-L} = \begin{cases} 0.5\rho_{a2,j}^{OK-PSD-L}W_a & (j = \text{Type III}) \\ \rho_{a2,j}^{OK-PSD-L}W_a & (j = \text{Type IV,VI}) \\ \rho_{a2,j}^{OK-PSD-L}W_a + 0.5\rho_{a3,j}^{OK-PSD-L}W_a & (j = \text{Type V}) \end{cases}
\end{cases} \quad . \quad (6.7)
$$

Therefore, total m_{abs} considering PSD effect in each layer ($m_{abs1,T}^{OK-PSD-L}$ and $m_{abs2,T}^{OK-PSD-L}$) and in combined layers ($m_{abs,T}^{OK-PSD-L}$) are given as,

$$
\begin{cases}
m_{abs1,T}^{OK-PSD-L} = \sum_{j=1}^{6} \sum_{i \in Type\ j} \frac{2V_{s,i}}{W_i} m_{abs1,j}^{OK-PSD-L} \\
m_{abs2,T}^{OK-PSD-L} = \sum_{j=1}^{6} \sum_{i \in Type\ j} \frac{2V_{s,i}}{W_i} m_{abs2,j}^{OK-PSD-L} \\
m_{abs,T}^{OK-PSD-L} = m_{abs1,T}^{OK-PSD-L} + m_{abs2,T}^{OK-PSD-L}
\end{cases} \quad . \quad (6.8)
$$

The differences in the methodologies used in our previous work[75] and this work are highlighted in **Figure 6-2**. In our previous work[75], the adsorption model characterized in the OK model and the GCMC simulations have a one-to-one correspondence, while the discrete pore sizes cannot represent the continuous PSDs in actual shale samples. In this work, the PSD of each adsorption type from **Type I** to **VI** is lumped in the corresponding pore size range. ρ_{am}, ε and ε_s are three unknown parameters, which are obtained by fitting $m_{ex,T}^{MC}$. For each specific adsorption type, the non-linear equations can be solved iteratively. Subsequently, the actual adsorbed phase densities in each layer are obtained.
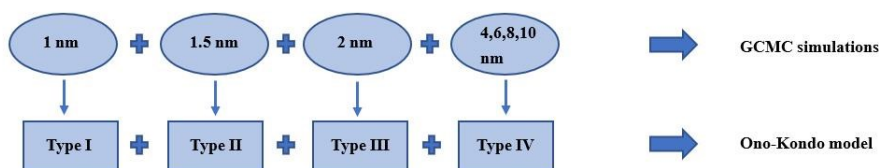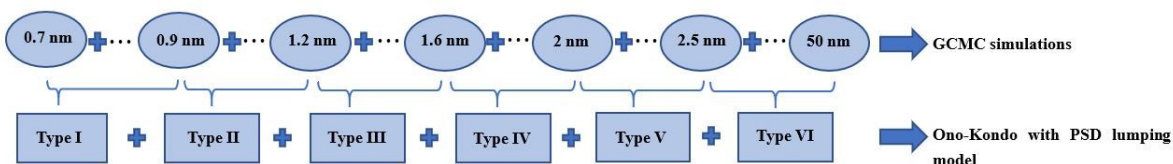
Figure 6-2 OK-PSD models applied in our previous work[40] and this work.

6.2.4 Nanoporous media model

The range of randomly generated PSD (referring to W_i) is from 0.7 nm to 50 nm and all the tested samples have equal SPV. Based on the International Union of Pure and Applied Chemistry (IUPAC) classification, pores with width below 2 nm are classified as micropores, while those with width ranging from 2 nm to 50 nm are defined as mesopores. A number of works have shown that micropores and mesopores can provide the majority of total SPV in various shale and isolated kerogen samples[30, 169, 204, 205]. Therefore, a truncated pore width at 50 nm in this work can largely account for CH_4 adsorption in kerogen nanoporous media. The continuous PSDs in kerogen nanoporous media are ensured by using small intervals in discretized pore widths: The interval of pore width under 2.5 nm is fixed as 0.1 nm, while the pore width larger than 2.5 nm is set as 0.5 nm.

Varying range of pore volumes in isolated kerogen samples from various formations have

been reported[48, 64, 88, 206, 207]. According to these measurements, we fix the total SPV of kerogen nanoporous media as 0.05 cm^3/g, which represents the cumulative void volume of each pore. On the other hand, it is reported that the percentage of kerogen micropore volume in the micropore-plus-mesopore volume can range from 12.5% to 28.5% in different shale formations[88, 206, 208]. Therefore, we generate five different cases of micropore volume proportions (micPVs) (5%, 10%, 15%, 25% and 35%, denoted as 5 % micPV, 10% micPV, 15% micPV, 25% micPV, and 35% micPV, respectively). For each case, 250 sets of PSDs are randomly generated, following the procedures as: (a) two series of random number $R_{mic,i}$ and $R_{mes,i}$ in the interval (0,1) are generated for pore i in micropore and mesopore ranges, respectively. The weight percent of each pore volume in micropore and mesopore ranges can be expressed as $w_{mic,i} = R_{mic,i} / \sum\limits_{i=0.7\,\mathrm{nm}}^{2\,\mathrm{nm}} R_{mic,i}$ and $w_{mes,i} = R_{mes,i} / \sum\limits_{i>2\,\mathrm{nm}}^{50\,\mathrm{nm}} R_{mes,i}$, respectively, which ensure $\sum\limits_{i=0.7\,\mathrm{nm}}^{2\,\mathrm{nm}} w_{mic,i} = 1$ and $\sum\limits_{i>2\,\mathrm{nm}}^{50\,\mathrm{nm}} w_{mes,i} = 1$;

(b) with the total SPV ($V_{s,T} = 0.05\,\mathrm{cm}^3$/g) and micPV, the incremental pore volume of pore i in either micropore or mesopore range can be given as $V_{s,i} = V_{s,T} \times w_{mic,i} \times micPV$ and $V_{s,i} = V_{s,T} \times w_{mes,i} \times (1 - micPV)$, respectively. Therefore, by assuming slit geometry in nanoporous media, the SSA of pore i can be derived from the incremental pore volume $V_{s,i}$ (m^2/g) and W_i, given as $SSA_i = 2V_{s,i} / W_i$. The total SSA of kerogen nanoporous media is the summation of SSA_i for entire pore range. The percentage of the micropore SSA in the total SSA in randomly generated PSD samples are shown in **Figure 6-3 (a)**. As micPV

increases, the resulting contribution of micropore SSA to the total SSA ranges from 29% to 88%. We also present example PSDs (in terms of $V_{s,i}$ for each pore i) with different micPVs in **Figure 6-3 (b)**.
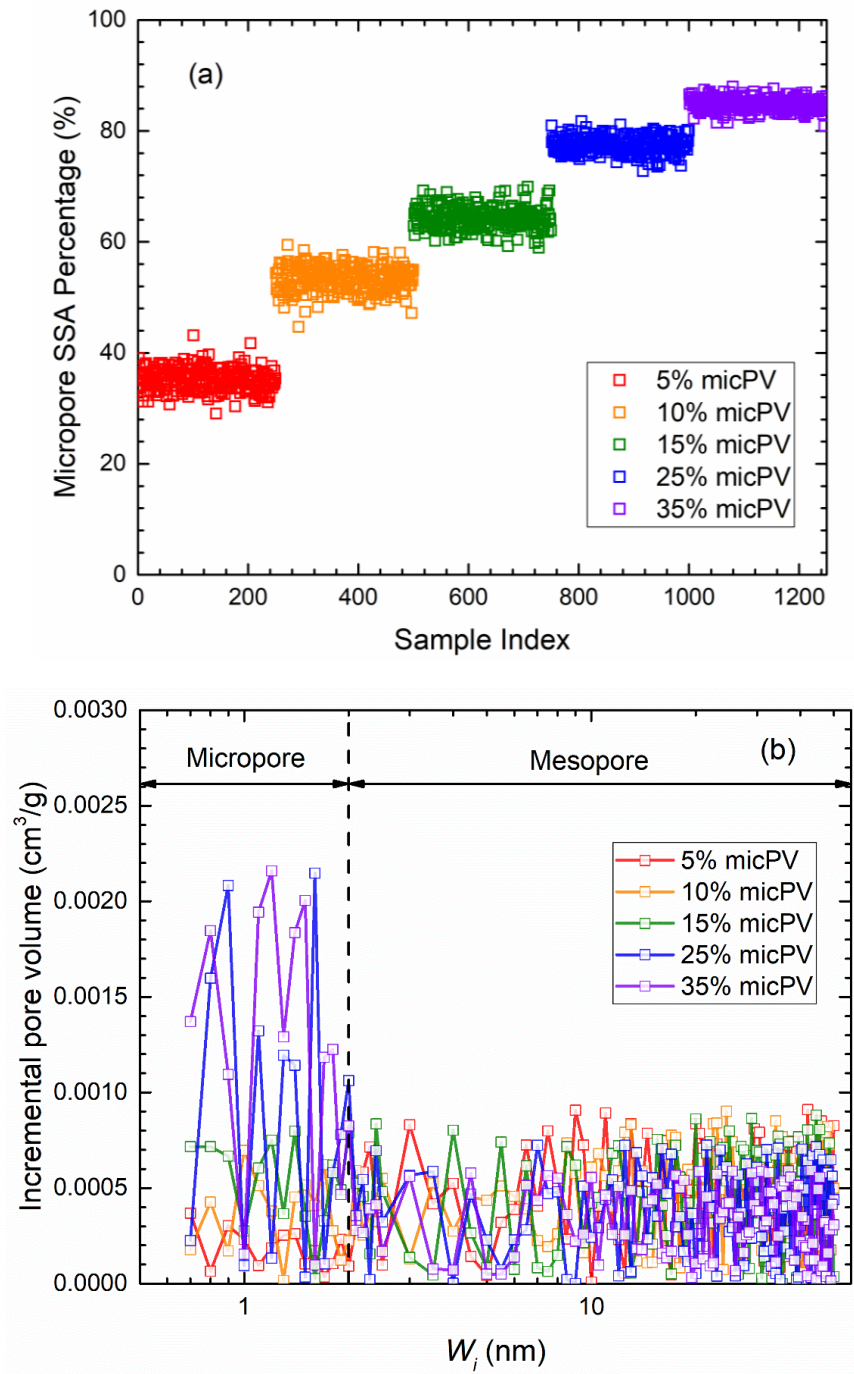
Figure 6-3 (a) The percentage of micropore SSA in the total SSA in randomly generated PSD samples with different micPVs; (b) Example PSDs ($V_{s,i}$) with different micPVs.

As these samples have equivalent total SPV, the higher micPV results in a significant enhancement in SSA. The total adsorption amount (mmol/g) in 1250 randomly generated PSD samples is presented in **Figure E6**. It shows that as micPV increases, both m_{ex} and m_{abs} increase, because there are more smaller pores with a higher SSA.

6.3 Results and discussion

In this section, we first present the total absolute adsorption from the OK-PSD-L model and the GCMC simulations. We also compare the OK-PSD-L model with the commonly used models for varying micPVs.

6.3.1 CH₄ adsorption behavior from the OK model

The $m_{ex,T}^{OK-PSD-L}$ from the OK-PSD-L model is regressed to $m_{ex,T}^{MC}$ of 1250 randomly generated PSD samples, with distinct sets of fitting parameters. In **Table E2**, we list the averaged fitting parameters in the OK-PSD-L model. We present the regression performance of the OK-PSD-L model by comparing to the GCMC simulations in **Figure 6-4**. We also present the root-mean square deviations (RMSDs) in various adsorption amounts (obtained through **Eq. E19** in **Appendix**) in **Table 6-2**. Overall, the OK-PSD-L model shows a good agreement with the GCMC simulations. For example, the RMSD in

m_{ex} for all samples is only 0.0047 mmol/g, while the RMSD in m_{abs} is 0.0082 mmol/g, which is larger than those in m_{abs1} and m_{abs2}. In addition, as micPV increases, the RMSDs increase. For example, RMSD in m_{abs} in 35% micPV can be more than 3 times of that in 5% micPV.
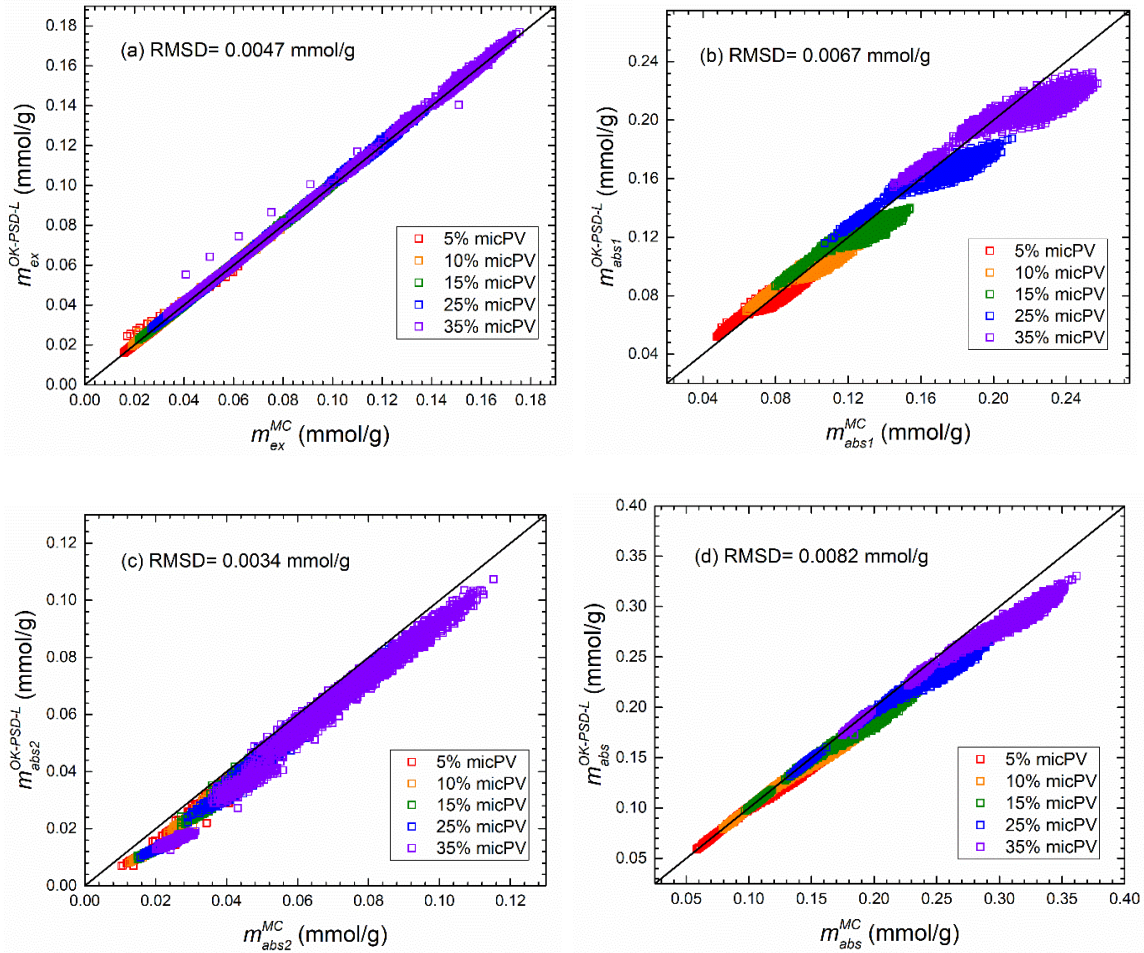
Figure 6-4 Comparison between adsorption amount calculated from the OK-PSD-L model and the GCMC simulations with 1250 randomly generated PSD samples at 333.15 K. (a) $m_{ex,T}^{MC}$ and $m_{ex,T}^{OK}$; (b) $m_{abs1,T}^{MC}$ and $m_{abs1,T}^{OK}$; (c) $m_{abs2,T}^{MC}$ and $m_{abs2,T}^{OK}$; (d) $m_{abs,T}^{MC}$ and $m_{abs,T}^{OK}$.

We present the mean relative errors between the OK model and the GCMC simulations in

Figure 6-5 (obtained through **Eq. E22-23** in **Appendix**). MRE_{ex} is between -4% and 0.4% for all cases, indicating an excellent performance by the OK-PSD-L model. MRE_{abs1} is firstly less than 0 at low pressures, then larger than 0 at high pressures, ranging from -9.2% to 10.6%. On the other hand, $m_{abs2,T}^{OK-PSD-L}$ is always underestimated, while MRE_{abs2} can be as high as 37% at 50 bar. However, as pressure increases, MRE_{abs2} decreases and is around 7% at 500 bar, which is related to the actual shale reservoir pressure. MRE_{abs} is within -0.1%~ 9.6% for all cases. Similar to the RMSDs as shown in **Table 6-2**, the mean relative errors increase as micPV increases. **Figure 6-6** compares the mean relative errors in micropores and mesopores. It shows that the proposed OK model with PSD lumping can also predict the adsorption amounts in micropores and mesopores well.
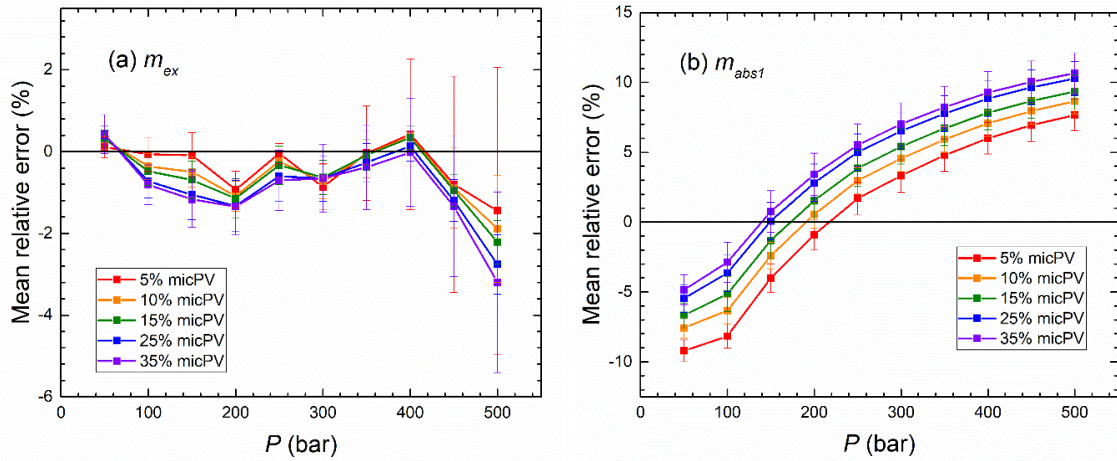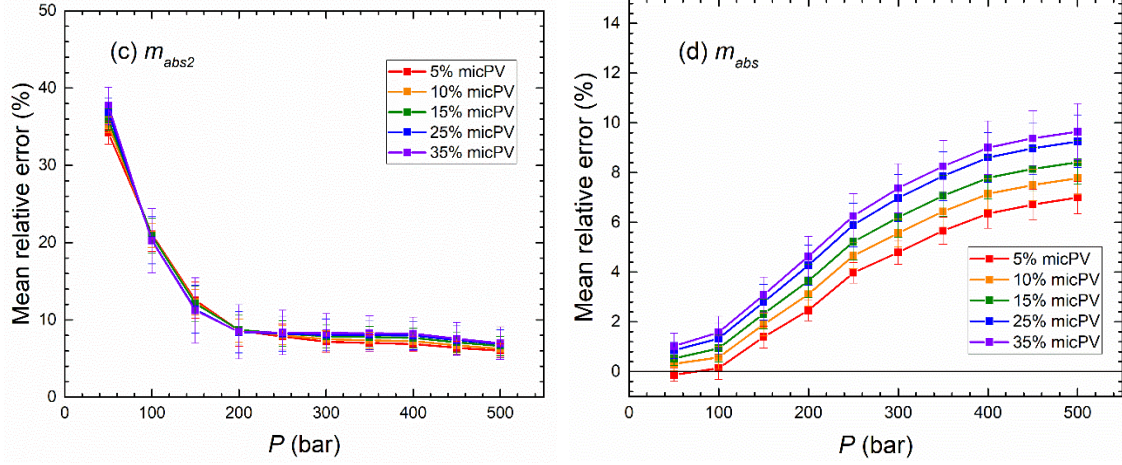
Figure 6-5 Mean relative errors in adsorption amounts calculated from the OK-PSD-L model and GCMC simulations with 1250 PSD samples at 333.15 K for different micPVs. (a) $m_{ex,T}^{MC}$; (b) $m_{abs1,T}^{MC}$; (c) $m_{abs2,T}^{MC}$ and (d) $m_{abs,T}^{MC}$. For clarity, error bars are presented.

6.3.2 Comparison with monolayer and multilayer adsorption models

The Langmuir and SDR models have been widely applied to convert the experimentally measured m_{ex} to m_{abs} [101, 183, 187] based on monolayer adsorption and pore filling theory, respectively. Here, we test the performance of both models for m_{abs} predictions in kerogen nanoporous media with continuous PSDs, which are given as[185, 209],

$$\begin{cases} m_{ex}^{LA} = m_{\max,LA} \dfrac{P}{P_L + P}\left(1 - \dfrac{\rho_b}{\rho_{a,LA}}\right) \\ m_{abs}^{LA} = m_{\max,LA} \dfrac{P}{P_L + P} \end{cases}, \tag{6.9}$$

$$\begin{cases} m_{ex}^{SDR} = m_{\max,SDR} \exp\left\{-D\left[\ln\left(\dfrac{\rho_{a,SDR}}{\rho_b}\right)\right]^2\right\}\left(1 - \dfrac{\rho_b}{\rho_{a,SDR}}\right) \\ m_{abs}^{SDR} = m_{\max,SDR} \exp\left\{-D\left[\ln\left(\dfrac{\rho_{a,SDR}}{\rho_b}\right)\right]^2\right\} \end{cases}, \qquad (6.10)$$

where m_{ex}^{LA}, m_{abs}^{LA} and $m_{\max,LA}$ are excess adsorption, absolute adsorption and maximum adsorption capacity in the Langmuir model, mmol/g, respectively; $\rho_{a,LA}$ and P_L are the adsorbed phase density (kg/m^3) and the pressure at which the adsorbed amount reaches the half of the maximum adsorption capacity, respectively; m_{ex}^{SDR}, m_{abs}^{SDR} and $m_{\max,SDR}$ are excess adsorption, absolute adsorption and maximum adsorption capacity in the SDR model, mmol/g, respectively; $\rho_{a,SDR}$ and D are the adsorbed phase density (kg/m^3) and interaction constant in the SDR model, respectively.

Multilayer adsorption models have also been used to characterize CH$_4$ adsorption behavior in shale. Brunauer-Emmett-Teller (BET) model[210] is one of the most commonly multilayer adsorption models which can be applied for the determination of surface area in porous media through low temperature nitrogen adsorption experiment[211]. The original BET model is proposed for subcritical gas adsorption[146], while under *in-situ* condition, CH$_4$ is supercritical. Zhou *et al.*[54] proposed a supercritical BET model to investigate supercritical CH$_4$ adsorption in shale by restricting the number of adsorption layers and using density instead of pressure, which is given as,

$$
\begin{cases}
m_{ex}^{SBET} = m_{max,SBET} \dfrac{c\rho_b}{\rho_{a,SBET}} \dfrac{1-(n_{BET}+1)\left(\rho_b/\rho_{a,SBET}\right)^{n_{BET}} + n_{BET}\left(\rho_b/\rho_{a,SBET}\right)^{n_{BET}+1}}{1+(c-1)\left(\rho_b/\rho_{a,SBET}\right) - c\left(\rho_b/\rho_{a,SBET}\right)^{n_{BET}+1}} \\[4mm]
m_{abs}^{SBET} = m_{max,SBET} \dfrac{c\rho_b/\rho_{a,SBET}}{1-\rho_b/\rho_{a,SBET}} \dfrac{1-(n_{BET}+1)\left(\rho_b/\rho_{a,SBET}\right)^{n_{BET}} + n_{BET}\left(\rho_b/\rho_{a,SBET}\right)^{n_{BET}+1}}{1+(c-1)\left(\rho_b/\rho_{a,SBET}\right) - c\left(\rho_b/\rho_{a,SBET}\right)^{n_{BET}+1}}
\end{cases}
$$

$$(6.11)$$

where m_{ex}^{SBET}, m_{abs}^{SBET} and $m_{max,SBET}$ are excess adsorption, absolute adsorption and maximum adsorption capacity in the SBET model, mmol/g, respectively; $\rho_{a,SBET}$, c and n_{BET} are the adsorbed phase density (kg/m^3), energy parameter related to adsorption heat and number of adsorption layers in the SBET model, respectively. We note that while BET model can describe multilayer adsorption behaviors, in SBET model, the absolute adsorption conversion from the excess adsorption is still based on the single-layer assumption.

In addition, in order to compare with the OK-PSD-L model, the single-parameter multilayer OK model without considering PSD (OK-w/o-PSD) used by Xiong *et al.* [59] is applied by using SSA and LJ diameter 0.38 nm to identify the adsorbed phase volume of each layer, and three adsorption layers from each surface. The generalized OK-w/o-PSD model is given as,

$$\begin{cases} m_{ex}^{OK-w/o-PSD} = \rho_{am}^{OK-w/o-PSD} W_a SSA \sum_{k=1}^{n} (x_k - x_b) \\ m_{abs1}^{OK-w/o-PSD} = \rho_{am}^{OK-w/o-PSD} W_a SSA x_1 \\ m_{abs2}^{OK-w/o-PSD} = \rho_{am}^{OK-w/o-PSD} W_a SSA x_2 \\ m_{abs}^{OK-w/o-PSD} = m_{abs1}^{OK-w/o-PSD} + m_{abs2}^{OK-w/o-PSD} \end{cases} , \qquad (6.12)$$

It should be noted that the OK-w/o-PSD model consider the adsorption amount as the contribution from each layer subject to the entire SSA in kerogen nanoporous media, while the OK-PSD-L model specifically accounts for each adsorption type and their corresponding SSAs.

Based on the regression results of each layer density, we find that the contributions from first two adsorption layers dominate the adsorption amount, while the 3rd layer density approaches bulk density, which is consistent with our findings in previous work[156].

For Langmuir, SDR and SBET models, we adopt three different methods each (parameters of each are shown in **Table 6-1**) following experimental works [39, 54, 170, 182, 183] to determine adsorbed phase density: the freely fitted adsorbed phase density, fixed adsorbed phase densities as 373 kg/m^3 and 424 kg/m^3, respectively. After fitting with $m_{ex,T}^{MC}$, the regression variables are shown in **Table E2**, and the performance for each method for 1250 PSD samples are shown in **Figure E10**. We note that the comparison in the absolute adsorption is made between the models and the 1st adsorption layer from the GCMC simulations, as the single-layer adsorption model is used in Langmuir and SDR models.

For SBET model, as shown in **Table E2**, the M1 method with freely fitted density has averaged number of adsorption layers to 0.93, while M2 and M3 with pre-set densities regress the number of layers to the averaged values of 0.062 and 0.11, respectively. In Zhou *et al.*'s work[54], the regressed number of layers from experimental results show an averaged number of 2.12, 0.85 and 0.63 for freely fitted density, fixed 0.373 g/cm^3 and 0.423 g/cm^3, respectively. The mean relative errors from the Langmuir, SDR and SBET models in m_{ex} and m_{abs} in the 1st adsorption layer at various pressures and different micPVs are shown in **Figure E11**. The freely fitted adsorbed phase densities in the Langmuir, SDR and SBET models have similar values in each micropore volume ratio, and the M1 methods perform significantly better than those using 373 or 424 kg/m^3. The maximum adsorption capacity in Langmuir, SDR and SBET models increases as the micropore volume proportion increases, while P_L and D show a opposite trend. Moreover, as micPV increases, the P_L and D turn to 0 by using fixed adsorbed phase density, resulting in a poor regression performance in m_{ex} and m_{abs}. It indicates that using liquid phase densities as the adsorbed phase density would lead to large errors in absolute adsorption prediction[54]. The large RMSDs in the Langmuir-M2, Langmuir-M3, SDR-M2, and SDR-M3 models can be observed in **Figure 6-7 (a)** and **Table 6-2.** The OK-PSD-L model shows the smallest RMSDs in estimating the 1st layer absolute adsorption. As for different models, Langmuir-M3 and SDR-M3 exhibit the largest RMSDs which can be more than two times larger than those in the OK-PSD-L model, while SDR-M1 has

relatively small deviations. In addition, the RMSDs of multilayer models including OK-w/o-PSD and SBET model are shown in **Figure 6-7 (b)**. A similar behavior of SBET model to Langmuir and SDR models can be observed, and the RMSDs in both m_{ex} and m_{abs1} from OK-w/o-PSD are higher than those from OK-PSD-L model.
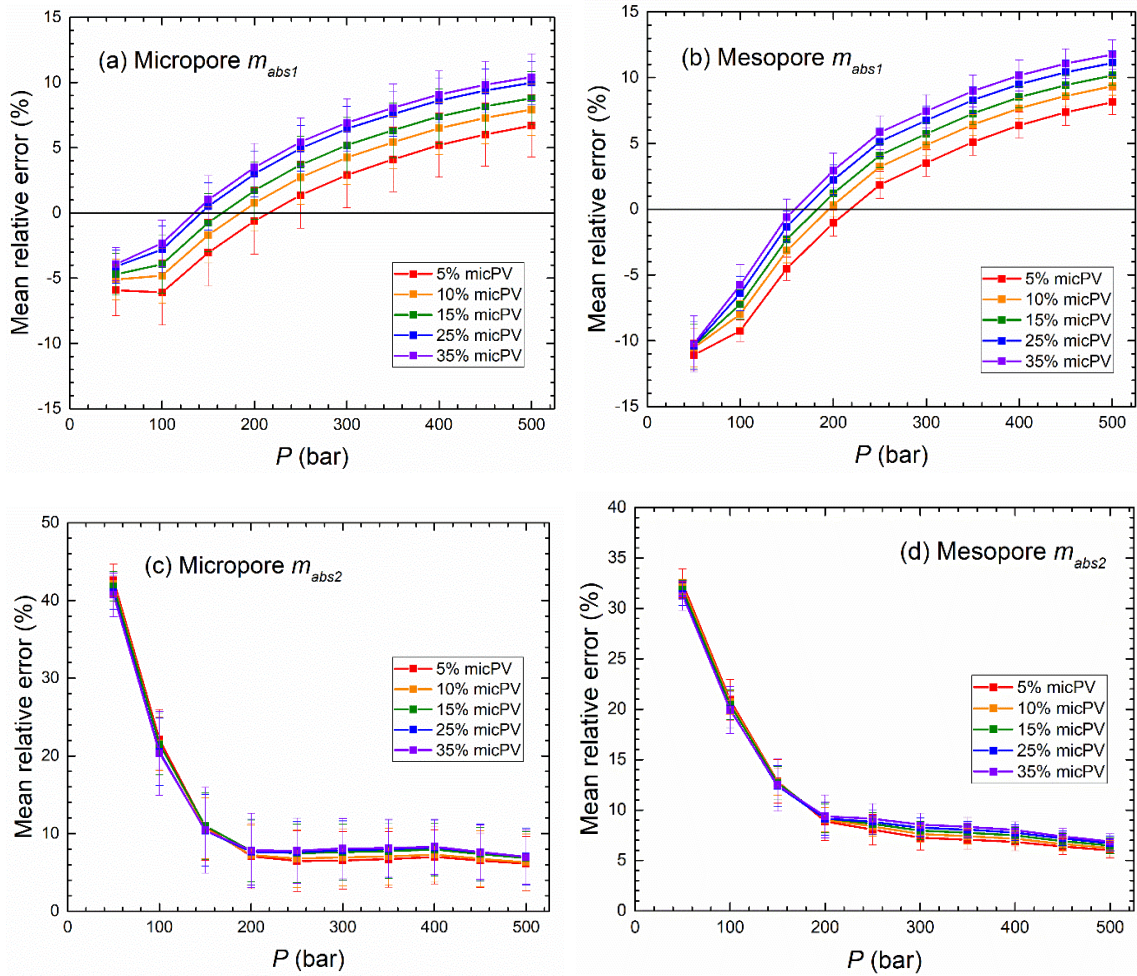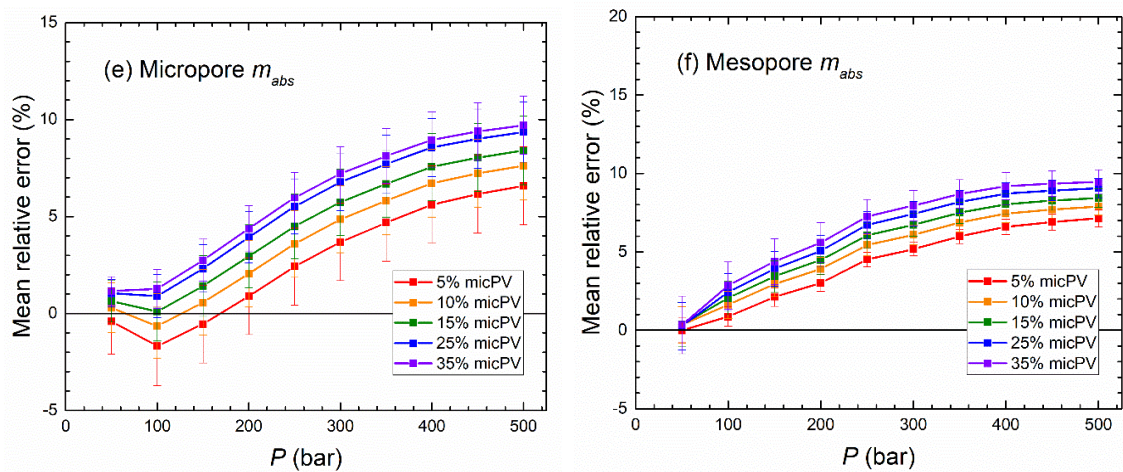
Figure 6-6 Mean relative errors in adsorption amounts calculated from the OK-PSD-L model and GCMC simulations with 1250 PSD samples at 333.15 K for different micPVs. (a) micropore m_{abs1}^{MC}; (b) mesopore m_{abs1}^{MC}; (c) micropore m_{abs2}^{MC}; (d) mesopore m_{abs2}^{MC}; (e) micropore m_{abs}^{MC} and (f) mesopore m_{abs}^{MC}. For clarity, error bars are presented.
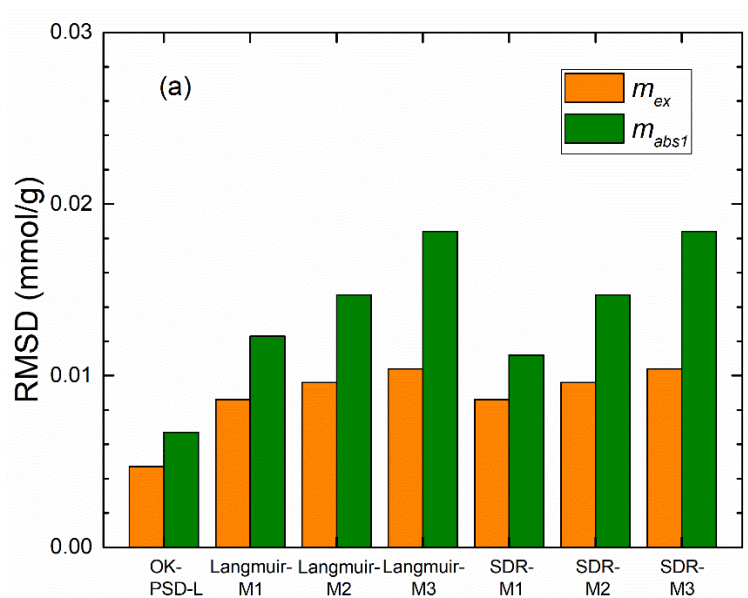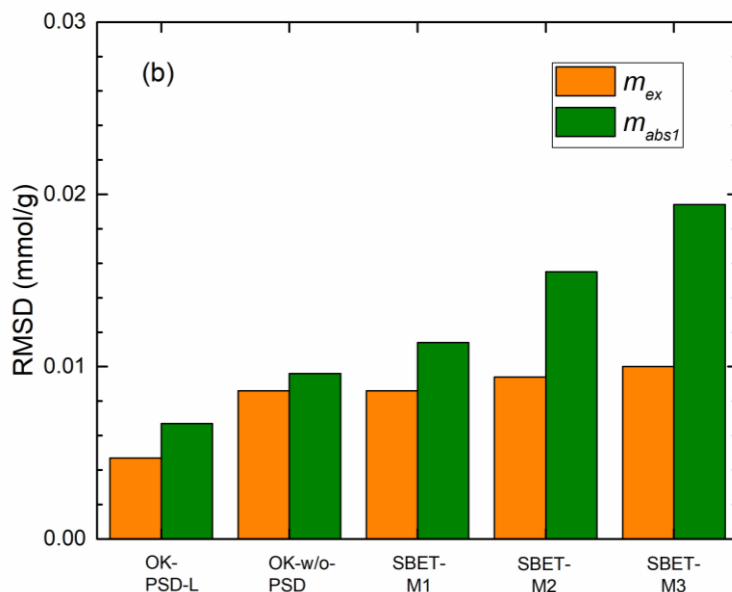
Figure 6-7 Comparison between RMSDs of excess and absolute adsorption amount of OK-PSD-L model, Langmuir model, SDR model, SBET model and OK-w/o-PSD model with GCMC simulations for 1250 PSD samples at 333.15 K.

Table 6-1 Three methods in terms of adsorbed phase density applied in Langmuir, SDR, and SBET model

Methods		Parameters	Denote as
Langmuir model	ρ_a as fixed parameter	$m_{max,LA}$, P_L and $\rho_{a,LA}$	Langmuir-M1
	$\rho_a = 373$ kg/m^3	$m_{max,LA}$ and P_L	Langmuir-M2
	$\rho_a = 424$ kg/m^3	$m_{max,LA}$ and P_L	Langmuir-M3
	ρ_a as fixed parameter	$m_{max,SDR}$, D and $\rho_{a,SDR}$	SDR-M1

	$\rho_a = 373$ kg/m^3	$m_{max,SDR}$ and D	SDR-M2
SDR model	$\rho_a = 424$ kg/m^3	$m_{max,SDR}$ and D	SDR-M3
SBET model	ρ_a as fixed parameter	$m_{max,SBET}$, C, n_{BET} and $\rho_{a,SBET}$	SBET-M1
	$\rho_a = 373$ kg/m^3	$m_{max,SBET}$, C and n_{BET}	SBET-M2
	$\rho_a = 424$ kg/m^3	$m_{max,SBET}$, C and n_{BET}	SBET-M3

Table 6-2 Root mean square deviations of predicted adsorption amount from the OK-PSD-L model, the OK-w/o-PSD model, the Langmuir model, the SDR model, and the SBET model in different micropore volume.

Adsorption amount	Micropore volume (%)	5%	10%	15%	25%	35%
	Methods	RMSD given in Eq. (S) (mmol/g)				
m_{ex}	OK-PSD-L	0.0018	0.0030	0.0039	0.0053	0.0072
	OK-w/o-PSD	0.0037	0.0058	0.0074	0.0100	0.0129
	Langmuir-M1	0.0040	0.0059	0.0075	0.0101	0.0130
	Langmuir-	0.0049	0.0067	0.0083	0.0112	0.0145

	M2					
	Langmuir-M3	0.0055	0.0072	0.0089	0.0120	0.0157
	SDR-M1	0.004	0.0059	0.0075	0.0101	0.0130
	SDR-M2	0.0049	0.0067	0.0083	0.0112	0.0145
	SDR-M3	0.0055	0.0072	0.0089	0.0120	0.0157
	SBET-M1	0.0037	0.0058	0.0074	0.0100	0.0129
	SBET-M2	0.0045	0.0064	0.0080	0.0108	0.0140
	SBET-M3	0.0050	0.0068	0.0084	0.0115	0.0149
m_{abs1}	OK-PSD-L	0.0030	0.0040	0.0051	0.0077	0.0108
	OK-w/o-PSD	0.0037	0.0054	0.0073	0.0113	0.0155
	Langmuir-M1	0.0098	0.0093	0.0106	0.0139	0.0175
	Langmuir-M2	0.0061	0.0088	0.0114	0.0175	0.0240
	Langmuir-M3	0.0094	0.0122	0.0149	0.0214	0.0287
	SDR-M1	0.0081	0.0081	0.0096	0.0131	0.0167

	SDR-M2	0.0061	0.0088	0.0114	0.0175	0.0241
	SDR-M3	0.0094	0.0123	0.0149	0.0214	0.0287
	SBET-M1	0.0083	0.0080	0.0094	0.0126	0.0162
	SBET-M2	0.0062	0.0091	0.0117	0.0179	0.0248
	SBET-M3	0.0096	0.0124	0.0153	0.0222	0.0300
m_{abs2}	OK-PSD-L	0.0027	0.0028	0.0030	0.0036	0.0045
	OK-w/o-PSD	0.0101	0.0168	0.0241	0.0384	0.0533
m_{abs}	OK-PSD-L	0.0043	0.0054	0.0066	0.0093	0.0127
	OK-w/o-PSD	0.0120	0.0199	0.0283	0.0444	0.0615

We also compare the performance of different models in the prediction of the 1st layer absolute adsorption in each adsorption type as shown in **Figure 6-8(a)**. The RMSDs in each adsorption type are given in Eq. (A6.20). The ratio of SSA in the specific adsorption type to the total SSA is applied to quantitatively compare the RMSDs in each adsorption type, assuming that the adsorption capacity is proportional to the homogeneous surface adsorption site as well as surface area. It should be noted that in OK-PSD-L model the characterized absolute adsorption in **Type I** only account for one layer between two pore surfaces, while in other models the considered adsorption layers are counted as from a single surface. The M1 methods of Langmuir, SDR and SBET model cannot capture the

behavior in different types, especially in micropore range where the densities of 2nd layer in **Type III** and **Type IV** are obviously higher than the bulk density, and the unique behavior in **Type I** where only one molecular layer exist in pore space. On the other hand, OK-w/o-PSD model cannot describe different adsorption phenomenon as in **Type I** and **Type II**. The comparison of RMSDs in terms of adsorption type from two OK models in m_{abs1}, m_{abs2} and m_{abs} are shown in **Figure 6-8 (b)-(d)**, where the increase of micPV leads to larger deviations. Even OK-PSD-L model show a larger deviation in **Type I** comparing with other adsorption types probably due to the inconsistency of adsorption layer width between OK model and GCMC simulation. A significant error of m_{abs2} in OK-w/o-PSD model can be found in **Figure 6-8 (c)** especially for **Type I-III**, while **Type IV-VI** show less deviations. In addition, we compare the prediction of m_{abs2} in terms of pressures from two OK models in **Figure 6-9**. OK-w/o-PSD model presents large deviations which increase with pressures, and the RMSD can be even more than 10 folds of that from the OK-PSD-L model at $P = 500$ bar. The densities of 2nd adsorption layer in transition zone in mesopores continuously increase with pressures as shown in our previous study[15], and those filled in micropores have even larger densities, indicating the importance of considering PSD for different adsorption mechanisms. In contrast, RMSD in m_{abs2} from the OK-PSD-L model is less sensitive to pressure. Thus, the OK-PSD-L model generally outperforms these popular models widely used to obtain m_{abs} from m_{ex}.
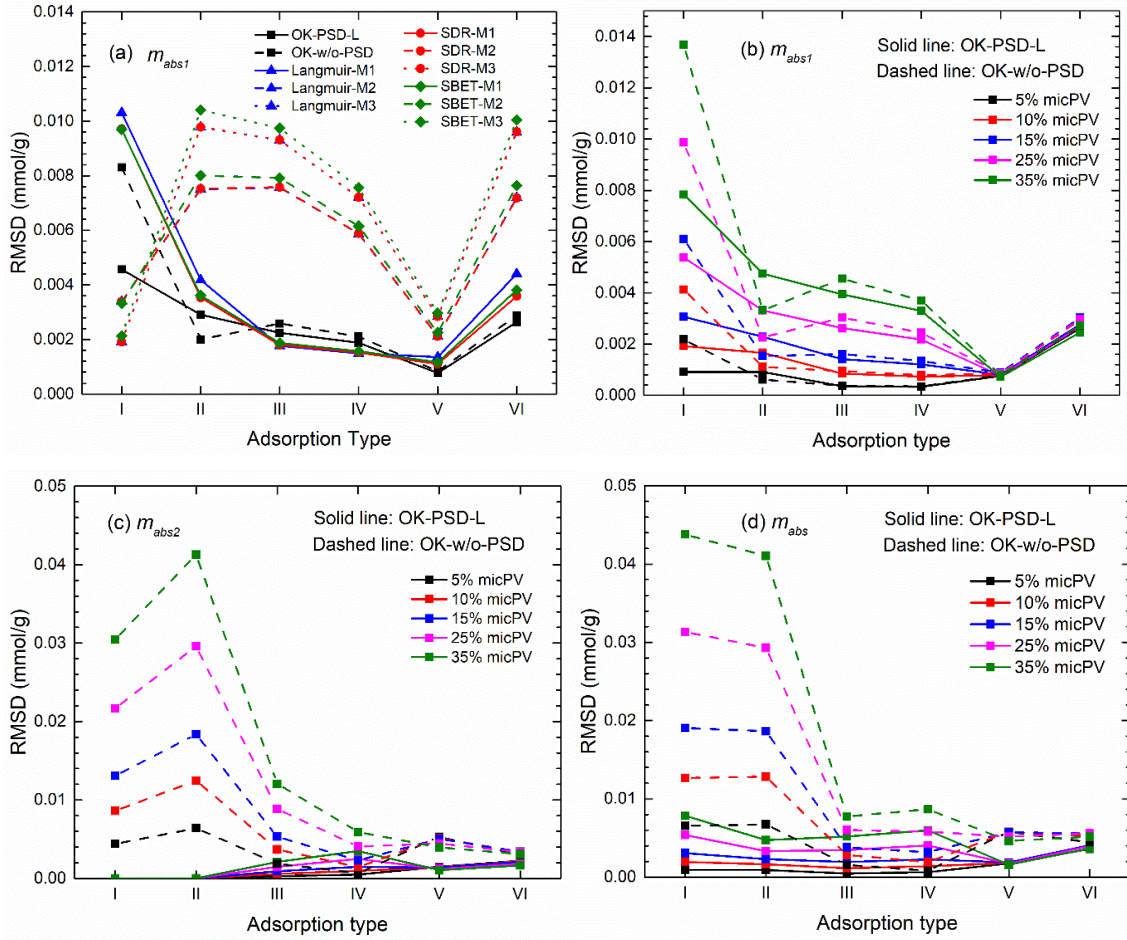
Figure 6-8 Comparison between RMSDs of absolute adsorption amount of OK-PSD-L model, Langmuir model, SDR model, SBET model and OK-w/o-PSD model with GCMC simulations for 1250 PSD samples at 333.15 K.
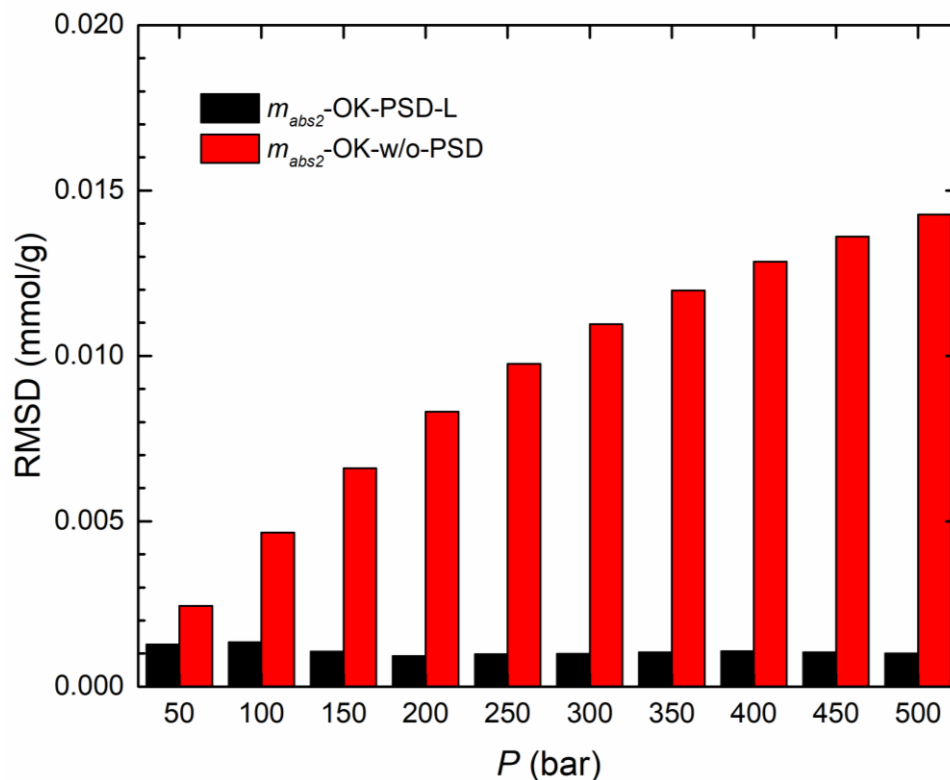
Figure 6-9 Comparison between RMSDs in the 2nd layer absolute adsorption amount from OK-PSD-L model and OK-w/o-PSD model with GCMC simulations at different pressures for 1250 PSD samples at 333.15 K.

6.4 Conclusions

In this work, GCMC simulations are used to investigate CH_4 adsorption in various kerogen nanopores at pressures up to 500 bar. The excess adsorption in each pore is obtained by the volumetric method, and the different adsorption behaviors in kerogen nanoporous media are studied. Based on GCMC simulations, we characterize different adsorption types in terms of pore sizes. The non-monotonic behavior of excess adsorption versus pore size is observed in micropores. However, the excess adsorption becomes independent of pore size, when $W_i \geq 2.5$ nm. The new adsorption model consisting of six different adsorption types

are proposed based on the density profiles obtained from the GCMC simulations. Coupling the adsorption types from the GCMC simulations, the OK-PSD-L model can reliably predict the excess adsorption and absolute adsorption in 1250 randomly generated kerogen nanoporous media. In contrast to the GCMC simulations, the OK-PSD-L model can significantly reduce the calculation time. On the other hand, the Langmuir, SDR and SBET models with fixed density and OK-w/o-PSD model are used to regress the excess adsorption in kerogen nanoporou media. The first three methods (Langmuir, SDR and SBET models) using the adsorbed phase density as one of fitting parameters perform better than those with a fixed density (373 kg/m^3 or 424 kg/m^3). However, the proposed OK-PSD-L model outperforms these models. As the performance of the OK-PSD-L model has been calibrated by comparing to the GCMC simulations in 1250 randomly generated kerogen nanoporous media the experimentally measured excess adsorption to obtain the absolute adsorption in kerogen.

In addition, it has been reported that clay minerals in transitional shales can have a high specific surface area[43] and gas adsorption in clay can significantly contribute to adsorbed gas capacity[81]. Due to different CH$_4$ adsorption behaviors in organic[156] and inorganic[51] matters, it is necessary to take into account the rock heterogeneity in CH$_4$ absolute adsorption characterization in shale nanoporous media.

Acknowledgement

Nomenclature

c energy parameter related to adsorption heat in SBET model

D interaction constant in SDR model

i type of pore that has different pore width

j specific adsorption type

k adsorption layer

m_{abs} absolute adsorption amount per surface area, mmol/m^2

$m_{abs1,i}^{MC}$, $m_{abs2,i}^{MC}$, $m_{abs,i}^{MC}$ absolute adsorption amount per surface area in 1st, 2nd and combined adsorption layer of pore i obtained in GCMC simulation, mmol/m^2

$m_{abs1,j}^{OK-PSD-L}$, $m_{abs2,j}^{OK-PSD-L}$ absolute adsorption amount per surface area in the 1st and weak adsorption layer of adsorption type j obtained in OK-PSD-L model, mmol/m^2

$m_{abs1,T}^{MC}$, $m_{abs2,T}^{MC}$, $m_{abs,T}^{MC}$ absolute adsorption amount per surface area in 1st, weak and combined adsorption layer of porous media obtained in GCMC simulation, mmol/m^2

$m_{abs1,T}^{OK-PSD-L}$, $m_{abs2,T}^{OK-PSD-L}$, $m_{abs,T}^{OK-PSD-L}$ absolute adsorption amount per surface area in the 1st, weak and combined adsorption layer of adsorption type j obtained in OK-PSD-L model, mmol/m^2

$m_{abs1}^{OK-w/o-PSD}$, $m_{abs2}^{OK-w/o-PSD}$, $m_{abs}^{OK-w/o-PSD}$ absolute adsorption amount per surface area in the

1st, weak and combined adsorption layer of adsorption type j obtained in OK-w/o-PSD

model, mmol/m^2

m_{abs}^{LA}, m_{abs}^{SDR}, m_{abs}^{SBET} absolute adsorption amount in Langmuir, SDR and SBET model,

respectively, mmol/g

m_{ex} excess adsorption amount per surface area, mmol/m^2

m_{ex}^{LA}, m_{ex}^{SDR}, m_{ex}^{SBET} excess adsorption amount in Langmuir, SDR and SBET model,

respectively, mmol/g

$m_{ex,i}^{MC}$ excess adsorption amount per surface area of pore i obtained in GCMC simulation,

mmol/m^2

$m_{ex,j}^{OK-PSD-L}$ excess adsorption amount per surface area of adsorption type j obtained in

OK-PSD-L model, mmol/m^2

$m_{ex,T}^{MC}$ excess adsorption amount per surface area in porous media obtained in GCMC

simulation, mmol/m^2

$m_{ex,T}^{OK-PSD-L}$ excess adsorption amount per surface area in porous media obtained in OK-

PSD-L model, mmol/m^2

$m_{max,LA}$, $m_{max,SDR}$, $m_{max,SBET}$ maximum adsorption capacity in Langmuir, SDR and SBET

model, respectively, mmol/g

MRE mean relative deviation, mmol/g

N_A Avogadro constant

n_{BET} number of adsorption layers in SBET model

$\left\langle N_{C_1,i} \right\rangle$ ensemble averaged number of CH$_4$ molecules in pore i

n_j number of layers in adsorption type j

μ chemical potential of methane

P pressure, bar

P_L Langmuir pressure that represents the pressure at which the adsorbed amount reaches

the half of the maximum adsorption capacity, bar

p proportion of micropore volume to the total pore volume, %

$R_{i-micro}$, R_{i-meso} random number between 0 to 1 of pore i in micropore and mesopore

range, respectively

RMSD root mean square deviation, mmol/g

ρ_a adsorbed phase density, kg/m^3

$\rho_{a1,i}^{MC}$, $\rho_{a2,i}^{MC}$, $\rho_{a3,i}^{MC}$ adsorbed phase density in the 1st, 2nd and 3rd adsorption layer of pore i

obtained in GCMC simulation, respectively, kg/m^3

$\rho_{a1,j}^{OK}$, $\rho_{a2,j}^{OK}$, $\rho_{a3,j}^{OK}$ adsorbed density in the 1st, 2nd and 3rd adsorption layer of adsorption type

j characterized in OK-PSD-L model, respectively, kg/m^3

$\rho_{a,k,j}$ adsorbed density of layer k in adsorption type j , kg/m^3

$\rho_{a,LA}$, $\rho_{a,SDR}$, $\rho_{a,SBET}$ adsorbed phase density in Langmuir, SDR and SBET model,

respectively, kg/m^3

$\rho_{am}^{OK-PSD-L}$ maximum adsorbed density in each layer in OK-PSD-L model, kg/m^3

$\rho_{am}^{OK-w/o-PSD}$ maximum adsorbed density in each layer in OK-w/o-PSD, kg/m^3

ρ_b CH$_4$ bulk density, kg/m^3

$\rho_{C_1,b}^m$ CH$_4$ bulk molar density, mol/m^3

S_a surface area of carbon slit, nm^2

SSA_i specific surface area of pore i, m^2/g

T temperature, K

σ_f LJ diameter, nm

$V_{i-micro}$, V_{i-meso} volume of micropore and mesopore, respectively, cm^3/g

$V_{p,i}$ effective pore volume of pore i, nm^3

$V_{s,i}$ incremental pore volume of pore i, cm^3/g

V_T total pore volume of micropore and mesopore, respectively, cm^3/g

W_a constant adsorption layer width of 0.38 nm applied in OK models (OK-PSD-L model and OK-w/o-PSD model)

W_i the separation distance of pore i, nm

$W_{p,i}$ effective pore width of pore i, nm

$W_{a1,i}^{MC}$, $W_{a2,i}^{MC}$, $W_{a3,i}^{MC}$ width of the 1st, 2nd and 3rd adsorption layer of pore i obtained in GCMC simulation, respectively, nm

$w_{mic,i}$, $w_{mes,i}$, weight percent of the volume of pore i to the micropore and mesopore volume, respectively.

x_b occupation fraction of bulk phase

$x_{k,j}$ occupation fraction of adsorbed phase in layer k in adsorption type j

$z_{AB,i}$ separation distance in terms of effective pore width and local minima between 1st and 2nd adsorption layer, nm

$z_{BC,i}$ separation distance in terms of local minima between 1st and 2nd adsorption layer and local minima between 2nd layer and free gas zone, nm

$z_{CC',i}$ separation distance of local minima between 2nd layer and free gas zone of each surface, nm

CHAPTER 7 ABSOLUTE ADSORPTON OF METHANE IN SHALE NANOPOROUS MEDIA: CHALLENGES ARISING FROM DUAL-HETEROGENEITIES

A version of this chapter will be submitted to *Energy & Fuels*.

Abstract

The knowledge and understanding of shale gas adsorption capacity is important for gas-in-place (GIP) evaluation in shale formation as well as well productivity. Previous findings from molecular simulation have shown that the adsorption behavior of methane is influenced by pressure, temperature, and the mechanism of adsorption is also dependent on pore size distribution (PSD). Moreover, despite the relative higher adsorption capacity of methane adsorption in organic pores, it is revealed by experimental work that clay minerals would have obviously positive contribution on specific surface area (SSA) as well as methane adsorption amount. Adsorption models in previous observations mostly focus on applying on shale sample as a whole or focus on single type of heterogeneity (adsorption potential varies in pore size or generalized dual sites), leading to the lack of application of separating, evaluating and predicting the adsorption amount by different compositions. Considering the effect of both PSD and rock compositions on accurately obtaining the absolute adsorption from excess adsorption in shale nanopores, the Ono-Kondo dual-heterogeneity (OK-DH) lattice model is proposed according to various pore size distributions contributed by different rock compositions and is calculated based on the amounts of methane adsorbed by various rock compositions in different ranged pore sizes and characterization from molecular simulations. The grand canonical Monte Carlo (GCMC) simulation of methane in carbon and illite slit-like nanopores are performed under 333.15 K and various pressures to represent methane adsorption in organic and inorganic

matters, respectively. The adsorption of methane is divided into different types for organic and inorganic nanopores, on the basis of density profiles of different pore widths from GCMC simulation so that the corresponding adsorption models can be utilized in the OK-DH model. Considering the influence of enhanced adsorption in micropores and adsorption potential difference in organic and inorganic matters, 19200 sets of artificial PSDs regarding 6 types of different micropore volume ratios are generated with finely defined pore sizes ranging from 0.7 nm to 50 nm for validating the applicability of OK model. By regressing the total excess adsorption isotherm obtained by GCMC simulations considering PSD effect and contributions by organic and inorganic nanopores, OK-DH model coupled with new adsorption models is in good agreement with absolute adsorption amount that obtained from GCMC simulation. We find that the predictions of both separated absolute amount in terms of specific compositions and total adsorption amount in porous media agree very well with molecular simulations. Comparing with other thermodynamic models with single or no heterogeneity such as Langmuir, Dubinin-type, BET-type, Toth, Langmuir-Freundlich and OK single rock model with PSD lumping, the OK-DH model show the best performance in describing adsorption phenomena. Our work shows the potential of applying OK model for predicting the excess and absolute adsorption amount in shale nanoporous media contributed by various rock compositions and should provide important insights into evaluation of gas-in-place in shale reservoir.

Keywords: Methane adsorption; Dual-heterogeneity; PSD; Rock type; Absolute

adsorption; Excess adsorption.

7.1 Introduction

Shale/tight gas exploitation plays an important role to meet the ever-growing global energy demand and reach the net-zero carbon emission[212, 213]. Shale gas has a lower carbon footprint than coal, with its global reserve over 7299 trillion cubic feet[214, 215]. Shale has an extensive amount of nanoscale pores as small as sub-1 nm[5, 216], leading to extremely-low porosity and permeability. Shale gas generally consists of free gas existing in mesopores, macropores or fractures; adsorbed gas which fills pore throats or adsorbed on the pore surface due to strong fluid-surface interaction; absorbed gas which is dissolved within shale matrix[213, 217]. The adsorbed gas can be up to 85% of the total shale gas content[141]. Therefore, the accurate characterization of adsorbed gas amount is crucial to the gas-in-place (GIP) and well productivity estimations, which are imperative to the economic viability of shale reservoirs[213].

While there have been a number of experimental measurements on CH_4 adsorption in shale samples using either the gravimetric[64, 218, 219] or volumetric method[172, 220, 221], the adsorption isotherms often refer to the excess adsorption m_{ex} [222]. The absolute adsorption m_{abs} which represents the total adsorbed gas amount needs to be converted from m_{ex} [148, 223]. Based on the single-layer adsorption assumption, a number of models have been applied to convert the experimentally measured m_{ex} to obtain m_{abs},

such as Langmuir model[224-226] and supercritical Dubinin–Radushkevich (SDR) model[182, 184, 186]. In our most recent review work[213], we have systematically and critically reviewed various conversion methods and discussed their working mechanisms as well as limitations. Nevertheless, molecular simulation works have shown that CH_4 adsorption in carbon[156] and clay mesopores[51] may render a multi-layer adsorption behavior. Therefore, the commonly applied single-layer adsorption model may become inapplicable to convert the experimentally measured m_{ex} to obtain m_{abs}.

In addition, shale rocks have a broad pore size distribution (PSD), ranging from sub-1 nm to a few micrometers[5, 216]. By using molecular simulation, Mosher *et al.*[67] have shown that CH_4 adsorption in micropores and small mesopores can have layering structures due to the strong fluid-surface interactions, while in large mesopores CH_4 density in the middle of the pores can regress to the free gas density. Shao et al.[227] applied GCMC simulation of methane adsorption in slit-like carbonaceous material activated carbon fiber (ACF) with PSD, and the simulated capacity is in agreement with experimental results. Li *et al.*[228] proposed the modified Langmuir model of methane adsorption in shale nanoporous media considering adsorption energy distribution from PSD effect. Recently, we have characterized different CH_4 adsorption models in various organic micropores and mesopores by using grand canonical Monte Carlo (GCMC) simulations[75, 229]. We also built a model kerogen nanoporous media with a continuous PSD ranging from 0.7 nm to 50 nm to study CH_4 adsorption behaviors[52]. The m_{ex} obtained by GCMC simulations

is converted to m_{abs} by the Ono-Kondo (OK) model considering various CH4 adsorption models, which shows an excellent agreement with GCMC simulations.

On the other hand, shale consists of organic and inorganic matters[5] (the so-called rock heterogeneity[213]). The organic matter mainly consists of kerogen, while inorganic matter consists of clay minerals (e.g. illite, kaolinite, and chlorite) and non-clay minerals (e.g. quartz, feldspar, and carbonate)[5, 230]. As shown in the previous works[165, 180], the positive correlation of CH4 adsorption uptake and total organic carbon (TOC) indicates that CH4 adsorption capacity is highly related to the organic matter content[22, 172]. On the other hand, experimental studies have shown that clay minerals can significantly contribute to adsorbed gas capacity[231], and the methane adsorption capacity substantially increases with the clay content especially in low TOC shales[46, 232, 233]. Molecular simulation works also reported that CH4 adsorption in clay nanopores is lower than that in organic nanopore, indicating a weaker fluid-surface affinity[6, 51]. Therefore, it is imperative to take into account both the rock heterogeneity and PSD in the conversion of experimentally measured m_{ex} to obtain m_{abs} [213].

In terms of works regarding methane adsorption modelling taking into account the rock heterogeneity, Wu *et al.*[23] proposed a modified simplified local density (SLD) model to regress CH4 m_{ex} by considering rock type distributions in certain pore ranges. The adsorption amount in their study consists of those from organic micropores, inorganic micropores and inorganic mesopores. The total adsorption amount is divided into three

parts utilizing their specific averaged pore widths instead of the explicitly continuous PSD. Recently, Chen *et al.*[234] proposed the correlations regarding pore size distributions contributed by various components (PSDCVC) and the amounts of methane adsorbed by various components (AMAVC). In their method, both the information of shale rock pore structure (such as pore volume) and methane adsorption amount are contributed by pore space located in organic and inorganic matters, and thus the expressions can be linked to the weight percent of each compositions. However, although the predicted pore volume and adsorption amount of each component from PSDCVC and AMAVC are in good agreement with experimental measurements, the calculated methane densities in certain ranged pores mainly depend on the equation of mass balance, resulting a very thin adsorption layer thickness in macropores at intermediate pressures (e.g. calculated adsorbed methane layer thickness in 100-200 nm pore at 100 bar can be less than 0.3 nm, while the methane LJ diameter is around 0.38 nm[137, 235]).

In this work, we build model shale nanoporous media consisting of organic and inorganic matters with realistic PSDs to study CH_4 adsorption behaviors by using GCMC simulations. For simplicity, we use carbon nanopores to represent the organic matter, while using illite nanopores to represent the inorganic matter. Lu *et al.*[97] mentioned the illite might be the factor to be responsible for the significant methane storage in low TOC (less than 1%) shale samples. Holmes et al.[236] mixed carbon and illite powder to synthesis idealized shale rock for discovering the impact arising from rock compositions, and they

found the positive linear relationship between shale gas capacity and TOC, while the reduced capacity is found when clay content is lower. Therefore, we propose an OK dual-heterogeneity (OK-DH) model for describing adsorption behaviors contributed by organic and inorganic nanopores, with fluid-surface interactions of methane-organic pores and methane-clay pores are explicitly constructed, and the fluid-fluid interactions keep uniform in all types of pores. The total adsorption amount can be regarded as a collection of adsorption amount in different sized and different types of slit-shaped nanopores. For characterizing the adsorption behavior in inorganic pores, slit-shaped illite model is used in this work as it is the one of the most common clay minerals and abundant in shale[237, 238]. By coupling GCMC simulations and varying PSDs in organic and inorganic pores, we effectively model methane adsorption in nanoporous media. Wide range of micropore volume ratios and possible distributions of organic and inorganic in micropore and mesopore range are randomly generated with 19200 sets of PSDs in total for model validation. We compare the proposed OK-DH model with other widely applied models (Langmuir, Dubinin-type, BET-type, OK model, etc.) without consideration of any heterogeneities, and unsurprisingly find the excellent agreement of OK-DH model with GCMC simulation not only in total adsorption amount, but also agrees the single adsorption amount contributed by each composition. In addition, we found that performance of Langmuir dual site model considering rock type heterogeneity and surface areas is evaluated to have a good prediction of absolute adsorption, which shows the potential for

effectively application. Our work should provide important insights into the predictions of adsorption capacity by different shale compositions and the accurate estimation of GIP in shale.

The remainder of this paper is organized as follows. In **Section 7.2**, we investigate the adsorption behavior and characterize adsorption models of illite nanopores according to density profiles from molecular simulation. In **Section 7.3**, we explain the generation of nanoporous samples. In **Section 7.4**, we introduce the OK-DH model to link adsorption amount from each composition to total porous media and describe the proposed OK-DH model in varying sized organic and inorganic nanopores. In **Section 7.5**, we firstly evaluate OK-DH model by lumping PSD into the proposed adsorption types which are characterized as six adsorption types and five adsorption types in organic and inorganic matters, respectively. The OK-DH model is applied to regress total m_{ex} in 19200 sets of independent nanoporous media samples which ensure distinct PSDs (as well as specific surface areas (SSAs) and pore volumes), and compare m_{abs} of total and separated amount by compositions with GCMC simulations. Then, the assessment of classical thermodynamic models with no heterogeneity and dual energy sites are made to compare converted absolute adsorption amount. In **Section 7.6**, we summarize key findings and conclusions.

7.2 Observation and Characterization of Methane Adsorption in Organic and Inorganic Nanopores from GCMC simulation

7.2.1 Molecular model and adsorption amount from GCMC simulation

In this work, methane adsorption in carbon and illite nanopores are performed in GCMC simulation to represent organic and inorganic matters, respectively. As for organic materials, graphene slabs are adopted to model kerogen slit nanopores for simplicity, and the details about description of substrates and force fields can be found through our recent work[239]. Since illite has been reported to be abundant in shale samples from experiments, it is selected to represent typical inorganic matter in molecular simulation. The illite is a type of 2:1 clay which consists of two Si-O tetrahedral layers and one Al-O octahedral layer, and it is modeled based on its unit cell formula of $Si_2AlO_5(OH)$ in which the corresponding coordinates can be found from X-ray diffraction (XRD) of Pyrophyllite-1Tc powder. A single illite surface is obtained by replicating the unit cell by 8*4*1 in x, y and z direction, respectively. For every four-unit cells (40 atoms), one Si^{4+} in tetrahedral sheet is substituted by Al^{3+} to form negative charge in clay minerals, where K^+ ions in pore space are used to neutralize the whole system. Therefore, illite nanopores can be constructed by fixing two illite surfaces of pore i with designed pore width W_i, which is the distance between oxygen atoms in the two inner Si-O tetrahedral layers of different surfaces. The schematic representation of illite nanopore structure is shown in **Figure F1**. In order to characterize inorganic adsorption patterns in continuous pore widths and to be

consistent with the previous work of carbon nanopores[239], we perform series of W_i ranging from micropore to mesopores, specifically, spanning 0.7, 0.8, 0.9, 1.0, 1.1, 1.2, 1.3, 1.4, 1.5, 1.6, 1.7, 1.8, 1.9, 2.0, 2.1, 2.2, 2.3, 2.4, 2.5, 4.0, 6.0, 8.0 and 10.0 nm.

TraPPE model and 10-4-3 Steele potential are used to represent CH_4 molecules and fluid-surface interaction in graphene slit pores, respectively, and can be referred to previous work. CLAYYFF forcefield is selected to describe fluid interactions in illite nanopore, which has been applied in many works. The parameters of unit cell, schematic representation of K-illite nanopores and force field parameters can be found elsewhere in Zhang *et al.*'s work[6]. We perform GCMC of methane in organic and inorganic nanopores at conditions of 333.15 K and various pressures from 100 bar to 500 bar. It should be noted that the details related to GCMC simulation including ways to obtain chemical potential, number of cycles for particle insertion, deletion and translation are reported in Pang and Jin[239], and we will not state specifically in this work.

7.2.2 Characterization of Methane Adsorption in Shale

Unlike the free gas whose amount can be estimated by conventional equation of state, the adsorbed gas distribution is inhomogeneous due to the competition of fluid-fluid interaction with fluid-surface interaction[206, 240]. The influence of confinement effect on CH_4 phase and adsorption behaviors in different nanopores have been reported in many works[158, 241-243]. In our recent work[239], the accommodation of methane adsorption

layers in different sized carbon nanopores has been studied through density distributions, and that can be clearly explained the effect of pore width on adsorption capacity. Similar effects of pore width on density distributions can be found in illite nanopores[244, 245]. In **Figure F2**, we show CH_4 density distributions in several illite nanopores at various pressures. Similar to the effect of confinement in organic pores, the highly packed CH_4 can be found in ultra-micropores (around 0.7 nm) and is easily saturated at relatively low pressures because of strong overlapping potential between adsorbate-adsorbent and limited pore space. As W_i increases, the available space increases to accommodate more CH_4 adsorption layers, leading to varying adsorption behaviors. When pore width approaches to mesopore ($W_i > 2$ nm), the free gas zone exists between two weak adsorption layers in the pore space. Based on the discussion in carbon nanopores, different adsorption type in inorganic pores in terms of pore width can be characterized. Referring to the density profiles of methane, the peak value of both 1st and 2nd layer in illite nanopores are smaller than those in carbon nanopores, showing relatively weaker fluid-surface interactions. Such weak interaction can also affect adsorption behaviors, for example in 2.0- 2.5 nm pores, the declining interactions between surface and fluid molecules located in the middle of the pore is much significant in illite than in carbon nanopores, leading to the occurrence of free gas phase when $W_i > 2$ nm. Moreover, as can be found from **Figure F2** that in the range of mesopore (2.0 nm to 10.0 nm), the peak value and widths of adsorbed phase are independent to the pore widths.

Therefore, based on the density profile of methane in illite, we characterize five typic types to describe methane adsorption in illite nanopores, as plotted in **Figure F3**. Following the characterization as discussed in our recent study in organic matters (see **Figure 7-1** in Pang and Jin[239]), each adsorption types in illite nanopores cover a certain pore range to classify each adsorption layer, and the density (marked as the height of each zone) of each adsorption layer as well as in free gas zone can be calculated by averaging over the defined width from methane density profile. The widths of each layer in illite nanopores are determined by high-pressure (500 bar) GCMC density distributions, which have been introduced in previous characterizations[24]. The total pore widths occupied by characterized adsorption types are obtained from injecting helium into pore space from GCMC simulation followed by experiments and are characterized as effective pore widths. The comparison of effective pore widths between carbon and illite is shown in **Figure F4**, and the less effective pore widths are discovered in illite nanopores because stronger fluid-surface interactions of helium atoms in carbon will lead to accumulation of helium atoms near the surface. Therefore, the corresponding pore width ranges for each type of adsorption in illite nanopores are classified as: **Type I**: 0.7-0.9 nm; **Type II**: 0.9-1.3 nm; **Type III**: 1.3-1.7 nm; **Type IV**: 1.7-2.0 nm; **Type V**: 2.0-50 nm. Due to different adsorption behaviors in carbon and illite nanopores, the adsorption types in carbon are classified as: **Type I**: 0.7-0.9 nm; **Type II**: 0.9-1.2 nm; **Type III**: 1.2-1.6 nm; **Type IV**: 1.6-2 nm; **Type V**: 2-2.5 nm; **Type VI**: 2.5-50 nm.

6.2.3 Comparison of Adsorption Amount in Organic and Inorganic Nanopores

Considering the dominant role of specific surface area in adsorption capacity, the excess adsorption amount of illite ($m_{ex,i,ilt}^{MC}$) per surface area (SA) in given pore width i is regarded as an effective quantity to link simulation to experiments. The $m_{ex,i,ilt}^{MC}$ can be calculated from GCMC simulation through volumetric method, where the expressions can be referred to description in previous work[24], and the calculated $m_{ex,i,ilt}^{MC}$ in various pore widths at 333.15 K and various pressures are shown in **Figure F5**. $m_{ex,i,ilt}^{MC}$ are observed to firstly increase with pressures than decrease from even small micropores, which is consistent with other investigations in simulations and experiments. Different from the non-monotonic behavior with pore size increases in organic pores, the excess adsorption amount in inorganic pores increases with pore width and become insensitive when $W_i > 2$ nm. Compares with excess adsorption of methane in carbon nanopores, the $m_{ex,i,car}^{MC}$ is generally found to be larger than $m_{ex,i,ilt}^{MC}$ in tested pore range because of the stronger fluid-surface interactions, and the range of excess adsorption amount in the tested pore size ranges at typical in-situ pressure (300 bar) are 0.0015- 0.0038 mmol/m^2 and 0.0006- 0.0016 mmol/m^2 in organic and inorganic pores, respectively.

Therefore, based on the characterized adsorption phase and type in illite, the absolute adsorption amount per SA (m_{abs}) of each pore i in different types can be obtained based on the adsorbed phase density and volume, and are given as:

$$\begin{cases}
\text{Type I:} & \begin{cases} m^{MC}_{abs1,i,ilt} = 0.5\rho^{MC}_{a1,i,ilt}W^{MC}_{a1,i,ilt} = 0.5\rho^{MC}_{a1,i,ilt}z_{AB,i,ilt} \\ m^{MC}_{abs2,i,ilt} = 0 \end{cases} \\[2mm]
\text{Type II:} & \begin{cases} m^{MC}_{abs1,i,ilt} = \rho^{MC}_{a1,i,ilt}W^{MC}_{a1,i,ilt} = \rho^{MC}_{a1,i,ilt}z_{AB,i,ilt} \\ m^{MC}_{abs2,i,ilt} = 0 \end{cases} \\[2mm]
\text{Type III:} & \begin{cases} m^{MC}_{abs1,i,ilt} = \rho^{MC}_{a1,i,ilt}W^{MC}_{a1,i,ilt} = \rho^{MC}_{a1,i,ilt}z_{AB,i,ilt} \\ m^{MC}_{abs2,i,ilt} = 0.5\rho^{MC}_{a2,i,ilt}W^{MC}_{a2,i,ilt} = 0.5\rho^{MC}_{a2,i,ilt}z_{BC,i,ilt} \end{cases} \\[2mm]
\text{Type IV:} & \begin{cases} m^{MC}_{abs1,i,ilt} = \rho^{MC}_{a1,i,ilt}W^{MC}_{a1,i,ilt} = \rho^{MC}_{a1,i,ilt}z_{AB,i,ilt} \\ m^{MC}_{abs2,i,ilt} = \rho^{MC}_{a2,i,ilt}W^{MC}_{a2,i,ilt} = \rho^{MC}_{a2,i,ilt}z_{BC,i,ilt} \end{cases} \\[2mm]
\text{Type V:} & \begin{cases} m^{MC}_{abs1,i,ilt} = \rho^{MC}_{a1,i,ilt}W^{MC}_{a1,i,ilt} = \rho^{MC}_{a1,i,ilt}z_{AB,i,ilt} \\ m^{MC}_{abs2,i,ilt} = \rho^{MC}_{a2,i,ilt}W^{MC}_{a2,i,ilt} = \rho^{MC}_{a2,i,ilt}z_{BC,i,ilt} \end{cases} \\[2mm]
m^{MC}_{abs,i,ilt} = m^{MC}_{abs1,i,ilt} + m^{MC}_{abs2,ilt}
\end{cases} \qquad (7.2)$$

where $m^{MC}_{abs1,i,ilt}$, $m^{MC}_{abs2,i,ilt}$ and $m^{MC}_{abs,i,ilt}$ describe m_{abs} per SA in the strong first adsorption layer, 2nd adsorption layer and combined layers of illite pore i, respectively; $\rho^{MC}_{a1,i,ilt}$ and $\rho^{MC}_{a2,i,ilt}$ represent the calculated averaged densities of 1st and 2nd layer of illite pore i from density profiles, respectively; $W^{MC}_{a1,i,ilt}$ and $W^{MC}_{a2,i,ilt}$ depict the widths of 1st and 2nd layer of pore i in illite nanopores, respectively.

We plot the $m^{MC}_{abs1,i,ilt}$ together with $m^{MC}_{abs2,i,ilt}$ of nanopores ranging from 0.7 nm to 4 nm in **Figure F6**. The general effect of pore size on absolute adsorption amount is similar to the discussion in organic nanopores: the fluid is easily saturated at relative low pressures in small micropores for $m^{MC}_{abs1,i,ilt}$, while $m^{MC}_{abs1,i,ilt}$ in lager pores and $m^{MC}_{abs2,i,ilt}$ become monotonically increase with pressures. It is found that the $m^{MC}_{abs1,i,ilt}$ become insensitive to the pore width when $W_i > 1.5$ nm, and $m^{MC}_{abs2,i,ilt}$ become insensitive to the pore width

when $W_i > 2$ nm. As a result, we believe the phenomenon of adsorbed phase obtained in the largest pore width (10 nm) performed in GCMC simulation can be used to represent pore width of $W_i > 10$ nm. Compared with $m_{abs1,i,car}^{MC}$ and $m_{abs2,i,car}^{MC}$ in carbon nanopores, one can find out the adsorption capacity in carbon nanopores is higher than that in illite nanopores, which have also been studied through simulation works and experiments. It should be noted that, both pore widths and rock compositions can affect adsorption amount significantly. For instance, the $m_{abs1,i}^{MC}$ which is considered as the primary adsorption amount range from 0.0045- 0.0075 mmol/m^2 and 0.0025-0.0065 mmol/m^2 in carbon and illite nanopores at 333.15 K and 300 bar, respectively.

By comparing with excess and absolute adsorption amount in illite and carbon nanopores, we can find: (i) the adsorption behavior is different in different sized nanopores, indicating the necessity of considering the effect of PSD; (ii) the adsorption capacity in organic nanopores is higher than that in inorganic matters, which have been discussed in either simulation work[6, 65] or experimental measurements[101]. We found that the maximum excess adsorption of carbon for methane is around 2.6 times larger than of illite for methane due to the stronger interactions between organic matter and methane molecules, indicating the different properties of confined fluids in different compositions; (iii) The contribution of weak adsorption layer in excess adsorption can be found in both organic and inorganic matters, which in turn affect the conversion to absolute adsorption.

7.2.4 Generation of Nanoporous Media Model Specified with Dual Heterogeneity

Adopted the previous approaches[239], the continuous PSD and different micropore volume ratios are applied to ensure a wide range of pore width and comprehensive distribution of micropores in shale nanoporous media. Generally, the total organic carbon (TOC) and clay content are two important factors to evaluate the properties of shale core samples from experiments[199, 238]. However, depending only on these two factors without obtaining the knowledge of specific pore size distribution for each component would not provide an important understanding of total adsorption analysis. In **Table F1**, we summarize and list the properties of several shale samples from different formations. It can be found that the TOC content is highly influenced by the depositional environment, and marine sediment usually possess higher TOC. In addition, the ratios of micropore and mesopore volume contributed by organic matter (OM) and clay differ in various cases: typically, a higher TOC content indicate higher ratios of shale micropore volume contributed by OM, however, the range of shale micropore volume contributed by OM can be from 8.4%- 63% for samples with similar TOC and clay content. Different scenarios are used to cover the distributions of micropore and mesopore contributed by different rocks as much as possible and thus the samples with potentially various TOC and clays can be built. In this work, the ratios of micropore and mesopore volume contributed by OM are θ_1 and θ_2, respectively, and are assumed to range from 20% to 80% with 20% as the interval. Therefore, the resulting micropore and mesopore volume contributed by clay are

$(1-\theta_1)$ and $(1-\theta_2)$, respectively, so that 16 different scenarios can be built according to the combinations and the denotations are listed in **Table F2**. For each scenario in specific micropore volume case, 200 sets of PSDs are randomly generated following the procedures: (a) four series of random number $R_{mic,i,ilt}$, $R_{mes,i,ilt}$, $R_{mic,i,car}$ and $R_{mes,i,car}$ are generated in the interval (0,1) for pore i in inorganic micropore, inorganic mesopore, organic micropore and organic mesopore, respectively. The weight percent of each pore volume in micropore and mesopore ranges can be expressed as $w_{mic,i} = R_{mic,i} / \sum_{i=0.7\,\mathrm{nm}}^{2\,\mathrm{nm}} R_{mic,i}$

and $w_{mes,i} = R_{mes,i} / \sum_{i>2\,\mathrm{nm}}^{50\,\mathrm{nm}} R_{mes,i}$, respectively, which ensure $\sum_{i=0.7\,\mathrm{nm}}^{2\,\mathrm{nm}} w_{mic,i} = 1$ and

$\sum_{i>2\,\mathrm{nm}}^{50\,\mathrm{nm}} w_{mes,i} = 1$; (b) based on the known properties of total specific pore volume ($V_{s,T} = 0.05$

cm^3/g), micPV, ratios of OM that contribute micropore and mesopore volume (θ_1 and θ_2, respectively), the incremental pore volume of pore i in in inorganic micropore, inorganic mesopore, organic micropore and organic mesopore range can be given as

$V_{s,i,ilt} = V_{s,T} \times w_{mic,i} \times micPV \times (1-\theta_1)$, $V_{s,i,ilt} = V_{s,T} \times w_{mes,i} \times (1-micPV) \times (1-\theta_2)$,

$V_{s,i,car} = V_{s,T} \times w_{mic,i} \times micPV \times \theta_1$ and $V_{s,i,car} = V_{s,T} \times w_{mes,i} \times (1-micPV) \times \theta_2$, respectively,

in the unit of cm^3/g. Therefore, the validation of our model is based on $200 \times 16 \times 6 = 19200$ samples in total, and the SSA of pore i in rock composition c can be derived from the incremental pore volume $V_{s,i,c}$ and W_i are given as $SSA_{i,c} = 2V_{s,i,c} / W_i$ by assuming slit geometry in nanoporous media, in the unit of m^2/g . The total SSA of shale nanoporous

media is given as $\sum\limits_{i=0.7nm}^{50nm}\sum\limits_{c=ilt}^{ilt,car} SSA_{i,c}$ for entire pore sizes and all types of tested rock

compositions. The percentage of the micropore SSA in the total SSA in randomly

generated PSD samples are shown in **Figure 7-1 (a)**. The resulting contribution of

micropore SSA to the total SSA ranges from 29% to 88% as micPV increases. We also

present example PSDs (in terms of incremental specific pore volume for each pore i) in

organic and inorganic matters with given micPV and different θ_1 and θ_2 in **Figure 7-1**

(b).

(a)   (b)
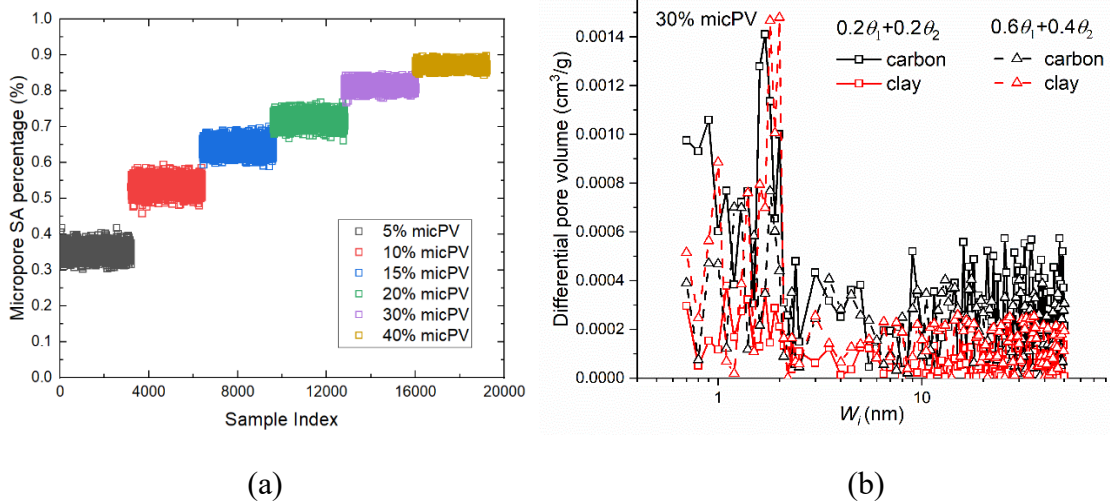
Figure 7-1 Generation of nanoporous media (a) distribution of micropore surface area percentage; (b) examples of PSD in 30% micropore volume case with different clay and carbon concentration.

As a result, the excess and absolute adsorption amount in shale nanoporous media in terms

of composition c in different pore ranges and total amount are given as,

$$\begin{cases} m_{ex,c,micro}^{MC} = \sum_{i=0.7nm}^{2nm} \dfrac{2V_{s,i,c}}{W_i} m_{ex,i,c}^{MC} \\[2ex] m_{ex,c,meso}^{MC} = \sum_{i>2nm}^{50nm} \dfrac{2V_{s,i,c}}{W_i} m_{ex,i,c}^{MC} \\[2ex] m_{ex,T}^{MC} = \sum_c m_{ex,c,micro}^{MC} + m_{ex,c,meso}^{MC} \end{cases} , \qquad (7.3)$$

$$\begin{cases} m_{abs1,c,micro}^{MC} = \sum_{i=0.7nm}^{2nm} \dfrac{2V_{s,i,c}}{W_i} m_{abs1,i,c}^{MC}; \; m_{abs1,c,meso}^{MC} = \sum_{i>2nm}^{50nm} \dfrac{2V_{s,i,c}}{W_i} m_{abs1,i,c}^{MC} \\[2ex] m_{abs2,c,micro}^{MC} = \sum_{i=0.7nm}^{2nm} \dfrac{2V_{s,i,c}}{W_i} m_{abs2,i,c}^{MC}; \; m_{abs2,c,meso}^{MC} = \sum_{i>2nm}^{50nm} \dfrac{2V_{s,i,c}}{W_i} m_{abs2,i,c}^{MC} \\[2ex] m_{abs1,c,T}^{MC} = m_{abs1,c,micro}^{MC} + m_{abs1,c,meso}^{MC}; \; m_{abs2,c,T}^{MC} = m_{abs2,c,micro}^{MC} + m_{abs2,c,meso}^{MC} \\[2ex] m_{abs,T}^{MC} = \sum_c m_{abs1,T}^{MC} + m_{abs2,T}^{MC} \end{cases} , \quad (7.4)$$

where $m_{ex,T}^{MC}$, $m_{abs1,T}^{MC}$, $m_{abs2,T}^{MC}$ and $m_{abs,T}^{MC}$ are the total excess adsorption, 1st layer and 2nd layer (weak adsorption layers) absolute adsorption amount, and combined absolute adsorption amount in shale nanoporous media contributed by different rock compositions in the unit of mmol/g; $m_{ex,c,micro}^{MC}$ and $m_{ex,c,meso}^{MC}$ represent the excess adsorption per SA in composition c in the unit of mmol/g, respectively; $m_{abs1,c,micro}^{MC}$ and $m_{abs2,c,micro}^{MC}$ represent the 1st layer and beyond the 1st layer (weak adsorption layers) absolute adsorption amount in micropores of composition c in the unit of mmol/g, respectively; $m_{abs1,c,meso}^{MC}$ and $m_{abs2,c,meso}^{MC}$ represent the 1st layer and beyond the 1st layer (weak adsorption layers) absolute adsorption amount in mesopores of composition c in the unit of mmol/g, respectively.

As these samples have equivalent total SPV, the different micPV and distribution of rock

compositions will significantly influence the resulting SSA and total adsorption amount. It can be observed from **Figure F7** that, the different scenarios regarding organic and inorganic matter distributions can also lead to different contributions by each rock composition in adsorption amount. Therefore, the importance of considering dual-heterogeneity (DH) can be concluded as much possible cases considering both pore size effect and rock compositions can be investigated.

7.3 OK-DH model in shale nanoporous media

Ono-Kondo lattice model was firstly proposed by Ono and Kondo[246], further developed by Donohue and his coworkers[247-249] and now have been applied for describing supercritical gas adsorption in petroleum and coal industry[58, 133]. We adopt a three-dimensional OK model with a simple cubic geometry and mean-field approximation which is similar to our previous works and the detailed derivation and general equations of OK model are given in previous literatures[156].

On the basis of the characterization of illite nanopores exhibited in **Figure F3** and carbon nanopores introduced in Pang and Jin[239], the OK models are divided into five and six types for illite and carbon nanopores, respectively. We divide the total adsorption as contributed by two basic compositions, carbon and illite, while different compositions are classified into different adsorption types. The general governing equations from **Type I** to **Type IV** are similar in both compositions, as stronger adsorption effect dominates in

micropores. The free gas zone occurs in **Type V** for illite and **Type VI** for carbon nanopores, and the density beyond 2nd adsorption layer is very close to bulk. The **Type V** for carbon represents a micropore to mesopore transition pore range, where the density in the 3rd adsorption layer is still higher than bulk density. It should be noted that (i) we assume three-layer structure OK model from each surface in **Type V** and **Type VI** for illite and carbon nanopores, respectively, as density beyond 2nd adsorption layer is close to bulk and is proved in our previous work for carbon nanopores; (ii) the occupation fraction ($x_{k,j,c}$) of adsorbed phase in each layer k in adsorption type j in composition c is given as $x_{k,j,c} = \rho_{a,k,j,c} / \rho_{am,c}$, where $\rho_{a,k,j,c}$ and $\rho_{am,c}$ represent the adsorbed phase density of component c in type j and layer k, and the maximum adsorbed layer density of component c, respectively. It should be noted that such occupation fraction can be different in same layer and same composition but with different type; (iii) the occupation fraction in different composition is different since two distinct energy parameters are applied to describe methane-carbon and methane-illite interactions; (iv) the mean-field theory has been applied in OK-DH model, with uniform ε to describe fluid-fluid interactions in all types of pores, and explicit energetic parameters of ε_{s-car} and ε_{s-ilt} to express fluid-surface interactions of methane with organic and inorganic matters, respectively. The general OK equations in nanoporous media of each adsorption layer in terms of various adsorption types can be referred to Pang and Jin[239].

As a result, the excess adsorption per SA in adsorption type j in composition c by

assuming the fixed adsorption layer width W_a as methane LJ diameter 0.38 nm is given as,

$$m_{ex,j,c}^{OK-DH} = \rho_{am,c} W_a \sum_{k=1}^{n_{k,c}} \left(x_{k,j,c} - x_{b,c} \right), \qquad (7.5)$$

where $n_{k,c}$ and $m_{ex,j,c}^{OK-DH}$ are the number of layers and excess adsorption amount per SA in adsorption type j in composition c, respectively; $x_{b,c}$ is the fraction of molecules in bulk phase, and is given as $x_{b,c} = \rho_b / \rho_{am,c}$. Therefore, total excess adsorption in composition c in nanoporous media ($m_{ex,T,c}$) obtained from OK model by considering PSD effect is given as,

$$\begin{cases} m_{ex,T,c}^{OK-DH} = \sum_{j=1}^{n_{j,c}} \sum_{i \in Typej} \frac{2V_{s,i,c}}{W_i} \left[\rho_{am,c}^{OK-DH} W_a \sum_{k=1}^{n_j} \left(x_{k,j,c} - x_{b,c} \right) \right] \\ m_{ex,T}^{OK-DH} = \sum_c m_{ex,T,c}^{OK-DH} \end{cases} \qquad (7.6)$$

where $n_{j,c}$ is the number of adsorption types in composition c, while $n_{j,car}$=6 and $n_{j,ilt}$ =5 for carbon and illite nanopores, respectively. In OK model, the effect of PSD in different adsorption type in carbon and illite nanopores is considered by the sum of the incremental pore volume in composition c divided by W_i of pore i which belong to Type j with PSD lumping in the proposed pore size range as listed in **section 7.3.1**. Therefore, m_{abs} per SSA of different adsorption layer ($m_{abs1,T,c}^{OK}$ and $m_{abs2,T,c}^{OK}$) and combined layer $m_{abs,T,c}^{OK}$ in composition c and Type j can be defined based on the adsorbed phase density and

volume from OK model, are given as,

$$
\begin{cases}
m_{abs1,j,c}^{OK-DH} = \begin{cases} 0.5\rho_{a1,j,c}^{OK-DH}W_a & (j=\text{Type I}) \\ \rho_{a1,j,c}^{OK-DH}W_a & (j \neq \text{Type I}) \end{cases} \\[2em]
m_{abs2,j,c}^{OK-DH} = \begin{cases} 0.5\rho_{a2,j,c}^{OK-DH}W_a & (j = \text{Type III}) \\ \rho_{a2,j,c}^{OK-DH}W_a & (\text{if } c=\text{ilt}, j = \text{Type IV,V};\\ & \text{if } c=\text{car}, j = \text{Type IV,VI}) \\ \rho_{a2,j,c}^{OK-DH}W_a + 0.5\rho_{a3,j,c}^{OK-DH}W_a & (\text{if } c=\text{car}, j = \text{Type V}) \end{cases}
\end{cases}
\tag{7.7}
$$

Therefore, by combining different rock compositions, the total absolute adsorption amount

in 1st layer, 2nd layer and combined layers are given as,

$$
\begin{cases}
m_{abs1,T}^{OK-DH} = \sum_c \sum_{j=1}^{n_{j,c}} \sum_{i\in\text{Type j}} \frac{2V_{s,i,c}}{W_i} m_{abs1,j,c}^{OK-PSD-L} \\[1.5em]
m_{abs2,T,c}^{OK-DH} = \sum_c \sum_{j=1}^{n_{j,c}} \sum_{i\in\text{Type j}} \frac{2V_{s,i,c}}{W_i} m_{abs2,j,c}^{OK-PSD-L} \\[1.5em]
m_{abs,T,c}^{OK-DH} = m_{abs1,T,c}^{OK-DH} + m_{abs2,T,c}^{OK-DH}
\end{cases}
\tag{7.8}
$$

There are five regression parameters in OK model, which are ρ_{am-car}, ρ_{am-ilt}, ε, ε_{s-car}

and ε_{s-ilt}. The constraints of specific parameters which have a broad range are followed as

our previous works[29]. In addition, considering the fact based on the investigate from

GCMC simulation that the adsorbed phase density and fluid-surface interaction in carbon

is higher than illite nanopores, we make additional constraints as follows: $\rho_{am-ilt} < \rho_{am-car}$

and $\varepsilon_{s,car} / k_B T < \varepsilon_{s,ilt} / k_B T < \varepsilon / k_B T < 0$. On the basis of obtaining Eq. (7.6) with total

excess adsorption in porous media and known pore size distributions of each composition

for each sample, non-linear equations in OK model can be solved by regressing total excess

adsorption in GCMC simulation. Therefore, the occupation fraction $x_{k,j,c}$ in each layer, type and composition are solved iteratively and the basic information regarding adsorption behavior can be known specifically.

7.4 Results and discussion

In this section, based on the absolute adsorption amount from GCMC simulation and properties of pore structure for each sample, we first compare the regression results obtained by proposed OK-DH model. Then, the performance of almost all widely used adsorption models with different adsorbed phase density or volume treatment and consideration of different adsorption sites are evaluated. The number of models assessed reaches 171 including Langmuir, SDR, improved D-A, BET model with pseudo-saturation pressure, supercritical BET, OK, Toth, Langmuir-Freundlich and direct conversion methods. We have shown the deviations of predicted absolute adsorption amount to GCMC results and models with superior performance have been selected as the recommendation for further application.

7.4.1 CH₄ adsorption behavior predicted from OK-DH model

The averaged regression parameters of OK model are shown in **Table 7-1** with varying micropore volume ratios. The regressed maximum adsorbed phase densities in carbon and clay nanopores are around 319.4 and 290.5 kg/m³, respectively, indicating the higher adsorption potential of supercritical methane in organic matter than inorganic matter. The

averaged regression variable of fluid-fluid interaction parameter over all evaluated

scenarios shows consistent behavior with increasing micropore volume ratios, indicating

the robustness of OK-DH model. However, with the increased amount of micropores, the

fluid-surface interaction in carbon become much significant, while the mean-field theory

(MFT) used in this study may become one of the limitations of describing adsorbate

behavior accurately in fine nanopores, and the mismatch of adsorbed phase layer in

micropores might also lead to such issue[75]. The number behind plus-minus sign presents

one standard error which indicate the uncertainty of OK-DH parameters, and the fractions

of standard deviation to the mean value in total evaluated samples are in acceptable range

from 3.58% to 14.7%. We present the comparison of the regression results obtained by OK

model with GCMC simulation in **Figure 7-2 (a)** of total excess adsorption in evaluated

samples, while **Figure F8** specifically shows excess adsorption in carbon and illite

nanopores, respectively. It can be found in that an excellent fitting quality of OK model in

predicting excess adsorption either in total nanoporous material or in contributions by

organic and inorganic matter. Additionally, **Figure 7-2 (b)** compares the adsorption

amount of both excess and absolute, organic and inorganic matters of one shale example

in the scenario with 20% micropore volume & separated clay content in organic and

inorganic matter of 0.2 θ_1+ 0.6 θ_2. Although slight deviations can be found in predictions

of m_{abs1} in organic pores at higher pressure, the performance of both excess and absolute

adsorption amount in total shale and 1st adsorption layer which dominates the adsorption

capacity are very well described by OK model. In **Table 7-2**, we show the minimum, maximum and averaged behavior of OK-DH model prediction in different adsorption layer, adsorption type and rock type in this specified range. It is shown that although general properties of total and micropore pore volume and clay content have specified, the pore size distributions of different rock type would make the broad range of absolute adsorption amount, and the results show good agreement of OK-DH model with GCMC results in prediction the detailed adsorption amount.

(a)   (b)
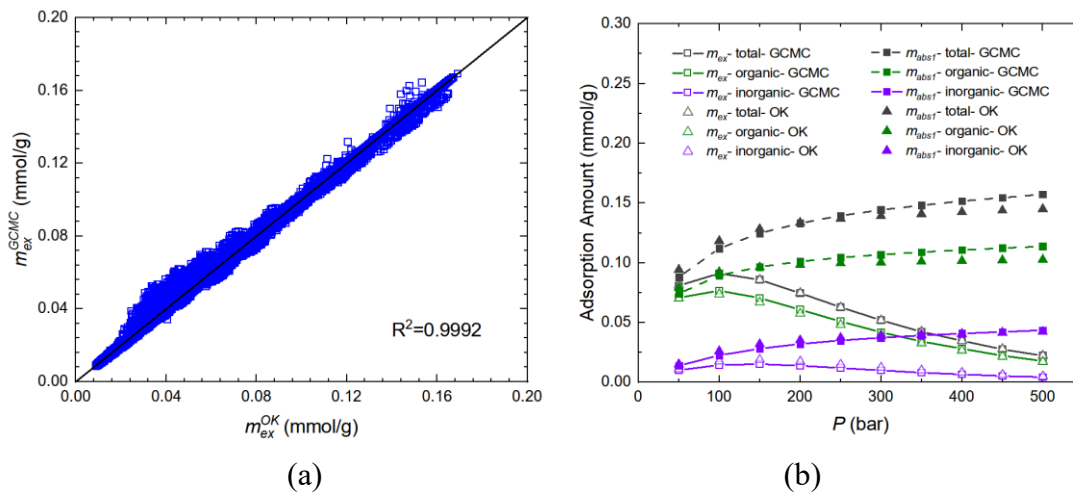
Figure 7-2 Regression of excess adsorption in (a) total behavior; and (b) excess adsorption in GCMC and predicted value from OK-DH model of case 20% micropore volume & separated clay content in organic and inorganic matter of 0.2 θ_1+ 0.6 θ_2.

Table 7-1 Averaged regressed parameters in different micropore volumes

	Parameters[1*]	Micropore pore volume (%)						Total[2*]
		5%	10%	15%	20%	30%	40%	
OK-DH model	$\rho_{am-organic,OK}$ (kg/m³)	323.93±7.66	319.58±9.79	318.13±10.40	318.10±11.65	318.00±12.29	318.78±14.49	319.42±11.44
	$\rho_{am-inorganic,OK}$ (kg/m³)	295.76±11.35	295.76±12.65	292.73±11.63	289.93±11.70	287.13±11.45	281.68±15.38	290.50±13.41
	$\varepsilon_{ff} / k_B T$	-0.37±0.05	-0.36±0.04	-0.36±0.04	-0.36±0.04	-0.37±0.05	-0.35±0.05	-0.36±0.05
	$\varepsilon_{of} / k_B T$	-2.27±0.21	-2.32±0.18	-2.35±0.18	-2.38±0.18	-2.44±0.18	-2.53±0.31	-2.38±0.23
	$\varepsilon_{if} / k_B T$	-0.99±0.07	-0.98±0.08	-0.97±0.11	-0.95±0.14	-0.91±0.18	-0.94±0.18	-0.95±0.14

Note:

[1*]: the plus-minus sign shows one standard deviaiton of regressed variable; [2*]: calculation over all evaluated samples in considered micropore volume ratios in nanoporous media.

Table 7-2 Predicted absolute adsorption from OK model compared with GCMC simulaiton in each layer in different adsorption type in organic and inorganic nanopores at 333.15 K and 300 bar of case 20% micropore volume & separated clay content in organic and inorganic matter of 0.2 θ_1+ 0.6 θ_2.

Rock Type	Adsorption Amount	Methods	Adsorption Type					
			Type I	Type II	Type III	Type IV	Type V	Type VI

Organic	m_{abs1} (mmol/g)	OK-DH	mean	0.0109	0.0308	0.0218	0.0170	0.0040	0.0137
			min	0.0001	0.0029	0.0025	0.0018	0.0009	0.0084
			max	0.0464	0.1037	0.0854	0.0540	0.0083	0.0193
		GCMC	mean	0.0144	0.0305	0.0234	0.0184	0.0043	0.0147
			min	0.0002	0.0027	0.0028	0.0019	0.0009	0.0092
			max	0.0623	0.1031	0.0886	0.0570	0.0089	0.0201
	m_{abs2} (mmol/g)	OK-DH	mean	-	-	0.0078	0.0116	0.0027	0.0092
			min	-	-	0.0009	0.0012	0.0005	0.0058
			max	-	-	0.0298	0.0363	0.0056	0.0126
		GCMC	mean	-	-	0.0088	0.0137	0.0032	0.0104
			min	-	-	0.0011	0.0013	0.0007	0.0065
			max	-	-	0.0310	0.0426	0.0065	0.0142
	m_{abs1} (mmol/g)	OK-DH	mean	0.0035	0.0059	0.0044	0.0018	0.0234	-
			min	0.0001	0.0005	0.0003	0.0001	0.0118	-
			max	0.0127	0.0200	0.0148	0.0076	0.0325	-
		GCMC	mean	0.0035	0.0057	0.0043	0.0017	0.0225	-
			min	0.0001	0.0004	0.0003	0.0001	0.0149	-

Inorganic	m_{abs2} (mmol/g)		max	0.0127	0.0198	0.0142	0.0071	0.0306	-
		OK-DH	mean	-	-	0.0018	0.0014	0.0179	-
			min	-	-	0.0001	0.0001	0.0116	-
			max	-	-	0.0059	0.0058	0.0243	-
		GCMC	mean	-	-	0.0019	0.0013	0.0202	-
			min	-	-	0.0001	0.0001	0.0134	-
			max	-	-	0.0064	0.0055	0.0275	-

Moreover, as to demonstrate the importance of considering dual heterogeneity, we calculate the root-mean-square deviation (RMSD) of m_{abs1} and m_{abs2} with different considerations in **Figure 7-3**. Four types of OK model have been compared: the OK multilayer model without considering PSD, the OK with single heterogeneity of PSD lumping and OK-DH model. It should be noted that since our shale nanoporous media contains two different rock types, the OK single heterogeneity model adopted two types of adsorption based on characterization in carbon and illite, respectively. The significant increase of accuracy in predicting m_{abs1} can be found in **Figure 7-3 (a)** when heterogeneity is considered in OK model, while the dual heterogeneity model has improved the most with the lowest RMSD of 0.006 mmol/g compared with single pore size heterogeneity models. The prediction of absolute adsorption in 2nd layer shows good improvement in **Figure 7-3 (b)** when considering single- and dual-heterogeneity, while less decrease in OK-DH model can be found. Considering the fact that the adsorption in 1st layer contributes the total adsorption potential, it is believed the OK-DH model can describe the absolute adsorption by constructing specific fluid-surface interactions and PSD lumping method.
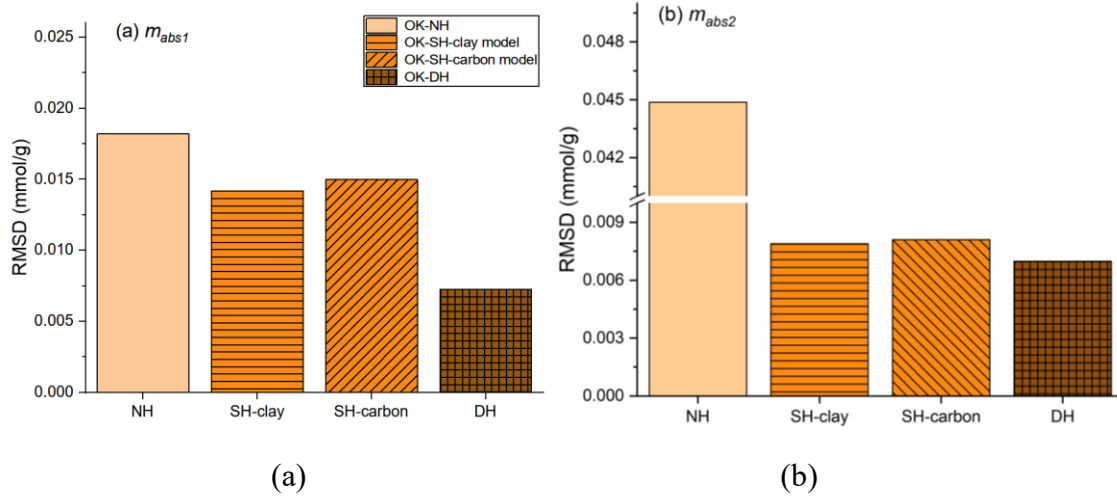
Figure 7-3 RMSD of applied four types OK models of no-heterogeneity, single-heterogeneity ultilizing PSD lumping via clay adsorption model, single-heterogeneity ultilizing PSD lumping via carbon adsorption model and dual-heterogeneity model in (a) m_{abs1} and (b) m_{abs2}.

7.4.2 Widely Applied Single Parameter Models

In experimental applications, macroscopic thermodynamic models have been used to calculate absolute adsorption from measured excess adsorption based on monolayer adsorption based on different mechanisms. The evaluation of these models on accurate prediction of kerogen porous media considering PSD effect have been reported in our previous works[75, 229]. Here, in order to assess the importance and performance of considering DH effect, we adopt these single-parameter models which regard the adsorption in shale sample as a whole system, thus none of heterogeneities and the simple dual site are considered on the basis of dual-site Langmuir (DSL) model[250].

7.4.2.1 Thermodynamic models and heterogeneities

7.4.2.1.1 Langmuir model

The original Langmuir model assumes gas adsorbed on flat homogeneous surface[209], which is given as,

$$\begin{cases} m_{abs}^{LA-NH} = m_{\max}^{LA-NH} \dfrac{P}{P_L^{LA-NH} + P} \\ m_{ex}^{LA-NH} = m_{\max}^{LA-NH} \dfrac{P}{P_L^{LA-NH} + P}\left(1 - \dfrac{\rho_b}{\rho_a^{LA-NH}}\right) \end{cases} \tag{7.9}$$

where m_{abs}^{LA-NH}, m_{ex}^{LA-NH} and $m_{\max}^{LA-NH}$ are absolute adsorption, excess adsorption and maximum adsorption capacity in the Langmuir model, mmol/g, respectively; P_L^{LA-NH} and $\rho_a^{LA-SH-\beta}$ are Langmuir pressures at which the adsorbed amount reaches the half of the maximum adsorption capacity and the adsorbed phase densities (kg/m^3) in the adsorption site.

Considering the nature of heterogeneities in shale nanoporous media, single heterogeneity Langmuir model has been widely used in regressing excess adsorption. Xu *et al.* [250] proposed a dual-site Langmuir (DSL) model to simplify the heterogeneous properties of shale and coal into two different adsorption sites with distinct adsorption energies and are weighted by a coefficient α. The constant adsorbed phase density for two different sites and an increasing adsorbed phase volume are assumed, while the fraction of one single adsorption site α is obtained from regressions. Different from their work that apply same pressure-independent density for two energy sites, we propose single-heterogeneity (SH)

model to classify the surface energy sites into two parts, of which the adsorption energies will be different, and the resulting surface coverage and adsorbed phase densities vary from one site to the other. In addition, two different types of single heterogeneities are considered in terms of pore sizes and rock distributions. Therefore, the modified equations of Langmuir-SH model (LA-SH) are given as,

$$m_{abs}^{LA-SH-\beta} = m_{\max}^{LA-SH-\beta} \cdot \left[\alpha_\beta \frac{P}{P_{L1}^{LA-SH-\beta} + P} + \left(1-\alpha_\beta\right) \frac{P}{P_{L2}^{LA-SH-\beta} + P} \right] \qquad (7.10)$$

where β is the type of heterogeneity in SH model that includes pore size heterogeneity and rock heterogeneity; $m_{abs}^{LA-SH-\beta}$, $m_{ex}^{LA-SH-\beta}$ and $m_{\max}^{LA-SH-\beta}$ are absolute adsorption, excess adsorption and maximum adsorption capacity in the Langmuir model, mmol/g, respectively; $P_{L1}^{LA-SH-\beta}$ and $P_{L2}^{LA-SH-\beta}$ are Langmuir pressures at which the adsorbed amount reaches the half of the maximum adsorption capacity in adsorption site 1 and 2, respectively; α_β is the weight parameter of heterogenous surface and is determined according to the ratio of surface area for each SH type to the total porous media, which is given as,

$$\begin{cases} \beta\text{=pore size heterogeneity, } \alpha_\beta = \sum_c \sum_{i=0.7nm}^{2nm} SSA_{i,c} / \sum_c \sum_{i=0.7nm}^{50nm} SSA_{i,c} \\ \beta\text{=rock heterogeneity, } \alpha_\beta = \sum_{i=0.7nm}^{50nm} SSA_{i,c} / \sum_c \sum_{i=0.7nm}^{50nm} SSA_{i,c} \end{cases} \qquad (7.11)$$

7.4.2.1.2 Supercritical Dubinin−Radushkevich (SDR) and improved Dubinin- Astakhov (iDA) model

Sakurus *et al.* [185] modified the original Dubinin−Radushkevich (DR) model which based

on pore filling theory for the application of supercritical gas adsorption in coal by replacing the ratio of saturation pressure to the pressure by the density of adsorbed phase to the bulk phase. The modified SDR model with no heterogeneity considered is give as,

$$\text{SDR-NH model: } m_{abs}^{SDR-NH} = m_{\max}^{SDR-NH} \exp\left\{-D\left[\ln\left(\frac{\rho_a^{SDR-NH}}{\rho_b}\right)\right]^2\right\} \tag{7.12}$$

where D is defined as the constant representing the affinity of adsorbate to the adsorbent that depends on the structural property of porous media. Similar as the Langmuir-SH model, the SDR model can be used to express system consists of two types of adsorption site with different adsorption energy and their fractions, which is given as,

$$\text{SDR-SH model: } m_{abs}^{SDR-SH-\beta} = m_{\max}^{SDR-SH-\beta}\left\{\alpha_\beta \exp\left\{-D_1\left[\ln\left(\frac{\rho_{a1}^{SDR-SH-\beta}}{\rho_b}\right)\right]^2\right\} + \left(1-\alpha_\beta\right)\exp\left\{-D_2\left[\ln\left(\frac{\rho_{a2}^{SDR-SH-\beta}}{\rho_b}\right)\right]^2\right\}\right\}$$

$$\tag{7.13}$$

The Dubinin-Astakhov (DA) model[251] is also based on Polanyi potential theory to express gas adsorption isotherm for subcritical condition. The pore structure properties have been taken into account by substituting the exponential as a variable, which can be given as,

$$m_{abs}^{DA-SH} = m_{\max}^{DA-SH} \exp\left\{-D\left[\ln\left(\frac{P}{P_0}\right)\right]^t\right\} \tag{7.14}$$

where P and P_0 are gas pressure and saturation pressure, respectively. In order to overcome the application under supercritical region, the improved DA (iDA) model[252] has been revised according to the empirical equation that describes the pseudo-saturation

pressure (P_s),

$$\text{iDA-NH model: } m_{abs}^{iDA-NH} = m_{max}^{iDA-NH} \exp\left\{-D\left[\ln\left(\frac{P_s}{P}\right)\right]^t\right\} \tag{7.15}$$

The expression of empirical pseudo- saturation vapor pressure will be introduced later in

section 7.4.2.1.3. Therefore, the single heterogeneity iDA (iDA-SH) model is expressed

as,

$$\text{iDA-SH model: } m_{abs}^{iDA-SH-\beta} = m_{max}^{iDA-SH-\beta}\left\{\alpha_\beta \exp\left\{-D_1\left[\ln\left(\frac{P_s}{P}\right)\right]^{t_1}\right\} + \left(1-\alpha_\beta\right)\exp\left\{-D_2\left[\ln\left(\frac{P_s}{P}\right)\right]^{t_2}\right\}\right\}$$

$$\tag{7.16}$$

7.4.2.1.3 BET based models

BET equation assumes an infinite number of adsorption layers on adsorbent at

saturation[210] to account for multilayer subcritical gas adsorption on homogeneous flat

surface, which is originally given as,

$$m_{abs}^{BET} = \frac{m_{max}^{BET} k_0 P / P_0}{1 - P / P_0}\left[\frac{1-\left(n+1\right)\left(P / P_0\right)^n + n\left(P / P_0\right)^{n+1}}{1+\left(k_0-1\right)P / P_0 - k_0\left(P / P_0\right)^{n+1}}\right], \tag{7.17}$$

where m_{abs}^{BET} and m_{max}^{BET} are adsorbed gas amount and maximum adsorption capacity in

BET model, respectively, k_0 reflects the energetic of adsorption in the system, P and P_0

are bulk pressure and saturation pressure of gas molecules. Yu *et al.*[133] used the pseudo-

saturation vapor pressure (P_s)[253] to replace the saturation pressure of subcritical

methane, which is given by the Antoine equation[254] in terms of temperature,

$$\ln P_s = 7.7437 - \frac{1306.5485}{19.4362 + T} \tag{7.18}$$

Such pseudo-saturation vapor pressure is also used in iDA model. Therefore, the BET-pseudo-saturation pressure (BETp) model without heterogeneity is given as,

$$\text{BETp-NH model: } m_{abs}^{BETp-NH} = \frac{m_{max}^{BETp-NH} k_0 P/P_s}{1-P/P_s}\left[\frac{1-(n+1)(P/P_s)^n + n(P/P_s)^{n+1}}{1+(k_0-1)P/P_s - k_0(P/P_s)^{n+1}}\right] \tag{7.19}$$

Similarly, the BET-p model considering two adsorption sites (BETp-SH) can then be expressed as,

$$\text{BETp-SH model: } m_{abs}^{BETp-SH-\beta} = m_{max}^{BETp-SH-\beta}\left[\begin{array}{c}\alpha_\beta \dfrac{c_1 P/P_s}{1-P/P_s}\dfrac{1-(n_{1,BETp}+1)(P/P_s)^{n_{1,BETp}} + n_{1,BETp}(P/P_s)^{n_{1,BETp}+1}}{1+(c_1-1)(P/P_s)-c_1(P/P_s)^{n_{1,BETp}+1}} \\[2mm] +(1-\alpha_\beta)\dfrac{c_2 P/P_s}{1-P/P_s}\dfrac{1-(n_{2,BETp}+1)(P/P_s)^{n_{2,BETp}} + n_{2,BET}(P/P_s)^{n_{2,BETp}+1}}{1+(c_2-1)(P/P_s)-c_1(P/P_s)^{n_{2,BETp}+1}}\end{array}\right]$$

$$\tag{7.20}$$

On the other hand, Zhou *et al*.[54] proposed a supercritical BET (SBET) model in terms of bulk density and adsorbed phase density, which is given as,

$$m_{abs}^{SBET} = \frac{m_{max}^{SBET} k_0 \rho_b/\rho_a^{SBET}}{1-\rho_b/\rho_a^{SBET}}\left[\frac{1-(n+1)(\rho_b/\rho_a^{SBET})^n + n(\rho_b/\rho_a^{SBET})^{n+1}}{1+(k_0-1)\rho_b/\rho_a^{SBET} - k_0(\rho_b/\rho_a^{SBET})^{n+1}}\right], \tag{7.21}$$

In their work, the fitting parameters include m_{max}^{SBET}, n, ρ_a^{SBET} and k_0, while the conversion is conducted under single-layer adsorption model. Xiong *et al*.[255] compared the performance of different adsorption models and found that the absolute adsorption obtained from SBET keeps increasing and is significantly higher than that predicted by the

Langmuir model. Moreover, the SBET based model with a constant adsorbed density is found to present negative adsorption at high pressures.

Similar as the above descriptions, the SBET model considering single heterogeneity can be given as,

SBET-SH model:
$$m_{abs}^{SBET-SH-\beta} = m_{\max}^{SBET-SH-\beta} \left[\begin{array}{c} \alpha_{\beta} \dfrac{c_1 \rho_b / \rho_{a1}^{SBET-SH-\beta}}{1-\rho_b / \rho_{a1}^{SBET-SH-\beta}} \dfrac{1-\left(n_{1,SBET}+1\right)\left(\rho_b / \rho_{a1}^{SBET-SH-\beta}\right)^{n_{1,SBET}} + n_{1,SBET}\left(\rho_b / \rho_{a1}^{SBET-SH-\beta}\right)^{n_{1,SBET}+1}}{1+\left(c_1-1\right)\left(\rho_b / \rho_{a1}^{SBET-SH-\beta}\right)-c_1\left(\rho_b / \rho_{a1}^{SBET-NH-\beta}\right)^{n_{1,SBET}+1}} \\ +\left(1-\alpha_{\beta}\right) \dfrac{c_2 \rho_b / \rho_{a2}^{SBET-SH-\beta}}{1-\rho_b / \rho_{a2}^{SBET-SH-\beta}} \dfrac{1-\left(n_{2,SBET}+1\right)\left(\rho_b / \rho_{a2}^{SBET-SH-\beta}\right)^{n_{2,SBET}} + n_{2,SBET}\left(\rho_b / \rho_{a2}^{SBET-SH-\beta}\right)^{n_{2,SBET}+1}}{1+\left(c_2-1\right)\left(\rho_b / \rho_{a2}^{SBET-SH-\beta}\right)-c_1\left(\rho_b / \rho_{a2}^{SBET-SH-\beta}\right)^{n_{2,SBET}+1}} \end{array} \right]$$

(7.22)

7.4.2.1.4 Toth and Langmuir-Freundlich model

Toth model is a semi-empirical equation based on the Langmuir model and the rearrangement is proposed for gas adsorption on heterogeneous surface[256]. The expression is given as,

$$m_{abs}^{Toth} = m_{\max} \frac{bP}{\left(1+\left(bP\right)^t\right)^{\frac{1}{t}}}$$

(7.23)

where b is the Toth constant in the equation, and t represent the parameter related to the adsorbent heterogeneity.

The Langmuir-Freundlich (LF) model is proposed by Sips[257] by combing the form of Langmuir[209] and Freundlich[258] model, while the original Freundlich model describes an empirical relationship between the quantity of a gas adsorbed into a solid surface and the gas pressure. The LF model does not conform to the Henry law and at lower

concentrations, it can be simplified to the Freundlich adsorption model. The equation can be expressed as,

$$m_{abs}^{LF} = m_{max} \frac{bP^t}{1+(bP)^t} \qquad (7.24)$$

where b is the LF constant and t can be used for heterogeneity correction for adsorbent and adsorbate. It shows clearly that the LF model is regressed to Langmuir model when $t = 1$, indicating a homogeneous surface for adsorbed gas molecules.

7.4.2.1.5 Ono-Kondo Model

In spite of the aforementioned four types of OK model, we also evaluate the dual-site OK model without the application of PSD lumping by using fixed adsorbed phase volume (fv) of surface area and constant adsorbed phase width ($W_a = 0.38$ nm). The dual-site (single heterogeneity) OK-fv model is given as,

$$m_{abs}^{OK-SH-fv} = \alpha_\beta \rho_{am,1}^{OK-SH-fv} W_a SSA \sum_{k=1}^{n_k} (x_{1,k}) + (1-\alpha_\beta) \rho_{am,2}^{OK-SH-fv} W_a SSA \sum_{k=1}^{n_k} (x_{2,k}) \qquad (7.25)$$

where $x_{1,k}$ and $x_{2,k}$ are fraction of adsorbed phase layer k of component "1" and "2", respectively.

In addition, the OK model can also be expressed by regressing maximum adsorbed phase capacity (mc) method, which has been applied in many studies[120]. Sudibandriyo *et al.*[202] applied the proposed OK monolayer adsorption model with maximum adsorbed phase capacity, they found the maximum capacity decreases with temperature and the averaged absolute deviation of excess adsorption regression can be down to 3.6%. Based

on our previous findings of methane adsorption in carbon 4 nm pore, we decide to adopt

multilayer adsorption in OK-mc method. Therefore, the non-heterogeneity and single

heterogenic model can be given as,

$$
\begin{cases}
m_{abs}^{OK-NH-mc} = C_{OK-mc} SSA \sum_{k=1}^{n_k} (x_k) \\
m_{abs}^{OK-SH-mc} = \alpha_\beta C_{OK-mc} SSA \sum_{k=1}^{n_k} (x_{1,k}) + (1-\alpha_\beta) C_{OK-mc} SSA \sum_{k=1}^{n_k} (x_{2,k})
\end{cases}
\tag{7.26}
$$

7.4.2.1.6 Direct Conversion Method

The direct conversion method utilizes the experimentally measured excess adsorption data

with assumed adsorption phase properties such as constant volume (cv) and constant

density (cd) to directly calculate absolute adsorption. These two types of direct conversion

method are expressed as,

$$
\begin{cases}
m_{abs}^{DC-cd} = m_{ex} / (1 - \rho_b / \rho_a) \\
m_{abs}^{DC-cv} = m_{ex} + \rho_b V_a
\end{cases}
\tag{7.27}
$$

7.4.3 Model comparison and recommendations

As has been mentioned in many studies that most of the conversions via adsorption models

are made on the basis of the assumption of adsorbed phase properties. There are two

common approaches: (a) constant adsorbed phase density; and (b) constant adsorbed phase

volume. In terms of constant density method, the density of adsorbed phase keeps

unchanged with pressures, while different treatments are used to set up adsorbed density

and we adopt methods including liquid methane density at boiling point[183], van der Waals density[101] and empirical temperature dependent density[65] for the comparison. According to the previous study of our research group, Tian *et al.*[259] found better performance of direct conversion method using constant adsorbed phase volume compared with constant density method, while GCMC densities have been also applied for the absolute adsorption conversion in many studies[63, 187, 223], showing the demand of accurately gaining adsorbed phase fluid behavior. Moreover, the surface area associated with fixed adsorption layer width of 0.38 nm has been also considered into comparison, as we have found it can be implemented in Langmuir and SDR model and has good performance comparable with OK model[229]. **Table 7-3** lists the overview of total 171 models and their types, and the detailed equation of each type and treatment and variables that need to be regressed from excess adsorption can be referred to the **Table F3** and **Table F4**.

Table 7-3 Summary of number of models

Models	No heterogeneity	Single heterogeneity						Dual heterogeneity	Number of models
		Fixed ρ_a				Fixed V_a			
		Apparent ρ_a		Heterogeneous ρ_a		Fixed V_a			
		Rock heterogeneity	Pore size heterogeneity	Rock heterogeneity	Pore size heterogeneity	Rock heterogeneity	Pore size heterogeneity		
Langmuir	√	√	√	√	√	√	√	×	28
SDR	√	√	√	√	√	√	√	×	28
Improved D-A	√	√	√	√	√	√	√	×	28
SBET	√	√	√	√	√	√	√	×	28
BET-pseudosaturation pressure	√	√	√	√	√	√	√	×	28
OK	√	×	×	×	×	√	√	√	9

Toth	√	×	×	×	×	×	×	×	8
Langmuir-Freundlich	√	×	×	×	×	×	×	×	8
Direct conversion	√	×	×	×	×	×	×	×	6

In **Figure 7-4**, we show the averaged absolute deviation (AAD%) of all evaluated models over total tested samples with wide range of PSDs and pressures. As can be illustrated from the figure that two constant density methods of using liquid methane and van der Waals density show large deviations in regressing excess adsorption method, while the empirical correlation of Ozawa's density and a majority of other methods show the behavior of AAD less than 10%. Although many literatures reported relative acceptable regression of excess adsorption, they mostly focus on the measurement under low pressure condition, and the error might occur as the pressure becomes high in realistic reservoir condition and the necessity of performing high pressure experiments has highlighted in our previous study[229]. **Figure 7-5 (a)** summarize the RMSD of assessed 171 models on 1st layer absolute adsorption in 19200 samples. As can be observed from the figures that wide range of RSMD can be found even in same single models because of different treatment of adsorbed phase properties. Moreover, although simple dual-site approximation has been used in generalized models, the RMSDs of these single heterogeneity models do not perform any significant improvement, indicating the requirement of more detailed characterization of rock pore structures. The light pink region highlights the models with top 15% performance and is enlarged in **Figure 7-5 (b)**. Five models of the least RMSDs have been marked and the OK-DH model performs the best prediction in all evaluated models. We found that the dual-site Langmuir model with known surface area and fixed 0.38 nm adsorption layer by considering rock type heterogeneity can also perform a good

representation of absolute adsorption with GCMC simulation. Such approach attributes the accumulation of molecules to surface adsorption and thus the fixed maximum adsorbed phase volume might further guarantee the physical phenomenon, and the regressed variables are shown in **Table F5**. Considering the complexity of OK-DH model and the need of acquiring PSD in individual rick type, it is also recommended to use Langmuir model with the above assumptions for calculation. Moreover, it is shown that the OK-SH and SDR-SH model considering rock type heterogeneity provides the 4th and 5th good prediction, which also indicate the importance of the rock type effect on describing adsorption behavior.
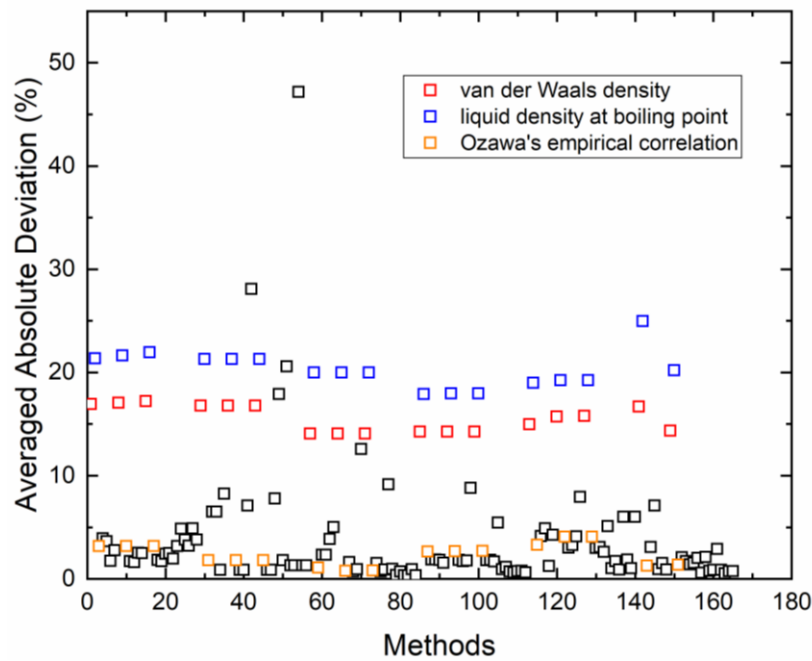
Figure 7-4 Averaged absolute deviation of excess adsorption of all evaluated samples over various models.

(a)   (b)
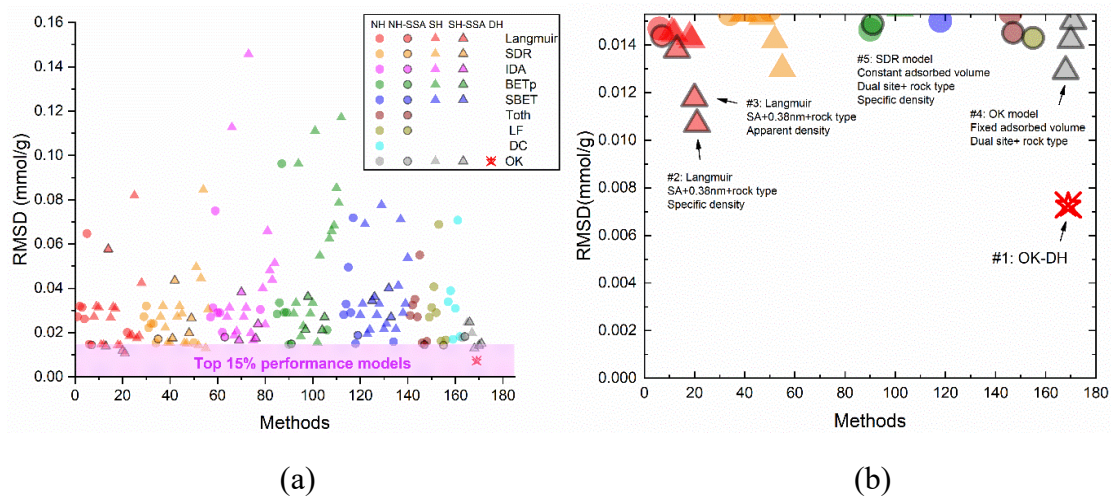
Figure 7-5 Performance of absolute adsorption prediction over 171 models through root-mean-square deviation (RMSD)

7.5 Conclusion

In this work, we apply GCMC simulation to study methane adsorption at temperature of 333.15 K and pressures up to 500 bar to investigate both rock type and pore size effect. The carbon slit pore and illite slit pore is used to represent the organic and inorganic matters in shale rock and the excess adsorption in different pore widths and different composition is compared, and we have found the excess adsorption per SSA in pore size ranges of $W \geq 2.5$ nm and $W \geq 2$ nm is independent to the pore sizes for carbon and illite nanopores due to different fluid surface interactions, respectively. Moreover, the absolute adsorption amount characterized from GCMC simulation reveals the stronger affinity of gas molecules to organic nanopores, and the presence of transition layer is clearly found in both two rock types. In other words, we have found the influenced

prediction of adsorption amount through molecular simulations arising from both pore size and rock heterogeneity (dual-heterogeneity). By following our recent works on characterization of methane adsorption types in carbon nanopores, five adsorption types in illite nanopores have been classified from GCMC simulation. The OK-DH model associated with both PSD lumping and the contribution of adsorption amount by different compositions is proposed to regress excess adsorption in total shale rock, and calculate absolute adsorption based on GCMC characterization. In order to test the validity of the proposed model, we apply 19200 sets of PSD and weight percent for organic and inorganic matters, respectively, thus a number of shale samples are generated randomly with same total pore volumes but different rock compositions and distribution of micropore volumes. In light of the good prediction of OK model shown in our previous work, we compare and test several versions of currently used OK models which include no heterogeneity, single heterogeneity with PSD lumping and dual heterogeneity. The results have shown the OK-DH model can perform well not only for total adsorption amount prediction but also can predict adsorption amount in different parts, which indicates the importance of considering dual heterogeneity. In addition, the comparison of prediction behaviors among almost all widely used adsorption models (over 170 models) associated with adsorbed phase properties assumptions is made and OK model with consideration of dual heterogeneity provides the most accurate prediction. The proposed OK-DH model indicates the potential application of to predict fluid properties in different rock types and specific pore size

range. At last, we also recommend to use dual-site Langmuir (DSL) model with known surface area and fixed 0.38 nm adsorption layer by considering rock type heterogeneity to achieve simple and fast evaluation of total absolute adsorption.

CHAPTER 8 CONCLUSIONS, CONTRIBUTIONS AND RECOMMENDATIONS

8.1 Conclusions and Scientific Contributions to the Literature

In this dissertation, the hydrocarbon adsorption behavior in shale nanoporous media is investigated through molecular simulation. Different adsorption mechanism and adsorbed phase properties have been studied, and the heterogeneity effect including pore size distribution and rock type has been highlighted in terms of the absolute adsorption conversion. Therefore, by adopting the observations from grand canonical Monte Carlo (GCMC) simulation, we develop the adsorption model of Ono-Kondo model on the basis of lattice density functional theory, which can account for both supercritical and multilayer adsorption. The modified Ono-Kondo model coupled with PSD and rock type effect can accurately describe the adsorption behavior via excess adsorption from experimental finding and predict the absolute adsorption. The main conclusions of this thesis are summarized as follows:

Chapter 2:

In this chapter, we performed GCMC simulation to investigate the methane adsorption in carbon nanopores at various pressures. We used the volumetric method to calculate the excess adsorption, using helium adsorption to determine the effective pore volume. Based on the density distributions, we proposed a modified adsorption model for methane to

better take into account the effect of transition zone. From the GCMC simulation, the following characteristics can be obtained,

1) The excess adsorption per specific surface area is found to increase with pressure then decreases, and the excess adsorption amount insensitive to the pore size, when $W \geq 4$ nm.

2) The second adsorption layer is observed, and the density can be very different from the bulk, indicating the transition zone. Such transition zone can negatively affect the accuracy of the absolute adsorption calculation based on the monolayer adsorption model.

We then adopt the Ono-Kondo multilayer adsorption model (OK-MU) to account for the methane adsorption in mesopore at the supercritical and *in situ* condition, and draw following conclusions:

1) OK-MU have shown excellent agreement with GCMC simulations on the excess adsorption and can accurately characterize the transition zone, while the single adsorption layer may deviate from the finding in molecular simulations.

2) We found that the absolute adsorption calculated by OK-MU yields a good agreement with GCMC simulation, and the maximum relative error between these two methods is less than 6 %. In addition, we used the arbitrary effective pore width to test OK-MU. Even though a significant change in excess adsorption occurs, the

OK-MU can still predict the methane absolute adsorption with an excellent agreement with GCMC simulations.

Chapter 3:

In this chapter, we conduct grand canonical Monte Carlo (GCMC) simulation to study propane adsorption in shale nanopores over a wide range of pressures at temperature higher than the critical temperature. Based on the investigations from propane density distribution, we propose a multi-layered adsorption model and use Ono-Kondo (OK) lattice model with multi-layered structure, and the following conclusions are drawn in this chapter:

1) We find that propane can form multiple adsorption layers. For pressure above 100 bar, three adsorption layers can be found clearly from density distributions. When pressure is lower than 100 bar, the effect of the fourth, fifth and sixth layer is non-negligible. Therefore, using single-layer adsorption model to obtain the absolute adsorption becomes unjustifiable.

2) Based on the density distribution from GCMC simulation, we use 6-layer structure to characterize the propane adsorption for all pressure conditions.

3) We take into account the correlation effect arising from the strong adsorbate-adsorbate interactions beyond mean field theory (MFT) and the only predetermined parameters are number of layers and adsorption layer width. The proposed OK model shows an excellent agreement with GCMC simulations on the excess

adsorption and absolute adsorption in each layer, with discrepancies less than 6 % above 50 bar. The proposed OK model can readily take into account the propane multi-layered adsorption behavior, while significantly reduce the calculation time.

Chapter 4:

In this chapter, we conduct GCMC simulation to identify the different adsorption mechanism of methane adsorption in organic nanopores considering various sized of nanopores. We draw following conclusions:

1) Methane shows varying adsorption behavior in micropores and mesopores. Therefore, it is necessary to consider the effect of PSD in the conversion of m_{ex} to obtain m_{abs}.

2) Based on the varying density profiles in different nanopores obtained from GCMC, we propose the corresponding methane adsorption model in each nanopore. We thus classify four distinct adsorption models: $W = 1$ nm, $W = 1.5$ nm, $W = 2$ nm and $W \geq 4$ nm.

3) Based on the proposed adsorption model, the governing equations in different types can be constructed. Only three parameters in OK model are needed to fit the total excess adsorption from GCMC simulations to obtain the absolute adsorption by coupling the pore size distribution.

4) We test the performance of the proposed OK-PSD model, and it presents an excellent agreement with GCMC simulations in the absolute adsorption in the first layer, while commonly used constant adsorbed phase densities as $\rho_a = 424$ kg/m^3 and $\rho_a = 373$ kg/m^3 based on single-layer adsorption model show noticeable deviations. Moreover, the optimized adsorbed phase density is quite different from these two values.

Chapter 5

As can be investigated from **Chapter 4** that the methane adsorption behavior depends on pore size and may be very different from the single-layer adsorption model. We systematically assess the validity of many conversion methods and single-layered model (such as Langmuir and SDR model) in the characterization of methane absolute adsorption in kerogen nanoporous materials, and the following conclusions are drawn in this chapter:

1) The predetermined density methods using 373 or 424 kg/m^3 may show unphysical phenomena and Langmuir as well as SDR models can largely overestimate the absolute adsorption. Ono-Kondo (OK) lattice model with PSD can accurately characterize the absolute adsorption in nanoporous media.

2) Langmuir and SDR models coupled with PSD can provide comparable predictions to OK model, indicating the need of accurate characterization of pore structure in nanoporous media.

3) We also suggest using the high-pressure excess adsorption data (up to 500 bar), instead of commonly used low-pressure excess adsorption measurements (up to 150 bar).

Chapter 6

In this chapter, the CH$_4$ adsorption in nanopores is divided into six distinct adsorption types based on density distributions. For each specific adsorption type, the specific pore size range is classified to appropriately account for adsorption modelling. Following conclusions are drawn:

1) Based on GCMC simulations, we characterize different adsorption types in terms of pore sizes. The non-monotonic behavior of excess adsorption versus pore size is observed in micropores. The excess adsorption becomes independent of pore size, when $W_i \geq 2.5$ nm.

2) The PSD lumping method is used to characterize CH$_4$ absolute adsorption in kerogen nanoporous media with pore size ranging from 0.7 nm to 50 nm. Coupling the adsorption types from the GCMC simulations, the OK-PSD-L model can reliably regress the excess adsorption and absolute adsorption in

3) We test the performance of our OK-PSD-lumping (OK-PSD-L) model by using 1250 randomly generated kerogen nanoporous media, and the validity of our proposed OK model with PSD lumping is tested by 5 cases with varying micropore

volume proportions from 5% to 35%, with each case containing 250 sets of randomly generated PSD samples. We find that by fitting the excess adsorption isotherm, the OK model with PSD lumping has an excellent agreement in terms of the absolute adsorption amounts with those obtained from the GCMC simulation, while deviations increase as micropore volume proportion increases.

Chapter 7

Despite the relative higher adsorption capacity of methane adsorption in organic pores, it is revealed by experimental work that clay minerals would have obviously positive contribution on specific surface area (SSA) as well as methane adsorption amount. In this chapter, we conduct GCMC simulation of methane adsorption in various sizes of illite nanopores. By investigating the adsorption characteristics, we develop the Ono-Kondo dual heterogeneity (OK-DH) model by considering both pore size distribution and rock type effect. The following conclusions can be drawn in this chapter:

1) The absolute adsorption amount characterized from GCMC simulation reveals the stronger affinity of gas molecules to organic nanopores than inorganic matter, but the accumulation of gas molecules is found near the surface and the presence of transition layer is clearly found in both two rock types. The influenced prediction of adsorption amount through molecular simulations arising from both pore size and rock heterogeneity.

2) Following our recent works in **Chapter 6**, five adsorption types in illite nanopores have been classified from GCMC simulation. The OK-DH model is constructed by considering different fluid-surface interaction energy and specific adsorption type in different sized and types of rock composition.

3) The OK-DH model associated with both PSD lumping and the contribution of adsorption amount by different types is validated to regress excess adsorption in total shale rock, and calculate absolute adsorption based on GCMC characterization.

4) We assess the performance of over 170 models to evaluate the performance of absolute adsorption prediction and raise the awareness of considering the importance of heterogeneities in shale. According to the evaluations, OK-DH performs the best, while the dual-site Langmuir (DSL) coupled with PSD in organic and inorganic matter presents the second best which can be further applied due to its simplicity.

8.2 Suggested Future Work

• In this thesis, we proposed and developed OK-DH model that can be used to describe methane adsorption in shale nanoporous media that take into account the effect of pore size distribution and rock type heterogeneity effect. The proposed model can also consider the multilayer adsorption and transition zone effect which

contribute to the adsorption amount as well. In the future,, we can apply the model with the collective information from pore structure characterization to obtain an accurate absolute adsorption prediction. Therefore, we can couple them into gas-in-place (GIP) estimation which can show the amount of fluid stored according to the *in-situ* condition.

- Apart from the distinct effect of PSD and rock type, some other effects that can influence the adsorption capacity need to be further studied. The moisture effect is readily observed under in-situ condition and can leads to the decrease of maximum adsorption capacity, while many studies conducted the isothermal adsorption isotherms under dry condition, which indicates the lack of corresponding model that can describe the adsorption capacity under moisture condition. In addition, the morphology of organic matter which dominates the shale gas adsorption also plays an important role in affecting the gas accumulation. However, there are not enough efforts working on characterization and considering the rough surface of kerogen into adsorption model.

- As mentioned in our Chapter 5 and Chapter 6 that the understanding and accurate characterization of PSD is critical to determine gas storage and flow mechanism. The microscopic approaches including non-local density functional theory (NLDFT) and molecular simulation becomes promising techniques to account for

PSD of micropores. However, the mostly applied kernel in NLDFT is carbon slit pore which neglects the surface chemical heterogeneity and pore geometric heterogeneity. Thus, the consideration and evaluation of those factors in PSD determination is needed for accurate pore morphology analysis.

BIBLIOGRAPHY

1. Li, W., et al., *The description of shale reservoir pore structure based on method of moments estimation.* PloS one, 2016. **11**(3): p. e0151631.

2. Ma, L., et al., *A novel upscaling procedure for characterising heterogeneous shale porosity from nanometer-to millimetre-scale in 3D.* Energy, 2019. **181**: p. 1285-1297.

3. Chalmers, G.R., D.J. Ross, and R.M. Bustin, *Geological controls on matrix permeability of Devonian Gas Shales in the Horn River and Liard basins, northeastern British Columbia, Canada.* International Journal of Coal Geology, 2012. **103**: p. 120-131.

4. Chalmers, G.R., R.M. Bustin, and I.M. Power, *Characterization of gas shale pore systems by porosimetry, pycnometry, surface area, and field emission scanning electron microscopy/transmission electron microscopy image analyses: Examples from the Barnett, Woodford, Haynesville, Marcellus, and Doig unitsCharacterization of Gas Shale Pore Systems.* AAPG bulletin, 2012. **96**(6): p. 1099-1119.

5. Ross, D.J. and R.M. Bustin, *The importance of shale composition and pore structure upon gas storage potential of shale gas reservoirs.* Marine and Petroleum Geology, 2009. **26**(6): p. 916-927.

6. Zhang, M., S. Zhan, and Z. Jin, *Recovery mechanisms of hydrocarbon mixtures in organic and inorganic nanopores during pressure drawdown and CO2 injection from molecular perspectives.* Chemical Engineering Journal, 2020. **382**: p. 122808.

7. Vandenbroucke, M. and C. Largeau, *Kerogen origin, evolution and structure.* Organic Geochemistry, 2007. **38**(5): p. 719-833.

8. Demaison, G.J. and G.T. Moore, *Anoxic environments and oil source bed genesis.* AApG Bulletin, 1980. **64**(8): p. 1179-1209.

9. Jin, Z. and A. Firoozabadi, *Thermodynamic modeling of phase behavior in shale media.* Spe Journal, 2016. **21**(01): p. 190-207.

10. Wu, Y.-S., et al., *A generalized framework model for the simulation of gas production in unconventional gas reservoirs.* Spe Journal, 2014. **19**(05): p. 845-857.

11. Feiyu, W., et al., *Evolution of overmature marine shale porosity and implication to the free gas volume.* Petroleum Exploration and Development, 2013. **40**(6): p. 819-824.

12. Romero-Sarmiento, M.-F., et al., *Quantitative evaluation of TOC, organic porosity and gas retention distribution in a gas shale play using petroleum system modeling: Application to the Mississippian Barnett Shale.* Marine and Petroleum Geology, 2013. **45**: p. 315-330.

13. Zhao, P., et al., *An improved model for estimating the TOC in shale formations.* Marine and Petroleum Geology, 2017. **83**: p. 174-183.

14. Witte, E., et al., *Structural modifications of kerogen during natural evolution as derived from 13C CP/MAS NMR, IR spectroscopy and Rock-Eval pyrolysis of Toarcian shales.* Organic geochemistry, 1988. **13**(4-6): p. 1039-1044.

15. Liao, L., et al., *Kinetic study of marine and lacustrine shale grains using Rock-Eval pyrolysis: Implications to hydrocarbon generation, retention and expulsion.* Marine and Petroleum Geology, 2018. **89**: p. 164-173.

16. Rimmer, S.M., D. Cantrell, and P.J. Gooding, *Rock-Eval pyrolysis and vitrinite reflectance trends in the Cleveland Shale Member of the Ohio Shale, eastern Kentucky.* Organic Geochemistry, 1993. **20**(6): p. 735-745.

17. Romero-Sarmiento, M.-F., et al., *New Rock-Eval method for characterization of unconventional shale resource systems.* Oil & Gas Science and Technology–Revue d'IFP Energies nouvelles, 2016. **71**(3): p. 37.

18. Bai, B., et al., *Rock characterization of Fayetteville shale gas plays.* Fuel, 2013. **105**: p. 645-652.

19. Hupp, B.N. and J.J. Donovan, *Quantitative mineralogy for facies definition in the Marcellus Shale (Appalachian Basin, USA) using XRD-XRF integration.* Sedimentary Geology, 2018. **371**: p. 16-31.

20. Fan, C., et al., *XRD and TG-FTIR study of the effect of mineral matrix on the pyrolysis and combustion of organic matter in shale char.* Fuel, 2015. **139**: p. 502-510.

21. Tong, J., et al., *Evaluation of structural characteristics of Huadian oil shale kerogen using direct techniques (solid-state 13C NMR, XPS, FT-IR, and XRD).* Energy & fuels, 2011. **25**(9): p. 4006-4013.

22. Zhang, T., et al., *Effect of organic-matter type and thermal maturity on methane adsorption in shale-gas systems.* Organic geochemistry, 2012. **47**: p. 120-131.

23. Wu, X., et al., *Pore characterization and inner adsorption mechanism investigation for methane in organic and inorganic matters of shale.* Energy & Fuels, 2020. **34**(4): p. 4106-4115.

24. Wang, C., et al., *Is China really ready for shale gas revolution—Re-evaluating shale gas challenges.* Environmental science & policy, 2014. **39**: p. 49-55.

25. Zou, C., et al., *Geological characteristics and resource potential of shale gas in China.* Petroleum exploration and development, 2010. **37**(6): p. 641-653.

26. Yang, F., et al., *Pore structure characteristics of lower Silurian shales in the southern Sichuan Basin, China: Insights to pore development and gas storage mechanism.* International Journal of Coal Geology, 2016. **156**: p. 12-24.

27. Li, T., et al., *Continental shale pore structure characteristics and their controlling factors: A case study from the lower third member of the Shahejie Formation, Zhanhua Sag, Eastern China.* Journal of Natural Gas Science and Engineering, 2017. **45**: p. 670-692.

28. Feng, G., et al., *Supercritical Methane Adsorption on Shale over Wide Pressure and Temperature Ranges: Implications for Gas-in-Place Estimation.* Energy & Fuels, 2020. **34**(3): p. 3121-3134.

29. Yuan, W., et al., *Experimental study and modelling of methane adsorption and diffusion in shale.* Fuel, 2014. **117**: p. 509-519.

30. Zheng, X., et al., *Pore structure characteristics and its effect on shale gas adsorption and desorption behavior.* Marine and Petroleum Geology, 2019. **100**: p. 165-178.

31. Zhang, H. and D. Cao, *Molecular simulation of displacement of shale gas by carbon dioxide at different geological depths.* Chemical Engineering Science, 2016. **156**: p. 121-127.

32. Wang, K., B. Zhang, and T. Kang, *Effect of Geological Depths on CH4 Adsorption, Diffusion, and Swelling in Kaolinite by Molecular Simulations.* Energy & Fuels, 2020. **34**(2): p. 1620-1626.

33. Liu, X.-Q., et al., *Mechanistic insight into the optimal recovery efficiency of CBM in sub-bituminous coal through molecular simulation.* Fuel, 2020. **266**: p. 117137.

34. Caineng, Z., et al., *Shale gas in China: Characteristics, challenges and prospects (I).* Petroleum Exploration and Development, 2015. **42**(6): p. 753-767.

35. Rexer, T.F., et al., *Methane adsorption on shale under simulated geological temperature and pressure conditions.* Energy & Fuels, 2013. **27**(6): p. 3099-3109.

36. Cipolla, C.L., et al. *Modeling well performance in shale-gas reservoirs.* in *SPE/EAGE Reservoir Characterization & Simulation Conference.* 2009. European Association of Geoscientists & Engineers.

37. Xianggang, D., et al., *Shale high pressure isothermal adsorption curve and the production dynamic experiments of gas well.* Petroleum Exploration and Development, 2018. **45**(1): p. 127-135.

38. Curtis, J.B., *Fractured shale-gas systems.* AAPG bulletin, 2002. **86**(11): p. 1921-1938.

39. Zhou, S., et al., *Experimental study of supercritical methane adsorption in Longmaxi shale: Insights into the density of adsorbed methane.* Fuel, 2018. **211**: p. 140-148.

40. Pang, W., Y. Ye, and Z. Jin, *Assessment of Various Approaches in the Prediction of Methane Absolute Adsorption in Kerogen Nanoporous Media.* Energy and Fuels, 2019. **33**: p. 6258-6263.

41. Gensterblum, Y., et al., *European inter-laboratory comparison of high pressure CO2 sorption isotherms. I: Activated carbon.* Carbon, 2009. **47**(13): p. 2958-2969.

42. Zhou, L., et al., *Comparative study of the excess versus absolute adsorption of CO2 on superactivated carbon for the near-critical region.* Langmuir, 2003. **19**(7): p. 2683-2690.

43. Zhou, L., et al., *Experimental and modeling study of the adsorption of supercritical methane on a high surface activated carbon.* Langmuir, 2000. **16**(14): p. 5955-5959.

44. Khosrokhavar, R., K.-H. Wolf, and H. Bruining, *Sorption of CH4 and CO2 on a carboniferous shale from Belgium using a manometric setup.* International Journal of Coal Geology, 2014. **128**: p. 153-161.

45. Zhang, J., et al., *Methane and carbon dioxide adsorption on Illite.* Energy & Fuels, 2016. **30**(12): p. 10643-10652.

46. Gasparik, M., et al., *High-pressure methane sorption isotherms of black shales from the Netherlands.* Energy & fuels, 2012. **26**(8): p. 4995-5004.

47. Tian, H., et al., *Characterization of methane adsorption on overmature Lower Silurian–Upper Ordovician shales in Sichuan Basin, southwest China: Experimental results and geological implications.* International Journal of Coal Geology, 2016. **156**: p. 36-49.

48. Rexer, T.F., et al., *High-Pressure Methane Adsorption and Characterization of Pores in Posidonia Shales and Isolated Kerogens.* Energy & Fuels, 2014. **28**(5): p. 2886-2901.

49. Chen, L., et al., *Application of Langmuir and Dubinin–Radushkevich models to estimate methane sorption capacity on two shale samples from the Upper Triassic Chang 7 Member in the southeastern Ordos Basin, China.* Energy Exploration & Exploitation, 2017. **35**(1): p. 122-144.

50. Sakurovs, R., et al., *Application of a modified Dubinin− Radushkevich equation to adsorption of gases by coals under supercritical conditions.* Energy & fuels, 2007. **21**(2): p. 992-997.

51. Tian, Y., C. Yan, and Z. Jin, *Characterization of Methane Excess and Absolute Adsorption in Various Clay Nanopores from Molecular Simulation.* Scientific Reports, 2017. **7**(1): p. 12040.

52. Pang, W. and Z. Jin, *Methane Absolute Adsorption in Kerogen Nanoporous Media with Realistic Continuous Pore Size Distributions.* Energy & Fuels, 2020. **34**(10): p. 12158-12172.

53. Yu, W., K. Sepehrnoori, and T.W. Patzek, *Modeling gas adsorption in Marcellus shale with Langmuir and BET isotherms.* SPE Journal, 2016. **21**(02): p. 589-600.

54. Zhou, S., et al., *A modified BET equation to investigate supercritical methane adsorption mechanisms in shale.* Marine Petroleum Geology, 2019. **105**: p. 284-292.

55. Liu, Y., J. Hou, and C. Wang, *Absolute adsorption of CH 4 on shale with the simplified local-density theory.* SPE Journal, 2020. **25**(01): p. 212-225.

56. Pang, Y., et al., *Characterization of adsorption isotherm and density profile in cylindrical nanopores: modeling and measurement.* Chemical Engineering Journal, 2020: p. 125212.

57. Mohammad, S.A., et al., *Measurements and modeling of excess adsorption of pure and mixed gases on wet coals.* Energy & fuels, 2012. **26**(5): p. 2899-2910.

58. Sudibandriyo, M., et al., *Ono–Kondo lattice model for high-pressure adsorption: Pure gases.* Fluid Phase Equilibria, 2010. **299**(2): p. 238-251.

59. Xiong, F., et al., *On the pressure and temperature dependence of adsorption densities and other thermodynamic properties in gas shales.* Chemical Engineering Journal, 2020. **395**: p. 124989.

60. Hwang, J. and R. Pini, *Supercritical CO2 and CH4 uptake by illite-smectite clay minerals.* Environmental Science & Technology, 2019. **53**(19): p. 11588-11596.

61. Memon, A., et al., *Gas adsorption and controlling factors of shale: review, application, comparison and challenges.* Natural Resources Research, 2020: p. 1-22.

62. Etminan, S.R., et al., *Measurement of gas storage processes in shale and of the molecular diffusion coefficient in kerogen.* International Journal of Coal Geology, 2014. **123**: p. 10-19.

63. Wu, T., et al., *Absolute adsorption of light hydrocarbons and carbon dioxide in shale rock and isolated kerogen.* Fuel, 2019. **235**: p. 855-867.

64. Zhao, H., T. Wu, and A. Firoozabadi, *High pressure sorption of various hydrocarbons and carbon dioxide in Kimmeridge Blackstone and isolated kerogen.* Fuel, 2018. **224**: p. 412-423.

65. Xiong, J., et al., *Adsorption of methane in organic-rich shale nanopores: An experimental and molecular simulation study.* Fuel, 2017. **200**: p. 299-315.

66. Wang, T., et al., *Molecular simulation of CO2/CH4 competitive adsorption on shale kerogen for CO2 sequestration and enhanced gas recovery.* The Journal of Physical Chemistry C, 2018. **122**(30): p. 17009-17018.

67. Mosher, K., et al., *Molecular simulation of methane adsorption in micro-and mesoporous carbons with applications to coal and gas shale systems.* International Journal of Coal Geology, 2013. **109**: p. 36-44.

68. Liu, J., S. Xi, and W.G. Chapman, *Competitive Sorption of CO2 with Gas Mixtures in Nanoporous Shale for Enhanced Gas Recovery from Density Functional Theory.* Langmuir, 2019. **35**(24): p. 8144-8158.

69. Wang, T.-Y., et al., *Pore structure characterization and its effect on methane adsorption in shale kerogen.* Petroleum Science, 2020: p. 1-14.

70. Song, W., et al., *Grand canonical Monte Carlo simulations of pore structure influence on methane adsorption in micro-porous carbons with applications to coal and shale systems.* Fuel, 2018. **215**: p. 196-203.

71. Huang, L., et al., *Molecular simulation of adsorption behaviors of methane, carbon dioxide and their mixtures on kerogen: Effect of kerogen maturity and moisture content.* Fuel, 2018. **211**: p. 159-172.

72. Zhou, J., Z. Jin, and K.H. Luo, *The role of brine in gas adsorption and dissolution in kerogen nanopores for enhanced gas recovery and CO2 sequestration.* Chemical Engineering Journal, 2020. **399**: p. 125704.

73. Zhou, J., Z. Jin, and K.H. Luo, *Effects of Moisture Contents on Shale Gas Recovery and CO2 Sequestration.* Langmuir, 2019. **35**(26): p. 8716-8725.

74. Huang, L., et al., *Molecular Insights into Kerogen Deformation Induced by CO2/CH4 Sorption: Effect of Maturity and Moisture.* Energy and Fuels, 2019. **33**: p. 4792-4805.

75. Pang, W., et al., *Tackling the challenges in the estimation of methane absolute adsorption in kerogen nanoporous media from molecular and analytical approaches.* Fuel, 2019. **242**: p. 687-698.

76. Li, Z., D. Cao, and J. Wu, *Layering, condensation, and evaporation of short chains in narrow slit pores.* The Journal of chemical physics, 2005. **122**(22): p. 224701.

77. Zhao, X., et al., *Layering and orientational ordering of propane on graphite: An experimental and simulation study.* The Journal of chemical physics, 2002. **117**(16): p. 7719-7731.

78. Jarvie, D.M., et al., *Unconventional shale-gas systems: The Mississippian Barnett Shale of north-central Texas as one model for thermogenic shale-gas assessment.* AAPG bulletin, 2007. **91**(4): p. 475-499.

79. Montgomery, S.L., et al., *Mississippian Barnett Shale, Fort Worth basin, north-central Texas: Gas-shale play with multi–trillion cubic foot potential.* AAPG bulletin, 2005. **89**(2): p. 155-175.

80. Chalmers, G.R. and R.M. Bustin, *Lower Cretaceous gas shales in northeastern British Columbia, Part I: geological controls on methane sorption capacity.* Bulletin of Canadian petroleum geology, 2008. **56**(1): p. 1-21.

81. Bi, H., et al., *Ono–Kondo model for supercritical shale gas storage: A case study of Silurian Longmaxi shale in southeast Chongqing, China.* Energy & Fuels, 2017. **31**(3): p. 2755-2764.

82. Ross, D.J. and R.M. Bustin, *Shale gas potential of the lower jurassic gordondale member, northeastern British Columbia, Canada.* Bulletin of Canadian Petroleum Geology, 2007. **55**(1): p. 51-75.

83. Chalmers, G.R. and R.M. Bustin, *The organic matter distribution and methane capacity of the Lower Cretaceous strata of Northeastern British Columbia, Canada.* International Journal of Coal Geology, 2007. **70**(1-3): p. 223-239.

84. Ross, D.J. and R.M. Bustin, *Characterizing the shale gas resource potential of Devonian–Mississippian strata in the Western Canada sedimentary basin: Application of an integrated formation evaluation.* AAPG bulletin, 2008. **92**(1): p. 87-125.

85. Strapoc, D., et al., *Geochemical constraints on the origin and volume of gas in the New Albany Shale (Devonian–Mississippian), eastern Illinois Basin.* AAPG bulletin, 2010. **94**(11): p. 1713-1740.

86. Gasparik, M., et al., *Geological controls on the methane storage capacity in organic-rich shales.* International Journal of Coal Geology, 2014. **123**: p. 34-51.

87. Hao, F., H. Zou, and Y. Lu, *Mechanisms of shale gas storage: Implications for shale gas exploration in ChinaMechanisms of Shale Gas Storage.* AAPG bulletin, 2013. **97**(8): p. 1325-1346.

88. Xiong, F., et al., *Pore structure of transitional shales in the Ordos Basin, NW China: Effects of composition on gas storage capacity.* Fuel, 2017. **206**: p. 504-515.

89. Ji, L., et al., *Experimental investigation of main controls to methane adsorption in clay-rich rocks.* Applied Geochemistry, 2012. **27**(12): p. 2533-2545.

90. Busch, A. and Y. Gensterblum, *CBM and CO2-ECBM related sorption processes in coal: a review.* International Journal of Coal Geology, 2011. **87**(2): p. 49-71.

91. Jin, Z. and A. Firoozabadi, *Methane and carbon dioxide adsorption in clay-like slit pores by Monte Carlo simulations.* Fluid Phase Equilibria, 2013. **360**: p. 456-465.

92. Li, J., et al., *Water distribution characteristic and effect on methane adsorption capacity in shale clay.* International Journal of Coal Geology, 2016. **159**: p. 135-154.

93. Tang, X., et al., *Thermodynamic analysis of high pressure methane adsorption in Longmaxi shale.* Fuel, 2017. **193**: p. 411-418.

94. Zhao, H., Z. Lai, and A. Firoozabadi, *Sorption Hysteresis of Light Hydrocarbons and Carbon Dioxide in Shale and Kerogen.* Scientific Reports, 2017. **7**(1): p. 16209.

95. Zhong, J., et al., *Experimental study of the impact on methane adsorption capacity of continental shales with thermal evolution.* Journal of Natural Gas Geoscience, 2016. **1**(2): p. 165-172.

96. Zhou, S., et al., *Difference between excess and absolute adsorption capacity of shale and a new shale gas reserve calculation method.* Natural Gas Industry, 2016. **36**(11): p. 12-20.

97. Lu, X.-C., F.-C. Li, and A.T. Watson, *Adsorption measurements in Devonian shales.* Fuel, 1995. **74**(4): p. 599-603.

98. Myers, A.L. and P.A. Monson, *Physical adsorption of gases: the case for absolute adsorption as the basis for thermodynamic analysis.* Adsorption, 2014. **20**(4): p. 591-622.

99. Mertens, F.O., *Determination of absolute adsorption in highly ordered porous media.* Surface Science, 2009. **603**(10–12): p. 1979-1984.

100. Li, Z., Z. Jin, and A. Firoozabadi, *Phase Behavior and Adsorption of Pure Substances and Mixtures and Characterization in Nanopore Structures by Density Functional Theory.* SPE Journal, 2014. **19**(06): p. 1096-1109.

101. Heller, R. and M. Zoback, *Adsorption of methane and carbon dioxide on gas shale and pure mineral samples.* Journal of unconventional oil and gas resources, 2014. **8**: p. 14-24.

102. Ren, W., et al., *Adsorption and surface diffusion of supercritical methane in shale.* Industrial & Engineering Chemistry Research, 2017. **56**(12): p. 3446-3455.

103. Tsai, M.C., et al., *Adsorption of gas mixture on activated carbon.* Carbon, 1985. **23**(2): p. 167-173.

104. Lewis, W.K., et al., *Pure gas isotherms.* Industrial & Engineering Chemistry, 1950. **42**(7): p. 1326-1332.

105. Grant, R.J. and M. Manes, *Correlation of Some Gas Adsorption Data Extending to Low Pressures and Supercritical Temperatures.* Industrial & Engineering Chemistry Fundamentals, 1964. **3**(3): p. 221-224.

106. Didar, B.R. and I.Y. Akkutlu. *Pore-size dependence of fluid phase behavior and properties in organic-rich shale reservoirs*. in *SPE International Symposium on Oilfield Chemistry*. 2013. Society of Petroleum Engineers.

107. Cristancho-Albarracin, D., et al., *Shale gas storage in kerogen nanopores with surface heterogeneities.* Applied Geochemistry, 2017. **84**: p. 1-10.

108. Langmuir, I., *The constitution and fundamental properties of solids and liquids. Part I. Solids.* Journal of the American chemical society, 1916. **38**(11): p. 2221-2295.

109. Gensterblum, Y., et al., *High-pressure CH4 and CO2 sorption isotherms as a function of coal maturity and the influence of moisture.* International Journal of Coal Geology, 2013. **118**: p. 45-57.

110. Benard, P. and R. Chahine, *Determination of the adsorption isotherms of hydrogen on activated carbons above the critical temperature of the adsorbate over wide temperature and pressure ranges.* Langmuir, 2001. **17**(6): p. 1950-1955.

111. Dubinin, M., *Porous structure and adsorption properties of active carbons.* Chemistry and physics of carbon, 1966. **9**: p. 51-119.

112. Dubinin, M.i., *Physical adsorption of gases and vapors in micropores*, in *Progress in surface and membrane science*. 1975, Elsevier. p. 1-70.

113. Chen, S. and R. Yang, *Theoretical basis for the potential theory adsorption isotherms. The Dubinin-Radushkevich and Dubinin-Astakhov equations.* Langmuir, 1994. **10**(11): p. 4244-4249.

114. Sakurovs, R., et al., *Application of a Modified Dubinin−Radushkevich Equation to Adsorption of Gases by Coals under Supercritical Conditions.* Energy & Fuels, 2007. **21**(2): p. 992-997.

115. Ono, S. and S. Kondo, *Molecular theory of surface tension in liquids*, in *Structure of Liquids/Struktur der Flüssigkeiten*. 1960, Springer. p. 134-280.

116. Aranovich, G.L. and M.D. Donohue, *Adsorption isotherms for microporous adsorbents.* Carbon, 1995. **33**(10): p. 1369-1375.

117. Aranovich, G.L. and M.D. Donohue, *Adsorption of supercritical fluids.* Journal of colloid and interface science, 1996. **180**(2): p. 537-541.

118. Aranovich, G. and M. Donohue, *Predictions of multilayer adsorption using lattice theory.* Journal of colloid and interface science, 1997. **189**(1): p. 101-108.

119. Aranovich, G. and M. Donohue, *Vapor adsorption on microporous adsorbents.* Carbon, 2000. **38**(5): p. 701-708.

120. Bi, H., et al., *The Ono–Kondo model and an experimental study on supercritical adsorption of shale gas: a case study on Longmaxi shale in southeastern Chongqing, China.* Journal of Natural Gas Science and Engineering, 2016. **35**: p. 114-121.

121. Huo, P., et al., *CO 2 geological sequestration: displacement behavior of shale gas methane by carbon dioxide injection.* International Journal of Greenhouse Gas Control, 2017. **66**: p. 48-59.

122. Zhang, D.-F., et al., *Supercritical pure methane and CO2 adsorption on various rank coals of China: experiments and modeling.* Energy & Fuels, 2011. **25**(4): p. 1891-1899.

123. Chalmers, G.R., R.M. Bustin, and I.M. Power, *Characterization of gas shale pore systems by porosimetry, pycnometry, surface area, and field emission scanning electron microscopy/transmission electron microscopy image analyses: Examples from the Barnett, Woodford, Haynesville, Marcellus, and Doig units.* AAPG bulletin, 2012. **96**(6): p. 1099-1119.

124. Curtis, M.E., et al., *Development of organic porosity in the Woodford Shale with increasing thermal maturity.* International Journal of Coal Geology, 2012. **103**: p. 26-31.

125. Jin, Z. and A. Firoozabadi, *Phase behavior and flow in shale nanopores from molecular simulations.* Fluid Phase Equilibria, 2016. **430**: p. 156-168.

126. Jin, Z., *Bubble/dew point and hysteresis of hydrocarbons in nanopores from molecular perspective.* Fluid Phase Equilibria, 2018. **458**: p. 177-185.

127. Orendt, A.M., et al., *Three-dimensional structure of the Siskin Green River Oil Shale Kerogen Model: a comparison between calculated and observed properties.* Energy & Fuels, 2013. **27**(2): p. 702-710.

128. Ungerer, P., J. Collell, and M. Yiannourakou, *Molecular modeling of the volumetric and thermodynamic properties of kerogen: Influence of organic type and maturity.* Energy & Fuels, 2014. **29**(1): p. 91-105.

129. Bousige, C., et al., *Realistic molecular model of kerogen's nanostructure.* Nature materials, 2016. **15**(5): p. 576.

130. Zhou, S., *Comments on paper "the shale gas sorption capacity of transitional shales in the Ordos Basin, NW China".* Fuel, 2017.

131. Bénard, P. and R. Chahine, *Modeling of high-pressure adsorption isotherms above the critical temperature on microporous adsorbents: application to methane.* Langmuir, 1997. **13**(4): p. 808-813.

132. Merey, S. and C. Sinayuc, *Gas‐in‐place calculations in shale gas reservoirs using experimental adsorption data with adsorption models.* The Canadian Journal of Chemical Engineering, 2016. **94**(9): p. 1683-1692.

133. Merey, S. and C. Sinayuc, *Analysis of carbon dioxide sequestration in shale gas reservoirs by using experimental adsorption data and adsorption models.* Journal of Natural Gas Science and Engineering, 2016. **36**: p. 1087-1105.

134. Chen, G., et al., *Keys to linking GCMC simulations and shale gas adsorption experiments.* Fuel, 2017. **199**: p. 14-21.

135. Chen, G., et al., *Adsorption behavior of hydrocarbon on Illite.* Energy & Fuels, 2016. **30**(11): p. 9114-9121.

136. Chen, G., et al., *Research of CO 2 and N 2 Adsorption Behavior in K-Illite Slit Pores by GCMC Method.* Scientific reports, 2016. **6**: p. 37579.

137. Ambrose, R.J., et al., *Shale gas-in-place calculations part I: new pore-scale considerations.* SPE Journal, 2012. **17**(01): p. 219-229.

138. Luo, X., et al., *Adsorption of methane, carbon dioxide and their binary mixtures on Jurassic shale from the Qaidam Basin in China.* International Journal of Coal Geology, 2015. **150**: p. 210-223.

139. Do, D. and H. Do, *Adsorption of supercritical fluids in non-porous and porous carbons: analysis of adsorbed phase volume and density.* Carbon, 2003. **41**(9): p. 1777-1791.

140. Do, D., et al., *On the existence of negative excess isotherms for argon adsorption on graphite surfaces and in graphitic pores under supercritical conditions at pressures up to 10,000 atm.* Langmuir, 2010. **26**(7): p. 4796-4806.

141. Wu, Y., et al., *Methane adsorption capacities of the lower paleozoic marine shales in the Yangtze Platform, South China.* Energy & Fuels, 2015. **29**(7): p. 4160-4167.

142.   Liu, Y., et al., *Determination of the absolute adsorption/desorption isotherms of CH 4 and n-C 4 H 10 on shale from a nano-scale perspective.* Fuel, 2018. **218**: p. 67-77.

143.   Gasparik, M., et al., *First international inter-laboratory comparison of high-pressure CH4, CO2 and C2H6 sorption isotherms on carbonaceous shales.* International Journal of Coal Geology, 2014. **132**: p. 131-146.

144.   Pang, W. and Z. Jin, *Revisiting Methane Absolute Adsorption in Organic Nanopores from Molecular Simulation and Ono-Kondo Lattice Model.* Fuel, 2018. **Under Review**.

145.   Jin, Z., Y. Tang, and J. Wu, *A perturbative density functional theory for square-well fluids.* The Journal of chemical physics, 2011. **134**(17): p. 174702.

146.   Aranovich, G. and M. Donohue, *Theory of multilayer adsorption with correct critical behavior.* Langmuir, 2003. **19**(9): p. 3822-3829.

147.   Hughes, J.D., *Energy: A reality check on the shale revolution.* Nature, 2013. **494**(7437): p. 307.

148.   Pang, W. and Z. Jin, *Ono-Kondo lattice model for propane multilayer adsorption in organic nanopores in relation to shale gas.* Fuel, 2019. **235**: p. 158-166.

149.   Hill, D.G. and C. Nelson, *Gas productive fractured shales: an overview and update.* Gas Tips, 2000. **6**(3): p. 4-13.

150.   Perez, F. and D. Devegowda, *Estimation of adsorbed-phase density of methane in realistic overmature kerogen models using molecular simulations for accurate gas in place calculations.* Journal of Natural Gas Science and Engineering, 2017. **46**: p. 865-872.

151.   Tsai, M., et al., *Adsorption of gas mixture on activated carbon.* Carbon, 1985. **23**(2): p. 167-173.

152.   Lewis, W., *Adsorption Equilibria, Pure Gas Isotherms.* Ind. Eng. Chem., 1950. **42**: p. 1326-1332.

153.   Grant, R. and M. Manes, *Correlation of some gas adsorption data extending to low pressures and supercritical temperatures.* Industrial & Engineering Chemistry Fundamentals, 1964. **3**(3): p. 221-224.

154.   Gensterblum, Y., et al., *European inter-laboratory comparison of high pressure CO2 sorption isotherms II: Natural coals.* International Journal of Coal Geology, 2010. **84**(2): p. 115-124.

155.   Clarkson, C.R. and B. Haghshenas. *Modeling of supercritical fluid adsorption on organic-rich shales and coal.* in *SPE unconventional resources conference-USA.* 2013. Society of Petroleum Engineers.

156.   Pang, W. and Z. Jin, *Revisiting methane absolute adsorption in organic nanopores from molecular simulation and Ono-Kondo lattice model.* Fuel, 2019. **235**: p. 339-349.

157.   Lowell, S., et al., *Characterization of porous solids and powders: surface area, pore size and density*. Vol. 16. 2012: Springer Science & Business Media.

158.   Jin, Z., *Effect of nano-confinement on high pressure methane flow characteristics.* Journal of Natural Gas Science and Engineering, 2017. **45**: p. 575-583.

159.   Jin, Z. and A. Firoozabadi, *Effect of water on methane and carbon dioxide sorption in clay minerals by Monte Carlo simulations.* Fluid Phase Equilibria, 2014. **382**: p. 10-20.

160.   Kadoura, A., A.K. Narayanan Nair, and S. Sun, *Molecular dynamics simulations of carbon dioxide, methane, and their mixture in montmorillonite clay hydrates.* The Journal of Physical Chemistry C, 2016. **120**(23): p. 12517-12529.

161.   Zhang, J. and S. Choi, *Molecular dynamics simulation of methane in potassium montmorillonite clay hydrates.* Journal of Physics B: Atomic, Molecular and Optical Physics, 2006. **39**(18): p. 3839.

162.   Suping, Y., et al., *Advances in research of coal and kerogen nanostructure.* Advances in Earth Sciences, 2012. **27**(4): p. 367-378.

163.   Tan, Z. and K.E. Gubbins, *Adsorption in carbon micropores at supercritical temperatures.* Journal of Physical Chemistry, 1990. **94**(15): p. 6061-6069.

164.   Liu, Y., et al., *Molecular simulation of methane adsorption in shale based on grand canonical Monte Carlo method and pore size distribution.* Journal of Natural Gas Science and Engineering, 2016. **30**: p. 119-126.

165.   Yang, F., et al., *Investigations on the methane sorption capacity of marine shales from Sichuan Basin, China.* International Journal of Coal Geology, 2015. **146**: p. 104-117.

166.   Hill, D. and C. Nelson, *Gas Productive Fractured Shales; an Overview and Update: GasTIPS (Summer)*. 2000, Hart Energy Publishing, Houston, Texas.

167.   Wang, Y., et al., *Investigation of supercritical methane adsorption of overmature shale in Wufeng-Longmaxi Formation, Southern Sichuan Basin, China.* Energy & fuels, 2019. **33**(3): p. 2078-2089.

168.   Clarkson, C.R. and B. Haghshenas, *Modeling of supercritical fluid adsorption on organic-rich shales and coal*, in *SPE Unconventional Resources Conference-USA*. 2013, Society of Petroleum Engineers: Woodlands, Texax, USA.

169.   Li, A., et al., *Investigation of the methane adsorption characteristics of marine shale: a case study of lower cambrian qiongzhusi shale in eastern Yunnan Province, South China.* Energy & Fuels, 2017. **31**(3): p. 2625-2635.

170.   Li, T., et al., *Geochemical characterization and methane adsorption capacity of overmature organic-rich Lower Cambrian shales in northeast Guizhou region, southwest China.* Marine and Petroleum Geology, 2017. **86**: p. 858-873.

171.   Ji, W., et al., *Estimation of marine shale methane adsorption capacity based on experimental investigations of Lower Silurian Longmaxi formation in the Upper Yangtze Platform, south China.* Marine and Petroleum Geology, 2015. **68**: p. 94-106.

172.   Wang, Y., et al., *Methane adsorption measurements and modeling for organic-rich marine shale samples.* Fuel, 2016. **172**: p. 301-309.

173.   Carstens, H. and H. Dypvik, *Abnormal formation pressure and shale porosity.* AAPG Bulletin, 1981. **65**(2): p. 344-350.

174.   Hottmann, C. and R. Johnson, *Estimation of formation pressures from log-derived shale properties.* Journal of Petroleum Technology, 1965. **17**(06): p. 717-722.

175. Didar, B.R. and I.Y. Akkutlu, *Pore-size dependence of fluid phase behavior and properties in organic-rich shale reservoirs*, in *SPE International Symposium on Oilfield Chemistry*. 2013, Society of Petroleum Engineers: Woodlands, Texas, USA.

176. Dubinin, M. *The equation of the characteristic curve of activated charcoal*. in *Dokl. Akad. Nauk. SSSR*. 1947.

177. Huang, L., et al., *Effect of organic type and moisture on CO2/CH4 competitive adsorption in kerogen with implications for CO2 sequestration and enhanced CH4 recovery.* Applied Energy, 2018. **210**: p. 28-43.

178. Ross, D.J.K. and R.M. Bustin, *Shale gas potential of the Lower Jurassic Gordondale member, northeastern British Columbia, Canada.* Bulletin of Canadian Petroleum Geology, 2007. **55**: p. 51-75.

179. Liu, Y. and J. Hou, *Absolute Adsorption of CH 4 on Shale with the Simplified Local-Density Theory.* SPE Journal, 2019: p. 1-14.

180. Yang, R., et al., *Pore characterization and methane sorption capacity of over-mature organic-rich Wufeng and Longmaxi shales in the southeast Sichuan Basin, China.* Marine and Petroleum Geology, 2016. **77**: p. 247-261.

181. Jiang, W. and M. Lin, *Molecular dynamics investigation of conversion methods for excess adsorption amount of shale gas.* Journal of Natural Gas Science and Engineering, 2018. **49**: p. 241-249.

182. Hu, H., et al., *Investigation of methane sorption of overmature Wufeng-Longmaxi shale in the Jiaoshiba area, Eastern Sichuan Basin, China.* Marine and Petroleum Geology, 2018. **91**: p. 251-261.

183. Tian, H., et al., *Characterization of methane adsorption on overmature Lower Silurian-Upper Ordovician shales in Sichuan Basin, southwest China: Experimental results and geological implications.* International Journal of Coal Geology, 2016. **156**: p. 36-49.

184. Song, X., et al., *A modified supercritical Dubinin–Radushkevich model for the accurate estimation of high pressure methane adsorption on shales.* International Journal of Coal Geology, 2018. **193**: p. 1-15.

185. Sakurovs, R., et al., *Application of a modified Dubinin - Radushkevich equation to adsorption of gases by coals under supercritical conditions.* Energy and Fuels, 2007. **21**: p. 992-997.

186. Li, J., et al., *Characterization of methane adsorption on shale and isolated kerogen from the Sichuan Basin under pressure up to 60 MPa: Experimental results and geological implications.* International Journal of Coal Geology, 2018. **189**: p. 83-93.

187. Yu, W., K. Sepehrnoori, and T.W. Patzek, *Modeling gas adsorption in marcellus shale with langmuir and bet isotherms.* SPE Journal, 2016. **21**: p. 589-600.

188. Li, Z.Z., et al., *Investigation of methane adsorption and its effect on gas transport in shale matrix through microscale and mesoscale simulations.* International Journal of Heat and Mass Transfer, 2016. **98**: p. 675-686.

189.   Ottiger, S., et al., *Measuring and Modeling the Competitive Adsorption of CO2, CH4, and N2 on a Dry Coal.* Adsorption, 2008. **14**: p. 539-556.

190.   Ottiger, S., et al., *Competitive adsorption equilibria of CO2 and CH4 on a dry coal.* Adsorption, 2008. **14**: p. 539-556.

191.   Mohammad, S.A., et al., *Measurements and modeling of excess adsorption of pure and mixed gases on wet coals.* Energy and Fuels, 2012. **26**: p. 2899-2910.

192.   Lee, L.L., *Molecular thermodynamics of nonideal fluids.* 2016.

193.   Bahadori, S.Z.A., *Shale Oil and Gas Handbook: Theory, Technologies, and Challenges.* 2016.

194.   Nan, Y., W. Li, and Z. Jin, *Slip length of methane flow under shale reservoir conditions: Effect of pore size and pressure.* Fuel, 2020. **259**.

195.   Wang, Y., et al., *Pore characterization and its impact on methane adsorption capacity for organic-rich marine shales.* Fuel, 2016. **181**: p. 227-237.

196.   Martin, M.G. and J.I. Siepmann, *Transferable Potentials for Phase Equilibria. 1. United-Atom Description of n-Alkanes.* The Journal of Physical Chemistry B, 1998. **102**(14): p. 2569-2577.

197.   Liu, Y. and J. Wilcox, *Molecular simulation of CO2 adsorption in micro- and mesoporous carbons with surface heterogeneity.* International Journal of Coal Geology, 2012. **104**: p. 83-95.

198.   Zhao, T., et al., *Molecular simulation of methane adsorption on type II kerogen with the impact of water content.* Journal of Petroleum Science and Engineering, 2018. **161**: p. 302-310.

199.   Zou, J., R. Rezaee, and K. Liu, *Effect of Temperature on Methane Adsorption in Shale Gas Reservoirs.* Energy and Fuels, 2017. **31**: p. 12081-12092.

200.   Chen, G., et al., *Adsorption Behavior of Hydrocarbon on Illite.* Energy and Fuels, 2016. **30**: p. 9114-9121.

201.   Sudibandriyo, M., et al., *Ono-Kondo model for high-pressure mixed-gas adsorption on activated carbons and coals.* Energy and Fuels, 2011. **25**: p. 3355-3367.

202.   Sudibandriyo, M., et al., *Ono-Kondo lattice model for high-pressure adsorption: Pure gases.* Fluid Phase Equilibria, 2010. **299**: p. 238-251.

203.   Bénard, P. and R. Chahine, *Modeling of high-pressure adsorption isotherms above the critical temperature on microporous adsorbents: Application to methane.* Langmuir, 1997. **13**: p. 808-812.

204.   Wang, Y., et al., *Characteristics of the Nanoscale Pore Structure in Northwestern Hunan Shale Gas Reservoirs Using Field Emission Scanning Electron Microscopy, High-Pressure Mercury Intrusion, and Gas Adsorption.* Energy & Fuels, 2014. **28**: p. 945-955.

205.   Liu, K., M. Ostadhassan, and J. Cai, *Characterizing Pore Size Distributions of Shale.* Petrophysical Characterization and Fluids Transport in Unconventional Reservoirs, 2019: p. 3-20.

206. Psarras, P., et al., *Methane and CO2 Adsorption Capacities of Kerogen in the Eagle Ford Shale from Molecular Simulation.* Accounts of Chemical Research, 2017. **50**: p. 1818-1828.

207. Cao, T., et al., *Characterization of pore structure and fractal dimension of Paleozoic shales from the northeastern Sichuan Basin, China.* Journal of Natural Gas Science and Engineering, 2016. **35**: p. 882-895.

208. Liu, K., et al., *Nanopore structures of isolated kerogen and bulk shale in Bakken Formation.* Fuel, 2018. **226**: p. 441-453.

209. Langmuir, I., *The Adsorption of Gases on Plane Surfaces of Glass, Mica and Plantinum.* Journal of the American Chemical Society, 1918. **40**: p. 1361-403.

210. Brunauer, S., P.H. Emmett, and E.J.J.o.t.A.c.s. Teller, *Adsorption of gases in multimolecular layers.* 1938. **60**(2): p. 309-319.

211. Wei, M., et al., *The effect of sample particle size on the determination of pore structure parameters in shales.* International Journal of Coal Geology, 2016. **163**: p. 177-185.

212. EIA. *Annual energy outlook 2019 with projections to 2050.* 2019; Available from: https://www.eia.gov/outlooks/aeo/pdf/aeo2019.pdf.

213. Pang, W., Y. Wang, and Z. Jin, *Comprehensive Review about Methane Adsorption in Shale Nanoporous Media.* Energy & Fuels, 2021.

214. Saha, D., et al., *Postextraction Separation, On-Board Storage, and Catalytic Conversion of Methane in Natural Gas: A Review.* Chemical Reviews, 2016. **116**: p. 11436-11499.

215. Wang, H., et al., *Review of molecular simulation method for gas adsorption/desorption and diffusion in shale matrix.* Journal of Thermal Science, 2019. **28**(1): p. 1-16.

216. Chalmers, G.R., R.M. Bustin, and I.M. Power, *Characterization of gas shale pore systems by porosimetry, pycnometry,surfacearea,andfield emission scanning electron microscopy/ transmission electron microscopy image analyses: Examples from the Barnett, Woodford, Haynesville, Marcellus,andDoig units.* AAPG Bulletin, 2012. **96**: p. 1099-1119.

217. Pang, Y., Y. He, and S. Chen, *An innovative method to characterize sorption-induced kerogen swelling in organic-rich shales.* Fuel, 2019. **254**: p. 115629.

218. Li, T. and C. Wu, *Continual refined isothermal adsorption of pure illite in shale with gravimetric method.* Journal of Petroleum Science and Engineering, 2019. **172**: p. 190-198.

219. Ottiger, S., et al., *Measuring and Modeling the Competitive Adsorption of CO2, CH4, and N2 on a Dry Coal.* Langmuir, 2008. **24**(17): p. 9531-9540.

220. Aljamaan, H., M. Al Ismail, and A.R. Kovscek, *Experimental investigation and Grand Canonical Monte Carlo simulation of gas shale adsorption from the macro to the nano scale.* Journal of Natural Gas Science and Engineering, 2017. **48**: p. 119-137.

221. Dang, W., et al., *Isotherms, thermodynamics and kinetics of methane-shale adsorption pair under supercritical condition: Implications for understanding the nature of shale gas adsorption process.* Chemical Engineering Journal, 2020. **383**: p. 123191.

222. Myers, A.L., *Thermodynamics of adsorption in porous materials.* AIChE Journal, 2002. **48**: p. 145-160.

223.   Liu, Y., et al., *Determination of the absolute adsorption/desorption isotherms of CH4 and n-C4H10 on shale from a nano-scale perspective.* Fuel, 2018. **218**: p. 67-77.

224.   Wang, J., Y. Wei, and Z. Ma, *Modified Dual-Site Langmuir Adsorption Equilibrium Models from A GCMC Molecular Simulation.* Applied Sciences, 2020. **10**(4): p. 1311.

225.   Ye, Z., et al., *An improved Langmuir model for evaluating methane adsorption capacity in shale under various pressures and temperatures.* Journal of Natural Gas Science and Engineering, 2016. **31**: p. 658-680.

226.   Liu, D., et al., *High-pressure adsorption of methane on montmorillonite, kaolinite and illite.* Applied Clay Science, 2013. **85**: p. 25-30.

227.   Shao, X., W. Wang, and X. Zhang, *Experimental measurements and computer simulation of methane adsorption on activated carbon fibers.* Carbon, 2007. **45**(1): p. 188-195.

228.   Li, J., et al., *Effects of energetic heterogeneity on gas adsorption and gas storage in geologic shale systems.* Applied Energy, 2019. **251**: p. 113368.

229.   Pang, W., Y. Ye, and Z. Jin, *Assessment of Various Approaches in the Prediction of Methane Absolute Adsorption in Kerogen Nanoporous Media.* Energy & Fuels, 2019. **33**: p. 6258-6263.

230.   Xiong, J., X. Liu, and L. Liang, *Experimental study on the pore structure characteristics of the Upper Ordovician Wufeng Formation shale in the southwest portion of the Sichuan Basin, China.* Journal of Natural Gas Science Engineering, 2015. **22**: p. 530-539.

231.   Wang, S., et al., *The methane sorption capacity of Paleozoic shales from the Sichuan Basin, China.* 2013. **44**: p. 112-119.

232.   Liu, Y., et al., *Reservoir characteristics and methane adsorption capacity of the Upper Triassic continental shale in Western Sichuan Depression, China.* Australian Journal of Earth Sciences, 2017. **64**(6): p. 807-823.

233.   Tan, J., et al., *Shale gas potential of the major marine shale formations in the Upper Yangtze Platform, South China, Part II: Methane sorption capacity.* Fuel, 2014. **129**: p. 204-218.

234.   Chen, F., et al., *Evaluation of the density and thickness of adsorbed methane in differently sized pores contributed by various components in a shale gas reservoir: A case study of the Longmaxi Shale in Southeast Chongqing, China.* Chemical Engineering Journal, 2019. **367**: p. 123-138.

235.   Tian, Y., C. Yan, and Z. Jin, *Characterization of methane excess and absolute adsorption in various clay nanopores from molecular simulation.* Scientific reports, 2017. **7**(1): p. 1-21.

236.   Holmes, R., et al., *Idealized Shale Sorption Isotherm Measurements To Determine Pore Capacity, Pore Size Distribution, and Surface Area.* Energy & Fuels, 2019. **33**(2): p. 665-676.

237.   Chen, G., et al., *GCMC simulations on the adsorption mechanisms of CH4 and CO2 in K-illite and their implications for shale gas exploration and development.* Fuel, 2018. **224**: p. 521-528.

238.   Ji, L., et al., *Experimental investigation of main controls to methane adsorption in clay-rich rocks.* Applied Geochemistry, 2012. **27**: p. 2533-2545.

239.   Pang, W., Z.J.E. Jin, and Fuels, *Methane Absolute Adsorption in Kerogen Nanoporous Media With Realistic Continuous Pore Size Distributions.* 2020.

240.   Yang, Y., et al., *Adsorption behaviors of shale oil in kerogen slit by molecular simulation.* Chemical Engineering Journal, 2020. **387**: p. 124054.

241.   Mosher, K., et al., *Molecular simulation of methane adsorption in micro- and mesoporous carbons with applications to coal and gas shale systems.* International Journal of Coal Geology, 2013. **109-110**: p. 36-44.

242.   Zhou, J., Z. Jin, and K.H. Luo, *Insights into recovery of multi-component shale gas by CO2 injection: A molecular perspective.* Fuel, 2020. **267**: p. 117247.

243.   Wang, Y. and Z. Jin, *Effect of pore size distribution on hydrocarbon mixtures adsorption in shale nanoporous media from engineering density functional theory.* Fuel, 2019. **254**: p. 115650.

244.   Xiong, J., et al., *Investigation of the factors influencing methane adsorption on illite.* Energy Science & Engineering, 2019. **7**(6): p. 3317-3331.

245.   Hao, Y., et al., *Molecular simulations of methane adsorption behavior in illite nanopores considering basal and edge surfaces.* Energy & Fuels, 2018. **32**(4): p. 4783-4796.

246.   Ono, S. and S. Kondo, *Molecular Theory of Surface Tension in Liquids.* Structure of Liquids / Struktur der Flüssigkeiten, 1960. **255**: p. 134-280.

247.   Aranovich, G. and M.J.T.J.o.c.p. Donohue, *A new model for lattice systems.* 1996. **105**(16): p. 7059-7063.

248.   Aranovich, G.L. and M.D. Donohue, *Surface compression in adsorption systems.* 2001. **188**: p. 95-108.

249.   Donohue, M.D. and G.L. Aranovich, *A new classification of isotherms for Gibbs adsorption of gases on solids.* Fluid Phase Equilibria, 1999. **158-160**: p. 557-563.

250.   Tang, X., et al., *A dual-site Langmuir equation for accurate estimation of high pressure deep shale gas resources.* Fuel, 2016. **185**: p. 10-17.

251.   Ozawa, S., S. Kusumi, and Y. Ogino, *Physical adsorption of gases at high pressure. IV. An improvement of the Dubinin—Astakhov adsorption equation.* Journal of Colloid and Interface Science, 1976. **56**(1): p. 83-91.

252.   Liang, L., et al., *An investigation into the thermodynamic characteristics of methane adsorption on different clay minerals.* Journal of Natural Gas Science and Engineering, 2016. **33**: p. 1046-1055.

253.   Clarkson, C., R. Bustin, and J. Levy, *Application of the mono/multilayer and adsorption potential theories to coal methane adsorption isotherms at elevated temperature and pressure.* Carbon, 1997. **35**(12): p. 1689-1705.

254.   Hao, S., et al., *Methane adsorption characteristics on coal surface above critical temperature through Dubinin–Astakhov model and Langmuir model.* Colloids and Surfaces A: Physicochemical and Engineering Aspects, 2014. **444**: p. 104-113.

255.   Xiong, F., et al., *Reexamining supercritical gas adsorption theories in nano-porous shales under geological conditions.* Fuel, 2020. **287**: p. 119454.

256.   Terzyk, A.P., et al., *Developing the solution analogue of the Toth adsorption isotherm equation.* Journal of colloid and interface science, 2003. **266**(2): p. 473-476.

257.   Sips, R., *Combined form of Langmuir and Freundlich equations.* J. Chem. Phys, 1948. **16**(429): p. 490-495.

258.   Freundlich, H., *Kapillarchemie: eine Darstellung der Chemie der Kolloide und verwandter Gebiete.* 1922: akademische Verlagsgesellschaft.

259.   Tian, Y., C. Yan, and Z. Jin, *Characterization of Methane Excess and Absolute Adsorption in Various Clay Nanopores from Molecular Simulation.* Scientific Reports, 2017. **7**: p. 1-21.

260.   Talu, O. and A.L. Myers, *Reference potentials for adsorption of helium, argon, methane, and krypton in high-silica zeolites.* Colloids and Surfaces A: Physicochemical and Engineering Aspects, 2001. **187-188**: p. 83-93.

261.   Steele, W.A., *The physical interaction of gases with crystalline solids: I. Gas-solid energies and properties of isolated adsorbed atoms.* Surface Science, 1973. **36**(1): p. 317-352.

262.   Widom, B., *Some Topics in the Theory of Fluids.* The Journal of Chemical Physics, 1963. **39**(11): p. 2808-2812.

263.   Metropolis, N., et al., *Equation of State Calculations by Fast Computing Machines.* The Journal of Chemical Physics, 1953. **21**(6): p. 1087-1092.

264.   Xiong, F., et al., *Reexamining supercritical gas adsorption theories in nano-porous shales under geological conditions.* Fuel, 2021. **287**: p. 119454.

265.   Zhang, J., et al., *Methane and Carbon Dioxide Adsorption on Illite.* Energy and Fuels, 2016. **30**: p. 10643-10652.

266.   Zhou, S., et al., *A modified BET equation to investigate supercritical methane adsorption mechanisms in shale.* 2019. **105**: p. 284-292.

267.   Tang, X., et al., *Adsorption models for methane in shales: Review, comparison, and application.* Energy & Fuels, 2017. **31**(10): p. 10787-10801.

268.   Wang, Z., et al., *Analyzing the adaption of different adsorption models for describing the shale gas adsorption law.* Chemical Engineering & Technology, 2016. **39**(10): p. 1921-1932.

Appendix

A. Derivation of Ono-Kondo model

Consider taking an adsorbate molecule at site k and moving it to an empty site infinitely distant, the exchange of the molecules in the lattice with a vacancy can be written as

$$M_k + V_\infty \rightarrow V_k + M_\infty,$$ (A1)

where M represents adsorbate molecule, V is the vacancy, k denotes the adsorbed site and ∞ is the site at infinite distance which can be seen as bulk.

If such exchange of molecules reaches equilibrium at isothermal and isobaric condition,

$$\Delta G_i = \Delta H_i - T\Delta S_i = 0,$$ (A2)

where ΔG_i, ΔH_i and ΔS_i are the Gibbs free energy, enthalpy and entropy changes in each layer due to molecule exchange and T is the absolute temperature. The entropy change can be written as [118],

$$\Delta S_i = k_B \ln W_{1,i} - k_B \ln W_{2,i},$$ (A3)

$$\frac{W_{1,i}}{W_0} = x_i \left(1 - x_b\right),$$ (A4)

$$\frac{W_{2,i}}{W_0} = x_b \left(1 - x_i\right),$$ (A5)

where k_B is Boltzmann's constant, $W_{1,i}$ refers to the number of configurations where the fluid molecule occupies the absorbed phase and the site in the bulk phase is at vacancy at layer i, $W_{2,i}$ is the number of configurations where the absorbed phase is empty and fluid molecule occupies bulk phase at layer i, W_0 refers to the overall number of system configurations, x_i is the fraction of absorbed phase molecules occupies the layer i and x_b is the fraction of molecules in the bulk phase. In this work, the occupation fractions are given as,

$$x_i = \frac{\rho_{a,i}}{\rho_{am}}, \tag{A6}$$

$$x_b = \frac{\rho_b}{\rho_{am}}, \tag{A7}$$

where $\rho_{a,i}$ is the density of layer i, ρ_{am} is the maximum adsorbed density in each layer and ρ_b is the bulk density.

By substituting Eqs. (A6) and (A7) into Eq. (A5), we can obtain

$$\Delta S_i = k_B \left[\frac{x_i (1 - x_b)}{x_b (1 - x_i)} \right]. \tag{A8}$$

The enthalpy change for three dimensional OK model can be represented by the interactions of neighboring molecules located in the same and adjacent layers based on the mean-field approximation [118],

$$\Delta H_i = -\varepsilon\left(z_1 x_{i+1} + z_2 x_i + z_1 x_{i-1} - z_0 x_b\right), \quad i \geq 2, \tag{A9}$$

where ε is adsorbate-adsorbate interaction energy, z_0 is the bulk coordination number, z_2 is the coordination number within one layer and $z_1 = (z_0 - z_2)/2$. For a cubic lattice configuration, $z_0 = 6$, $z_1 = 1$, $z_2 = 4$. Considering the interactions between adsorbate and adsorbent surface, ε_s, we have the enthalpy change when adsorbate is in the first layer:

$$\Delta H_i = -\varepsilon\left(z_1 x_{i+1} + z_2 x_i - z_0 x_b\right) - \varepsilon_s, \quad i = 1. \tag{A10}$$

B. Molecular Model

In this work, we carry out GCMC simulations to model methane adsorption behavior in carbon nanopores. In this work, the graphite slab is used to represent the pore surface wall which has the dimensions of 6 nm × 6 nm in $x - y$ plane parallel to pore surface with two-dimensional periodic boundary conditions. The pore width W is characterized by the separation of two rigid planar structureless carbon surfaces in z direction. The results from 6 nm by 6 nm dimensions in x-y plane can replicate that with larger dimensions (i.e., 8 nm by 8 nm). Therefore, we use 6 nm by 6 nm dimensions in our calculations.

In our simulation, we use a single site model to describe methane and helium molecules. The TraPPE force field is used to represent the methane intermolecular interactions [196]. Intermolecular interactions are represented by pairwise-additive Lennard-Jones (LJ) 12-6 potentials,

245

$$u_{LJ}(r) = 4\varepsilon_f \left[\left(\frac{\sigma_f}{r} \right)^{12} - \left(\frac{\sigma_f}{r} \right)^{6} \right],$$ (B1)

where r is the separation distance; $\sigma_f = 0.373$ nm and $\varepsilon_f / k_B = 148.0$ K are size and energy parameter for methane [196], respectively; The LJ parameter for -CH$_3$ are $\sigma = 0.375$ nm and $\varepsilon / k_B = 98.0$ K, respectively; for -CH$_2$- group are $\sigma = 0.395$ nm and $\varepsilon / k_B = 46.0$ K, respectively [196]; $\sigma_f = 0.264$ nm and $\varepsilon_f / k_B = 10.9$ K are size and energy parameter for helium [260], respectively.

The bond bending potential for propane U_{bend} is given as,

$$U_{bend}(\theta) = \frac{K_\theta}{2} \left(\theta - \theta_{eq} \right)^2,$$ (B2)

where $K_\theta = 62500$ K rad^{-2}, θ is the bond angle of propane and θ_{eq} is the equilibrium angle which is set as 114° [196].

In this work, pores are of slit geometry with smooth and structureless carbon surfaces. We use 10-4-3 Steele potentials to describe the fluid-wall interaction φ_{wf} [261],

$$\varphi_{wf}(z) = 2\pi \rho_w \varepsilon_{wf} \sigma_{wf}^2 \Delta \left[\frac{2}{5} \left(\frac{\sigma_{wf}}{z} \right)^{10} - \left(\frac{\sigma_{wf}}{z} \right)^4 - \frac{\sigma_{wf}^4}{3\Delta(0.61\Delta + z)^3} \right],$$ (B3)

where $\rho_w = 114$ nm^{-3}, $\varepsilon_{wf} = \sqrt{\varepsilon_w \varepsilon_f}$ with $\varepsilon_w = 28$ K, $\sigma_{wf} = (\sigma_w + \sigma_f)/2$ with $\sigma_w = 0.3345$ nm, and $\Delta = 0.335$ nm, respectively. The external potential Ψ in a slit pore is expressed as

$$\Psi(z) = \varphi_{wf}(z) + \varphi_{wf}(W - z), \qquad \text{(B4)}$$

where W is the slit-pore size.

The GCMC simulation is carried out under grand canonical (μVT) ensemble. In each MC cycle, a trial random displacement is applied to a randomly selected gas molecule and a gas molecule is randomly removed from or inserted into the simulation box at equal probability depending on the chemical potential of the gas. The chemical potentials of methane and helium molecules for given pressure and temperature conditions are obtained from the Widom insertion method [262] in canonical (NVT) ensemble in bulk. The bulk densities are obtained from National Institute of Standards and Technology (NIST) Chemistry Webbook. The MC moves are implemented by the Metropolis algorithm [263]. We conduct 0.5 million MC cycles per methane molecules for equilibration and 2 million MC cycles per methane molecules for sampling density distributions. We found that doubling MC cycles (one million for equilibration and 4 million for sampling) yields the same results.

In our GCMC simulation, excess adsorption is obtained based on the volumetric method [51],

$$m_{ex} = \frac{\langle N_{C_1} \rangle / N_A - V_p \rho_{C_1,b}^m}{2S_A}, \qquad \text{(B5)}$$

where $\langle N_{C_1} \rangle$ is the ensemble averaged number of methane molecules at given temperature and pressure in the nanopores, $\rho_{C_1,b}^m$ is the molar density of methane in the bulk at given

conditions and S_A is the specific surface area of the pore. In this work, we use mmol/m^2 to describe excess adsorption amount.

C. Helium adsorption in carbon materials

Helium adsorption is applied to obtain the effective pore width in carbon nanopores at 333.15 K. **Figure C1** shows the density profile of helium in 4 nm pores at various pressures. It can be seen from the figure that the helium shows an adsorption behavior near the surface, resulting in a larger effective pore width compared with our previous work [51] in clay minerals. As the same procedure of calculating effective pore width in our earlier studies, the linear relationship between $\langle N_{He} \rangle$ and $\rho_{He,b}^{m}$ is shown in **Figure C2**. Thus, the calculated effective pore widths at each pressure are depicted in **Figure C3** using the Eq. (2.13). The calculated effective pore width is smaller than 4 nm, because of the finite size of helium [134].
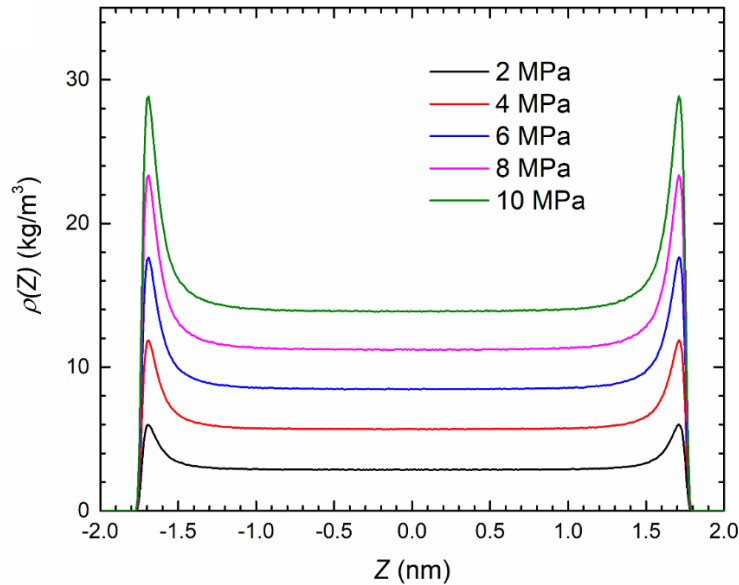
Figure C1 Density profiles of Helium in carbon nanopore of $W = 4$ nm at 333.15 K.
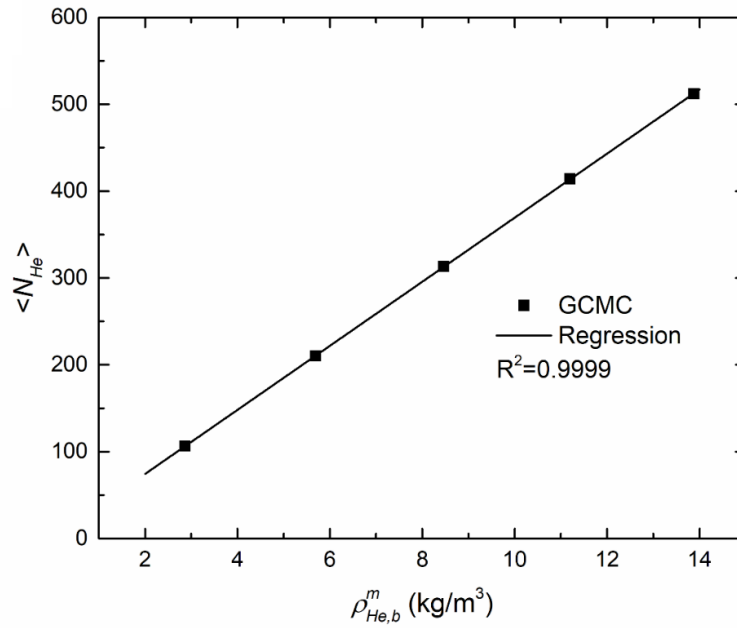
Figure C2 Relationship between total helium uptake and bulk density in carbon nanopore of $W = 4$ nm at 333.15 K.
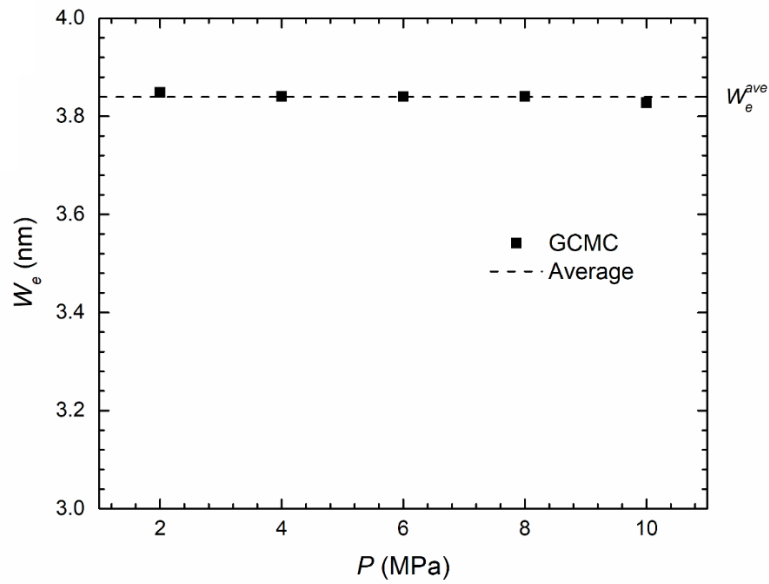
Figure C3 Effective pore width by helium adsorption at different pressures in carbon nanopore of $W = 4$ nm at 333.15 K, the dashed line points out the averaged pore width of calculated five pressure conditions.

D. Supporting information of Chapter 5

D.1 Pressure dependent density from GCMC density profile

Table D1 Adsorbed phase density of the first layer in 4 nm pore by GCMC simulation at 333.15 K

Pressure (bar)	Adsorbed phase density (kg/m³)
50	155.3357
100	200.6011
150	222.4834
200	236.0386
250	245.6331
300	252.9785
350	258.9108
400	264.2465
450	268.6055
500	272.2619

D.2 High-pressure and low-pressure fitting

Figure D1(a) shows the fitted $m_{ex,T}$ of 1000 samples from five adsorption models (LA, SDR, LA-0.38, SDR-0.38, and OK-PSD) up to 500 bar at 333.15 K. The symbols represent the averaged 1000-sample $m_{ex,T}$ and error bars are plotted. The low-pressure fitting results shown in **Figure D1(b)** present the excess adsorption regression of adsorption models from

25 bar to 150 bar, while higher pressure results are based on the extrapolation.
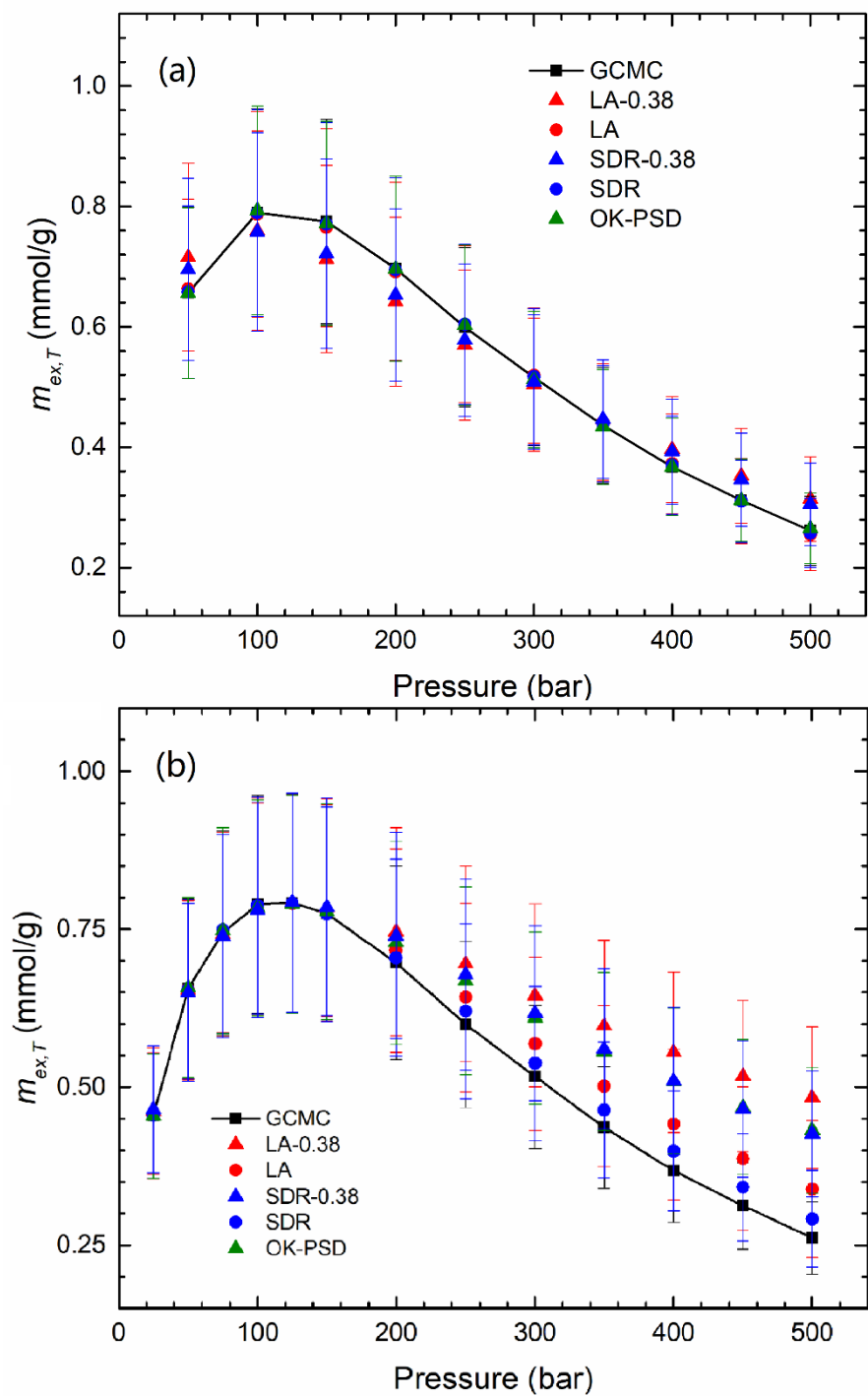
Figure D1 Excess adsorption amount (a) up to 500 bar; (b) up to 150 bar at 333.15 K.

The root-mean square deviation (*RMSD*) is defined as,

$$RMSD = \sqrt{\frac{1}{q}\sum_{i=1}^{q}\left(\left(m_{abs,tested}^{L1}\right)^2 - \left(m_{abs,GCMC}^{L1}\right)^2\right)}, \tag{C1}$$

which evaluates the deviations from GCMC simulation results. The R^2 of regressing excess adsorption and *RMSD*s of absolute adsorption for high-pressure and low-pressure fittings are listed in **Table D3** and **Table D4**, respectively.

Table D2 R^2 and *RMSD*s of high-pressure range fitting by different adsorption models

Methods	$R^2_{m_{ex,T}^{calculated}}$	$RMSD_{m_{abs,T}^{L1,calculated}}$ **(mmol/g)**
OK-PSD	0.9996	0.0540
LA	0.9986	0.2442
LA-0.38	0.9614	0.0621
SDR	0.9998	0.2018
SDR-0.38	0.9743	0.0697

Table D3 R^2 and *RMSD*s of low-pressure range fitting by different adsorption models

Methods	$R^2_{m_{ex,T}^{calculated}}$	$RMSD_{m_{abs,T}^{L1,calculated}}$ **(mmol/g)**
OK-PSD	0.8323	0.1504
LA	0.9375	0.1990
LA-0.38	0.7041	0.1090
SDR	0.9859	0.1770
SDR-0.38	0.8277	0.1241

E. Supporting information of Chapter 6

E.1 Root mean square deviations (RMSDs) of samples in adsorption amounts between GCMC and adsorption models

E1.1 Total adsorption amount

The RMSDs of total adsorption amount in 1250 samples of averaging over all adsorption types, micropore volumes and pressures are given as,

$$
\left\{
\begin{aligned}
RMSD_{ex} &= \sqrt{\frac{1}{75000} \sum_{PSD=1}^{1250} \sum_{P=50bar}^{500bar} \sum_{j=TypeI}^{TypeVI} \left(\left(m_{ex,PSD,P,j}^{MC} \right)^2 - \left(m_{ex,PSD,P,j}^{model} \right)^2 \right)} \\
RMSD_{abs1} &= \sqrt{\frac{1}{75000} \sum_{PSD=1}^{1250} \sum_{P=50bar}^{500bar} \sum_{j=TypeI}^{TypeVI} \left(\left(m_{abs1,PSD,P,j}^{MC} \right)^2 - \left(m_{abs1,PSD,P,j}^{model} \right)^2 \right)} \\
RMSD_{abs2} &= \sqrt{\frac{1}{75000} \sum_{PSD=1}^{1250} \sum_{P=50bar}^{500bar} \sum_{j=TypeI}^{TypeVI} \left(\left(m_{abs2,PSD,P,j}^{MC} \right)^2 - \left(m_{abs2,PSD,P,j}^{model} \right)^2 \right)} \\
RMSD_{abs} &= \sqrt{\frac{1}{75000} \sum_{PSD=1}^{1250} \sum_{P=50bar}^{500bar} \sum_{j=TypeI}^{TypeVI} \left(\left(m_{abs,PSD,P,j}^{MC} \right)^2 - \left(m_{abs,PSD,P,j}^{model} \right)^2 \right)}
\end{aligned}
\right. ,
$$

(E1)

where $RMSD_{ex}$, $RMSD_{abs1}$, $RMSD_{abs2}$ and $RMSD_{abs}$ represent the combined root mean square deviation of adsorption model with GCMC simulations in m_{ex}, m_{abs1}, m_{abs2} and m_{abs} in six different adsorption types for 1250 PSD samples, respectively.

E1.2 RMSD in each adsorption types and pressures

The RMSDs of total adsorption amount in 1250 samples in terms of adsorption type by

averaging over all micropore volumes and pressures are given as,

$$
\begin{cases}
RMSD_{ex,j}^{type} = \sqrt{\dfrac{1}{12500} \sum\limits_{PSD=1}^{1250} \sum\limits_{P=50bar}^{500bar} \left(\left(m_{ex,PSD,P,j}^{MC} \right)^2 - \left(m_{ex,PSD,P,j}^{model} \right)^2 \right)} \\[2.5ex]
RMSD_{abs1,j}^{type} = \sqrt{\dfrac{1}{12500} \sum\limits_{PSD=1}^{1250} \sum\limits_{P=50bar}^{500bar} \left(\left(m_{abs1,PSD,P,j}^{MC} \right)^2 - \left(m_{abs1,PSD,P,j}^{model} \right)^2 \right)} \\[2.5ex]
RMSD_{abs2,j}^{type} = \sqrt{\dfrac{1}{12500} \sum\limits_{PSD=1}^{1250} \sum\limits_{P=50bar}^{500bar} \left(\left(m_{abs2,PSD,P,j}^{MC} \right)^2 - \left(m_{abs2,PSD,P,j}^{model} \right)^2 \right)} \\[2.5ex]
RMSD_{abs,j}^{type} = \sqrt{\dfrac{1}{12500} \sum\limits_{PSD=1}^{1250} \sum\limits_{P=50bar}^{500bar} \left(\left(m_{abs,PSD,P,j}^{MC} \right)^2 - \left(m_{abs,PSD,P,j}^{model} \right)^2 \right)}
\end{cases}
\tag{E2}
$$

The RMSDs of total adsorption amount in 1250 samples in terms of pressures by averaging

over all adsorption types and micropore volumes are given as,

$$
\begin{cases}
RMSD_{ex,P}^{pressure} = \sqrt{\dfrac{1}{12500} \sum\limits_{PSD=1}^{1250} \sum\limits_{j=TypeI}^{TypeVI} \left(\left(m_{ex,PSD,P,j}^{MC} \right)^2 - \left(m_{ex,PSD,P,j}^{model} \right)^2 \right)} \\[2.5ex]
RMSD_{abs1,P}^{pressure} = \sqrt{\dfrac{1}{12500} \sum\limits_{PSD=1}^{1250} \sum\limits_{j=TypeI}^{TypeVI} \left(\left(m_{abs1,PSD,P,j}^{MC} \right)^2 - \left(m_{abs1,PSD,P,j}^{model} \right)^2 \right)} \\[2.5ex]
RMSD_{abs2,P}^{pressure} = \sqrt{\dfrac{1}{12500} \sum\limits_{PSD=1}^{1250} \sum\limits_{j=TypeI}^{TypeVI} \left(\left(m_{abs2,PSD,P,j}^{MC} \right)^2 - \left(m_{abs2,PSD,P,j}^{model} \right)^2 \right)} \\[2.5ex]
RMSD_{abs,P}^{pressure} = \sqrt{\dfrac{1}{12500} \sum\limits_{PSD=1}^{1250} \sum\limits_{j=TypeI}^{TypeVI} \left(\left(m_{abs,PSD,P,j}^{MC} \right)^2 - \left(m_{abs,PSD,P,j}^{model} \right)^2 \right)}
\end{cases}
\tag{E3}
$$

E.2 Mean relative errors (MREs) of samples in adsorption amounts between GCMC and adsorption models

The relative errors in various adsorption amounts between the GCMC simulations and the

adsorption model in each case are given as,

$$\begin{cases} \delta_{ex} = \left(m_{ex,T}^{MC} - m_{ex,T}^{model} \right) / m_{ex,T}^{MC} \\ \delta_{abs1} = \left(m_{abs1,T}^{MC} - m_{abs1,T}^{model} \right) / m_{abs1,T}^{MC} \\ \delta_{abs2} = \left(m_{abs2,T}^{MC} - m_{abs2,T}^{model} \right) / m_{abs2,T}^{MC} \\ \delta_{abs} = \left(m_{abs,T}^{MC} - m_{abs,T}^{model} \right) / m_{abs,T}^{MC} \end{cases}, \quad \text{(E4)}$$

where δ_{ex}, δ_{abs1}, δ_{abs2} and δ_{abs} represent the relative errors between the adsorption model and GCMC simulations in excess adsorption, absorption in 1st layer, absolute adsorption beyond 1st layer and absolute adsorption within combined layers, respectively. Then, the mean relative errors for 1250 PSD samples at each pressure condition can be given as,

$$\begin{cases} MRE_{ex} = \dfrac{1}{1250} \sum_{PSD=1}^{1250} \delta_{ex,PSD} \\ MRE_{abs1} = \dfrac{1}{1250} \sum_{PSD=1}^{1250} \delta_{abs1,PSD} \\ MRE_{abs2} = \dfrac{1}{1250} \sum_{PSD=1}^{1250} \delta_{abs2,PSD} \\ MRE_{abs} = \dfrac{1}{1250} \sum_{PSD=1}^{1250} \delta_{abs,PSD} \end{cases}, \quad \text{(E5)}$$

in which MRE_{ex}, MRE_{abs1}, MRE_{abs2} and MRE_{abs} represent the averages of δ_{ex}, δ_{abs1}, δ_{abs2} and δ_{abs} for 1250 samples, respectively.

255
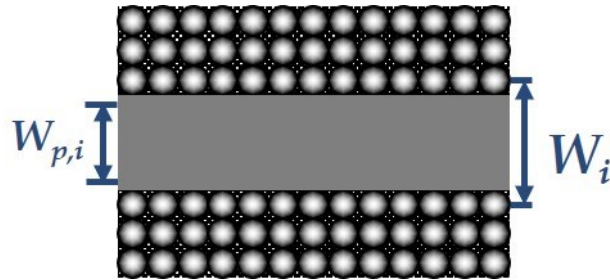
Figure E1 Schematic representation of carbon slit model. W_i refers to the separation distance between two rigid planar structureless carbon surfaces and $W_{p,i}$ refers to the effective pore width obtained from helium adsorption.
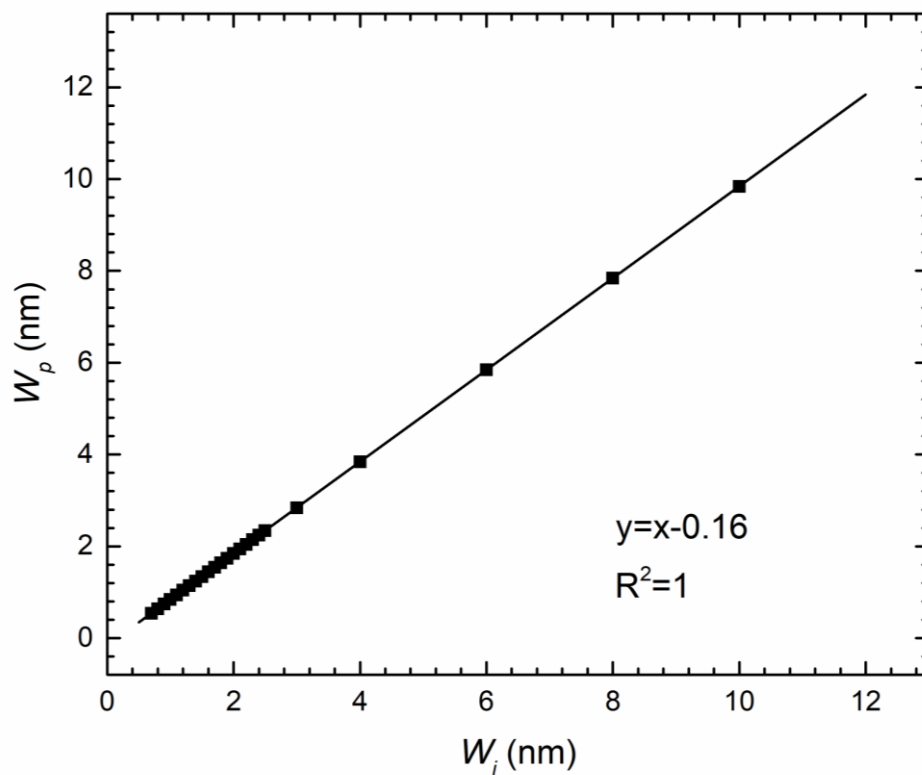
Figure E2 Relation between W_i and $W_{p,i}$. The solid squares represent $W_{p,i}$ and the line represents a linear fitting between W_i and $W_{p,i}$.
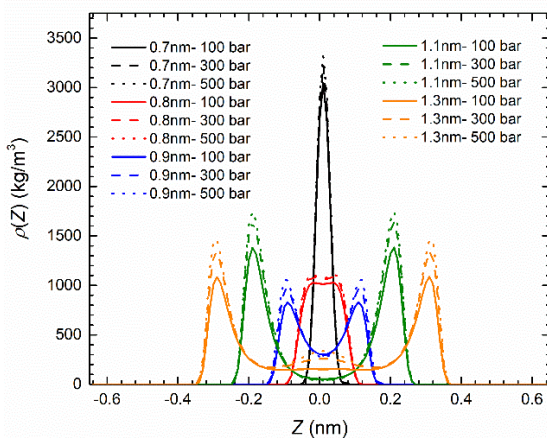
(a)
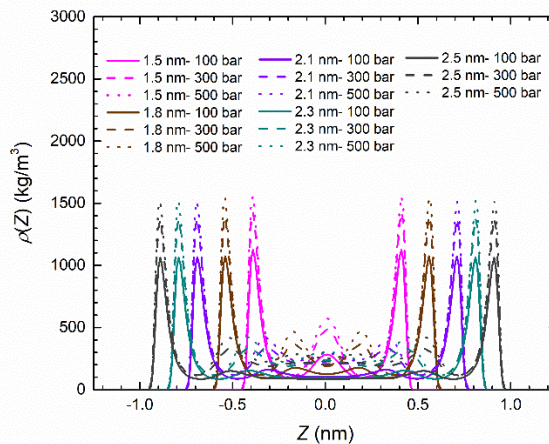
(b)
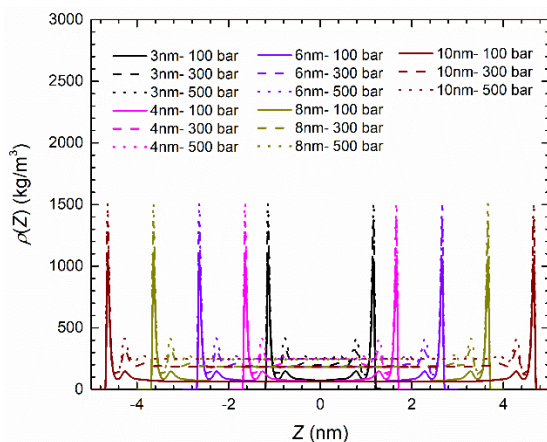
(c)
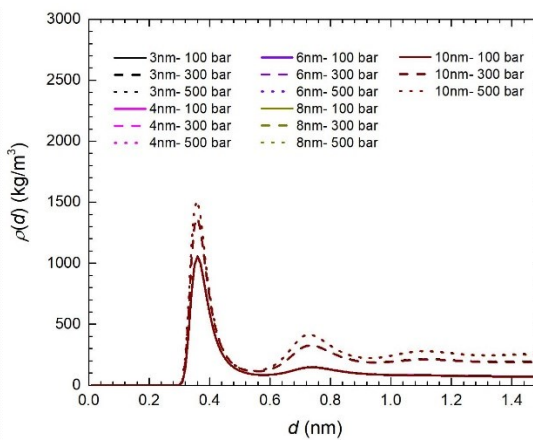
(d)

Figure E3 (a), (b) and (c) CH$_4$ density distributions in various nanopores at 100, 300 and 500 bar as well as 333.15 K from the GCMC simulations; (d) CH$_4$ density distributions in terms of the distance to the pore surface d at 100, 300 and 500 bar as well as 333.15 K from the GCMC simulations.

(a)

(b)

(c)
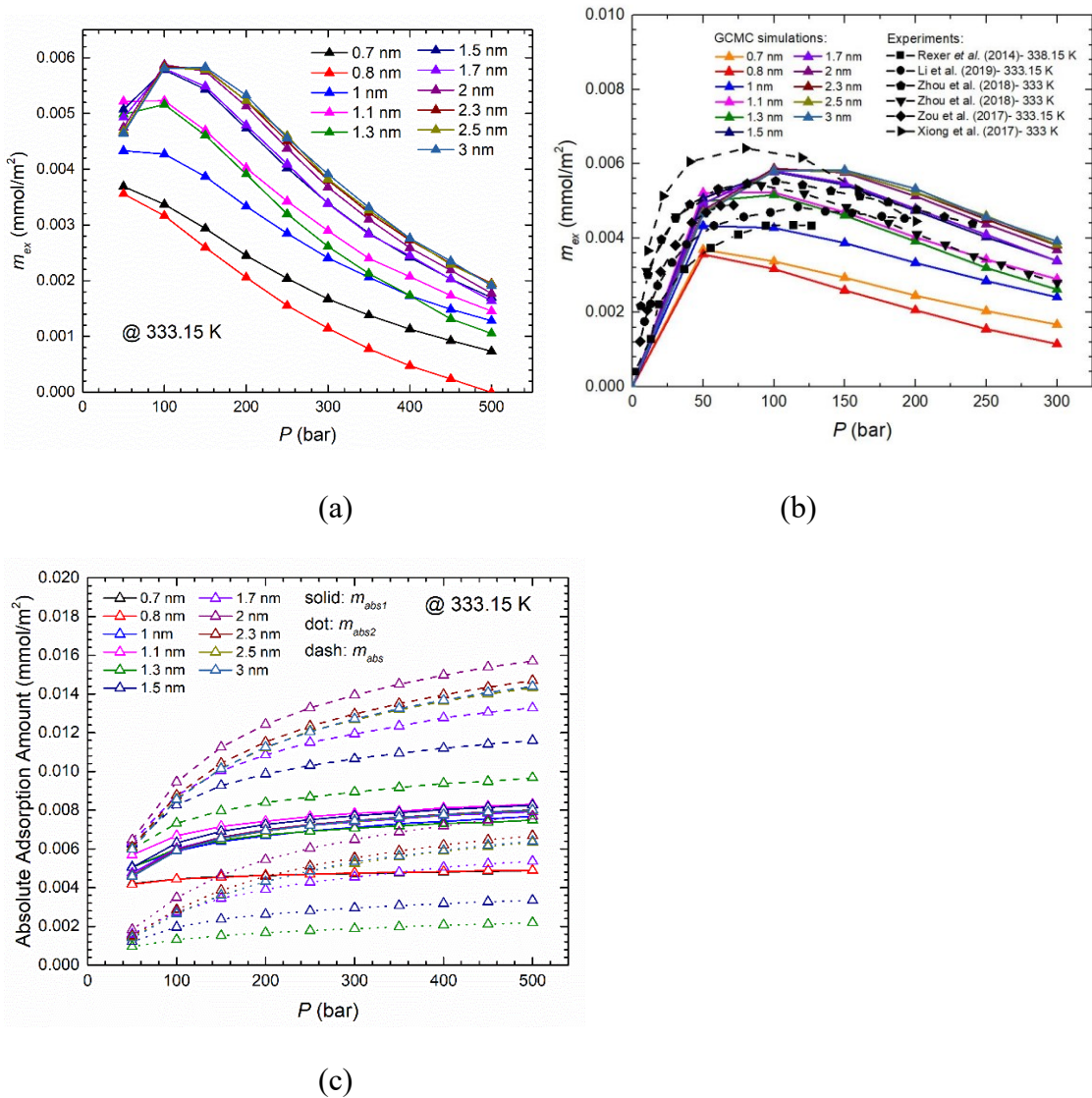
Figure E4 Adsorption amount obtained from the GCMC simulations at 333.15 K and various pressures: (a) Excess adsorption per SSA; (b) Comparison of excess adsorption amount between simulation and previous experiments[10, 18, 21, 62, 63]; (c) Absolute adsorption amount per SSA of 1st layer (m_{abs1}, solid line), 2nd layer (m_{abs2}, dotted line) and combined layers (m_{abs}, dashed line). It should be noted that the dashed line are only plotted for $W_i \geq 1.3$ nm, since the 2nd layer appears when $W_i \geq 1.3$ nm according to the characterization in **Figure 6-1** and the adsorption layer width shown in **Table E1.**
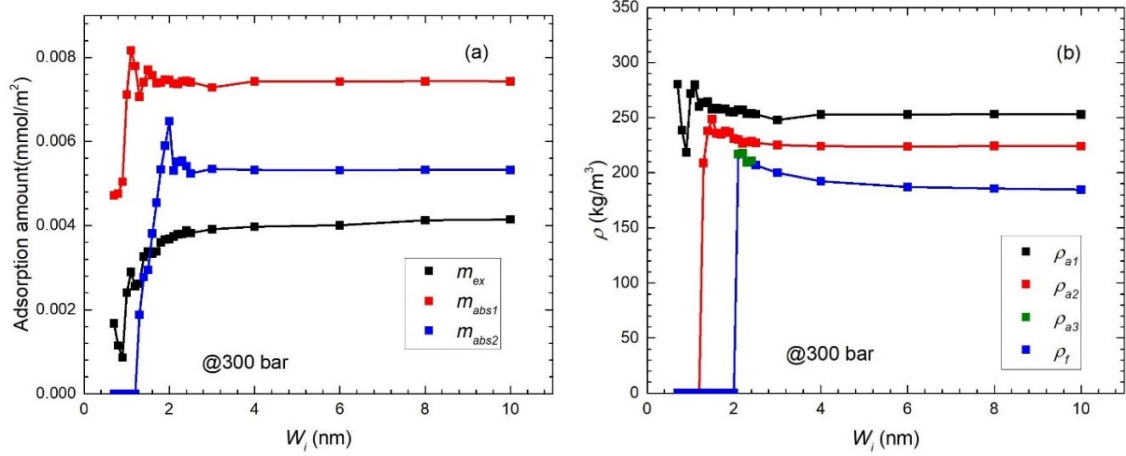
Figure E5 (a) Adsorption amount; (b) densities in different layers and free gas zone in terms of W_i at 300 bar and 333.15 K based on the characterization of adsorption types.
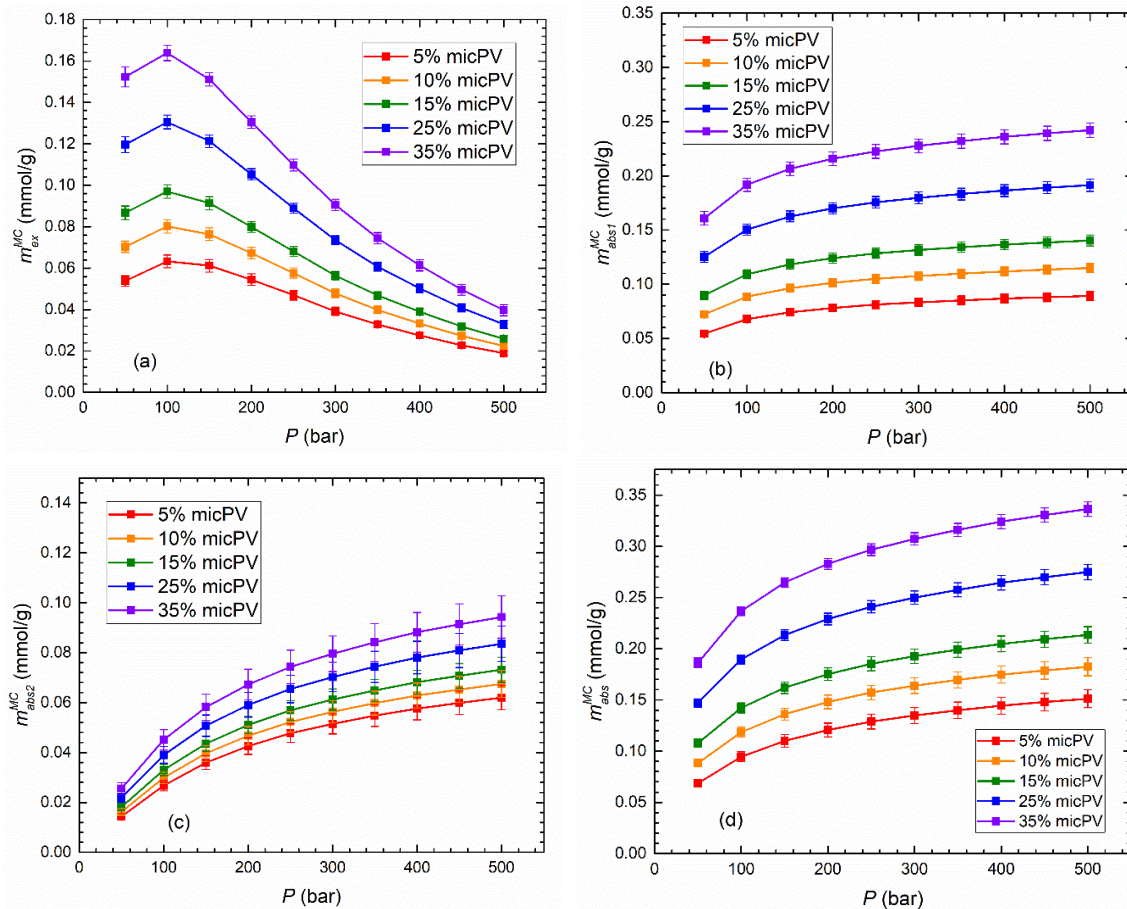
Figure E6 Adsorption amounts with different micropore volume ratios from the GCMC simulation.
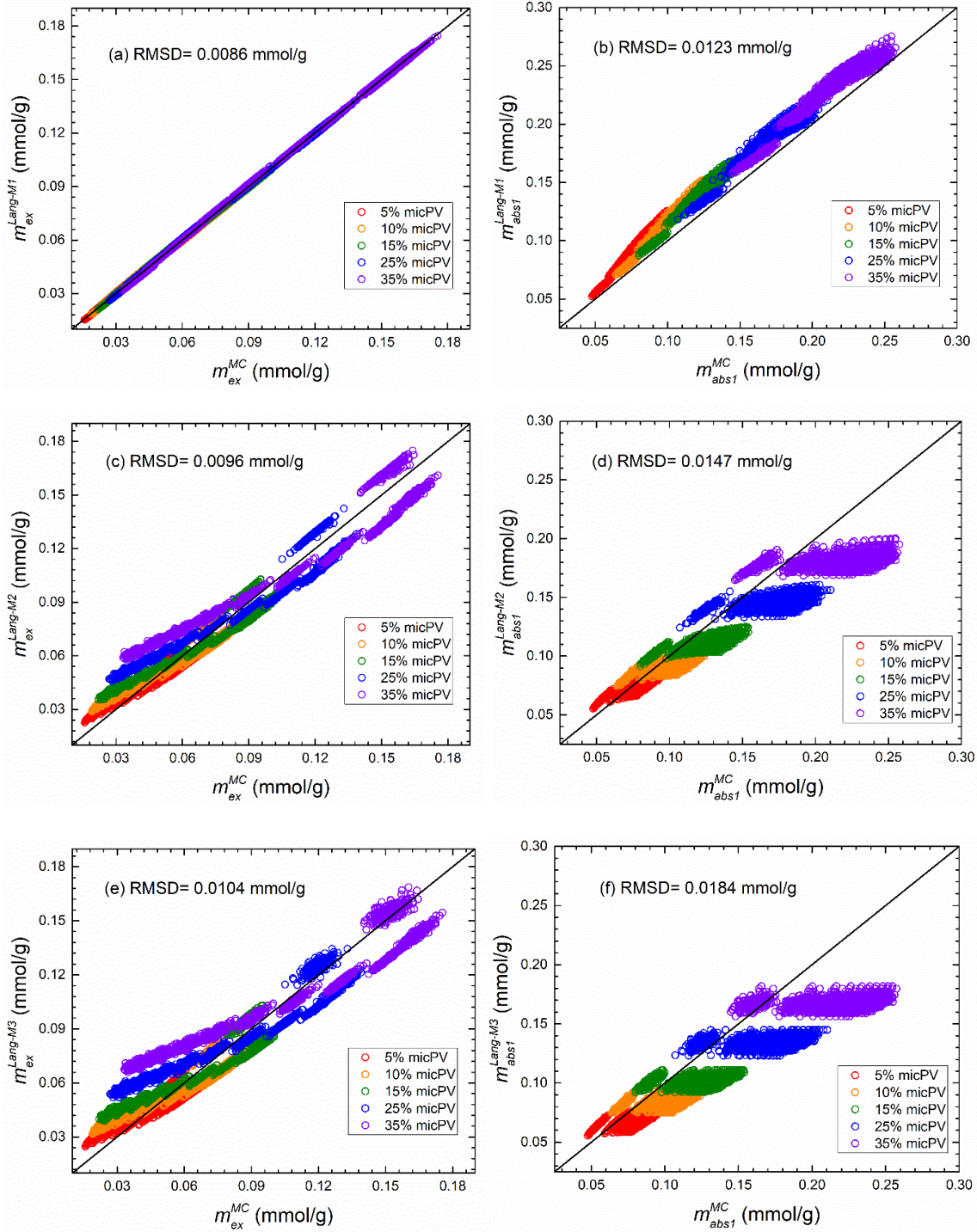
Figure E7 Regression behaviors of the Langmuir model.
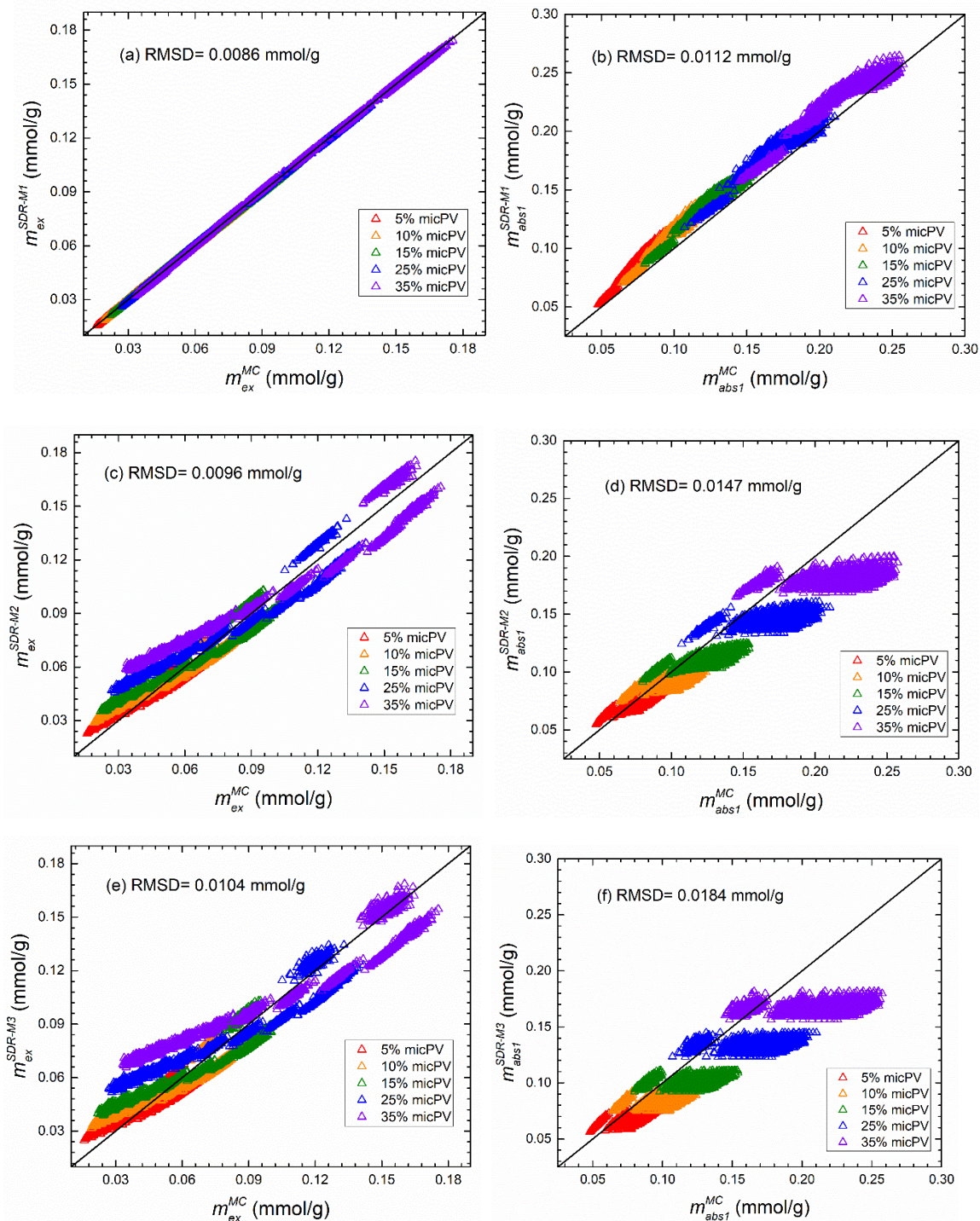
Figure E8 Regression behaviors of the SDR model.
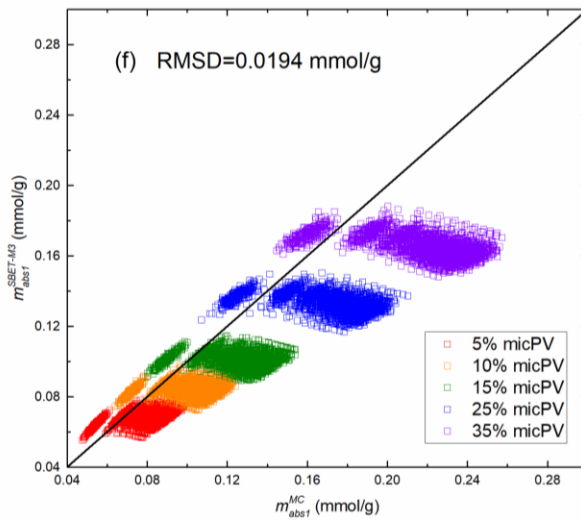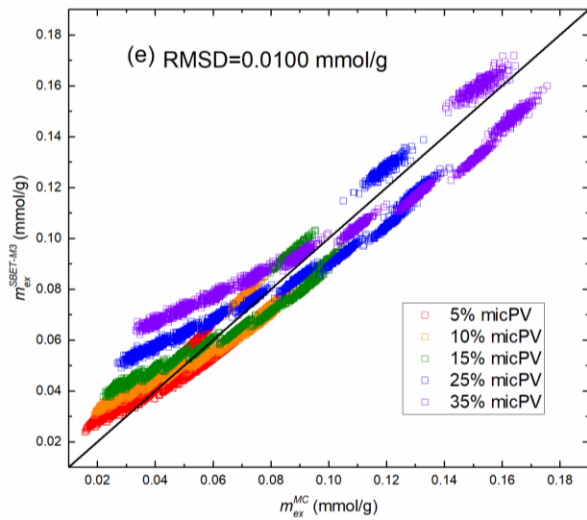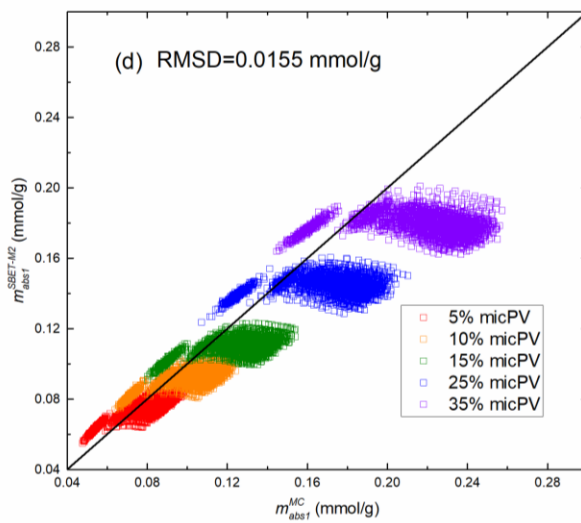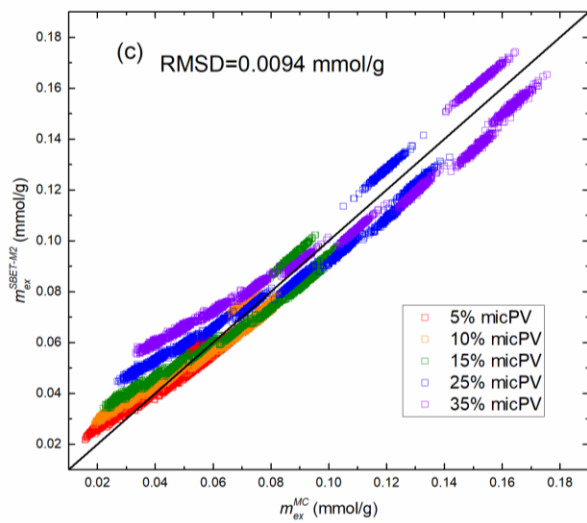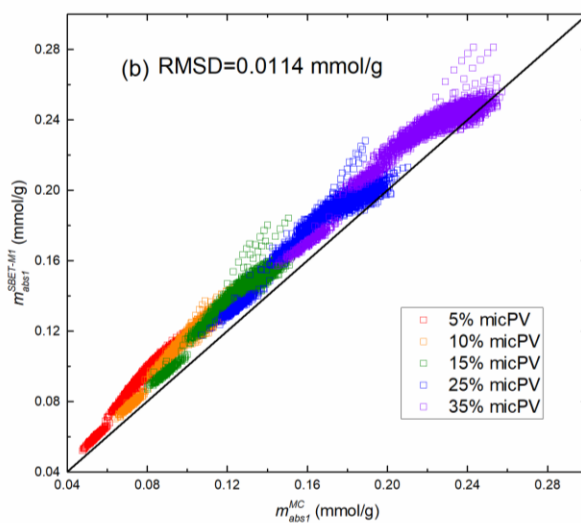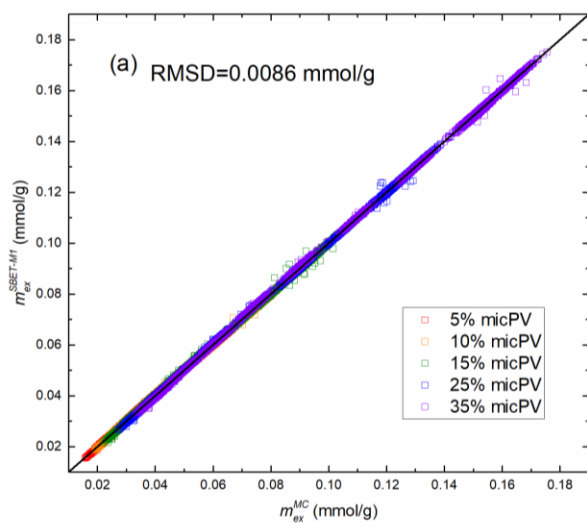
Figure E9 Regression behaviors of the SBET model.
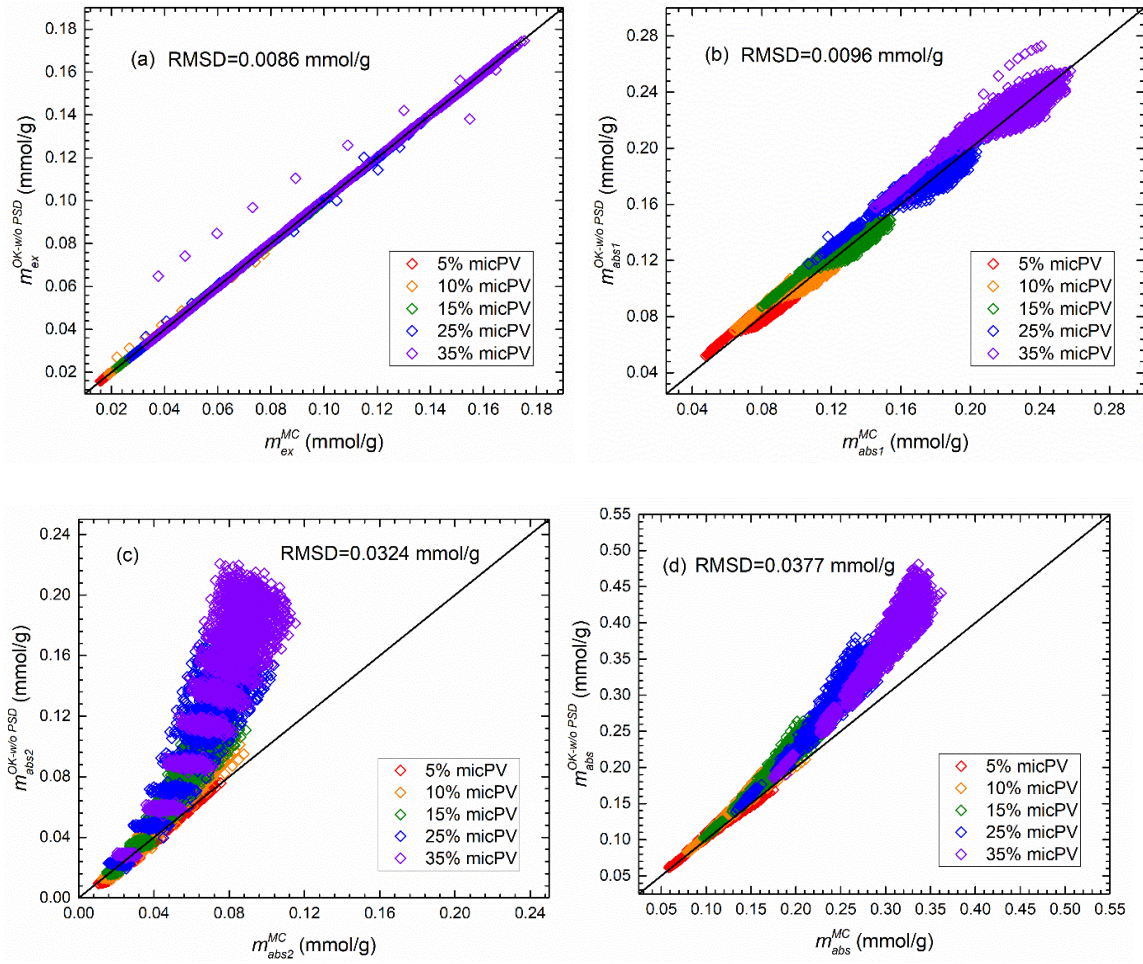
Figure E10 Regression behaviors of the OK-w/o-PSD model.
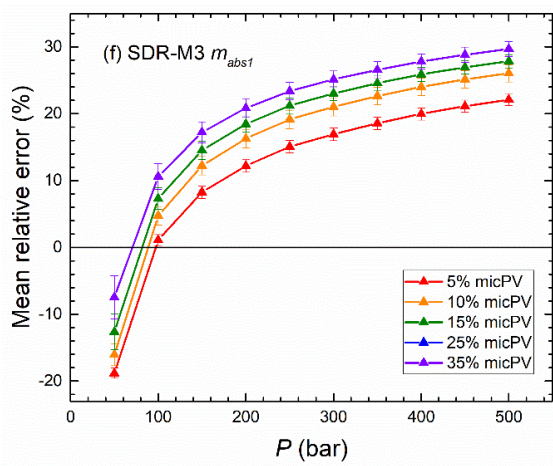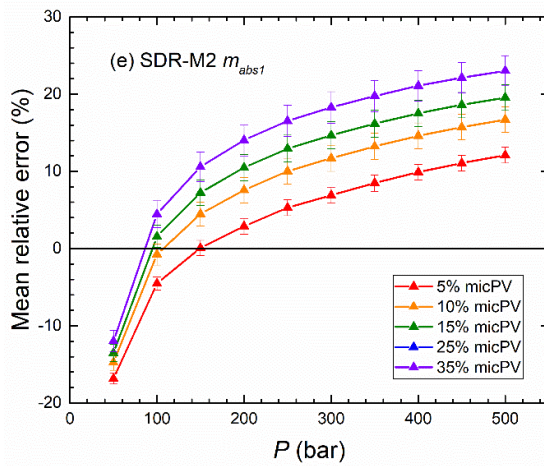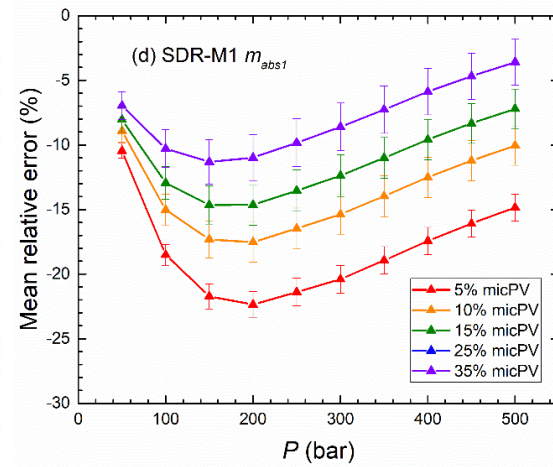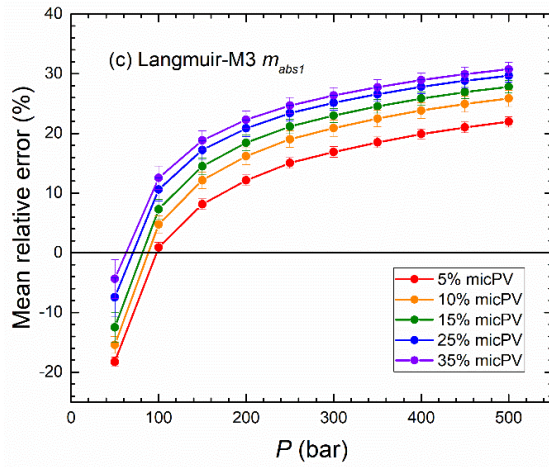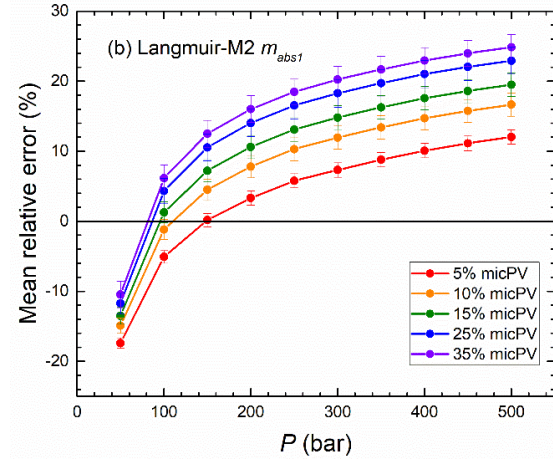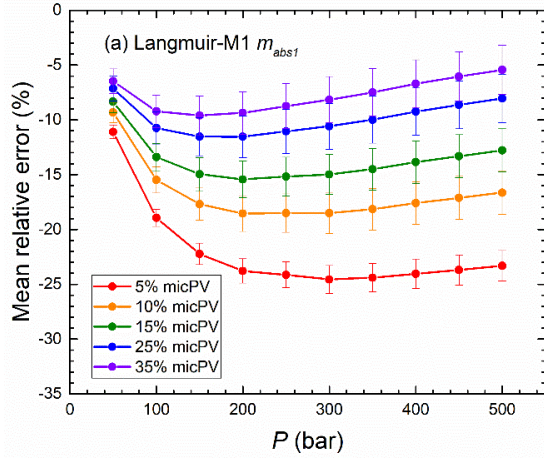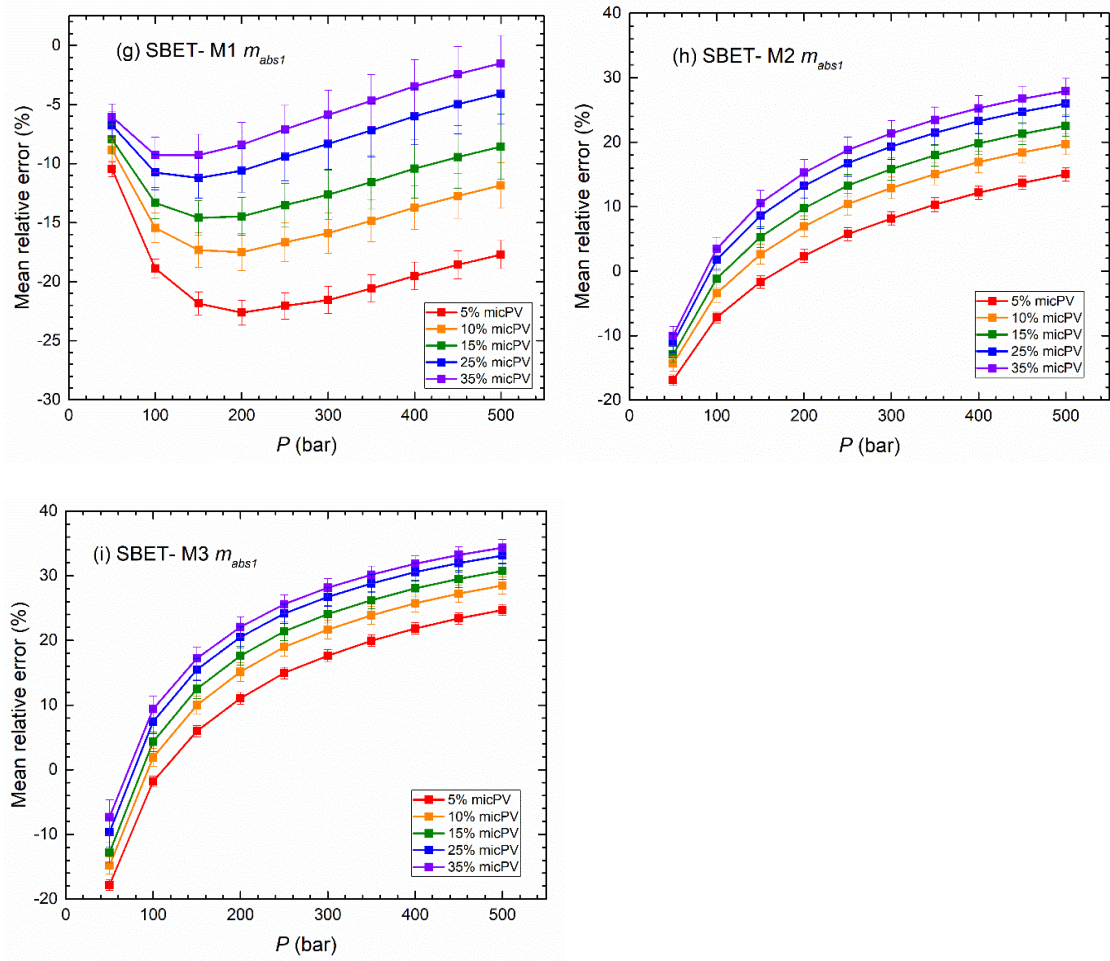
Figure E11 Mean relative errors from the Langmuir, SDR and SBET model in adsorption amounts for various micropore volume percentages.

Table E1 Width of adsorption layer in different sizes of nanopores characterized from GCMC simulation.

W (nm)	First layer width (nm)	Second layer width (nm)	W (nm)	First layer width (nm)	Second layer width (nm)
0.7	0.54	-	1.9	0.47	0.4
0.8	0.64	-	2.0	0.47	0.45
0.9	0.37	-	2.1	0.46	0.37
1.0	0.42	-	2.2	0.46	0.39
1.1	0.47	-	2.3	0.47	0.39
1.2	0.52	-	2.4	0.47	0.38
1.3	0.43	0.28	2.5	0.47	0.37

1.4	0.45	0.34	3.0	0.47	0.38
1.5	0.48	0.38	4.0	0.47	0.38
1.6	0.47	0.5	6.0	0.47	0.38
1.7	0.46	0.31	8.0	0.47	0.38
1.8	0.46	0.36	10.0	0.47	0.38

Table E2 Averaged regressed parameters in different methods and micropore volume

Methods		Parameters	Micropore pore volume (%)				
			5%	10%	15%	25%	35%
OK-PSD-L model		$\rho_{am}^{OK-PSD-L}$ (kg/m³)	324.0975±2.7144	319.2221±2.6129	315.9668±2.7415	312.1433±3.4142	309.4788±4.1181
		$\varepsilon / k_B T$	-1.8888±0.0895	-1.8853±0.0192	-1.8878±0.0214	-1.8902±0.0304	-1.8966±0.0370
		$\varepsilon_s / k_B T$	-0.4759±0.0379	-0.4790±0.0101	-0.4810±0.0127	-0.4843±0.0159	-0.4840±0.0217
OK-w/o-PSD model		$\rho_{am}^{OK-w/o-PSD}$ (kg/m³)	319.0147±1.9744	311.8133±3.4727	307.0309±3.7272	301.3155±4.4984	297.7744±5.1673
		$\varepsilon / k_B T$	-2.0369±0.0224	-2.1650±0.0475	-2.2615±0.0621	-2.4245±0.1054	-2.5396±0.1267
		$\varepsilon_s / k_B T$	-0.4190±0.0113	-0.3724±0.0224	-0.3394±0.0293	-0.2842±0.0443	-0.2433±0.0560
Langmuir model	M1	$n_{max,LA}$ (mmol/g)	0.1211±0.0064	0.1454±0.0064	0.1701±0.0059	0.2198±0.0054	0.2699±0.0054
		P_L (bar)	50.3269±1.6345	42.1624±2.2625	37.4887±2.3526	31.9630±2.4897	28.9483±2.4666
		$\rho_{a,LA}$ (kg/m³)	294.0354±0.9650	292.7233±1.7157	291.5239±1.9418	290.0765±2.5869	288.8746±2.9544
	M2	$n_{max,LA}$ (mmol/g	0.0806±0.0042	0.0975±0.0045	0.1143±0.0043	0.1483±0.0047	0.1824±0.0053

Model	M	Parameter					
		)					
		P_L (bar)	13.1478±0.9608	8.7963±1.4757	6.1320±1.5787	3.0209±1.7257	1.4125±1.4691
	M3	$n_{max,LA}$ (mmol/g)	0.0703±0.0037	0.0854±0.0039	0.1013±0.0035	0.1345±0.0036	0.1676±0.0041
		P_L (bar)	4.7116±0.7710	1.3039±1.0427	0.1881±0.4882	0.0121±0.1155	0
SDR model	M1	$n_{max,SDR}$ (mmol/g)	0.1029±0.0052	0.1269±0.0052	0.1508±0.0050	0.1986±0.0046	0.2463±0.0047
		D	0.1034±0.0021	0.0926±0.0032	0.0859±0.0036	0.0771±0.0041	0.0720±0.0043
		$\rho_{a,SDR}$ (kg/m³)	299.3852±1.1079	296.8848±1.9398	295.0079±2.1715	292.8057±2.8242	291.2011±3.1691
	M2	$n_{max,SDR}$ (mmol/g)	0.0789±0.0041	0.0961±0.0044	0.1132±0.0041	0.1474±0.0045	0.1817±0.005
		D	0.0347±0.0023	0.0239±0.0038	0.0168±0.0043	0.0080±0.0049	0.0035±0.0041
	M3	$n_{max,SDR}$ (mmol/g)	0.0697±0.0036	0.0850±0.0037	0.1012±0.0035	0.1345±0.0036	0.1676±0.0041
		D	0.0111±0.0020	0.0023±0.0024	0.0002±0.0008	0±0.0002	0
SBET model	M1	$n_{max,SBET}$ (mmol/g)	0.1184±0.0078	0.1457±0.0083	0.1730±0.0122	0.2297±0.0140	0.2884±0.0148
		c	10.144±0.5038	12.0759±5.5139	14.2604±10.7688	15.6503±9.2172	16.3847±7.4998
		n_{BET}	0.9915±0.0	0.9566±0.1	0.9469±0.2	0.8965±0.1	0.8524±0.1

			623	23	313	792	380
		$\rho_{a,SBET}$ (kg/m^3)	297.6319± 1.0860	295.9169±2 .0354	294.408±2. 6571	292.8524±3 .0699	291.6604± 3.3557
M 2		$n_{\max,SBET}$ (mmol/g)	0.1607±0.0 086	0.1929±0.0 096	0.2235±0.0 096	0.2814±0.0 132	0.3373±0.0 172
		c	76.5431±9. 6773	128.5324±2 6.6581	169.9258±2 7.6124	195.0826±1 3.8657	198.9199± 6.2590
		n_{BET}	0.0779±0.0 091	0.0572±0.0 088	0.0501±0.0 061	0.0561±0.0 088	0.0672±0.0 140
M 3		$n_{\max,SBET}$ (mmol/g)	0.1326±0.0 075	0.1540±0.0 087	0.1753±0.0 084	0.2196±0.0 097	0.2658±0.0 104
		c	199.1104± 7.0152	200±0	200±0	200±0	200±0
		n_{BET}	0.0531±0.0 041	0.0753±0.0 104	0.0986±0.0 163	0.1374±0.0 232	0.1609±0.0 220

F. Supporting information of Chapter 7
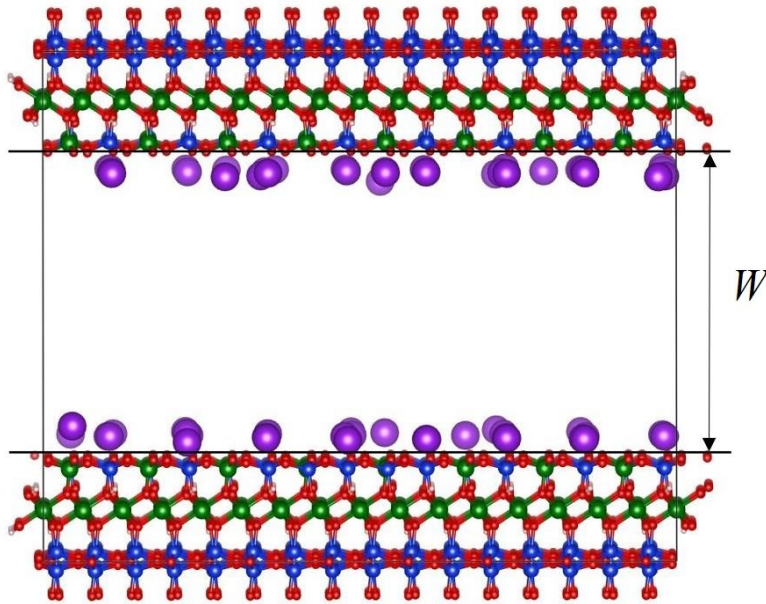
Figure F1 Schematic representation of K-illite. Red spheres are O atoms, green spheres are Al atoms, blue spheres are Si atoms, light pink spheres are H atoms and purple spheres are K^+ ions. The pore width W is defined as the distance between the center of mass of O atoms in the inner plane of two sheets.
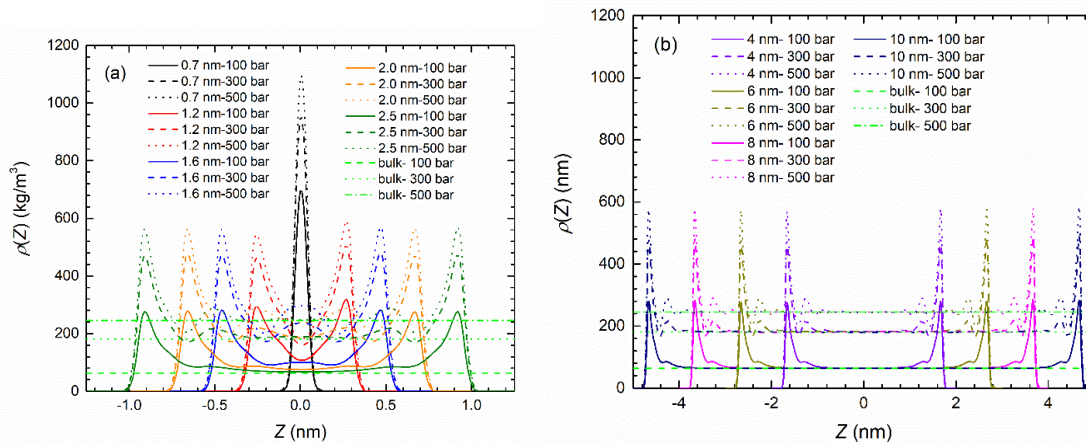
Figure F2 Density profiles of methane in illite nanopores at 333.15 K.
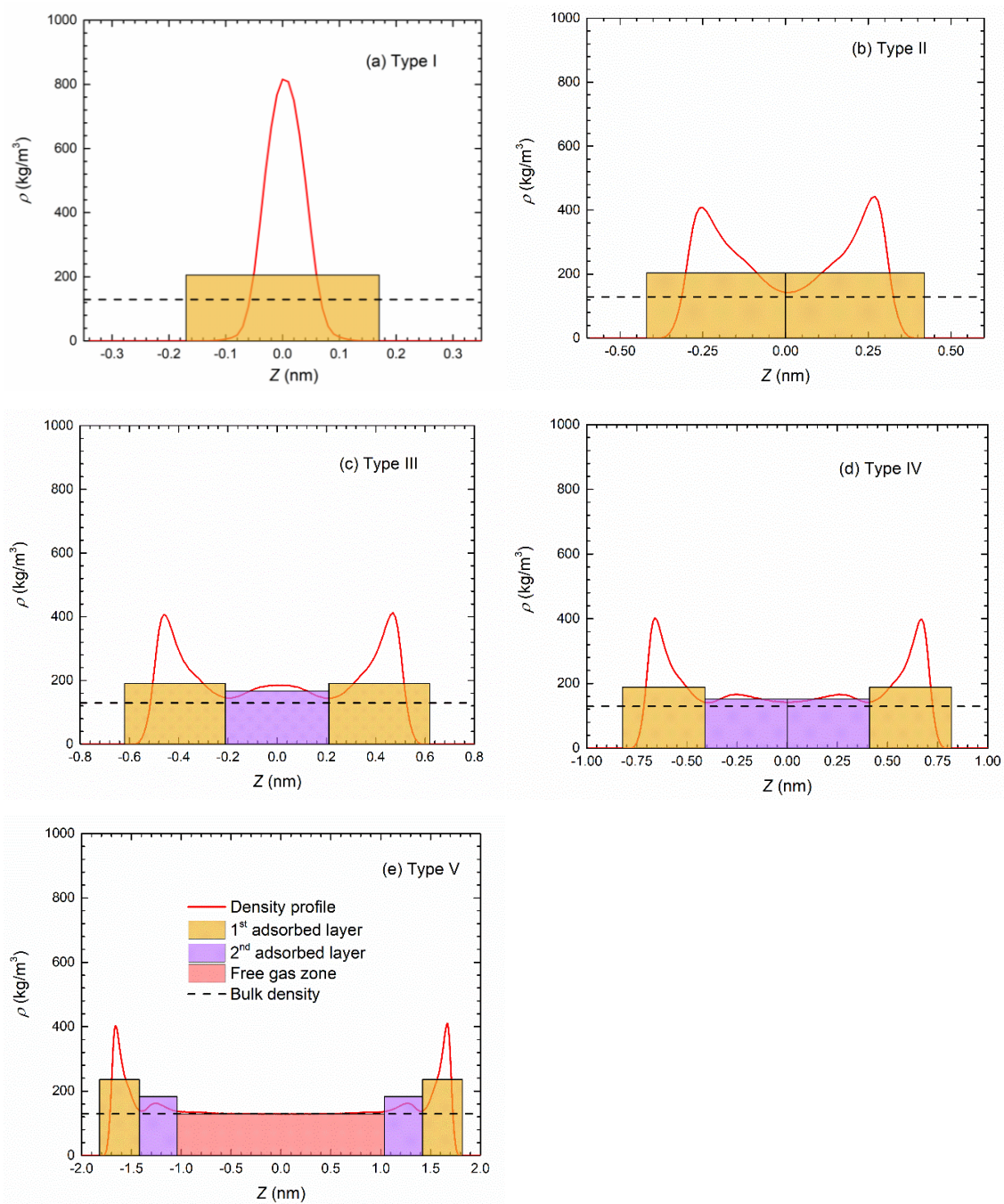
Figure F3 Characterized adsorption model in illite nanopores.
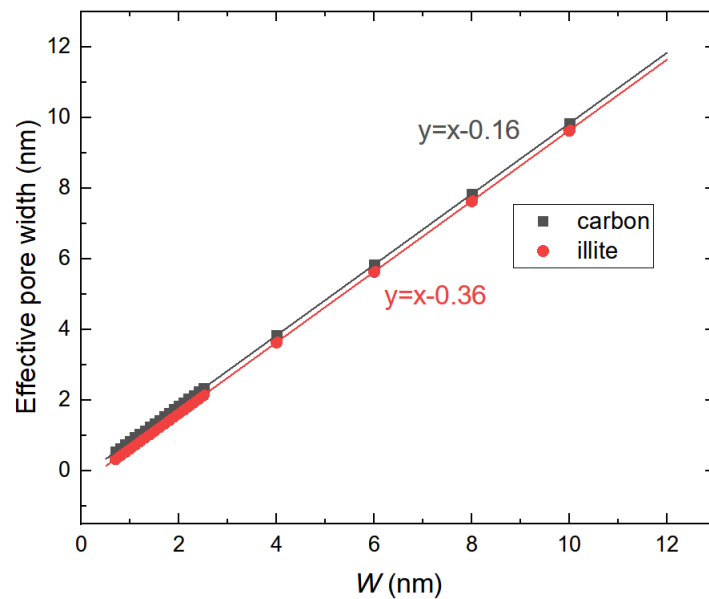
Figure F4 Comparison of effective pore width in carbon and illite nanopores.
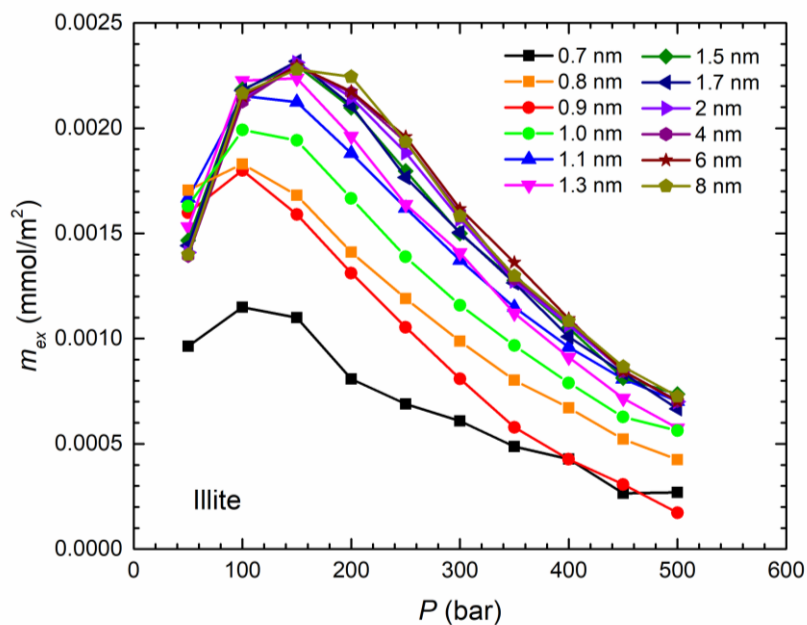
Figure F5 Excess adsorption per SSA of methane in illite nanopores at pressures up to 500 bar and temperature at 333.15 K.
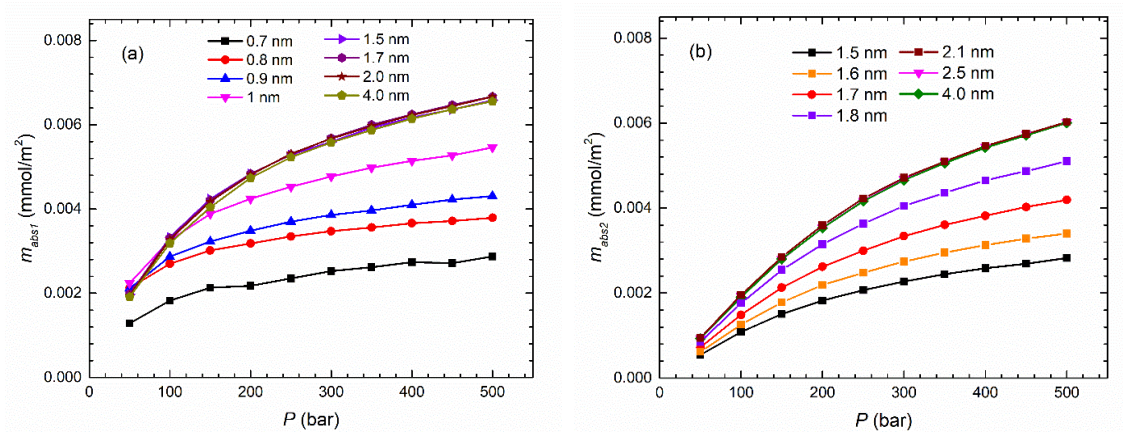
Figure F6 Absolute adsorption per SSA of methane adsorption in illite nanopores at pressures up to 500 bar and temperature at 333.15 K. (a) 1st adsorption layer; (b) 2nd (weak) adsorption layer.
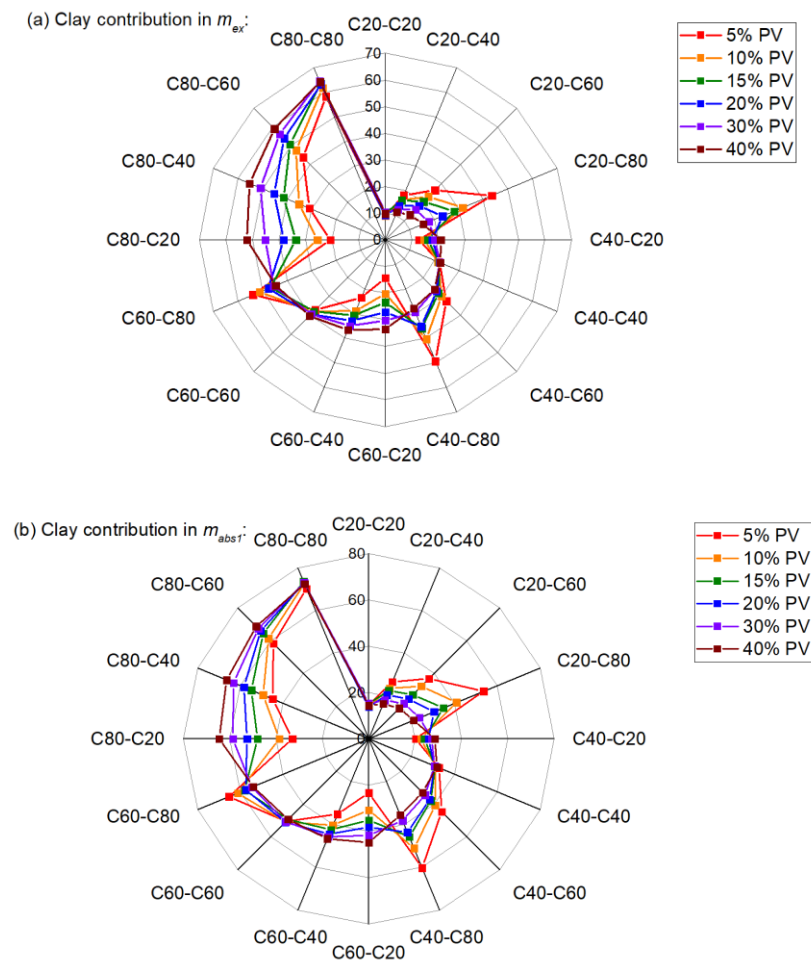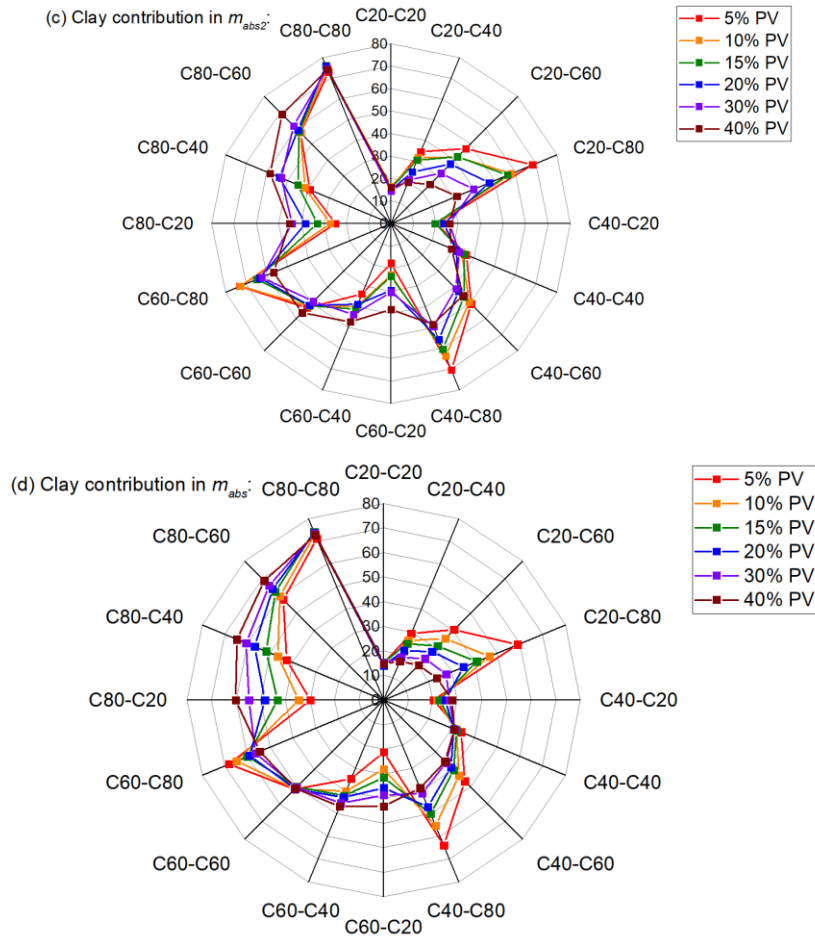
Figure F7 Clay contribution in adsorption amounts with different micropore volume ratios and different volume distributions of clay in micropore and mesopore. (a) m_{ex}; (b) m_{abs1}; (c) m_{abs2}; (d) m_{abs}.

(a)

(b)
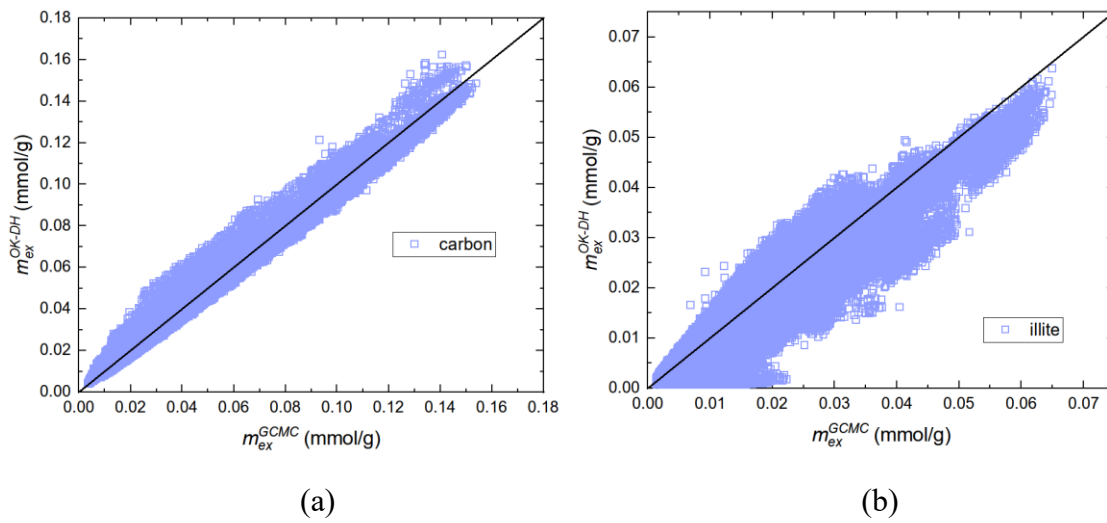
Figure F8 Comparison of excess adsorption results obtained from OK-DH model and GCMC simulation in (a) carbon and (b) illite nanopores from total regression.

Formation	TOC (%)	Clay content (%)	OM in micropore volume (%)	OM in mesopore volume (%)	Clay in micropore volume (%)	Clay in micropore volume (%)
Bakken[a]	11.07- 20.17	16.2- 28.6	68.4- 88.6	33.4- 98.2	NA	NA
Bakken[b]	11.07- 20.17	16.2- 28.6	Over 90%	23.7-52.5	NA	NA
Posidonia[c]	5.78- 10.92	23.3- 32.8	19- 22.4	NA	NA	NA
Longmaxi[d]	2.28- 3.61	15.2- 27.4	40- 67.5	62.9- 71	NA	NA
Longmaxi[e]	1.1- 3.06	23- 42.2	8.4- 31.4	28.4- 64.9	55- 88.1	31.6- 67.6
Wufeng-Longmaxi[f]	0.98- 3.61	15.7- 45.5	32- 63	0	37- 68	100
Shanxi and Benxi shale[g]	0.01- 1.09	54- 69	1.2	6.6	NA	NA

Table F1 Organic matter (OM) and clay volume distributions in bulk shale

[a] Liu, Kouqi, et al. "Nanopore structures of isolated kerogen and bulk shale in Bakken Formation." *Fuel* 226 (2018): 441-453.

[b] Yuan, Yujie, et al. "Impact of Composition on Pore Structure Properties in Shale: Implications for Micro-/Mesopore Volume and Surface Area Prediction." *Energy & Fuels* 33.10 (2019): 9619-9628.

[c] Rexer, Thomas F., et al. "High-pressure methane adsorption and characterization of pores in Posidonia shales and isolated kerogens." *Energy & Fuels* 28.5 (2014): 2886-2901.

[d] Qi, Rongrong, et al. "Measurements and modeling of high-pressure adsorption of CH4 and CO2 on shales." *Fuel* 242 (2019): 728-743.

[e] Chen, Fangwen, et al. "Evaluation of the density and thickness of adsorbed methane in differently sized pores contributed by various components in a shale gas reservoir: A case study of the Longmaxi Shale in Southeast Chongqing, China." *Chemical Engineering Journal* 367 (2019): 123-138.

[f] Wu, Xiaojun, et al. "Pore characterization and inner adsorption mechanism investigation for methane in organic and inorganic matters of shale." *Energy & Fuels* 34.4 (2020): 4106-4115.

[g] Xiong, Fengyang, et al. "Pore structure of transitional shales in the Ordos Basin, NW China: Effects of composition on gas storage capacity." *Fuel* 206 (2017): 504-515.

Volume fraction of clay in micropore and mesopore in nanoporous media	Denoted as	Volume fraction of clay in micropore and mesopore in nanoporous media	Denoted as
20%+ 20%	C20-C20	60%+ 20%	C60-C20
20%+ 40%	C20-C40	60%+ 40%	C60-C40
20%+ 60%	C20-C60	60%+ 60%	C60-C60
20%+ 80%	C20-C80	60%+ 80%	C60-C80
40%+ 20%	C40-C20	80%+ 20%	C80-C20
40%+ 40%	C40-C40	80%+ 40%	C80-C40
40%+ 60%	C40-C60	80%+ 60%	C80-C60
40%+ 80%	C40-C80	80%+ 80%	C80-C80

Table F2 Summary of volume fraction of clay in micropore and mesopore in nanoporous media in each micropore volume ratio case.

Table F3 Model descriptions

Model	Conversion	Heterogeneity	Consideration	Description	Notes	Denote as
Langmuir	Constant ρ_a (cr)	NH	Maximum Capacity	$$m_{ex}^{LA} = m_{max}\frac{V_L P}{P_L + P}\left(1 - \rho_b/\rho_a\right)$$ $$m_{abs}^{LA} = m_{max}\frac{V_L P}{P_L + P}$$	-	L-cr-1
			SSA with 0.38nm	$$m_{ex}^{LA} = SSA*0.38*\rho_a\frac{V_L P}{P_L + P}\left(1 - \rho_b/\rho_a\right)$$ $$m_{abs}^{LA} = SSA*0.38*\rho_a\frac{V_L P}{P_L + P}$$	-	L-cr-2
		SH	Maximum Capacity	$$m_{ex}^{LA} = m_{max}\left[\alpha\frac{P}{P_{L1} + P} + (1-\alpha)\frac{P}{P_{L2} + P}\right]\left(1 - \rho_b/\rho_a\right)$$ $$m_{abs}^{LA} = m_{max}\left[\alpha\frac{P}{P_{L1} + P} + (1-\alpha)\frac{P}{P_{L2} + P}\right]$$	Apparent density	L-cr-3
				$$m_{ex}^{LA} = m_{max}\alpha\frac{P}{P_{L1} + P}\left(1 - \rho_b/\rho_{a1}\right) + m_{max}(1-\alpha)\frac{P}{P_{L2} + P}\left(1 - \rho_b/\rho_{a2}\right)$$	Specific density for each site	L-cr-4

			$$m_{abs}^{LA} = m_{\max}\left[\alpha\frac{P}{P_{L1}+P}+(1-\alpha)\frac{P}{P_{L2}+P}\right]$$		
		SSA with 0.38nm	$$m_{ex}^{LA} = SSA*0.38*\rho_a\left[\alpha\frac{P}{P_{L1}+P}+(1-\alpha)\frac{P}{P_{L2}+P}\right](1-\rho_b/\rho_a)$$ $$m_{abs}^{LA} = SSA*0.38*\rho_a\left[\alpha\frac{P}{P_{L1}+P}+(1-\alpha)\frac{P}{P_{L2}+P}\right]$$	Apparent density	L-cr-5
			$$m_{ex}^{LA} = SSA_1*0.38*\rho_{a1}\frac{P}{P_{L1}+P}(1-\rho_b/\rho_{a1})+SSA_2*0.38*\rho_{a2}$$ $$\frac{P}{P_{L2}+P}(1-\rho_b/\rho_{a2})$$ $$m_{abs}^{LA} = SSA_1*0.38*\rho_{a1}\frac{P}{P_{L1}+P}+SSA_2*0.38*\rho_{a2}\frac{P}{P_{L2}+P}$$	Specific density for each site	L-cr-6
Constant V_a (cv)	NH	-	$$m_{ex}^{LA} = \rho_a V_a\frac{V_L P}{P_L+P}-\rho_b V_a$$ $$m_{abs}^{LA} = \rho_a V_a\frac{V_L P}{P_L+P}$$	-	L-cv-1
	SH	-	$$m_{ex}^{LA} = \rho_a V_a\left[\alpha\frac{P}{P_{L1}+P}+(1-\alpha)\frac{P}{P_{L2}+P}\right]-\rho_b V_a$$	Apparent density	L-cv-2

				$$m_{abs}^{LA} = \rho_a V_a \left[\alpha \frac{P}{P_{L1} + P} + (1-\alpha) \frac{P}{P_{L2} + P} \right]$$		
			-	$$m_{ex}^{LA} = \rho_{am1} V_a \alpha \frac{P}{P_{L1} + P} + \rho_{am2} V_a (1-\alpha) \frac{P}{P_{L2} + P} - \rho_b V_a$$ $$m_{abs}^{LA} = \rho_{am1} V_a \alpha \frac{P}{P_{L1} + P} + \rho_{am2} V_a (1-\alpha) \frac{P}{P_{L2} + P}$$	Specific density for each site	L-cv-3
			-	$$m_{ex}^{LA} = \rho_{am1} V_{a1} \frac{P}{P_{L1} + P} + \rho_{am2} V_{a2} \frac{P}{P_{L2} + P} - \rho_b (V_{a1} + V_{a2})$$ $$m_{abs}^{LA} = \rho_{am1} V_{a1} \frac{P}{P_{L1} + P} + \rho_{am2} V_{a2} \frac{P}{P_{L2} + P}$$	Specific density for each site	L-cv-4
SDR	Constant ρ_a	NH	Maximum Capacity	$$m_{ex}^{SDR} = m_{max} \exp\left\{ -D \left[\ln\left(\frac{\rho_a}{\rho_b} \right) \right]^2 \right\} (1 - \rho_b / \rho_a)$$ $$m_{abs}^{SDR} = m_{max} \exp\left\{ -D \left[\ln\left(\frac{\rho_a}{\rho_b} \right) \right]^2 \right\}$$	-	SDR-cr-1
			SSA with 0.38nm	$$m_{ex}^{SDR} = SSA * 0.38 * \rho_a \exp\left\{ -D \left[\ln\left(\frac{\rho_a}{\rho_b} \right) \right]^2 \right\} (1 - \rho_b / \rho_a)$$	-	SDR-cr-2

				$$m_{ex}^{SDR} = SSA*0.38*\rho_a \exp\left\{-D\left[\ln\left(\frac{\rho_a}{\rho_b}\right)\right]^2\right\}$$		
		SH	Maximum Capacity	$$m_{ex}^{SDR} = m_{max}\left\{\begin{array}{l}\alpha \exp\left\{-D_1\left[\ln\left(\frac{\rho_a}{\rho_b}\right)\right]^2\right\}+\\(1-\alpha)\exp\left\{-D_2\left[\ln\left(\frac{\rho_a}{\rho_b}\right)\right]^2\right\}\end{array}\right\}(1-\rho_b/\rho_a)$$ $$m_{abs}^{SDR} = m_{max}\left\{\alpha \exp\left\{-D_1\left[\ln\left(\frac{\rho_a}{\rho_b}\right)\right]^2\right\}+(1-\alpha)\exp\left\{-D_2\left[\ln\left(\frac{\rho_a}{\rho_b}\right)\right]^2\right\}\right\}$$	Apparent density	SDR - cr-3
				$$m_{ex}^{SDR} = m_{max}\alpha \exp\left\{-D_1\left[\ln\left(\frac{\rho_{a1}}{\rho_b}\right)\right]^2\right\}(1-\rho_b/\rho_{a1})$$ $$+m_{max}(1-\alpha)\exp\left\{-D_2\left[\ln\left(\frac{\rho_{a2}}{\rho_b}\right)\right]^2\right\}(1-\rho_b/\rho_{a2})$$ $$m_{abs}^{SDR} = m_{max}\alpha \exp\left\{-D_1\left[\ln\left(\frac{\rho_{a1}}{\rho_b}\right)\right]^2\right\}+m_{max}(1-\alpha)$$ $$\exp\left\{-D_2\left[\ln\left(\frac{\rho_{a2}}{\rho_b}\right)\right]^2\right\}$$	Specific density for each site	SDR - cr-4

				SSA with 0.38nm	$m_{ex}^{SDR} = SSA*0.38*\rho_a \begin{cases} \alpha\exp\left\{-D_1\left[\ln\left(\dfrac{\rho_a}{\rho_b}\right)\right]^2\right\}+ \\ (1-\alpha)\exp\left\{-D_2\left[\ln\left(\dfrac{\rho_a}{\rho_b}\right)\right]^2\right\} \end{cases}(1-\rho_b/\rho_a)$ $m_{abs}^{SDR} = SSA*0.38*\rho_a \begin{cases} \alpha\exp\left\{-D_1\left[\ln\left(\dfrac{\rho_a}{\rho_b}\right)\right]^2\right\}+ \\ (1-\alpha)\exp\left\{-D_2\left[\ln\left(\dfrac{\rho_a}{\rho_b}\right)\right]^2\right\} \end{cases}$	Apparent density	SDR - cr-5
					$m_{ex}^{SDR} = SSA_1*0.38*\rho_{a1}\exp\left\{-D_1\left[\ln\left(\dfrac{\rho_{a1}}{\rho_b}\right)\right]^2\right\}(1-\rho_b/\rho_{a1})$ $+SSA_2*0.38*\rho_{a2}\exp\left\{-D_2\left[\ln\left(\dfrac{\rho_{a2}}{\rho_b}\right)\right]^2\right\}(1-\rho_b/\rho_{a2})$ $m_{abs}^{SDR} = SSA_1*0.38*\rho_{a1}\alpha\exp\left\{-D_1\left[\ln\left(\dfrac{\rho_{a1}}{\rho_b}\right)\right]^2\right\}$ $+SSA_2*0.38*\rho_{a2}\exp\left\{-D_2\left[\ln\left(\dfrac{\rho_{a2}}{\rho_b}\right)\right]^2\right\}$	Specific density for each site	SDR - cr-6

	Constant V_a	NH	-	$$m_{ex}^{SDR} = \rho_a V_a \exp\left\{-D\left[\ln\left(\frac{\rho_a}{\rho_b}\right)\right]^2\right\} - \rho_b V_a$$ $$m_{abs}^{SDR} = \rho_a V_a \exp\left\{-D\left[\ln\left(\frac{\rho_a}{\rho_b}\right)\right]^2\right\} - \rho_b V_a$$	-	SDR - cv-1
		SH	-	$$m_{ex}^{SDR} = \rho_a V_a \left\{ \begin{array}{l} \alpha \exp\left\{-D_1\left[\ln\left(\frac{\rho_a}{\rho_b}\right)\right]^2\right\} + \\ (1-\alpha)\exp\left\{-D_2\left[\ln\left(\frac{\rho_a}{\rho_b}\right)\right]^2\right\} \end{array} \right\} - \rho_b V_a$$ $$m_{abs}^{SDR} = \rho_a V_a \left\{ \begin{array}{l} \alpha \exp\left\{-D_1\left[\ln\left(\frac{\rho_a}{\rho_b}\right)\right]^2\right\} + \\ (1-\alpha)\exp\left\{-D_2\left[\ln\left(\frac{\rho_a}{\rho_b}\right)\right]^2\right\} \end{array} \right\}$$	Apparent density	SDR - cv-2
			-	$$m_{ex}^{SDR} = \rho_{a1} V_a \alpha \exp\left\{-D_1\left[\ln\left(\frac{\rho_{a1}}{\rho_b}\right)\right]^2\right\} + \rho_{a2} V_a \alpha (1-\alpha)$$ $$\exp\left\{-D_2\left[\ln\left(\frac{\rho_{a2}}{\rho_b}\right)\right]^2\right\} - \rho_b V_a$$	Specific density for each site	SDR - cv-3

				$$m_{abs}^{SDR} = \rho_{a1}V_a\alpha\exp\left\{-D_1\left[\ln\left(\frac{\rho_{a1}}{\rho_b}\right)\right]^2\right\} + \rho_{a2}V_a\alpha(1-\alpha)$$ $$\exp\left\{-D_2\left[\ln\left(\frac{\rho_{a2}}{\rho_b}\right)\right]^2\right\}$$		
			-	$$m_{ex}^{SDR} = \rho_{a1}V_{a1}\exp\left\{-D_1\left[\ln\left(\frac{\rho_{a1}}{\rho_b}\right)\right]^2\right\} + \rho_{a2}V_{a2}$$ $$\exp\left\{-D_2\left[\ln\left(\frac{\rho_{a2}}{\rho_b}\right)\right]^2\right\} - \rho_b\left(V_{a1}+V_{a2}\right)$$ $$m_{abs}^{SDR} = \rho_{a1}V_{a1}\exp\left\{-D_1\left[\ln\left(\frac{\rho_{a1}}{\rho_b}\right)\right]^2\right\} +$$ $$\rho_{a2}V_{a2}\exp\left\{-D_2\left[\ln\left(\frac{\rho_{a2}}{\rho_b}\right)\right]^2\right\}$$	Specific density for each site	SDR - cv-4
Improved D-A	Constant ρ_a	NH	Maximum Capacity	$$m_{ex}^{iDA} = m_{max}\exp\left\{-\left[\frac{RT\ln\left(P_s/P\right)}{E}\right]^t\right\}(1-\rho_b/\rho_a)$$ $$m_{abs}^{iDA} = m_{max}\exp\left\{-\left[\frac{RT\ln\left(P_s/P\right)}{E}\right]^t\right\}$$	-	IDA- cr-1

		SSA with 0.38nm	$m_{ex}^{iDA} = SSA*0.38*\rho_a \exp\left\{-\left[\dfrac{RT\ln(P_s/P)}{E}\right]^t\right\}(1-\rho_b/\rho_a)$ $m_{abs}^{iDA} = SSA*0.38*\rho_a \exp\left\{-\left[\dfrac{RT\ln(P_s/P)}{E}\right]^t\right\}$	-	IDA - cr-2
	SH	Maximum Capacity	$m_{ex}^{iDA} = m_{max}\left\{\alpha\exp\left\{-\left[\dfrac{RT\ln(P_s/P)}{E_1}\right]^{t_1}\right\} +(1-\alpha)\exp\left\{-\left[\dfrac{RT\ln(P_s/P)}{E_2}\right]^{t_2}\right\}\right\}(1-\rho_b/\rho_a)$ $m_{abs}^{iDA} = m_{max}\left\{\alpha\exp\left\{-\left[\dfrac{RT\ln(P_s/P)}{E_1}\right]^{t_1}\right\} +(1-\alpha)\exp\left\{-\left[\dfrac{RT\ln(P_s/P)}{E_2}\right]^{t_2}\right\}\right\}$	Apparent density	IDA - cr-3
			$m_{ex}^{iDA} = m_{max}\alpha\exp\left\{-\left[\dfrac{RT\ln(P_s/P)}{E_1}\right]^{t_1}\right\}(1-\rho_b/\rho_{a1})$ $+m_{max}(1-\alpha)\exp\left\{-\left[\dfrac{RT\ln(P_s/P)}{E_2}\right]^{t_2}\right\}(1-\rho_b/\rho_{a2})$	Specific density for each site	IDA - cr-4

				$$m_{ex}^{iDA} = m_{max}\alpha\exp\left\{-\left[\frac{RT\ln(P_s/P)}{E_1}\right]^{t_1}\right\}$$ $$+m_{max}(1-\alpha)\exp\left\{-\left[\frac{RT\ln(P_s/P)}{E_2}\right]^{t_2}\right\}$$			
			SSA with 0.38nm	$$m_{ex}^{iDA} = SSA*0.38*\rho_a\left\{\begin{array}{l}\alpha\exp\left\{-\left[\frac{RT\ln(P_s/P)}{E_1}\right]^{t_1}\right\}\\+(1-\alpha)\exp\left\{-\left[\frac{RT\ln(P_s/P)}{E_2}\right]^{t_2}\right\}\end{array}\right\}(1-\rho_b/\rho_a)$$ $$m_{ex}^{iDA} = SSA*0.38*\rho_a\left\{\begin{array}{l}\alpha\exp\left\{-\left[\frac{RT\ln(P_s/P)}{E_1}\right]^{t_1}\right\}\\+(1-\alpha)\exp\left\{-\left[\frac{RT\ln(P_s/P)}{E_2}\right]^{t_2}\right\}\end{array}\right\}$$	Apparent density	IDA - cr-5
				$$m_{ex}^{iDA} = SSA_1*0.38*\rho_{a1}\exp\left\{-\left[\frac{RT\ln(P_s/P)}{E_1}\right]^{t_1}\right\}(1-\rho_b/\rho_{a1})$$ $$+SSA_2*0.38*\rho_{a2}\exp\left\{-\left[\frac{RT\ln(P_s/P)}{E_2}\right]^{t_2}\right\}(1-\rho_b/\rho_{a2})$$	Specific density for each site	IDA - cr-6

			$$m_{ex}^{iDA} = SSA_1 * 0.38 * \rho_{a1} \exp\left\{-\left[\frac{RT\ln(P_s/P)}{E_1}\right]^{t_1}\right\}$$ $$+SSA_2 * 0.38 * \rho_{a2} \exp\left\{-\left[\frac{RT\ln(P_s/P)}{E_2}\right]^{t_2}\right\}$$		
Constant V_a	NH	-	$$m_{ex}^{iDA} = \rho_a V_a \exp\left\{-\left[\frac{RT\ln(P_s/P)}{E}\right]^{t}\right\} - \rho_b V_a$$ $$m_{abs}^{iDA} = m_{\max} \exp\left\{-\left[\frac{RT\ln(P_s/P)}{E}\right]^{t}\right\}$$	-	IDA - cv-1
	SH		$$m_{ex}^{iDA} = \rho_a V_a \left\{ \alpha\exp\left\{-\left[\frac{RT\ln(P_s/P)}{E_1}\right]^{t_1}\right\} +(1-\alpha)\exp\left\{-\left[\frac{RT\ln(P_s/P)}{E_2}\right]^{t_2}\right\} \right\} - \rho_b V_a$$ $$m_{abs}^{iDA} = \rho_a V_a \left\{ \alpha\exp\left\{-\left[\frac{RT\ln(P_s/P)}{E_1}\right]^{t_1}\right\} +(1-\alpha)\exp\left\{-\left[\frac{RT\ln(P_s/P)}{E_2}\right]^{t_2}\right\} \right\}$$	Apparent density	IDA - cv-2

				$$m_{ex}^{iDA} = \rho_{a1}V_a\alpha\exp\left\{-\left[\frac{RT\ln(P_s/P)}{E_1}\right]^{t_1}\right\}$$ $$+\rho_{a2}V_a(1-\alpha)\exp\left\{-\left[\frac{RT\ln(P_s/P)}{E_2}\right]^{t_2}\right\}-\rho_bV_a$$ $$m_{abs}^{iDA} = \rho_{a1}V_a\alpha\exp\left\{-\left[\frac{RT\ln(P_s/P)}{E_1}\right]^{t_1}\right\}$$ $$+\rho_{a2}V_a(1-\alpha)\exp\left\{-\left[\frac{RT\ln(P_s/P)}{E_2}\right]^{t_2}\right\}$$	Specific density for each site	IDA - cv-3
				$$m_{ex}^{iDA} = \rho_{a1}V_{a1}\exp\left\{-\left[\frac{RT\ln(P_s/P)}{E_1}\right]^{t_1}\right\}$$ $$+\rho_{a2}V_{a2}\exp\left\{-\left[\frac{RT\ln(P_s/P)}{E_2}\right]^{t_2}\right\}-\rho_b\left(V_{a1}+V_{a2}\right)$$ $$m_{abs}^{iDA} = \rho_{a1}V_{a1}\exp\left\{-\left[\frac{RT\ln(P_s/P)}{E_1}\right]^{t_1}\right\}$$ $$+\rho_{a2}V_{a2}\exp\left\{-\left[\frac{RT\ln(P_s/P)}{E_2}\right]^{t_2}\right\}$$	Specific density for each site	IDA - cv-4

BETp	Constant ρ_a	NH	Maximum Capacity	$m_{ex}^{BETp} = m_{\max} \dfrac{cP/P_s}{1-P/P_s} \dfrac{1-(n+1)(P/P_s)^n + n(P/P_s)^n}{1+(c-1)(P/P_s)-c(P/P_s)^{n+1}}(1-\rho_b/\rho_a)$ $m_{abs}^{BETp} = m_{\max} \dfrac{cP/P_s}{1-P/P_s} \dfrac{1-(n+1)(P/P_s)^n + n(P/P_s)^n}{1+(c-1)(P/P_s)-c(P/P_s)^{n+1}}$	-	BETp-cr-1
			SSA with 0.38nm	$m_{ex}^{BETp} = SSA*0.38*\rho_a \dfrac{cP/P_s}{1-P/P_s} \dfrac{1-(n+1)(P/P_s)^n + n(P/P_s)^n}{1+(c-1)(P/P_s)-c(P/P_s)^{n+1}}$ $(1-\rho_b/\rho_a)$ $m_{abs}^{BETp} = SSA*0.38*\rho_a \dfrac{cP/P_s}{1-P/P_s} \dfrac{1-(n+1)(P/P_s)^n + n(P/P_s)^n}{1+(c-1)(P/P_s)-c(P/P_s)^{n+1}}$	-	BETp-cr-2
		SH	Maximum Capacity	$m_{ex}^{BETp} = m_{\max} \left[\alpha \dfrac{c_1 P/P_s}{1-P/P_s} \dfrac{1-(n_1+1)(P/P_s)^{n_1} + n_1(P/P_0)^{n_1+1}}{1+(c_1-1)(P/P_s)-c_1(P/P_s)^{n_1+1}} + (1-\alpha)\dfrac{c_2 P/P_s}{1-P/P_s} \dfrac{1-(n_2+1)(P/P_s)^{n_2} + n_2(P/P_s)^{n_2+1}}{1+(c_2-1)(P/P_s)-c_2(P/P_s)^{n_2+1}} \right](1-\rho_b/\rho_a)$ $m_{abs}^{BETp} = m_{\max} \left[\alpha \dfrac{c_1 P/P_s}{1-P/P_s} \dfrac{1-(n_1+1)(P/P_s)^{n_1} + n_1(P/P_0)^{n_1+1}}{1+(c_1-1)(P/P_s)-c_1(P/P_s)^{n_1+1}} + (1-\alpha)\dfrac{c_1 P/P_s}{1-P/P_s} \dfrac{1-(n_2+1)(P/P_s)^{n_2} + n_2(P/P_s)^{n_2+1}}{1+(c_2-1)(P/P_s)-c_2(P/P_s)^{n_2+1}} \right]$	Apparent density	BETp-cr-3

				$$m_{ex}^{BETp} = m_{max}\alpha\frac{c_1 P/P_s}{1-P/P_s}\frac{1-(n_1+1)(P/P_s)^{n_1}+n_1(P/P_0)^{n_1+1}}{1+(c_1-1)(P/P_s)-c_1(P/P_s)^{n_1+1}}(1-\rho_b/\rho_{a1})$$ $$+m_{max}(1-\alpha)\frac{c_2 P/P_s}{1-P/P_s}\frac{1-(n_2+1)(P/P_s)^{n_2}+n_2(P/P_s)^{n_2+1}}{1+(c_2-1)(P/P_s)-c_2(P/P_s)^{n_2+1}}(1-\rho_b/\rho_{a2})$$ $$m_{abs}^{BETp} = m_{max}\alpha\frac{c_1 P/P_s}{1-P/P_s}\frac{1-(n_1+1)(P/P_s)^{n_1}+n_1(P/P_0)^{n_1+1}}{1+(c_1-1)(P/P_s)-c_1(P/P_s)^{n_1+1}}$$ $$+m_{max}(1-\alpha)\frac{c_2 P/P_s}{1-P/P_s}\frac{1-(n_2+1)(P/P_s)^{n_2}+n_2(P/P_s)^{n_2+1}}{1+(c_2-1)(P/P_s)-c_2(P/P_s)^{n_2+1}}$$	Specific density for each site	BETp -cr-4
		SSA with 0.38nm	$$m_{ex}^{BETp} = SSA*0.38*\rho_a\left[\begin{array}{l}\alpha\frac{c_1 P/P_s}{1-P/P_s}\frac{1-(n_1+1)(P/P_s)^{n_1}+n_1(P/P_0)^{n_1+1}}{1+(c_1-1)(P/P_s)-c_1(P/P_s)^{n_1+1}}\\+(1-\alpha)\frac{c_2 P/P_s}{1-P/P_s}\frac{1-(n_2+1)(P/P_s)^{n_2}+n_2(P/P_s)^{n_2+1}}{1+(c_2-1)(P/P_s)-c_2(P/P_s)^{n_2+1}}\end{array}\right]$$ $$(1-\rho_b/\rho_a)$$ $$m_{abs}^{BETp} = SSA*0.38*\rho_a\left[\begin{array}{l}\alpha\frac{c_1 P/P_s}{1-P/P_s}\frac{1-(n_1+1)(P/P_s)^{n_1}+n_1(P/P_s)^{n_1+1}}{1+(c_1-1)(P/P_s)-c_1(P/P_s)^{n_1+1}}\\+(1-\alpha)\frac{c_2 P/P_s}{1-P/P_s}\frac{1-(n_2+1)(P/P_s)^{n_2}+n_2(P/P_s)^{n_2+1}}{1+(c_2-1)(P/P_s)-c_2(P/P_s)^{n_2+1}}\end{array}\right]$$	Apparent density	BETp -cr-5

				$$m_{ex}^{BETp} = SSA_1 * 0.38 * \rho_{a1}\, \frac{c_1 P/P_s}{1-P/P_s}\, \frac{1-(n_1+1)(P/P_s)^{n_1}+n_1(P/P_s)^{n_1+1}}{1+(c_1-1)(P/P_s)-c_1(P/P_s)^{n_1+1}}$$ $$(1-\rho_b/\rho_{a1}) + SSA_2 * 0.38 * \rho_{a2}\, \frac{c_2 P/P_s}{1-P/P_s}\, \frac{1-(n_2+1)(P/P_s)^{n_2}+n_2(P/P_s)^{n_2+1}}{1+(c_2-1)(P/P_s)-c_2(P/P_s)^{n_2+1}}$$ $$(1-\rho_b/\rho_{a2})$$ $$m_{abs}^{BETp} = SSA_1 * 0.38 * \rho_{a1}\, \frac{c_1 P/P_s}{1-P/P_s}\, \frac{1-(n_1+1)(P/P_s)^{n_1}+n_1(P/P_s)^{n_1+1}}{1+(c_1-1)(P/P_s)-c_1(P/P_s)^{n_1+1}}$$ $$+ SSA_2 * 0.38 * \rho_{a2}\, \frac{c_2 P/P_s}{1-P/P_s}\, \frac{1-(n_2+1)(P/P_s)^{n_2}+n_2(P/P_s)^{n_2+1}}{1+(c_2-1)(P/P_s)-c_2(P/P_s)^{n_2+1}}$$	Specific density for each site	BETp-cr-6
	Constant V_a	NH	-	$$m_{ex}^{BETp} = m_{max}\, \frac{cP/P_s}{1-P/P_s}\, \frac{1-(n+1)(P/P_s)^{n}+n(P/P_s)^{n}}{1+(c-1)(P/P_s)-c(P/P_s)^{n+1}}(1-\rho_b/\rho_a)$$ $$m_{abs}^{BETp} = m_{max}\, \frac{cP/P_s}{1-P/P_s}\, \frac{1-(n+1)(P/P_s)^{n}+n(P/P_s)^{n}}{1+(c-1)(P/P_s)-c(P/P_s)^{n+1}}$$		BETp-cv-1
		SH	-	$$m_{ex}^{BETp} = \rho_a V_a \left[\alpha\, \frac{c_1 P/P_s}{1-P/P_s}\, \frac{1-(n_1+1)(P/P_s)^{n_1}+n_1(P/P_2)^{n_1+1}}{1+(c_1-1)(P/P_s)-c_1(P/P_s)^{n_1+1}} + (1-\alpha)\frac{c_2 P/P_s}{1-P/P_s}\, \frac{1-(n_2+1)(P/P_s)^{n_2}+n_2(P/P_s)^{n_2+1}}{1+(c_2-1)(P/P_s)-c_2(P/P_s)^{n_2+1}} \right] - \rho_b V_a$$	Apparent density	BETp-cv-2

				$$m_{abs}^{BETp} = \rho_a V_a \left[\alpha \frac{c_1 P/P_s}{1-P/P_s} \frac{1-(n_1+1)(P/P_s)^{n_1} + n_1(P/P_s)^{n_1+1}}{1+(c_1-1)(P/P_s)-c_1(P/P_s)^{n_1+1}} + (1-\alpha)\frac{c_2 P/P_s}{1-P/P_s} \frac{1-(n_2+1)(P/P_s)^{n_2} + n_2(P/P_s)^{n_2+1}}{1+(c_2-1)(P/P_s)-c_1(P/P_s)^{n_2+1}} \right]$$		
				$$m_{ex}^{BETp} = \rho_{a1} V_a \alpha \frac{c_1 P/P_s}{1-P/P_s} \frac{1-(n_1+1)(P/P_s)^{n_1} + n_1(P/P_s)^{n_1+1}}{1+(c_1-1)(P/P_s)-c_1(P/P_s)^{n_1+1}}$$ $$+\rho_{a2} V_a (1-\alpha)\frac{c_2 P/P_s}{1-P/P_s} \frac{1-(n_2+1)(P/P_s)^{n_2} + n_2(P/P_s)^{n_2+1}}{1+(c_2-1)(P/P_s)-c_2(P/P_s)^{n_2+1}} - \rho_b V_a$$ $$m_{abs}^{BETp} = \rho_{a1} V_a \alpha \frac{c_1 P/P_s}{1-P/P_s} \frac{1-(n_1+1)(P/P_s)^{n_1} + n_1(P/P_s)^{n_1+1}}{1+(c_1-1)(P/P_s)-c_1(P/P_s)^{n_1+1}}$$ $$+\rho_{a2} V_a (1-\alpha)\frac{c_2 P/P_s}{1-P/P_s} \frac{1-(n_2+1)(P/P_s)^{n_2} + n_2(P/P_s)^{n_2+1}}{1+(c_2-1)(P/P_s)-c_2(P/P_s)^{n_2+1}}$$	Specific density for each site	BETp-cv-3
				$$m_{ex}^{BETp} = \rho_{a1} V_{a1} \frac{c_1 P/P_s}{1-P/P_s} \frac{1-(n_1+1)(P/P_s)^{n_1} + n_1(P/P_s)^{n_1+1}}{1+(c_1-1)(P/P_s)-c_1(P/P_s)^{n_1+1}}$$ $$+\rho_{a2} V_{a2} \frac{c_2 P/P_s}{1-P/P_s} \frac{1-(n_2+1)(P/P_s)^{n_2} + n_2(P/P_s)^{n_2+1}}{1+(c_2-1)(P/P_s)-c_2(P/P_s)^{n_2+1}} - \rho_b (V_{a1}+V_{a2})$$ $$m_{abs}^{BETp} = \rho_{a1} V_{a1} \frac{c_1 P/P_s}{1-P/P_s} \frac{1-(n_1+1)(P/P_s)^{n_1} + n_1(P/P_s)^{n_1+1}}{1+(c_1-1)(P/P_s)-c_1(P/P_s)^{n_1+1}}$$ $$+\rho_{a2} V_{a2} \frac{c_2 P/P_s}{1-P/P_s} \frac{1-(n_2+1)(P/P_s)^{n_2} + n_2(P/P_s)^{n_2+1}}{1+(c_2-1)(P/P_s)-c_2(P/P_s)^{n_2+1}} - \rho_b (V_{a1}+V_{a2})$$	Specific density for each site	BETp-cv-4

SBET	Constant ρ_a	NH	Maximum Capacity	$$m_{ex}^{SBET} = m_{\max} \frac{c\rho_b/\rho_a}{1-\rho_b/\rho_a} \frac{1-(n+1)(\rho_b/\rho_a)^n + n(\rho_b/\rho_a)^n}{1+(c-1)(\rho_b/\rho_a)-c(\rho_b/\rho_a)^{n+1}}(1-\rho_b/\rho_a)$$ $$m_{abs}^{SBET} = m_{\max} \frac{c\rho_b/\rho_a}{1-\rho_b/\rho_a} \frac{1-(n+1)(\rho_b/\rho_a)^n + n(\rho_b/\rho_a)^n}{1+(c-1)(\rho_b/\rho_a)-c(\rho_b/\rho_a)^{n+1}}$$	-	SBET-cr-1
			SSA with 0.38nm	$$m_{ex}^{SBET} = SSA*0.38*\rho_a \frac{c\rho_b/\rho_a}{1-\rho_b/\rho_a} \frac{1-(n+1)(\rho_b/\rho_a)^n + n(\rho_b/\rho_a)^n}{1+(c-1)(\rho_b/\rho_a)-c(\rho_b/\rho_a)^{n+1}}(1-\rho_b/\rho_a)$$ $$m_{abs}^{SBET} = SSA*0.38*\rho_a \frac{c\rho_b/\rho_a}{1-\rho_b/\rho_a} \frac{1-(n+1)(\rho_b/\rho_a)^n + n(\rho_b/\rho_a)^n}{1+(c-1)(\rho_b/\rho_a)-c(\rho_b/\rho_a)^{n+1}}$$	-	SBET-cr-2
		SH	Maximum Capacity	$$m_{ex}^{SBET} = m_{\max}\left[\alpha \frac{c_1\rho_b/\rho_a}{1-\rho_b/\rho_a}\frac{1-(n_1+1)(\rho_b/\rho_a)^{n_1}+n_1(\rho_b/\rho_a)^{n_1+1}}{1+(c_1-1)(\rho_b/\rho_a)-c_1(\rho_b/\rho_a)^{n_1+1}} + (1-\alpha)\frac{c_2\rho_b/\rho_a}{1-\rho_b/\rho_a}\frac{1-(n_2+1)(\rho_b/\rho_a)^{n_2}+n_2(\rho_b/\rho_a)^{n_2+1}}{1+(c_2-1)(\rho_b/\rho_a)-c_2(\rho_b/\rho_a)^{n_2+1}}\right](1-\rho_b/\rho_a)$$ $$m_{abs}^{SBET} = m_{\max}\left[\alpha \frac{c_1\rho_b/\rho_a}{1-\rho_b/\rho_a}\frac{1-(n_1+1)(\rho_b/\rho_a)^{n_1}+n_1(\rho_b/\rho_a)^{n_1+1}}{1+(c_1-1)(\rho_b/\rho_a)-c_1(\rho_b/\rho_a)^{n_1+1}} + (1-\alpha)\frac{c_2\rho_b/\rho_a}{1-\rho_b/\rho_a}\frac{1-(n_2+1)(\rho_b/\rho_a)^{n_2}+n_2(\rho_b/\rho_a)^{n_2+1}}{1+(c_2-1)(\rho_b/\rho_a)-c_2(\rho_b/\rho_a)^{n_2+1}}\right]$$	Apparent density	SBET-cr-3

					Specific density for each site	SBET-cr-4
			$m_{ex}^{SBET} = m_{max}\alpha \dfrac{c_1\rho_b/\rho_{a1}}{1-\rho_b/\rho_{a1}} \dfrac{1-(n_1+1)(\rho_b/\rho_{a1})^{n_1}+n_1(\rho_b/\rho_{a1})^{n_1+1}}{1+(c_1-1)(\rho_b/\rho_{a1})-c_1(\rho_b/\rho_{a1})^{n_1+1}}(1-\rho_b/\rho_{a1})$ $+m_{max}(1-\alpha)\dfrac{c_2\rho_b/\rho_{a2}}{1-\rho_b/\rho_{a2}} \dfrac{1-(n_2+1)(\rho_b/\rho_{a2})^{n_2}+n_2(\rho_b/\rho_{a2})^{n_2+1}}{1+(c_2-1)(\rho_b/\rho_{a2})-c_1(\rho_b/\rho_{a2})^{n_2+1}}(1-\rho_b/\rho_{a2})$ $m_{abs}^{SBET} = m_{max}\alpha \dfrac{c_1\rho_b/\rho_{a1}}{1-\rho_b/\rho_{a1}} \dfrac{1-(n_1+1)(\rho_b/\rho_{a1})^{n_1}+n_1(\rho_b/\rho_{a1})^{n_1+1}}{1+(c_1-1)(\rho_b/\rho_{a1})-c_1(\rho_b/\rho_{a1})^{n_1+1}}$ $+m_{max}(1-\alpha)\dfrac{c_2\rho_b/\rho_{a2}}{1-\rho_b/\rho_{a2}} \dfrac{1-(n_2+1)(\rho_b/\rho_{a2})^{n_2}+n_2(\rho_b/\rho_{a2})^{n_2+1}}{1+(c_2-1)(\rho_b/\rho_{a2})-c_1(\rho_b/\rho_{a2})^{n_2+1}}$		
		SSA with 0.38nm	$m_{ex}^{SBET} = SSA*0.38*\rho_a \left[\alpha \dfrac{c_1\rho_b/\rho_a}{1-\rho_b/\rho_a} \dfrac{1-(n_1+1)(\rho_b/\rho_a)^{n_1}+n_1(\rho_b/\rho_a)^{n_1+1}}{1+(c_1-1)(\rho_b/\rho_a)-c_1(\rho_b/\rho_a)^{n_1+1}} +(1-\alpha)\dfrac{c_2\rho_b/\rho_a}{1-\rho_b/\rho_a} \dfrac{1-(n_2+1)(\rho_b/\rho_a)^{n_2}+n_2(\rho_b/\rho_a)^{n_2+1}}{1+(c_2-1)(\rho_b/\rho_a)-c_2(\rho_b/\rho_a)^{n_2+1}} \right]$ $(1-\rho_b/\rho_a)$ $m_{abs}^{SBET} = SSA*0.38*\rho_a \left[\alpha \dfrac{c_1\rho_b/\rho_a}{1-\rho_b/\rho_a} \dfrac{1-(n_1+1)(\rho_b/\rho_a)^{n_1}+n_1(\rho_b/\rho_a)^{n_1+1}}{1+(c_1-1)(\rho_b/\rho_a)-c_1(\rho_b/\rho_a)^{n_1+1}} +(1-\alpha)\dfrac{c_2\rho_b/\rho_a}{1-\rho_b/\rho_a} \dfrac{1-(n_2+1)(\rho_b/\rho_a)^{n_2}+n_2(\rho_b/\rho_a)^{n_2+1}}{1+(c_2-1)(\rho_b/\rho_a)-c_2(\rho_b/\rho_a)^{n_2+1}} \right]$		Apparent density	SBET-cr-5

			$m_{ex}^{SBET} = SSA_1 * 0.38 * \rho_{a1} \dfrac{c_1 \rho_b / \rho_{a1}}{1 - \rho_b / \rho_{a1}} \dfrac{1 - (n_1+1)(\rho_b/\rho_{a1})^{n_1} + n_1(\rho_b/\rho_{a1})^{n_1+1}}{1 + (c_1-1)(\rho_b/\rho_{a1}) - c_1(\rho_b/\rho_{a1})^{n_1+1}}$ $(1 - \rho_b/\rho_{a1}) + SSA_2 * 0.38 * \rho_{a2} \dfrac{c_2 \rho_b / \rho_{a2}}{1 - \rho_b / \rho_{a2}} \dfrac{1 - (n_2+1)(\rho_b/\rho_{a2})^{n_2} + n_2(\rho_b/\rho_{a2})^{n_2+1}}{1 + (c_2-1)(\rho_b/\rho_{a2}) - c_1(\rho_b/\rho_{a2})^{n_2+1}}$ $(1 - \rho_b/\rho_{a2})$ $m_{abs}^{SBET} = SSA_1 * 0.38 * \rho_{a1} \dfrac{c_1 \rho_b / \rho_{a1}}{1 - \rho_b / \rho_{a1}} \dfrac{1 - (n_1+1)(\rho_b/\rho_{a1})^{n_1} + n_1(\rho_b/\rho_{a1})^{n_1+1}}{1 + (c_1-1)(\rho_b/\rho_{a1}) - c_1(\rho_b/\rho_{a1})^{n_1+1}}$ $+ SSA_2 * 0.38 * \rho_{a2} \dfrac{c_2 \rho_b / \rho_{a2}}{1 - \rho_b / \rho_{a2}} \dfrac{1 - (n_2+1)(\rho_b/\rho_{a2})^{n_2} + n_2(\rho_b/\rho_{a2})^{n_2+1}}{1 + (c_2-1)(\rho_b/\rho_{a2}) - c_1(\rho_b/\rho_{a2})^{n_2+1}}$	Specific density for each site	SBET -cr-6
Constant V_a	NH	-	$m_{ex}^{SBET} = m_{max} \dfrac{c \rho_b / \rho_a}{1 - \rho_b / \rho_a} \dfrac{1 - (n+1)(\rho_b/\rho_a)^n + n(\rho_b/\rho_a)^n}{1 + (c-1)(\rho_b/\rho_a) - c(\rho_b/\rho_a)^{n+1}}(1 - \rho_b/\rho_a)$ $m_{abs}^{SBET} = m_{max} \dfrac{c \rho_b / \rho_a}{1 - \rho_b / \rho_a} \dfrac{1 - (n+1)(\rho_b/\rho_a)^n + n(\rho_b/\rho_a)^n}{1 + (c-1)(\rho_b/\rho_a) - c(\rho_b/\rho_a)^{n+1}}$		SBET -cv-1
	SH	-	$m_{ex}^{SBET} = \rho_a V_a \left[\alpha \dfrac{c_1 \rho_b / \rho_a}{1 - P/P_s} \dfrac{1 - (n_1+1)(\rho_b/\rho_a)^{n_1} + n_1(\rho_b/\rho_a)^{n_1+1}}{1 + (c_1-1)(\rho_b/\rho_a) - c_1(\rho_b/\rho_a)^{n_1+1}} + (1-\alpha)\dfrac{c_2 \rho_b / \rho_a}{1 - P/P_s} \dfrac{1 - (n_2+1)(\rho_b/\rho_a)^{n_2} + n_2(\rho_b/\rho_a)^{n_2+1}}{1 + (c_2-1)(\rho_b/\rho_a) - c_2(\rho_b/\rho_a)^{n_2+1}} \right] - \rho_b V_a$	Apparent density	SBET -cv-2

				Equation	Note	Model
				$$m_{abs}^{SBET} = \rho_a V_a \left[\alpha \frac{c_1 \rho_b / \rho_a}{1 - P/P_s} \frac{1 - (n_1+1)(\rho_b/\rho_a)^{n_1} + n_1(\rho_b/\rho_a)^{n_1+1}}{1 + (c_1-1)(\rho_b/\rho_a) - c_1(\rho_b/\rho_a)^{n_1+1}} + (1-\alpha)\frac{c_2 \rho_b/\rho_a}{1-P/P_s}\frac{1-(n_2+1)(\rho_b/\rho_a)^{n_2}+n_2(\rho_b/\rho_a)^{n_2+1}}{1+(c_2-1)(\rho_b/\rho_a)-c_2(\rho_b/\rho_a)^{n_2+1}} \right]$$		
				$$m_{ex}^{SBET} = \rho_{a1} V_a \alpha \frac{c_1 \rho_b/\rho_{a1}}{1-\rho_b/\rho_{a1}}\frac{1-(n_1+1)(\rho_b/\rho_{a1})^{n_1}+n_1(\rho_b/\rho_{a1})^{n_1+1}}{1+(c_1-1)(\rho_b/\rho_{a1})-c_1(\rho_b/\rho_{a1})^{n_1+1}} + \rho_{a2}V_a(1-\alpha)\frac{c_1\rho_b/\rho_{a2}}{1-\rho_b/\rho_{a2}}\frac{1-(n_2+1)(\rho_b/\rho_{a2})^{n_2}+n_2(\rho_b/\rho_{a2})^{n_2+1}}{1+(c_2-1)(\rho_b/\rho_{a2})-c_2(\rho_b/\rho_{a2})^{n_2+1}} - \rho_b V_a$$ $$m_{abs}^{SBET} = \rho_{a1}V_a\alpha\frac{c_1\rho_b/\rho_{a1}}{1-\rho_b/\rho_{a1}}\frac{1-(n_1+1)(\rho_b/\rho_{a1})^{n_1}+n_1(\rho_b/\rho_{a1})^{n_1+1}}{1+(c_1-1)(\rho_b/\rho_{a1})-c_1(\rho_b/\rho_{a1})^{n_1+1}} + \rho_{a2}V_a(1-\alpha)\frac{c_1\rho_b/\rho_{a2}}{1-\rho_b/\rho_{a2}}\frac{1-(n_2+1)(\rho_b/\rho_{a2})^{n_2}+n_2(\rho_b/\rho_{a2})^{n_2+1}}{1+(c_2-1)(\rho_b/\rho_{a2})-c_2(\rho_b/\rho_{a2})^{n_2+1}}$$	Specific density for each site	SBET-cv-3
				$$m_{ex}^{SBET} = \rho_{a1}V_{a1}\frac{c_1\rho_b/\rho_{a1}}{1-\rho_b/\rho_{a1}}\frac{1-(n_1+1)(\rho_b/\rho_{a1})^{n_1}+n_1(\rho_b/\rho_{a1})^{n_1+1}}{1+(c_1-1)(\rho_b/\rho_{a1})-c_1(\rho_b/\rho_{a1})^{n_1+1}} + \rho_{a2}V_{a2}\frac{c_2\rho_b/\rho_{a2}}{1-\rho_b/\rho_{a2}}\frac{1-(n_2+1)(\rho_b/\rho_{a2})^{n_2}+n_2(\rho_b/\rho_{a2})^{n_2+1}}{1+(c_2-1)(\rho_b/\rho_{a2})-c_2(\rho_b/\rho_{a2})^{n_2+1}} - \rho_b(V_{a1}+V_{a2})$$ $$m_{abs}^{SBET} = \rho_{a1}V_{a1}\frac{c_1\rho_b/\rho_{a1}}{1-\rho_b/\rho_{a1}}\frac{1-(n_1+1)(\rho_b/\rho_{a1})^{n_1}+n_1(\rho_b/\rho_{a1})^{n_1+1}}{1+(c_1-1)(\rho_b/\rho_{a1})-c_1(\rho_b/\rho_{a1})^{n_1+1}} + \rho_{a2}V_{a2}\frac{c_2\rho_b/\rho_{a2}}{1-\rho_b/\rho_{a2}}\frac{1-(n_2+1)(\rho_b/\rho_{a2})^{n_2}+n_2(\rho_b/\rho_{a2})^{n_2+1}}{1+(c_2-1)(\rho_b/\rho_{a2})-c_2(\rho_b/\rho_{a2})^{n_2+1}}$$	Specific density for each site	SBET-cv-4

OK	-	NH	Maximum Capacity (mc)	$$m_{ex}^{OK} = C\sum_{k=1}^{n_k}(x_k - x_b)$$ $$m_{abs}^{OK} = C\sum_{k=1}^{n_k}(x_k)$$	-	OK-mc-1
			Fixed adsorbed phase volume (fv)	$$m_{ex}^{OK} = \rho_{am}^{OK} W_a SSA\sum_{k=1}^{n_k}(x_k - x_b)$$ $$m_{ex}^{OK} = \rho_{am}^{OK} W_a SSA\sum_{k=1}^{n_k}(x_k)$$	-	OK-fv-1
		SH	Maximum Capacity	$$m_{ex}^{OK} = \alpha C\sum_{k=1}^{n_k}(x_{1,k} - x_{1,b}) + (1-\alpha)C\sum_{k=1}^{n_k}(x_{2,k} - x_{2,b})$$ $$m_{abs}^{OK} = \alpha C\sum_{k=1}^{n_k}(x_{1,k}) + (1-\alpha)C\sum_{k=1}^{n_k}(x_{2,k})$$	-	OK-mc-2
			Constant adsorbed phase volume	$$m_{ex}^{OK} = \rho_{am,1} W_a SSA_1\sum_{k=1}^{n_k}(x_{1,k} - x_{1,b}) + \rho_{am,2} W_a SSA_2\sum_{k=1}^{n_k}(x_{2,k} - x_{2,b})$$ $$m_{abs}^{OK} = \rho_{am,1} W_a SSA_1\sum_{k=1}^{n_k}(x_{1,k}) + \rho_{am,2} W_a SSA_2\sum_{k=1}^{n_k}(x_{2,k})$$	-	OK-fv-2

		DH	Constant adsorbed phase volume	$$m_{ex}^{OK} = \sum_{j=1}^{5} \sum_{i \in \text{Type j}} \rho_{am,1} W_a SSA_i \sum_{k=1}^{n_k} \left(x_{1,k} - x_{1,b} \right) + \sum_{j=1}^{6} \sum_{i \in \text{Type j}} \rho_{am,2} W_a SSA_i \sum_{k=1}^{n_k} \left(x_{2,k} - x_{2,b} \right)$$ $$m_{abs}^{OK} = \sum_{j=1}^{5} \sum_{i \in \text{Type j}} \rho_{am,1} W_a SSA_i \sum_{k=1}^{n_k} \left(x_{1,k} \right) + \sum_{j=1}^{6} \sum_{i \in \text{Type j}} \rho_{am,2} W_a SSA_i \sum_{k=1}^{n_k} \left(x_{2,k} \right)$$		OK-DH
Toth	Constant ρ_a	NH	-	$$m_{ex}^{Toth} = m_{\max} \frac{bP}{\left(1 + (bP)^t\right)^{\frac{1}{t}}} \left(1 - \rho_b / \rho_a\right)$$ $$m_{abs}^{Toth} = m_{\max} \frac{bP}{\left(1 + (bP)^t\right)^{\frac{1}{t}}}$$		Toth-cr
	Constant V_a	NH	-	$$m_{ex}^{Toth} = \rho_a V_a \frac{bP}{\left(1 + (bP)^t\right)^{\frac{1}{t}}} - \rho_b V_a$$ $$m_{abs}^{Toth} = \rho_a V_a \frac{bP}{\left(1 + (bP)^t\right)^{\frac{1}{t}}}$$		Toth-fv

Langmuir-Freundlich	Constant ρ_a	NH	-	$$m_{ex}^{LF} = m_{max} \frac{bP^t}{1+(bP)^t}(1-\rho_b/\rho_a)$$ $$m_{abs}^{LF} = m_{max} \frac{bP^t}{1+(bP)^t}$$		LF-cr
	Constant V_a	NH	-	$$m_{ex}^{LF} = \rho_a V_a \frac{bP^t}{1+(bP)^t} - \rho_b V_a$$ $$m_{abs}^{LF} = \rho_a V_a \frac{bP^t}{1+(bP)^t}$$		LF-fv
Direct conversion	Constant ρ_a	NH	-	$$m_{abs} = m_{ex}/(1-\rho_b/\rho_a)$$		DC-cr
	Constant V_a	NH	-	$$m_{abs} = m_{ex} + \rho_b V_a$$		DC-cv

Table F4 Detailed information of 171 models

Model	Conversion method	Type	Details	Regression Parameters	Expression	Order
Langmuir[264]	Constant ρ_a	No-heterogeneity	ρ_a= 373 kg/m^3[101]	n_m, P_L	L-cr-1	#1
			ρ_a= 424 kg/m^3[167]		L-cr-1	#2
			$\rho_a = \rho_b \exp[-0.0025(T-T_b)]$ kg/m^3 [65]		L-cr-1	#3
			GCMC-4 nm- carbon[64]		L-cr-1	#4

			GCMC-4 nm- illite		L-cr-1	#5
			ρ_a freely fitted[183]	n_m, P_L, ρ_a	L-cr-1	#6
			ρ_a freely fitted+ SSA with 0.38 nm as layer width[40]	P_L, ρ_a	L-cr-2	#7
		Single-heterogeneity (pore width) [250]	ρ_a= 373 kg/m^3	n_m, P_{L1}, P_{L2}	L-cr-3	#8
			ρ_a= 424 kg/m^3		L-cr-3	#9
			ρ_a= ρ_b exp[-0.0025(T-T_b)] kg/m^3		L-cr-3	#10
			ρ_a freely fitted and apparent ρ_a for all sites (ρ_a)[250]	$n_m, P_{L1}, P_{L2}, \rho_a$	L-cr-3	#11
			ρ_a freely fitted and two types ρ_a for specific sites (ρ_{a1} and ρ_{a2})	$n_m, P_{L1}, P_{L2}, \rho_{a1}, \rho_{a2}$	L-cr-4	#12
			ρ_a freely fitted+ SSA with 0.38 nm as layer width+ apparent ρ_a (ρ_a)	P_{L1}, P_{L2}, ρ_a	L-cr-5	#13
			ρ_a freely fitted+ SSA with 0.38 nm as layer width+ two ρ_a (ρ_{a1} and ρ_{a2})	$P_{L1}, P_{L2}, \rho_{a1}, \rho_{a2}$	L-cr-6	#14
		Single-heterogeneity (rock heterogeneity)	ρ_a= 373 kg/m^3	n_m, P_{L1}, P_{L2}	L-cr-3	#15
			ρ_a= 424 kg/m^3		L-cr-3	#16
			ρ_a= ρ_b exp[-0.0025(T-T_b)] kg/m^3		L-cr-3	#17
			ρ_a freely fitted and apparent ρ_a for all sites (ρ_a)	$n_m, P_{L1}, P_{L2}, \rho_a$	L-cr-3	#18
			ρ_a freely fitted and two types ρ_a for specific sites (ρ_{a1} and	$n_m, P_{L1}, P_{L2}, \rho_{a1}, \rho_{a2}$	L-cr-4	#19

			ρ_{a2})			
			ρ_a freely fitted+ SSA with 0.38 nm as layer width+ apparent ρ_a (ρ_a)	P_{L1}, P_{L2}, ρ_a	L-cr-5	#20
			ρ_a freely fitted+ SSA with 0.38 nm as layer width+ two ρ_a (ρ_{a1} and ρ_{a2})	P_{L1}, P_{L2}, ρ_{a1}, ρ_{a2}	L-cr-6	#21
	Constant V_a	No-heterogeneity[265]	-	V_a, P_L, ρ_a	L-cv-1	#22
		Single-heterogeneity (pore width)	-	V_a, P_{L1}, P_{L2}, ρ_a	L-cv-2	#23
			-	V_a, P_{L1}, P_{L2}, ρ_{a1}, ρ_{a1}	L-cv-3	#24
			-	V_{a1}, V_{a2}, P_{L1}, P_{L2}, ρ_{a1}, ρ_{a1}	L-cv-4	#25
		Single-heterogeneity (rock heterogeneity)	-	V_a, P_{L1}, P_{L2}, ρ_a	L-cv-2	#26
			-	V_a, P_{L1}, P_{L2}, ρ_{a1}, ρ_{a1}	L-cv-3	#27
			-	V_{a1}, V_{a2}, P_{L1}, P_{L2}, ρ_{a1}, ρ_{a1}	L-cv-4	#28
SDR[183]	Constant ρ_a	No-heterogeneity	ρ_a= 373 kg/m^3	n_m, D	SDR-cr-1	#29
			ρ_a= 424 kg/m^3		SDR -cr-1	#30
			ρ_a= ρ_b exp[-0.0025(T-T_b)] kg/m^3		SDR -cr-1	#31
			GCMC-4 nm- carbon		SDR -cr-1	#32

			GCMC-4 nm- illite		SDR -cr-1	#33
			ρ_a freely fitted	n_m, D, ρ_a	SDR -cr-1	#34
			ρ_a freely fitted+ SSA with 0.38 nm as layer width	D, ρ_a	SDR -cr-2	#35
		Single-heterogeneity (pore width)	ρ_a= 373 kg/m^3	n_m, D_1, D_2	SDR -cr-3	#36
			ρ_a= 424 kg/m^3		SDR -cr-3	#37
			ρ_a= ρ_b exp[-0.0025(T-T_b)] kg/m^3		SDR -cr-3	#38
			ρ_a freely fitted and apparent ρ_a for all sites (ρ_a)	n_m, D_1, D_2, ρ_a	SDR -cr-3	#39
			ρ_a freely fitted and two types ρ_a for specific sites (ρ_{a1} and ρ_{a2})	n_m, D_1, D_2, ρ_{a1}, ρ_{a2}	SDR -cr-4	#40
			ρ_a freely fitted+ SSA with 0.38 nm as layer width+ apparent ρ_a (ρ_a)	D_1, D_2, ρ_a	SDR -cr-5	#41
			ρ_a freely fitted+ SSA with 0.38 nm as layer width+ two ρ_a (ρ_{a1} and ρ_{a2})	D_1, D_2, ρ_{a1}, ρ_{a2}	SDR -cr-6	#42
		Single-heterogeneity (rock heterogeneity)	ρ_a= 373 kg/m^3	n_m, D_1, D_2	SDR -cr-3	#43
			ρ_a= 424 kg/m^3		SDR -cr-3	#44
			ρ_a= ρ_b exp[-0.0025(T-T_b)] kg/m^3		SDR -cr-3	#45
			ρ_a freely fitted and apparent ρ_a for all sites (ρ_a)	n_m, D_1, D_2, ρ_a	SDR -cr-3	#46
			ρ_a freely fitted and two types ρ_a for specific sites (ρ_{a1} and	n_m, D_1, D_2, ρ_{a1}, ρ_{a2}	SDR -cr-4	#47

			ρ_{a2})			
			ρ_a freely fitted+ SSA with 0.38 nm as layer width+ apparent ρ_a (ρ_a)	D_1, D_2, ρ_a	SDR -cr-5	#48
			ρ_a freely fitted+ SSA with 0.38 nm as layer width+ two ρ_a (ρ_{a1} and ρ_{a2})	D_1, D_2, ρ_{a1}, ρ_{a2}	SDR -cr-6	#49
	Constant V_a	No-heterogeneity[259]	-	V_a, D, ρ_a	SDR-cv-1	#50
		Single-heterogeneity (pore width)	-	V_a, D_1, D_2, ρ_a	SDR -cv-2	#51
			-	V_a, D_1, D_2, ρ_{a1}, ρ_{a2}	SDR -cv-3	#52
			-	V_{a1}, V_{a2}, D_1, D_2, ρ_{a1}, ρ_{a2}	SDR -cv-4	#53
		Single-heterogeneity (rock heterogeneity)	-	V_a, D_1, D_2, ρ_a	SDR -cv-2	#54
			-	V_a, D_1, D_2, ρ_{a1}, ρ_{a2}	SDR -cv-3	#55
			-	V_{a1}, V_{a2}, D_1, D_2, ρ_{a1}, ρ_{a2}	SDR -cv-4	#56
Improved DA[252]	Constant ρ_a	No-heterogeneity	ρ_a= 373 kg/m^3	n_m, t, E	IDA-cr-1	#57
			ρ_a= 424 kg/m^3		IDA -cr-1	#58
			ρ_a= ρ_b exp[-0.0025(T-T_b)] kg/m^3		IDA -cr-1	#59
			GCMC-4 nm- carbon		IDA -cr-1	#60
			GCMC-4 nm- illite		IDA -cr-1	#61
			ρ_a freely fitted	n_m, t, E, ρ_a	IDA -cr-1	#62

			ρ_a freely fitted+ SSA with 0.38 nm as layer width	t, E, ρ_a	IDA -cr-2	#63
		Single-heterogeneity (pore width)	ρ_a= 373 kg/m^3	n_m, t_1, t_2, E_1, E_2	IDA -cr-3	#64
			ρ_a= 424 kg/m^3		IDA -cr-3	#65
			ρ_a= ρ_b exp[-0.0025(T-T_b)] kg/m^3		IDA -cr-3	#66
			ρ_a freely fitted and apparent ρ_a for all sites (ρ_a)	n_m, t_1, t_2, E_1, E_2, ρ_a	IDA -cr-3	#67
			ρ_a freely fitted and two types ρ_a for specific sites (ρ_{a1} and ρ_{a2})	n_m, t_1, t_2, E_1, E_2, ρ_{a1}, ρ_{a2}	IDA -cr-4	#68
			ρ_a freely fitted+ SSA with 0.38 nm as layer width+ apparent ρ_a (ρ_a)	t_1, t_2, E_1, E_2, ρ_a	IDA -cr-5	#69
			ρ_a freely fitted+ SSA with 0.38 nm as layer width+ two ρ_a (ρ_{a1} and ρ_{a2})	t_1, t_2, E_1, E_2, ρ_{a1}, ρ_{a2}	IDA -cr-6	#70
		Single-heterogeneity (rock heterogeneity)	ρ_a= 373 kg/m^3	n_m, t_1, t_2, E_1, E_2	IDA -cr-3	#71
			ρ_a= 424 kg/m^3		IDA -cr-3	#72
			ρ_a= ρ_b exp[-0.0025(T-T_b)] kg/m^3		IDA -cr-3	#73
			ρ_a freely fitted and apparent ρ_a for all sites (ρ_a)	n_m, t_1, t_2, E_1, E_2, ρ_a	IDA -cr-3	#74
			ρ_a freely fitted and two types ρ_a for specific sites (ρ_{a1} and ρ_{a2})	n_m, t_1, t_2, E_1, E_2, ρ_{a1}, ρ_{a2}	IDA -cr-4	#75

			ρ_a freely fitted+ SSA with 0.38 nm as layer width+ apparent ρ_a (ρ_a)	t_1, t_2, E_1, E_2, ρ_a	IDA -cr-5	#76
			ρ_a freely fitted+ SSA with 0.38 nm as layer width+ two ρ_a (ρ_{a1} and ρ_{a2})	t_1, t_2, E_1, E_2, ρ_{a1}, ρ_{a2}	IDA -cr-6	#77
	Constant V_a	No-heterogeneity	-	-	IDA-cv-1	#78
		Single-heterogeneity (pore width)	-	-	IDA -cv-2	#79
			-	-	IDA -cv-3	#80
			-	-	IDA -cv-4	#81
		Single-heterogeneity (rock heterogeneity)	-	-	IDA -cv-2	#82
			-	-	IDA -cv-3	#83
			-	-	IDA -cv-4	#84
BET-pseudocritical pressure[187]	Constant ρ_a	No-heterogeneity	ρ_a= 373 kg/m^3	n_m, C, n	BETp-cr-1	#85
			ρ_a= 424 kg/m^3		BETp -cr-1	#86
			ρ_a= ρ_b exp[-0.0025(T-T_b)] kg/m^3		BETp -cr-1	#87
			GCMC-4 nm- carbon		BETp -cr-1	#88
			GCMC-4 nm- illite		BETp -cr-1	#89
			ρ_a freely fitted	n_m, C, n, ρ_a	BETp -cr-1	#90
			ρ_a freely fitted+ SSA with 0.38 nm as layer width	C, n, ρ_a	BETp -cr-2	#91
		Single-heterogeneity (pore width)	ρ_a= 373 kg/m^3	n_m, C_1, C_2, n_1, n_2	BETp -cr-3	#92
			ρ_a= 424 kg/m^3		BETp -cr-3	#93
			ρ_a= ρ_b exp[-0.0025(T-T_b)] kg/m^3		BETp -cr-3	#94

				n_m, C_1, C_2, n_1, n_2, ρ_a	BETp -cr-3	#95
			ρ_a freely fitted and apparent ρ_a for all sites (ρ_a)			
			ρ_a freely fitted and two types ρ_a for specific sites (ρ_{a1} and ρ_{a2})	n_m, C_1, C_2, n_1, n_2, ρ_{a1}, ρ_{a2}	BETp -cr-4	#96
			ρ_a freely fitted+ SSA with 0.38 nm as layer width+ apparent ρ_a (ρ_a)	C_1, C_2, n_1, n_2, ρ_a	BETp -cr-5	#97
			ρ_a freely fitted+ SSA with 0.38 nm as layer width+ two ρ_a (ρ_{a1} and ρ_{a2})	C_1, C_2, n_1, n_2, ρ_{a1}, ρ_{a2}	BETp -cr-6	#98
		Single-heterogeneity (rock heterogeneity)	ρ_a= 373 kg/m^3	n_m, C_1, C_2, n_1, n_2	BETp -cr-3	#99
			ρ_a= 424 kg/m^3		BETp -cr-3	#100
			ρ_a= ρ_b exp[-0.0025(T-T_b)] kg/m^3		BETp -cr-3	#101
			ρ_a freely fitted and apparent ρ_a for all sites (ρ_a)	n_m, C_1, C_2, n_1, n_2, ρ_a	BETp -cr-3	#102
			ρ_a freely fitted and two types ρ_a for specific sites (ρ_{a1} and ρ_{a2})	n_m, C_1, C_2, n_1, n_2, ρ_{a1}, ρ_{a2}	BETp -cr-4	#103
			ρ_a freely fitted+ SSA with 0.38 nm as layer width+ apparent ρ_a (ρ_a)	C_1, C_2, n_1, n_2, ρ_a	BETp -cr-5	#104
			ρ_a freely fitted+ SSA with 0.38 nm as layer width+ two ρ_a (ρ_{a2}	C_1, C_2, n_1, n_2, ρ_{a1}, ρ_{a2}	BETp -cr-6	#105

			ρ_{a1} and ρ_{a2})			
	Constant V_a	No-heterogeneity	-	V_a, C, n, ρ_a	BETp-cv-1	#106
		Single-heterogeneity (pore width)	-	V_a, C_1, C_2, n_1, n_2, ρ_a	BETp -cv-2	#107
			-	V_a, C_1, C_2, n_1, n_2, ρ_{a1}, ρ_{a2}	BETp -cv-3	#108
			-	V_{a1}, V_{a2}, C_1, C_2, n_1, n_2, ρ_{a1}, ρ_{a2}	BETp -cv-4	#109
		Single-heterogeneity (rock heterogeneity)	-	V_a, C_1, C_2, n_1, n_2, ρ_a	BETp -cv-2	#110
			-	V_a, C_1, C_2, n_1, n_2, ρ_{a1}, ρ_{a2}	BETp -cv-3	#111
			-	V_{a1}, V_{a2}, C_1, C_2, n_1, n_2, ρ_{a1}, ρ_{a2}	BETp -cv-4	#112
SBET[266]	Constant ρ_a	No-heterogeneity	ρ_a= 373 kg/m^3	n_m, C, n	SBET-cr-1	#113
			ρ_a= 424 kg/m^3		SBET -cr-1	#114
			ρ_a= ρ_b exp[-0.0025(T-T_b)] kg/m^3		SBET -cr-1	#115
			GCMC-4 nm- carbon		SBET -cr-1	#116
			GCMC-4 nm- illite		SBET -cr-1	#117
			ρ_a freely fitted	n_m, C, n, ρ_a	SBET -cr-1	#118
			ρ_a freely fitted+ SSA with 0.38 nm as layer width	C, n, ρ_a	SBET -cr-2	#119
		Single-heterogeneity	ρ_a= 373 kg/m^3	n_m, C_1, C_2, n_1, n_2	SBET -cr-3	#120
			ρ_a= 424 kg/m^3		SBET -cr-3	#121

			Description	Parameters	Method	#
		(pore width)	$\rho_a = \rho_b \exp[-0.0025(T-T_b)]$ kg/m³		SBET -cr-3	#122
			ρ_a freely fitted and apparent ρ_a for all sites (ρ_a)	$n_m, C_1, C_2, n_1, n_2, \rho_a$	SBET -cr-3	#123
			ρ_a freely fitted and two types ρ_a for specific sites (ρ_{a1} and ρ_{a2})	$n_m, C_1, C_2, n_1, n_2, \rho_{a1}, \rho_{a2}$	SBET -cr-4	#124
			ρ_a freely fitted+ SSA with 0.38 nm as layer width+ apparent ρ_a (ρ_a)	$C_1, C_2, n_1, n_2, \rho_a$	SBET -cr-5	#125
			ρ_a freely fitted+ SSA with 0.38 nm as layer width+ two ρ_a (ρ_{a1} and ρ_{a2})	$C_1, C_2, n_1, n_2, \rho_{a1}, \rho_{a2}$	SBET -cr-6	#126
		Single-heterogeneity (rock heterogeneity)	$\rho_a = 373$ kg/m³	n_m, C_1, C_2, n_1, n_2	SBET -cr-3	#127
			$\rho_a = 424$ kg/m³		SBET -cr-3	#128
			$\rho_a = \rho_b \exp[-0.0025(T-T_b)]$ kg/m³		SBET -cr-3	#129
			ρ_a freely fitted and apparent ρ_a for all sites (ρ_a)	$n_m, C_1, C_2, n_1, n_2, \rho_a$	SBET -cr-3	#130
			ρ_a freely fitted and two types ρ_a for specific sites (ρ_{a1} and ρ_{a2})	$n_m, C_1, C_2, n_1, n_2, \rho_{a1}, \rho_{a2}$	SBET -cr-4	#131
			ρ_a freely fitted+ SSA with 0.38 nm as layer width+ apparent ρ_a (ρ_a)	$C_1, C_2, n_1, n_2, \rho_a$	SBET -cr-5	#132
			ρ_a freely fitted+ SSA with 0.38 nm as layer width+ two ρ_a (	$C_1, C_2, n_1, n_2, \rho_{a1},$	SBET -cr-6	#133

				ρ_{a2}		
			ρ_{a1} and ρ_{a2})			
	Constant V_a	No-heterogeneity	-	V_a, C, n, ρ_a	SBET-cv-1	#134
		Single-heterogeneity (pore width)	-	V_a, C_1, C_2, n_1, n_2, ρ_a	SBET -cv-2	#135
			-	V_a, C_1, C_2, n_1, n_2, ρ_{a1}, ρ_{a2}	SBET -cv-3	#136
			-	V_{a1}, V_{a2}, C_1, C_2, n_1, n_2, ρ_{a1}, ρ_{a2}	SBET -cv-4	#137
		Single-heterogeneity (rock heterogeneity)	-	V_a, C_1, C_2, n_1, n_2, ρ_a	SBET -cv-2	#138
			-	V_a, C_1, C_2, n_1, n_2, ρ_{a1}, ρ_{a2}	SBET -cv-3	#139
			-	V_{a1}, V_{a2}, C_1, C_2, n_1, n_2, ρ_{a1}, ρ_{a2}	SBET -cv-4	#140
Toth[267]	Constant ρ_a	No-heterogeneity	ρ_a= 373 kg/m^3	n_m, b, t	Toth-cr	#141
			ρ_a= 424 kg/m^3		Toth-cr	#142
			ρ_a= $\rho_b \exp[-0.0025(T-T_b)]$ kg/m^3		Toth-cr	#143
			GCMC-4 nm- carbon		Toth-cr	#144
			GCMC-4 nm- illite		Toth-cr	#145
			ρ_a freely fitted	n_m, b, t, ρ_a	Toth-cr	#146
			ρ_a freely fitted+ SSA with 0.38 nm as layer width	b, t, ρ_a	Toth-cr	#147
	Constant V_a	No-heterogeneity	-		Toth-cv	#148

Langmuir-Freundlich[268]	Constant ρ_a	No-heterogeneity	ρ_a= 373 kg/m^3	n_m, b, t	LF-cr	#149
			ρ_a= 424 kg/m^3		LF-cr	#150
			ρ_a= ρ_b exp[-0.0025(T-T_b)] kg/m^3		LF-cr	#151
			GCMC-4 nm- carbon		LF-cr	#152
			GCMC-4 nm- illite		LF-cr	#153
			ρ_a freely fitted	n_m, b, t, ρ_a	LF-cr	#154
			ρ_a freely fitted+ SSA with 0.38 nm as layer width	b, t, ρ_a	LF-cr	#155
	Constant V_a	No-heterogeneity	-		LF-cv	#156
OK model[40]	Constant V_a	No-heterogeneity	Maximum capacity	C, ρ_m, ε_s, ε	OK-mc-1	#157
			Fixed adsorbed phase volume	ρ_m, ε_s, ε	OK-fv-1	#158
		Single-heterogeneity (pore width)	Maximum capacity	C, ρ_{m1}, ρ_{m2}, ε_{s1}, ε_{s2}, ε	OK-mc-2	#159
			Fixed adsorbed phase volume	ρ_{m1}, ρ_{m2}, ε_{s1}, ε_{s2}, ε	OK-fv-2	#160
			Fixed adsorbed phase volume- carbon PSD lumping	ρ_m, ε_s, ε	OK-fv-3	#161
			Fixed adsorbed phase volume- clay PSD lumping	ρ_m, ε_s, ε	OK-fv-4	#162
		Single-heterogeneity (rock heterogeneity)	Maximum capacity	C, ρ_{m1}, ρ_{m2}, ε_{s1}, ε_{s2}, ε	OK-mc-2	#163
			Fixed adsorbed phase volume	ρ_{m1}, ρ_{m2}, ε_{s1}, ε_{s2}, ε	OK-fv-2	#164
		Dual-heterogeneity	Fixed adsorbed phase volume	ρ_{m1}, ρ_{m2}, ε_{s1}, ε_{s2}, ε	OK-DH	#165
Direct conversi	Constant ρ_a	No-heterogeneity	ρ_a= 373 kg/m^3	-	DC-cr	#166
			ρ_a= 424 kg/m^3	-	DC-cr	#167

on[259]			$\rho_a= \rho_b \exp[-0.0025(T\text{-}T_b)]$ kg/m^3	-	DC-cr	#168
			GCMC-4 nm- carbon	-	DC-cr	#169
			GCMC-4 nm- illite	-	DC-cr	#170
	Constant V_a	No-heterogeneity	-	-	DC-cv	#171

Table F5 Regression variables of Langmuir-SH model considering rock type heterogeneity

	Parameters	Micropore pore volume (%)					
		5%	10%	15%	20%	30%	40%
Langmuir-SH model (SA+0.38 nm)	$P_{L-inorganic}$ (bar)	58.45	59.64	64.19	69.51	82.89	97.09
	$P_{L-organic}$ (bar)	48.49	47.11	43.42	40.05	33.09	27.82
	$\rho_{a-inorganic}$ (kg/m^3)	278.65	273.62	270.67	268.95	267.33	266.95
	$\rho_{a-organic}$ (kg/m^3)	320.48	313.94	309.54	306.55	302.42	300.04